A Structural Investigation of Chlorine-Containing and Fluorine-Containing Oxide Glasses Using Molecular Dynamics, Neutron Diffraction, and X-ray Absorption Spectroscopy

Laura Ann Swansbury

September 2017

A THESIS SUBMITTED TO THE UNIVERSITY OF KENT IN THE SUBJECT OF PHYSICS FOR THE DEGREE OF DOCTOR OF PHILOSOPHY

“One moment of pain is worth a lifetime of glory.”

Louis Zamperini

Abstract

Scientific developments have enabled glasses to fulfil an array of applications, from windows to bioactive glasses in regenerative medicine. To further exploit the capability of this versatile material, it is imperative that their structure is understood. In this thesis, the structure of three glass systems containing halides as anions were investigated. The first of these was the intermediate glass former $ZnCl_2$ which was modelled computationally using classical molecular dynamics (MD). The addition of the adiabatic core-shell model was able to account for anion polarisability. This enabled the first fully tetrahedral model of $ZnCl_2$ glass to be attained. While 86% of the $ZnCl_4$ tetrahedral units were corner-sharing, 14% were found to be edge-sharing. The calculated total neutron and x-ray structure factors closely replicated those obtained experimentally in other works. The intermediate glass former $ZnCl_2$ was later compared to the strong glass former SiO_2. The main contribution in the first sharp diffraction peaks came from the cation-anion contribution, rather than the cation-cation contribution as previously reported.

Next to be investigated was a $CaO\text{-}SiO_2\text{-}CaCl_2$ glass series. This was to help elucidate the structure of more complex $CaO\text{-}SiO_2\text{-}P_2O_5\text{-}CaCl_2$ chlorine-containing bioactive glass compositions. A glass series was synthesised by collaborators, and compositional analysis in this work revealed that chlorine losses via chlorine volatilisation occurred as HCl. The glass series was studied experimentally using neutron diffraction (ND) and x-ray absorption spectroscopy (XAS) at the Ca and Cl K-edge. By probing the calcium environment using ND and XAS, generally good agreement between the Ca-O and Ca-Cl coordination numbers was achieved. The total correlation functions from neutron diffraction did not exhibit a noticeable contribution around 2.1Å which would have been expected for Si-Cl bonding. Computational modelling was performed using MD with the addition of the adiabatic core-shell model. No Si-Cl bonding was observed, and the calculated total neutron structure factors closely resembled those obtained experimentally. The glass models were found to become phase separated with increasing $CaCl_2$ content to form a biphasic system of calcium silicate and calcium chloride phases. Interestingly, there was a tendency towards phase separation even in glass models containing small amounts of $CaCl_2$.

The remaining glass system, $CaO\text{-}SiO_2\text{-}CaF_2$, was studied to help elucidate the structure of more complex $CaO\text{-}SiO_2\text{-}P_2O_5\text{-}CaF_2$ fluorine-containing bioactive glasses. Following the synthesis of the $CaO\text{-}SiO_2\text{-}CaF_2$ glass series, compositional analysis revealed that fluorine losses due to fluorine volatilisation occurred as HF. The calcium environment of the glasses was probed using ND and XAS at the Ca K-edge. Distinguishing the overlapping Ca-F and Ca-O paths around 2.3Å and 2.4Å respectively was challenging. The glass series was modelled computationally using MD with the addition of the adiabatic core-shell model. The calculated

total neutron structure factors closely replicated those from experiment. The glass models also revealed that while fluorine ions overwhelmingly bond with calcium ions, small amounts of Si-F bonding are observed which conceivably cannot be resolved experimentally.

Acknowledgements

This PhD has been long hard slog and I'd like to thank a number of people for helping me through it. First and foremost, I'd like to thank my supervisor Dr. Gavin Mountjoy. You have been incredibly supportive, kind, and patient throughout the PhD. Not only are you the best supervisor and an outstanding lecturer, but you are also a genius. I really look up to you and will sorely miss working with you (and our tea breaks). I am glad that I didn't gain your ambition to try as many different cakes as possible in a lifetime though!

I'd like to say a massive thank you to my family and in particular, my mum and dad. You are amazing and I love you so much. You have worked so hard to provide for me and Matthew and I hope we have made you proud. I'm sure me doing this PhD has been as stressful for you as it has me. When you think about it though, I inherited my work ethic from you. Therefore, you are both to blame for this thesis! My grampy has also always been very supportive, although he does still think that I have exams and long holidays… I wish I had! I also need to thank my brother Matthew and my auntie Debbie for always being there to cheer me up and for their numerous motivational speeches.

I am very fortunate to have such good friends. Sinead; we have shared many good times together ever since the first year of our undergraduate degree. Watching TV is going to be so quiet without you! Sarah, Louise, Toheed, and Stuart thank you for cheering me up when I've been stressed. I need to make up for not seeing you much during the PhD.

Getting back to the PhD, I need to thank our collaborators Xiaojing Chen, Natalia Karpukhina, and Robert Hill at Queen Mary University of London for allowing me to use the $CaO\text{-}SiO_2\text{-}CaCl_2$ glass samples you prepared, for letting me make the $CaO\text{-}SiO_2\text{-}CaF_2$ glass samples in your lab, and for our useful discussions. I've really enjoyed working with you. Other $CaO\text{-}SiO_2\text{-}CaCl_2$ glass samples were prepared by Louis Chungong and Richard Martin at Aston University.

I'd also like to thank Alex Hannon for helping us prepare fusion beads for XRF measurements, for help during our neutron diffraction (ND) experiments, and for our useful discussions regarding ND analysis. Thanks also needs to go to David Apperly at the EPSRC UK National Solid-State NMR Service for performing ^{19}F and ^{29}Si MAS-NMR measurements. I also need to thank the wonderful Tim Kinnear, Phil Whittlesea, and Dave Pickup for their technical advice. I should probably thank the EPSRC for funding too.

Table of Contents

Publications and Presentations

1 Publications

L. A. Swansbury, G. Mountjoy, X. Chen, N. Karpukhina, and R. Hill, "Modelling the Onset of Phase Separation in CaO-SiO_2-$CaCl_2$ Chlorine-Containing Silicate Glasses," *J. Phys. Chem. B*, vol. 121, no. 22, pp. 5647–5653, 2017.

L. A. Swansbury and G. Mountjoy, "A fully tetrahedral and highly corner-sharing network model of $ZnCl_2$ glass and its comparison to SiO_2 glass," *J. Chem. Phys.*, vol. 147, no. 4, p. 44502, 2017.

L. A. Swansbury and G. Mountjoy, "Homogeneity of modifier ion distributions and the mixed alkaline earth effect in MgO-CaO-SiO_2 silicate glasses using molecular dynamics," *Phys. Chem. Glas. Eur. J. Glas. Sci. Technol. B*, vol. 58, no. 4, pp. 165–170, 2017.

L. Forto Chungong, **L. A. Swansbury**, G. Mountjoy, A. C. Hannon, A. F. Lee, and R. A. Martin, "Atomic structure of chlorine containing calcium silicate glasses by neutron diffraction and ^{29}Si solid-state NMR," *Int. J. Appl. Glas. Sci.*, 2017.

2 Conference and Colloquium Presentations

"Molecular Dynamics Modelling of Chlorine-Containing Oxide Glasses", Society of Glass Technology Centenary Conference, Sheffield, UK, 2016.

"Molecular Dynamics Modelling of Chlorine-Containing Oxide Glasses", 13th International Conference on the Structure of Non-Crystalline Materials (NCM13), Halifax, Nova Scotia, Canada, 2016.

"Molecular Dynamics Modelling of Chlorine-Containing Oxide Glasses", School of Physical Sciences Colloquium, Canterbury, UK, 2016. (**Best Postgraduate Colloquium Talk Prize**)

"Molecular Dynamics Modelling of $ZnCl_2$ Glass", School of Physical Sciences Away Day Conference, Canterbury, UK, 2015. (**Best Student Talk Prize**)

"Molecular Dynamics Modelling of $ZnCl_2$ Glass", Society of Glass Technology Glass Reflections Conference, Cambridge, UK, 2015. (**Paul Award for Best Postgraduate Talk**)

3 Poster Presentations

"Molecular Dynamics Modelling of $ZnCl_2$ Glass", School of Physical Sciences Colloquium, Canterbury, UK, 2015.

"Molecular Dynamics Modelling of $ZnCl_2$ Glass", CCP5 Summer School, Manchester, UK, 2015.

1. Introduction

Glass is a strong and often transparent material that we see in our everyday lives and probably take for granted. A glass is defined as a non-crystalline solid that undergoes a glass transition, and far from being new, early glassmaking was discovered around 2300 BC [1]. Three readily available ingredients including sand (silicon dioxide), soda ash or natron (sodium oxide), and lime (calcium oxide) were melted on a fire before being rapidly cooled to form glass [1]. More recently, scientific developments have exploited the versatility of glass, enabling a plethora of applications. Expectedly, window glass is the dominant application with approximately 55 million tonnes of flat glass being produced in 2010 alone (worth an estimated €23 billion) [2]. Additional common applications include container glass, fiber optics, and lighting glass, but glass is also used for more exotic applications that are more obscure. To name but a few, glasses can be used as sealants in solid oxide fuel cells in the energy sector [3], used to drastically increase the strength of concrete in the building sector [4], and even used as bioactive glasses in regenerative medicine [5]. However, in order to fully exploit the capabilities of glass, it is fundamental to understand their structure.

This short chapter briefly introduces the content and assembly of this thesis in which the structure of several glass systems was investigated. Some of the key concepts used to describe glass structure are detailed in chapter 2. In this work, the structure of $ZnCl_2$, $CaO\text{-}SiO_2\text{-}CaF_2$, and $CaO\text{-}SiO_2\text{-}CaCl_2$ glasses were investigated. These glasses will be fully introduced later in the thesis, at the beginning of chapters in which results are presented. The three glass systems all contain halides (i.e. chlorine and fluorine) as anions. In addition, two of the systems are oxide glasses, making this study different from the more frequent studies on oxide glasses that contain only oxide anions.

The first results presented in this thesis are for one of the simplest glass systems involving halides, $ZnCl_2$. Although a number of experimental studies have probed the glass structure of $ZnCl_2$ [6]–[11], there have been fewer computational studies [10]–[13]. In fact, the previous glass models have not been successful in achieving the fully tetrahedral model that is expected. A common technique used to produce glass models for analysis is classical molecular dynamics (MD). Since $ZnCl_2$ is an intermediate glass former, it is important to consider the anion polarisability of chlorine. By incorporating the adiabatic core-shell model into MD simulations, anion polarisability can be accounted for. A detailed description of the key principles and methods behind MD, including the adiabatic core-shell model, can be found in chapter 2. The results of modelling $ZnCl_2$ glass using this approach are presented in chapter 4.

The following two chapters, chapters 5 and 6, present results on the $CaO\text{-}SiO_2\text{-}CaCl_2$ glass system. Recently, complex $CaO\text{-}SiO_2\text{-}P_2O_5\text{-}CaCl_2$ chlorine-containing bioactive glasses have been considered for dental applications such as toothpastes [14], [15], although no structural characterisation has been performed. It is therefore intuitive to first investigate the structure of less complex $CaO\text{-}SiO_2\text{-}CaCl_2$ glasses which have seldom been investigated [14], [15]. Neutron diffraction (ND) and X-ray absorption spectroscopy (XAS) are examples of central facility techniques used to characterise glass structure. These techniques are first described in chapter 3 which details the experimental techniques used in this work. The results of using ND and XAS at the Ca K-edge and the Cl K-edge to probe the $CaO\text{-}SiO_2\text{-}CaCl_2$ glass samples prepared by collaborators are presented in chapter 5. To compliment experimental findings, the glass samples were also modelled computationally using MD with the addition of the adiabatic core-shell model, as described in chapter 6.

The following two chapters, chapters 7 and 8, present results on the $CaO\text{-}SiO_2\text{-}CaF_2$ glass system. Although studies on fluorine-containing bioactive glasses for dental applications have been more numerous than those on chlorine-containing bioactive glasses, their structure continues to be debated e.g. [16], [17]. In particular, the structural role of fluorine is unclear. Less complex $CaO\text{-}SiO_2\text{-}CaF_2$ glasses have predominantly been studied for mould flux applications during the continuous casting of steel. Despite numerous studies, their structure also remains uncertain. Therefore, to help elucidate the structure of complex $CaO\text{-}SiO_2\text{-}P_2O_5\text{-}CaF_2$ fluorine-containing bioactive glasses, it is first intuitive to investigate the $CaO\text{-}SiO_2\text{-}CaF_2$ glass structure. As presented in chapter 7, a $CaO\text{-}SiO_2\text{-}CaF_2$ glass series was synthesised and characterised in this work. Details on the synthesis and the laboratory-based characterisation methods are given in chapter 3. Chapter 7 also presents the results of using ND and XAS at the Ca K-edge to probe the $CaO\text{-}SiO_2\text{-}CaF_2$ glass structures. As detailed in chapter 8, it was of interest to model the glass series computationally to compliment experimental findings. For consistency, the $CaO\text{-}SiO_2\text{-}CaF_2$ and $CaO\text{-}SiO_2\text{-}CaCl_2$ glass series were modelled using the same computational method with a consistent set of interatomic potential parameters.

Finally, chapter 9 summarises and discusses the key results attained in this work. In addition, comparisons are made between the experimental and computational results for each of the $CaO\text{-}SiO_2\text{-}CaF_2$ and $CaO\text{-}SiO_2\text{-}CaCl_2$ glass series. Furthermore, comparisons are also made between the $CaO\text{-}SiO_2\text{-}CaF_2$ and $CaO\text{-}SiO_2\text{-}CaCl_2$ glass series. Some comments regarding future work are also provided. As noted in the Publications and Presentations section, some of the work in this thesis has now been published.

References

[1] K. T. Luckner, “Ancient glass,” *Art Inst. Chicago Museum Stud.*, vol. 20, no. 1, pp. 79–

91, 1994.

[2] NSG Group, “The Glass Industry.” [Online]. Available: http://www.nsg.com/en/about-nsg/whatwedo. [Accessed: 14-Dec-2017].

[3] C. Lara, M. J. Pascual, and A. Duran, “Glass-forming ability, sinterability and thermal properties in the systems RO-BaO-SiO_2 (R= Mg, Zn).,” *J. Non. Cryst. Solids*, vol. 348, pp. 149–155, 2004.

[4] S. Cangiano, A. Meda, and G. A. Plizzari, “Rapid hardening concrete for the construction of a small span bridge,” *Constr. Build. Mater.*, vol. 23, no. 3, pp. 1329–1337, 2009.

[5] J. Jones and A. Clare, *Bio-Glasses: An Introduction*. John Wiley & Sons, 2012.

[6] J. Wong and F. W. Lytle, “EXAFS studies of glassy and liquid ZnCl2: A comparison with vitreous GeO2,” *J. Non. Cryst. Solids*, vol. 37, pp. 273–284, 1980.

[7] M. Wilson and P. Madden, “Voids, Layers, and the First Sharp Diffraction Peak in $ZnCl_2$,” *Phys. Rev. Lett.*, vol. 80, no. 3, pp. 532–535, 1998.

[8] S. N. Yannopoulos, A. G. Kalampounias, A. Chrissanthopoulos, and G. N. Papatheodorou, “Temperature induced changes on the structure and the dynamics of the ‘tetrahedral’ glasses and melts of ZnCl2 and ZnBr2,” *J. Chem. Phys.*, vol. 118, no. 7, pp. 3197–3214, 2003.

[9] P. S. Salmon, R. A. Martin, P. E. Mason, and G. J. Cuello, “Topological versus chemical ordering in network glasses at intermediate and extended length scales.,” *Nature*, vol. 435, no. 7038, pp. 75–78, 2005.

[10] A. Zeidler *et al.*, “Structure of liquid and glassy $ZnCl_2$,” *Phys. Rev. B - Condens. Matter Mater. Phys.*, vol. 82, pp. 1–17, 2010.

[11] A. Zeidler *et al.*, “Structure of the network glass-former $ZnCl_2$: From the boiling point to the glass,” *J. Non. Cryst. Solids*, vol. 407, pp. 235–245, 2015.

[12] P. N. Kumta, P. A. Deymier, and S. H. Risbud, “Improved Rigid Ion Model of Molten Zinc Chloride,” *Phys. B Condens. Matter*, vol. 153, pp. 85–92, 1988.

[13] L. Pusztai and R. L. McGreevy, “The Structure of Glassy Zinc Chloride: A Reverse Monte Carlo Study,” *J. Non. Cryst. Solids*, vol. 117/118, pp. 627–630, 1990.

[14] X. Chen, N. Karpukhina, D. S. Brauer, and R. G. Hill, “Novel Highly Degradable Chloride Containing Bioactive Glasses,” *Biomed. Glas.*, vol. 1, no. 1, pp. 108–118, 2015.

[15] X. Chen, “Novel Halide Containing Bioactive Glasses,” Queen Mary University of London, 2015.

[16] D. S. Brauer, N. Karpukhina, R. V. Law, and R. G. Hill, “Structure of fluoride-containing bioactive glasses,” *J. Mater. Chem.*, vol. 19, no. July 2016, p. 5629, 2009.

[17] A. Pedone, T. Charpentier, and M. C. Menziani, “The structure of fluoride-containing bioactive glasses: New insights from first-principles calculations and solid state NMR spectroscopy,” *J. Mater. Chem.*, vol. 22, no. 25, pp. 12599–12608, 2012.

2. Background of Glass Structure and Computational Methodology

2.1 Glass Structure

Both glass and crystalline structures can be formed by cooling a melt. If a melt is cooled slowly, a sudden significant decline in volume at the melting temperature of the material leads to the formation of a crystalline structure (figure 1) which has long-range order. If instead a melt is cooled rapidly, there is no abrupt change in volume and the melt becomes a supercooled liquid below its melting temperature. The structure of the supercooled liquid changes continuously as the temperature declines until the increasing viscosity prevents the atoms from rearranging further. At this point, the supercooled liquid becomes a solid glass with no long-range order. The region between which the viscosity of the supercooled liquid increases until the atoms can no longer rearrange themselves is referred to as the glass transformation region [1]. Glasses are therefore non-crystalline amorphous solids that undergo a glass transition. Most glasses are based on silicates, and the ubiquitous glass former SiO_2 for example comprises of silicon ions that are covalently bonded with oxygen ions to form tetrahedral SiO_4 structural units.

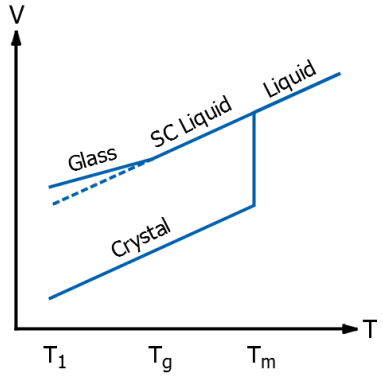

Figure 1: Volume-Temperature plot of glass and crystal formation. The term 'SC Liquid' denotes a supercooled liquid. The terms T_1, T_g, and T_m refer to room temperature, glass transition temperature, and melting temperature respectively.

Zachariasen's [2] early random network model (RNM) on glass structure primarily focussed on A_mO_n oxide glasses (e.g. SiO_2 glass), where 'A' refers to a cation. The RNM proposed that a glass structure is a modification of its corresponding crystalline structure. As corner-sharing polyhedral structural units are often observed in crystalline oxide structures, the RNM suggested that this corner-sharing must also be fundamental in the oxide glass structure. The structural difference between a glass and its corresponding crystal was attributed to A-O-A

bond angle variation in the glass which was not observed in the crystalline structure (figure 2). The RNM also assumed that modifier ions simply went into gaps in the glass network. The RNM was later developed to explicitly include modifier ions such as alkaline earth ions, and referred to as the modified random network (MRN) model [3]. The MRN model proposed that the modifier ions form channels in the glass network. This caused more obvious disruption to the glass network (figure 3).

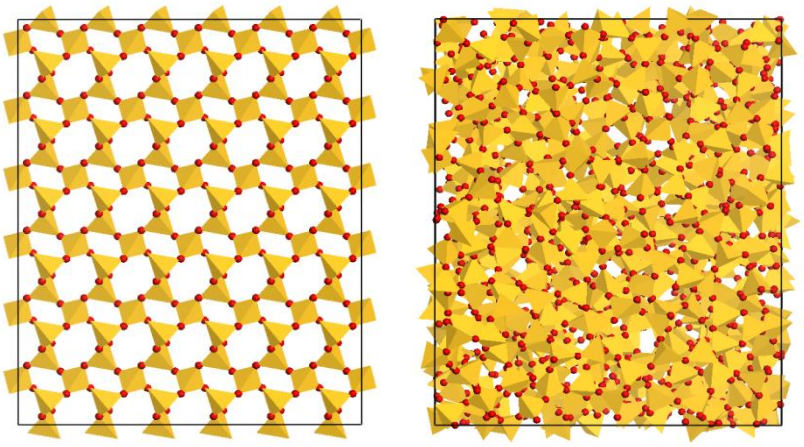

Figure 2: Crystalline α-SiO_2 to the left and SiO_2 glass to the right. The yellow tetrahedra represent silicon ions and the red spheres correspond to oxygen ions.

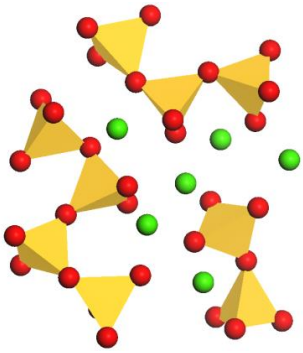

Figure 3: The SiO_2 glass network being disrupted by the substitution of calcium ions such as in a calcium silicate glass. The yellow tetrahedra represent silicon ions, and the red and green spheres correspond to oxygen and calcium ions respectively.

2.2 Glass Structure Characterisation

Since glasses have no long-range order, it is necessary to use statistical averages to describe their structure. The glass structural characterisation techniques applied in this work are detailed below, and can be achieved computationally. Most can also be achieved experimentally.

2.2.1 Real-Space Correlation Functions

Real-space correlation functions illustrate the probability of finding an atom at a particular distance r from a reference atom. They are used to identify the average separation distances between two atoms in a correlation and can be described in different ways mathematically. To begin the derivation of these real-space correlation functions, a system of atomic number density ρ^0 is considered. The atomic number density ρ^0 can be calculated according to equation 1, where the terms N and V correspond to the number of atoms in the system and the system volume respectively.

$$\rho^0 = \frac{N}{V} \qquad \text{Equation 1}$$

If a spherical shell of radius r and thickness Δr (where $r \gg \Delta r$) is then considered around a reference atom (figure 4), the volume of that spherical shell, v, can be calculated using equation 2. With the knowledge of the atomic number density and the spherical shell volume, the average number of atoms, n, contained within that spherical shell can be determined using equation 3. Equation 3 can be rearranged to yield equation 4.

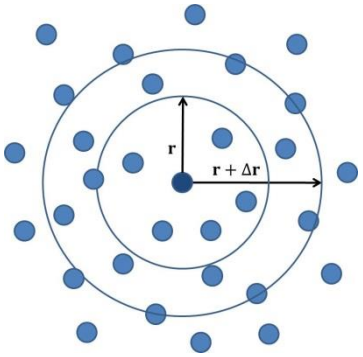

Figure 4: Illustration of a shell of radius r and thickness Δr around a reference atom.

$$v = 4\pi r^2 \Delta r \qquad \text{Equation 2}$$

$$n = 4\pi r^2 \Delta r \rho^0 \qquad \text{Equation 3}$$

$$\frac{n}{\Delta r} = 4\pi r^2 \rho^0 \qquad \text{Equation 4}$$

Whilst the average atomic number density of the system remains constant, the radial density $\rho(r)$ would vary as a function of r. By considering equation 4 in terms of a radial density function, an expression for the radial distribution function, $j(r)$, can be obtained (equation 5).

$$j(r) = 4\pi r^2 \rho(r) \qquad \text{Equation 5}$$

Dividing the radial distribution function in equation 5 by the radial distance r yields the total correlation function, $g_{tot}(r)$, which is shown in equation 6.

$$g_{tot}(r) = \frac{j(r)}{r} = 4\pi r\rho(r) \quad \text{Equation 6}$$

The average total correlation function, $g_{tot}{}^{0}(r)$, can be calculated using equation 7.

$$g_{tot}{}^{0}(r) = 4\pi r\rho^{0} \quad \text{Equation 7}$$

By subtracting equation 7 from equation 6, the differential correlation function, $d(r)$, can be defined (equation 8). These different types of real-space correlation functions are illustrated in figure 5.

$$d(r) = g_{tot}(r) - g_{tot}{}^{0}(r) = 4\pi r[\rho(r) - \rho^{0}] \quad \text{Equation 8}$$

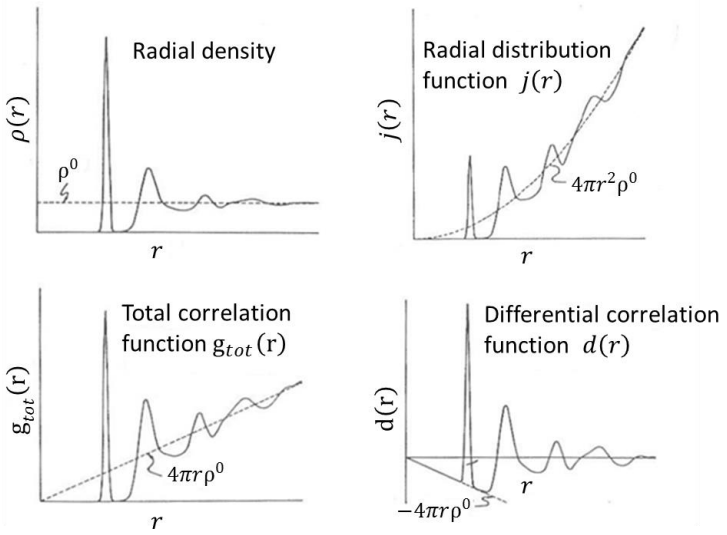

Figure 5: Examples of the different types of real-space correlation functions modified from [4].

For multicomponent systems, it is common to calculate the pair correlation functions, $g_{ij}(r)$, between two atom types (i and j). This can be achieved using equation 9, where $\rho_{ij}(r)$ is the number density of type i atoms at a distance r from the type j atoms. These pair correlation functions can be weighted according to the concentration of atom type i (denoted as c_i), and summed to form a total correlation function as shown in equation 10.

$$g_{ij}(r) = 4\pi r\rho_{ij}(r) \quad \text{Equation 9}$$

$$g_{tot}(r) = \sum_i \sum_j c_i g_{ij}(r) \quad \text{Equation 10}$$

2.2.2 Cumulative Coordination Numbers

The integration of a pair correlation function yields a cumulative coordination number plot as shown in figure 6. By applying an appropriate cut-off distance to the cumulative coordination number plot, the coordination number, $N_{ij}(r)$, can be obtained. A coordination number is defined as the average number of type j atoms surrounding a type i atom within the applied cut-off distance and is described mathematically using equation 11. In the case of figure 6, an appropriate cut-off distance in the Si-O pair correlation function would be 2Å. As shown by the cumulative coordination number plot, this corresponds to a coordination number of 4. Hence, on average, there are four oxygens ions surrounding each silicon ion as expected for a tetrahedral structural unit.

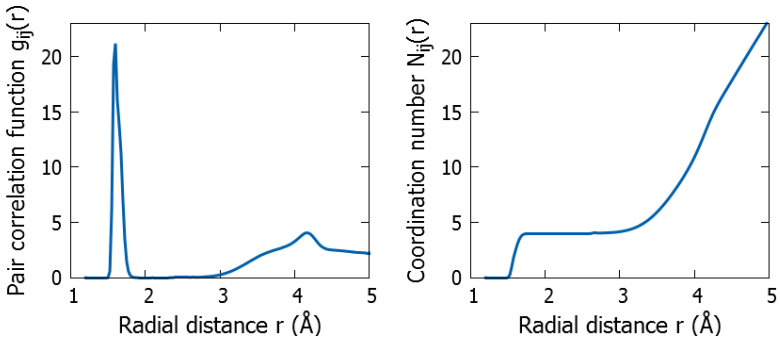

Figure 6: A pair correlation function (left) and a cumulative coordination number plot (right) for the Si-O correlation in $CaSiO_3$ glass.

$$N_{ij}(r) = \int_0^{r_{cut}} g_{ij}(r) r dr \qquad \text{Equation 11}$$

2.2.3 Structure Factors

Structure factors can be obtained from scattering experiments in order to obtain information about pair correlation functions. While the theory behind X-ray and neutron scattering is detailed in chapter 3, some initial details on structure factors are provided here. For glass systems, the total structure factor, $S(Q)$, can be defined by equation 12 [5], where Q is the magnitude of the scattering vector. The term ω_{ij} refers to a weighting factor involving atom types i and j of concentration c_j, and the term δ_{ij} is a Kronecker delta function. The weighting factors in equations 13 and 14 relate to neutron and X-ray scattering respectively, where the term b is the neutron scattering length and the term Z is the atomic number. A total structure factor can be Fourier transformed to obtain a total correlation function as shown in equation 15.

$$S(Q) = 1 + \int_0^{\infty} \sum_{ij} \frac{\omega_{ij}}{c_j} \left(g_{ij}(r) - 4\pi r \rho_j\right) \frac{\sin(Qr)}{Q} dr \qquad \text{Equation 12}$$

$$\omega_{ij} = \frac{(2-\delta_{ij})c_i c_j b_i b_j}{[\bar{b}]^2}$$ Equation 13

$$\omega_{ij} = \frac{(2-\delta_{ij})c_i c_j Z_i Z_j}{[\bar{Z}]^2}$$ Equation 14

$$g_{tot}(r) = 4\pi r\rho^0 + \frac{2}{\pi}\int_0^\infty Q(S(Q)-1)\sin(Qr)\,dQ$$ Equation 15

The contribution of each correlation in the total structure factor can be calculated using equation 16, where $S_{ij}^{FZ}(Q)$ is the partial Faber-Ziman structure factor. The corresponding pair correlation functions can also be calculated in accordance with equation 17.

$$S_{ij}^{FZ}(Q) = 1 + \int_0^\infty \frac{1}{c_j}\left(g_{ij}(r) - 4\pi r\rho_j\right)\frac{\sin(Qr)}{Q}\,dr$$ Equation 16

$$g_{ij}(r) = 4\pi r\rho^0 + \frac{2}{\pi}\int_0^\infty \left[S_{ij}^{FZ}(Q)-1\right]Q\sin(Qr)\,dQ$$ Equation 17

2.2.4 Bond Angle Distributions

Bond angle distribution functions illustrate the probability of obtaining a particular bond angle between three bonded atoms. The O-Si-O bond angle in a tetrahedral SiO_4 structural unit for example is typically 110° as shown in figure 7. This corresponds to the ideal tetrahedral bond angle [6].

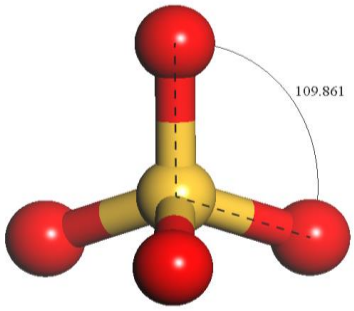

Figure 7: A SiO_4 tetrahedral structural unit where the yellow and red spheres correspond to silicon and oxygen ions respectively. The O-Si-O bond angle is shown.

2.2.5 Silicon Network Connectivity

The silicon network connectivity, Q^n, refers to the number of bridging oxygens n per silicon tetrahedra [1], where a bridging oxygen connects two network polyhedra together. As shown in figure 8, a silicon tetrahedra surrounded by four bridging oxygens would be fully connected in the silicate network and denoted as Q^4. Conversely, a non-bridging oxygen does not connect two network polyhedra together. A silicon tetrahedra surrounded by four non-bridging oxygens would be segregated in the silicate network and denoted as Q^0. By calculating the different Q^n concentrations, average Q^n values can be obtained. These

average Q^n values elucidate the average connectivity of the silicate network. For example, $CaSiO_3$ glass is a metasilicate and on average, its glass network is made up of Q^2 species [7].

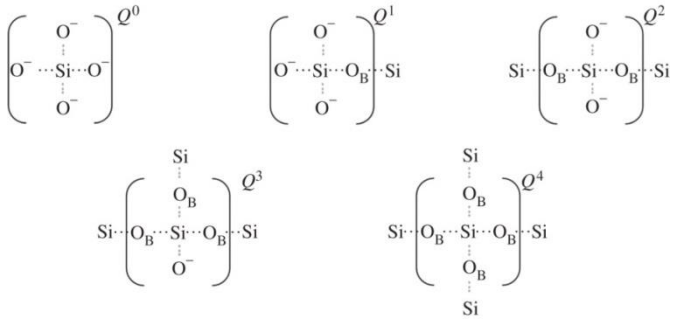

Figure 8: Schematic of the different Q^n species in a silicate network from [8].

2.3 Molecular Dynamics Simulations

Two types of molecular dynamics simulation used to attain computational models of glass (whose structure can be elucidated using the techniques in section 2.2) are classical and first principles molecular dynamics. Classical molecular dynamics relies on the laws of classical physics and involves considering atoms to be rigid spheres which interact according to given interatomic potential parameters [9]. As a result, electrons are not considered and point charges are assigned to the spheres instead. This reduces the computational cost of running a simulation, and enables large system sizes (often of thousands of atoms) to be modelled over relatively long timescales.

In contrast, first principles simulations use quantum mechanics to consider the electron wavefunctions of atoms [10]. This improves the accuracy of the simulation, but comes at a significant computational cost. As a result, the model sizes are limited to a few hundred atoms and simulations can only be performed over relatively short timescales.

A different type of computational simulation is reverse Monte Carlo modelling (RMC) [9] which relies on experimental diffraction data. During a RMC simulation, a randomly chosen atom from the configuration is displaced by a random amount. If this atom displacement improves the agreement with experimental diffraction findings, then this new atom position gets accepted. If instead the agreement with experimental findings deteriorates, then the atom move may be rejected and the old atomic configuration retained. There remains however some probability that this atom displacement will still be accepted. This process of displacing a random atom is repeated large numbers of times to ultimately reproduce the experimental results.

In this thesis, all computational simulations were run using classical molecular dynamics. This is because large system sizes can be modelled without bias towards experimental results.

The rest of this chapter focusses on the considerations involved in running classical molecular dynamics simulations, and the general method of how these simulations were performed in this work. The particular details of each simulation are presented in the results chapters.

2.3.1 Types of Atomic Interactions

The atomic interactions in a system of atoms are governed by the potential energy, V which can be written as a series expansion of two-body, three-body, etc. terms [10]. Since the two-body interactions dominate, they can be used to approximate the potential energy, although three-body and higher terms are still sometimes incorporated [10]. The two-body interactions can be separated into long-range and short-range interactions. The long-range interactions are defined using Coulomb's law (equation 18), where q_i and q_j are the charges on ions i and j respectively, r is the separation between the ions, and ϵ_0 is the permittivity of free space. This Coulomb interaction can be an attractive or repulsive term depending on the charges of the ions involved in the interaction. If both charges are positive, or both are negative, then the interaction will be repulsive. If one of the charges is positive and the other is negative, then the interaction will be attractive.

$$V_{ij}(r) = \frac{q_i q_j}{4\pi\epsilon_0 r} \qquad \text{Equation 18}$$

The short-range interactions are more complex and take account of the Pauli exclusion principle and the van der Waals interaction. The Pauli exclusion principle states that no two electrons can occupy the same state. Hence, when electron clouds begin to overlap, there is an increase in energy which manifests as a repulsive term to discourage the overlapping of electron clouds. The van der Waals interaction is caused by induced dipole/induced dipole interactions. This van der Waals interaction is generally an attractive interaction, although it may become repulsive if the ions get too close to each other. This is because the nuclei of the ions will repel, superseding any attractive contribution.

Three common short-range interatomic potential forms include the Born-Mayer, Lennard-Jones, and Buckingham interatomic potentials. The Born-Mayer interatomic potential accounts for the Pauli exclusion principle but fails to consider any van der Waals interaction. The Born-Mayer interatomic potential is shown in equation 19 where the terms A and ρ are variable parameters.

$$V_{ij}(r) = A_{ij}\exp\left(\frac{-r}{\rho_{ij}}\right) \qquad \text{Equation 19}$$

The Lennard-Jones interatomic potential is specified in equation 20 and accounts for both the Pauli exclusion principle and the van der Waals interaction using the variable parameters A and C respectively.

$$V_{ij}(r) = \frac{A_{ij}}{r^{12}} - \frac{C_{ij}}{r^{6}}$$ Equation 20

The Buckingham form is a combination of the Born-Mayer form and the Lennard-Jones form and is given in equation 21. The variable parameters A and ρ relate to the Pauli exclusion principle while the parameter C relates to the van der Waals interaction. Since this Buckingham equation contains three variable parameters, it can better represent the shape of the potential well compared to the Lennard-Jones interatomic potential. The two-body interatomic potentials used throughout this thesis were therefore of Buckingham form. By considering the distance dependence in the Coulomb and Buckingham interatomic potentials, a potential energy curve can be plotted (figure 9).

$$V_{ij}(r) = A_{ij}\exp\left(\frac{-r}{\rho_{ij}}\right) - \frac{C_{ij}}{r^{6}}$$ Equation 21

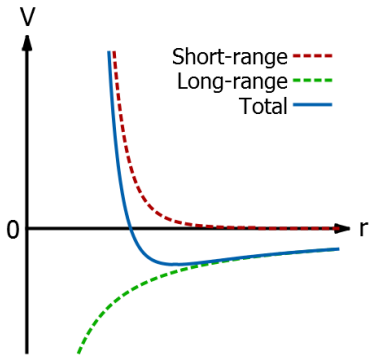

Figure 9: Plot of the short-range (Buckingham), long-range (Coulomb), and combined interatomic potential V as a function of distance r.

Three-body interatomic potentials involve the direct bonding of ions. Three body potentials not only take into account the distance between ions, but also their relative orientations [11]. Three-body interactions involving ions j, i, and k (where i is the central atom) of screened harmonic form [12] were used in this work and are defined using equation 22. The term k is a force constant, while θ_{jik} is the bond angle involving ions j, i and k, and θ_0 is the equilibrium bond angle. The terms r_{ij} and r_{ik} correspond to the separation distances between ions i and j, and between ions i and k respectively. The remaining term ρ is the potential cut-off distance.

$$V(\theta_{jik}) = \frac{k}{2}(\theta_{jik} - \theta_0)^2 \exp\left[-\left(\frac{r_{ij}}{\rho} + \frac{r_{ik}}{\rho}\right)\right]$$ Equation 22

2.3.2 Ion Polarisability

Since the ions in classical molecular dynamics simulations are solid spheres which do not get deformed, it can be challenging to reproduce the effects of ion polarisability. One approach

to overcome this is to use the polarisable ion model (PIM), where the dipole strength and orientation fluctuate throughout the simulation [13]. Another approach is to use the core-shell model [14] which is illustrated in figure 10. The core-shell model involves splitting an ion into a core and a shell unit, where the two are connected by a harmonic spring. The harmonic spring can be described using Hooke's Law in equation 23, where the force F is proportional to the displacement r of the ion shell from the ion core according to the spring constant $\mathrm{K_{cs}}$. The shell unit can either be massless (dynamic shell-model), or have a small proportion of the ion's mass (adiabatic core-shell model). As the ion charge is distributed between the core and shell units (where the core is assigned a positive charge and the shell is assigned a negative charge), the shell movement can replicate ion polarisation.

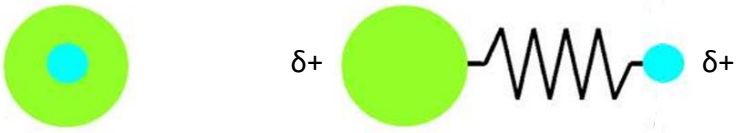

Figure 10: Illustration of an unpolarised ion (left) and a polarised ion (right). The green and blue circles correspond to ion cores and shells respectively and are connected by a harmonic spring.

$$\mathrm{F} = -\mathrm{K_{cs}r} \qquad \text{Equation 23}$$

Although the application of the core-shell model is known to increase the computational cost of running a simulation, the adiabatic core-shell model was applied in this work. In order to help balance the accuracy of the model against the computational cost, the core-shell model was only applied to anions in a simulation. This was because anions are more susceptible to ion polarisation due to their larger ionic radii as shown for the ions in this study in table 1.

Table 1: The ions involved in this work, and their corresponding ion polarisabilities [15], ionic radii [16], [17], and atomic masses [18].

Ion	Polarisability (Å^3)	Ionic radius (Å)	Atomic mass (u)
Si^{4+}	0.333	0.34	28.086
Zn^{2+}	0.340	0.74	65.38
Ca^{2+}	0.482	1.20	40.08
F^{1-}	1.295	1.25	18.998
O^{2-}	1.988	1.32	15.9994
Cl^{1-}	4.65	1.72	35.453

As the application of the core-shell model is known to sometimes cause instabilities, it may at times be appropriate to the apply frictional damping to the harmonic spring connecting the core and corresponding shell units [19], [20]. This can be implemented by adding a damping term to the force equation (equation 23) for the core-shell harmonic spring as

shown in equation 24, where the terms c and t are the damping coefficient and time respectively.

$$F = -c\frac{dr}{dt} - K_{cs}r \qquad \text{Equation 24}$$

2.3.3 Testing Atomic Interactions

The General Utility Lattice Program [21] (GULP) can be used to test the performance of interatomic potential parameters. This involves energy minimising known crystalline structures using the given interatomic potential parameters to form output structures. These energy-minimised output structures are then compared to the input crystalline structures, and the differences between them used to assess the performance of the given interatomic potential parameters. Interatomic potential parameters should preferably only cause minimal change to an input crystalline structure.

The GULP program was used in this work, but only an introductory overview of energy minimisation is provided below. More detailed descriptions can be found in [10], [21]. Energy minimisation is an iterative process which involves locating local minima in the potential energy landscape. This can be achieved using a Newton Raphson approach where a point on the potential energy landscape (written as a Taylor series expansion) iteratively approaches a local minimum. When a point (k) is close to a local minimum in the potential energy landscape, the system will behave harmonically and so the Taylor series expansion can be truncated at the second order as shown in equation 25.

$$V(x) = V(x_k) + (x - x_k)V'(x_k) + \frac{1}{2}(x - x_k)^2V''(x_k) \qquad \text{Equation 25}$$

The derivative of equation 25 is given in equation 26.

$$V'(x) = V'(x_k) + (x - x_k)V''(x_k) \qquad \text{Equation 26}$$

At a minimum point '*', equation 25 can be expressed using equation 27.

$$V(x) = V(x^*) + \frac{1}{2}(x - x^*)^2V''(x^*) \qquad \text{Equation 27}$$

The derivative of equation 27 is given by equation 28.

$$V'(x) = (x - x^*)V''(x^*) \qquad \text{Equation 28}$$

By using equations 26 and 28, together with the knowledge that for a purely quadratic equation $V''(x) = V''(x_k)$, equation 29 can be obtained.

$$V'(x_k) + (x - x_k)V''(x_k) = (x - x^*)V''(x_k) \qquad \text{Equation 29}$$

Rearranging equation 29 yields a Newton Raphson form (equation 30). For a multidimensional system, this Newton Raphson form is given by equation 31, where $\mathbf{V''^{-1}(x_k)}$ is the inverse of the Hessian matrix and $\mathbf{V'(x_k)}$ is the gradient vector.

$$x^* = x_k - V''^{-1}(x_k)\, V'(x_k) \qquad \text{Equation 30}$$

$$\mathbf{x^* = x_k - V''^{-1}(x_k)\, V'(x_k)} \qquad \text{Equation 31}$$

The mathematical approach used in GULP is similar to that described above, but is complicated by considerations being made for the potential energy surface not being harmonic, and the point k being far from a minimum.

2.3.4 Finite System Sizes

When simulating a limited number of atoms within a defined simulation cell, it is important to consider that the forces acting on atoms closer to the face of the simulation cell may be different to those that are surrounded by other atoms [22]. To help ensure that all atoms behave as though they are in a bulk, periodic boundary conditions can be applied. Periodic boundary conditions were applied to all simulations in this work and involve creating an infinite number of replicas of the simulation cell. The atoms within each of the replicas have the identical trajectories to those in the central cell. In the case that an atom leaves the central simulation cell, another atom is brought into that central cell from one of the surrounding replicas, and will enter from the opposite face to which the atom left (figure 11). This ensures the number density of the simulation cell remains constant.

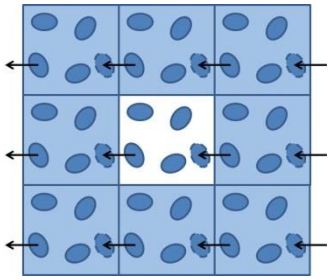

Figure 11: An illustration of periodic boundary conditions which has been adapted from [22].

The difficulty with applying periodic boundary conditions is that there are now an infinite number of interactions that need to be considered. Not only do the atoms in the central cell interact with other atoms in that central simulation cell, but each atom in the central cell also interacts with the other atoms in the replicas of the central simulation cell. It is therefore necessary to approximate these interactions to minimise the computational cost of running a simulation. This was achieved using potential truncation, neighbour lists, and the Ewald summation method in this work.

Potential truncation is used to approximate the short-range interactions by using minimum image convention [22]. A region of the same dimensions as the simulation cell is considered around each of the atoms in the central simulation cell as shown in figure 12. Only considering the interactions within each of these regions would significantly reduce the computational cost of running a simulation. The computational expense can be reduced further by only considering the interactions within a spherical shell of radius r_c within each region, where the r_c is less than half the length of the simulation cell. Not only can the maximum interaction radius r_c be imposed, but a minimum interaction radius can also be imposed. This would help prevent atoms from getting unphysically close to each other, improving simulation stability.

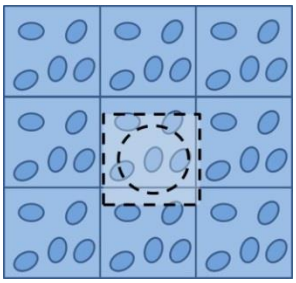

Figure 12: An illustration of potential truncation which has been adapted from [22].

Verlet proposed that the number of atomic interactions considered could be reduced by implementing a neighbour list [23]. This approach involves considering a cut-off radius r_{v1} and a larger cut-off radius r_{v2} around each atom in the simulation cell. The atoms within r_{v2} of each atom are used to make a neighbour list. Since the atoms neighbouring a reference atom do not vary significantly over 10 or 20 time-steps [10], the neighbour list is only updated at regular intervals. During these intervals, the atomic interactions between each atom and its neighbouring atoms within r_{v1} are calculated at each time-step. Hence, it is important that the neighbour array gets updated often enough to prevent atoms outside r_{v2} from moving to within r_{v1}, without being updated too often which would make the process inefficient.

The Ewald summation method can be used to approximate the long-range interactions. The Ewald summation method begins by considering the Coulomb interactions within the central simulation cell, and between the central simulation cell and the surrounding replicas of the simulation cell according to equation 32. In equation 32, n refers to the central simulation cell, and the notation $\sum'_{|n|=0}$ corresponds to the $i = j$ interaction being omitted for the central simulation cell.

$$V = \frac{1}{2}\sum'_{|n|=0}\sum_{i=1}^{N}\sum_{j=1}^{N}\frac{q_i q_j}{4\pi\varepsilon_0|r_{ij}+n|} \qquad \text{Equation 32}$$

The summation in equation 32 is conditionally convergent and the Coulomb interaction can vary significantly for small separation distances [9]. To overcome this, the summation in equation 32 can be split into two components which each converge more rapidly using the identity in equation 33 (which is illustrated in figure 13), where the term $\mathrm{f(r)}$ is a function. Equation 33 is capable of accounting for a rapidly changing $\frac{1-\mathrm{f(r)}}{\mathrm{r}}$ contribution for small values of r, and a slowly changing $\frac{\mathrm{f(r)}}{\mathrm{r}}$ contribution for larger values of r [9].

$$\frac{1}{\mathrm{r}} = \frac{\mathrm{f(r)}}{\mathrm{r}} + \frac{1-\mathrm{f(r)}}{\mathrm{r}}$$ Equation 33

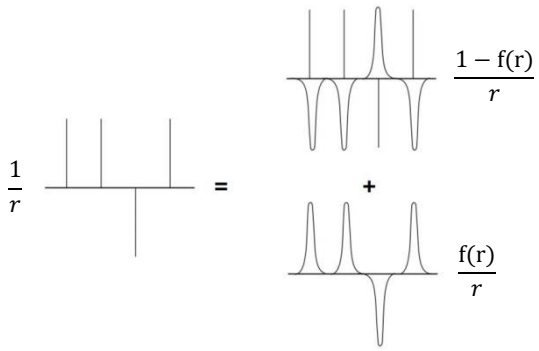

Figure 13: An illustration of the addition of Gaussian distributions in real space, and cancelling distributions in reciprocal space from [9].

Each point charge in the summation gets surrounded by a Gaussian charge distribution $-\mathrm{f(r)}$ of equal and opposite magnitude. These Gaussian charge distributions effectively shield each point charge. As a result, each point charge becomes short ranged and can be readily summed in real-space. In order to counterbalance this applied shielding, Gaussian charge distributions $\mathrm{f(r)}$ of equal and opposite charge to those initially considered are also included. As the Fourier transforms of these new Gaussian distributions converge more rapidly, it is preferable to evaluate their summation in reciprocal space. In computational simulations, the rate at which the series converges is determined by the width of the Gaussian distributions in accordance with the convergence parameter α [12].

2.3.5 Newton's Equations of Motion and Finite Difference Methods

A classical molecular dynamics simulation involves studying a system of atoms over a given period of time. The atoms within the system interact according to defined interatomic potential parameters, and abide by Newton's equations of motion. These are shown for a simple one-dimensional case along the x-axis in equations 34-36. In order to facilitate a classical molecular dynamics simulation, the initial atomic configuration first needs to be established. The atomic configuration is confined within a simulation cell of volume

corresponding to the desired density; and can be either arranged randomly, or according to a crystalline structure. A velocity v is then assigned to each of the atoms, ensuring the total momentum of the system is zero. The forces F on each of the atoms in the system can then be determined by differentiating the potential energy function V using equation 36. As the simulation progresses, the atom positions x begin to change. Subsequently, when an atom position changes, the forces exerted on it, and on any other atoms that interact with it also change. This creates a many-body problem which cannot be solved analytically [10]. Instead, the problem can be solved numerically using a finite difference method.

$$\mathrm{x}(\mathrm{t}+\Delta\mathrm{t}) = \mathrm{x}(\mathrm{t}) + \mathrm{v}(\mathrm{t})\Delta\mathrm{t} + \frac{1}{2}\frac{\mathrm{d}^2\mathrm{x}(\mathrm{t})}{\mathrm{dt}^2}(\Delta\mathrm{t})^2 \qquad \text{Equation 34}$$

$$\mathrm{v}(\mathrm{t}+\Delta\mathrm{t}) = \mathrm{v}(\mathrm{t}) + \frac{\mathrm{d}^2\mathrm{x}(\mathrm{t})}{\mathrm{dt}^2}\Delta\mathrm{t} \qquad \text{Equation 35}$$

$$\mathrm{F}(\mathrm{t}) = \mathrm{m}\frac{\mathrm{d}^2\mathrm{x}(\mathrm{t})}{\mathrm{dt}^2} = -\frac{\mathrm{dV}(\mathrm{x}(\mathrm{t}))}{\mathrm{dx}} \qquad \text{Equation 36}$$

A finite difference method involves approximating the solutions to partial differential equations on a grid by using the differences between values at neighbouring grid points [24]. These finite difference formulae may be obtained using a Taylor series expansion, and enable the atom trajectories in a classical molecular dynamics simulation to be calculated. One example of a finite difference method is the Verlet algorithm which is detailed in [9]. As shown in equation 37 and illustrated in figure 14, the Verlet algorithm works by using the current atom positions and accelerations at time t, as well as the previous atom positions at time $\mathrm{t} - \Delta\mathrm{t}$ to compute the new atom positions at time $\mathrm{t} + \Delta\mathrm{t}$. The process is then repeated at time $\mathrm{t} + 2\Delta\mathrm{t}$ and so on.

$$\mathrm{x}(\mathrm{t}+\Delta\mathrm{t}) = 2\mathrm{x}(\mathrm{t}) - \mathrm{x}(\mathrm{t}-\Delta\mathrm{t}) + \frac{\mathrm{F}(\mathrm{t})}{\mathrm{m}}\Delta\mathrm{t}^2 \qquad \text{Equation 37}$$

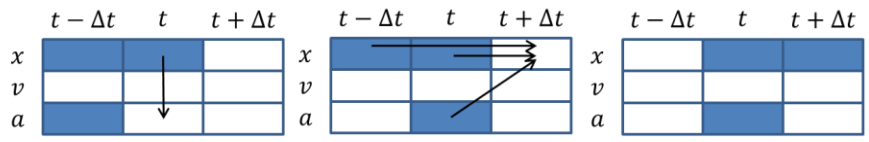

Figure 14: As reproduced from [22], an illustration of how the Verlet algorithm works. The rectangles shaded in blue correspond to the variables stored during a simulation. The arrows correspond to the variables that are used to compute the updated variables.

The disadvantage of the Verlet algorithm is that it does not explicitly involve the calculation of the atom velocities. This can be overcome using the Verlet leap-frog algorithm (equations 38 and 39) which was used in this work. In the Verlet leap-frog algorithm, the atom velocities at half integer time-steps are explicitly calculated to establish the new atom positions at integer time-steps. This means that the atom velocities and positions do not get calculated for the same time, causing the atom velocities to 'leap-frog' over the atom positions, before the atom positions later 'leap-frog' over the atom velocities as illustrated in figure 15.

However, by averaging the atom velocities in accordance with equation 40, the velocities at integer time-steps can be calculated.

$$v\left(t+\frac{\Delta t}{2}\right)=v\left(t-\frac{\Delta t}{2}\right)+\frac{F(t)}{m}\Delta t \qquad \text{Equation 38}$$

$$x(t+\Delta t)=x(t)+\ v\left(t+\frac{\Delta t}{2}\right)\Delta t \qquad \text{Equation 39}$$

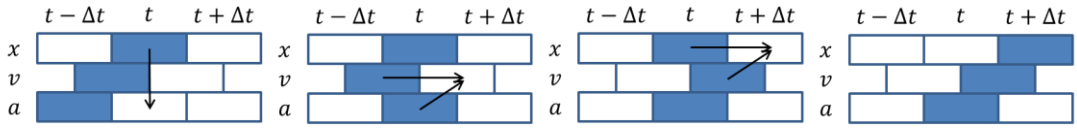

Figure 15: As reproduced from [22], an illustration of how the Verlet leap-frog algorithm works. The rectangles shaded in blue correspond to the variables stored during a simulation. The arrows correspond to the variables that are used to compute the updated variables.

$$v(t)=\frac{1}{2}\left[v\left(t+\frac{\Delta t}{2}\right)+v\left(t-\frac{\Delta t}{2}\right)\right] \qquad \text{Equation 40}$$

2.3.6 Thermodynamics

Atom trajectories need to be simulated under well-defined thermodynamic conditions. In an ensemble, there are a collection of microstates which individually may have different properties, but together have constant bulk properties. Molecular dynamics simulations can be performed in a number of different ensembles, the three most common of which are NVE, NPT, and NVT [22]. All three of these ensembles maintain the number of atoms within the system (N). In addition, the NVE ensemble (a microcanonical ensemble) maintains the system volume and energy. The NPT ensemble (an isothermic-isobaric ensemble) maintains the system pressure and temperature, and the NVT ensemble (a canonical ensemble) maintains the system volume and temperature. The NVE ensemble is not often used in simulations because the uncertainties in the system energy caused by using a finite difference method can result in the system energy not being conserved. Although the NPT ensemble can represent atomic interactions more closely, the NVT ensemble is preferred for modelling glasses. This is because it enables the system density to be controlled, and the behaviour of the system to be studied under different temperature conditions [10].

In the NVT ensemble, the kinetic energy of the atoms fluctuates causing instantaneous system temperature $T(t)$ variations. These can be calculated using equation 41, where the terms k_B and N_f are the Boltzmann constant and the number of degrees of freedom respectively.

$$T(t)=\sum_{i=1}^{N}\frac{m_i {v_i}^2(t)}{k_B N_f} \qquad \text{Equation 41}$$

The simplest way to control the instantaneous system temperature is to scale the velocity of the atoms at each time-step according to equation 42, where λ is the scaling factor. This process of velocity scaling is called equilibration.

$$\lambda = \sqrt{\frac{T(t)+\Delta T}{T(t)}} \qquad \text{Equation 42}$$

Another way to control the instantaneous system temperature is to couple the system of atoms to an external heat bath called a thermostat which is fixed at the desired temperature [10]. This coupling permits energy to be added or removed from the system of atoms in order to uphold the desired system temperature. One example is the Berendsen thermostat which was used in this work. Using a Berendsen thermostat involves scaling the atom velocities over a timescale, rather than for each time-step Δt as was the case for velocity scaling. The Berendsen thermostat is defined by equation 43, where τ is the timescale of heat transfer and T_{bath} is the temperature of the thermostat.

$$\lambda^2 = 1 + \frac{\Delta t}{\tau}\left(\frac{T_{bath}}{T(t)} - 1\right) \qquad \text{Equation 43}$$

2.4 Molecular Dynamics Simulations of Glasses Using DLPOLY

In this work, classical molecular dynamics simulations were run to obtain glass models. The simulations were run using the program DLPOLY [25] which took into account the considerations discussed in section 2.3. However, before running a simulation using DLPOLY, a number of input files are required. These include a CONFIG, a CONTROL, and a FIELD file. The CONFIG file contains information on the initial atomic configuration, while the CONTROL file details the control variables, and the FIELD file details the interatomic potential parameters [12]. Although the specific simulation details for each of the systems modelled in this work ($ZnCl_2$, $CaO\text{-}SiO_2\text{-}CaCl_2$, and $CaO\text{-}SiO_2\text{-}CaF_2$) are detailed in their respective chapters, a general overview of the process is provided here.

The first stage of all simulations in this work begins by heating an initial configuration of atoms at high temperature to form a random, homogeneous melt. In subsequent stages, the system temperature is reduced to become similar to the melting temperatures that would be used experimentally. The system is then rapidly quenched from above its melting temperature to 300K at a rate of 10^{13}K/s. A stage at 300K then ensures the formation of a solid glass model. A further stage at 300K forms a sampling stage and is used for analysis.

Following the completion of each simulation stage, a number of output files are generated. These are detailed in [12] and include REVCON, HISTORY, and OUTPUT files. The REVCON file

contains the final atomic configuration. Hence, as illustrated to the left of figure 16, the REVCON file may be renamed as a CONFIG file and used as an input file in the following simulation stage. The HISTORY file contains the atomic configurations recorded at set intervals throughout the simulation stage. The OUTPUT file summarises the input information, and details statistical data recorded at regular intervals throughout the simulation stage. In order to characterise the structure of the glass models obtained (from a sampling stage) using the techniques described in section 2.2, the REVCON, HISTORY, and OUTPUT files can be used (as shown to the right of figure 16). For example, average interatomic distances can be calculated from the atomic configurations in the HISTORY file, and used to form pair correlation functions (section 2.2.1).

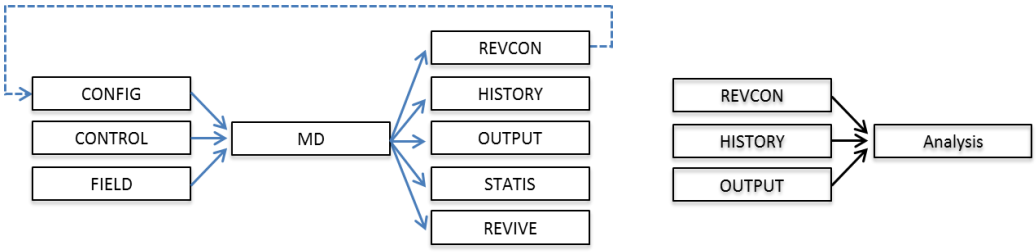

Figure 16: To the left, the process of running a molecular dynamics simulation using the program DLPOLY adapted from [12]. To the right, the output files used for structural characterisation.

2.5 References

[1] J. E. Shelby, *Introduction to glass science and technology*. Royal Society of Chemistry, 2005.

[2] W. H. Zachariasen, "The atomic arrangement in glass," *J. Am. Chem. Soc.*, vol. 54, no. 10, pp. 3841–3851, 1932.

[3] G. N. Greaves, "EXAFS and the structure of glass," *J. Non. Cryst. Solids*, vol. 71, no. 1–3, pp. 203–217, 1985.

[4] A. C. Wright, C. J. Simmons, and O. H. El-Bayoumi, "Experimental Techniques of Glass Science," *Am. Ceram. Soc. Westerville, OH*, p. 205, 1993.

[5] D. A. Keen, "A comparison of various commonly used correlation functions for describing total scattering," *J. Appl. Cryst.*, vol. 34, pp. 172–177, 2001.

[6] A. Zeidler *et al.*, "Structure of liquid and glassy $ZnCl_2$," *Phys. Rev. B - Condens. Matter Mater. Phys.*, vol. 82, pp. 1–17, 2010.

[7] R. N. Mead and G. Mountjoy, "A Molecular Dynamics Study of the Atomic Structure of $(CaO)_x$ $(SiO_2)_{1-x}$ Glasses," *J. Phys. Chem. B*, vol. 110, no. 29, pp. 14273–14278, 2006.

[8] R. A. Martin, S. Yue, J. V. Hanna, P. D. Lee, R. J. Newport, and M. E. Smith, "Characterizing the hierarchical structures of bioactive sol-gel silicate glass and hybrid scaffolds for bone regeneration," *Philos. Trans. R. Soc. A Math. Phys. Eng. Sci.*, vol. 370, pp. 1422–1443, 2012.

[9] D. Frenkel and B. Smit, *Understanding Molecular Simulation: From Algorithms to Applications*. Academic Press, 2001.

[10] A. R. Leach, *Molecular Modelling: Principles and Applications*. Prentice Hall, 2001.

[11] D. C. Rapaport, *The art of molecular dynamics simulation*. Cambridge university press, 2004.

[12] W. Smith, T. Forester, and I. Todorov, "The DL POLY Classic user manual," in *STFC, STFC Daresbury Laboratory, Daresbury, Warrington, Cheshire, WA4 4AD, United Kingdom, version, 1.*, 2012.

[13] M. Wilson and P. A. Madden, "Polarization effects in ionic systems from first principles," *J. Phys. Condens. Matter*, vol. 5, no. 17, pp. 2687–2706, 1999.

[14] B. Dick and A. Overhauser, "Theory of the Dielectric Constants of Alkali Halide Crystals," *Phys. Rev.*, vol. 112, no. 1, pp. 90–103, Oct. 1958.

[15] R. D. Shannon and R. X. Fischer, "Empirical electronic polarizabilities in oxides, hydroxides, oxyfluorides, and oxychlorides," *Phys. Rev. B - Condens. Matter Mater. Phys.*, vol. 73, no. 23, pp. 1–28, 2006.

[16] R. Gill, *Chemical fundamentals of geology*, Second. London : Chapman & Hall, 1996.

[17] F. Miyaji, Y. Kono, and Y. Suyama, "Formation and structure of zinc-substituted calcium hydroxyapatite," *Mater. Res. Bull.*, vol. 40, no. 2, pp. 209–220, 2005.

[18] N. K. Verma, S. K. Khanna, and B. Kapila, *Comprehensive chemistry XI*. Laxmi publications, 2010.

[19] A. Tilocca, N. H. De Leeuw, and A. N. Cormack, "Shell-model molecular dynamics calculations of modified silicate glasses," *Phys. Rev. B - Condens. Matter Mater. Phys.*, vol. 73, pp. 1–14, 2006.

[20] R. I. Ainsworth, D. Di Tommaso, J. K. Christie, and N. H. de Leeuw, "Polarizable force field development and molecular dynamics study of phosphate-based glasses.," *J. Chem. Phys.*, vol. 137, p. 234502, 2012.

[21] J. D. Gale and A. L. Rohl, "The General Utility Lattice Program (GULP)," *Mol. Simul.*, vol. 29, no. 5, pp. 291–341, 2003.

[22] D. J. Tildesley and M. P. Allen, "Computer simulation of liquids," *Clarendon, Oxford*, 1987.

[23] L. Verlet, "Computer' experiments' on classical fluids. I. Thermodynamical properties of Lennard-Jones molecules," *Phys. Rev.*, vol. 159, no. 1, p. 98, 1967.

[24] D. M. Causon and C. G. Mingham, *Introductory finite difference methods for PDEs*. Bookboon, 2010.

[25] W. Smith and T. R. Forester, "DL_POLY_2. 0: A general-purpose parallel molecular dynamics simulation package," *J. Mol. Graph.*, vol. 14, no. 3, pp. 136–141, 1996.

3. Experimental Methodology

This chapter describes the experimental techniques used in this work to synthesise and characterise glasses and their structures. The systems studied experimentally involve two CaO-SiO_2-$CaCl_2$ glass series that were prepared by collaborators [1], [2], and a CaO-SiO_2-CaF_2 glass series that was prepared in this work. As different approaches were used to prepare the glasses, only a general overview of glass synthesis via melt-quenching is provided here. The specific details can be found in [1], [2], as well as in the relevant experimental results chapters. The next part of this chapter concerns a number of laboratory-based techniques used to characterise glass. The techniques used include powder X-ray diffraction (PXRD), X-ray fluorescence spectroscopy (XRF), helium pycnometry, differential scanning calorimetry (DSC), Raman spectroscopy, and scanning electron microscopy (SEM), although not all of the techniques were used to study each glass series. Finally, following a brief discussion of diffraction theory, the central facility techniques used to characterise both the CaO-SiO_2-$CaCl_2$ and CaO-SiO_2-CaF_2 glass structures are described. These include neutron diffraction (ND) and X-ray absorption spectroscopy (XAS).

3.1 Glass Synthesis

The glasses studied in this work were prepared via a melt-quench route. Molar concentrations of the reagents were weighed out and mixed together before being placed into a platinum-rhodium crucible. The crucible and its contents were then placed into a furnace and melted at a sufficient temperature for a sufficient period of time to ensure a homogeneous melt. Subsequently, the crucible was removed from the furnace and the melt rapidly quenched to obtain a glass.

3.2 Powder X-ray Diffraction

Powder X-ray diffraction (PXRD) can be used to verify the amorphous nature of a glass sample. In this technique, X-ray production involves heating the metal filament in the X-ray tube. This causes the emission of electrons via thermionic emission which can be accelerated towards a metal target by applying a voltage. When the electrons bombard the metal target, inner shell electrons may be ejected which causes vacancies to occur. These vacancies are immediately filled by electrons from an outer shell. During these transitions, X-rays of energy equivalent to the energy difference between the two electron shells are

emitted. After passing through a monochromator and a collimator, the X-rays are incident on the sample which is rotated. When X-rays are elastically scattered by crystalline solids they can interfere constructively according to Bragg's law given in equation 1.

$$2d\sin\theta = n\lambda \qquad \text{Equation 1}$$

In equation 1, d is the spacing between the atomic layers, 2θ is the scattering angle, n is an integer, and λ is the wavelength of the incident X-rays. Bragg's law can be used to predict the scattering from a crystal. The presence of crystalline regions in a sample would lead to diffraction lines in the diffraction spectra known as Bragg peaks. The positions of these Bragg peaks can be used to identify the crystalline compounds present in a sample using a database of diffraction patterns. Conversely, when scattered X-rays interfere destructively, there is no contribution to the diffraction spectra. The presence of amorphous regions causes very broad scattering peaks because glasses have no long-range order [3]. Therefore, if the diffraction spectrum has a broad scattering peak with an absence of any Bragg peaks then the sample is amorphous.

In this work, glass samples were ground into a fine powder using an agate pestle and mortar and pressed into zero-background sample holders. The sample holders were then placed in a Rigaku MiniFlex 600 X-ray diffractometer to obtain PXRD spectra. A current of 15mA and a voltage of 40kV were used. The samples were rotated from a scattering angle (2θ) of 5° to 60° with a step size of 0.02° and a step time of 0.1°/min.

3.3 X-ray Fluorescence Spectroscopy

X-ray fluorescence spectroscopy (XRF) may be used to ascertain the composition of a glass sample. The X-rays used in X-ray fluorescence spectroscopy (XRF) are obtained using an X-ray tube as discussed in section 3.2. The X-rays incident on a sample cause core-electrons to be ejected as photoelectrons, leading to the formation of vacancies. Outer shell electrons then transition into the inner shell to occupy these vacancies, and in doing so emit fluorescent X-rays. These fluorescent X-rays are of lower energy compared to the incident X-rays. They are also characteristic of the fluorescing elements [4]. Therefore, while PXRD identifies crystalline compounds present in a sample, XRF identifies the elemental constituents of a sample. In addition, the intensity of fluorescent X-rays detected can be used to determine the concentration of each element in the sample [4]. However, the fluorescent X-rays from light elements (with an atomic number less than 12) are often absorbed in air and fail to reach the detector [5]. This makes quantifying the elemental contribution of light elements in a sample challenging. To help ensure the flat, homogeneous sample distributions necessary for quantitative compositional analysis [5],

fusion beads containing samples were prepared in this work as detailed in section 5.3. The fusion beads were measured using a PANalytical Epsilon 3 XRF spectrometer.

3.4 Helium Pycnometry

The density of a glass sample can be measured based on the Archimedes principle using a pycnometer. Within a pycnometer, there are two chambers of known volume including a reference chamber (of volume V_R), and a cell chamber (of volume V_C). Following the calibration of the pycnometer using steel balls of known volume, an amount of sample is weighed and placed into the cell chamber. The pycnometer is then purged with helium gas for a minimum of 10 minutes in order to remove air and moisture from the chambers [6]. Helium gas is then admitted into the empty reference chamber and is of pressure P_1. The helium gas is then allowed to flow into the cell chamber (which contains the glass sample), and occupy both chambers with a pressure of P_2. By using the volumes V_R and V_C, together with the pressures P_1 and P_2, the sample volume, V_S, can be calculated in accordance with equation 2. As the mass of sample, m_S, within the cell chamber is known, the density of the sample, ρ_S, can then be calculated using equation 3.

$$V_S = V_c - V_R\left[\left(\frac{P_1}{P_2}\right) - 1\right] \qquad \text{Equation 2}$$

$$\rho_S = \frac{m_S}{V_S} \qquad \text{Equation 3}$$

The density measurements in this work were performed using a Quantachrome MVP-6DC pycnometer. The glass samples were in the form of glass chips and approximately 1g of each sample was used. Ten density measurements on each sample yielded average density values.

3.5 Differential Scanning Calorimetry

Differential scanning calorimetry (DSC) can be used to identify the glass transition temperature of a glass sample. During a DSC measurement, a sample and an inert reference are heated under the same conditions. The temperatures of both are measured using thermocouples. One thermocouple is in contact with the sample, and the other is in contact with the inert reference. Any difference in heat flow between the sample and the inert reference will generate a signal. This signal can be plotted as a function of temperature to form a thermogram [5]. The heat flow to the sample will differ from that of the inert reference if the sample undergoes a change of phase (e.g. crystallisation). This is because physical changes often involve changes in enthalpy [5]. The glass transition is a

second order phase transition which manifests as a change in specific heat. The signature of a glass transition appears as a step change in the baseline of the thermogram [5]. The glass transition temperature can be identified as the point where the plot begins to deviate from the linearity of the baseline [7].

In this work, DSC measurements were performed using a Netzsch-Gerätebau GmbH-STA 409 PC Luxx Simultaneous thermal analyser. Approximately 30mg of sample was added into an alumina crucible which was inserted into the sample well of the instrument. An empty alumina crucible of the same size was placed into the reference well. The two crucibles were enclosed within a furnace and heated in air from room temperature to 900°C at a rate of 10°C/min to produce thermograms.

3.6 Raman Spectroscopy

Raman spectroscopy can be used to verify the homogeneous nature of a glass sample. The technique involves irradiating a sample with a source of monochromatic light which is usually in the visible part of the spectrum. This can be done using a laser. The irradiation can cause three types of scattering to occur. Rayleigh scattering describes elastic scattering, while Stokes and anti-Stokes scattering both describe inelastic scattering due to molecular vibrations [8]. In Stokes scattering, the energy of the scattered radiation is lower than that of the incident radiation due to the transfer of energy to a molecular vibration. Conversely, in anti-Stokes scattering the energy is higher due to the acceptance of energy from a molecular vibration. Collectively, Stokes and anti-Stokes scattering is known as Raman scattering and can be measured using a Raman spectrometer. By plotting the intensity of the Raman scattering as a function of the Raman wavenumber, a Raman spectrum can be attained. The Raman wavenumber, ω, is defined in equation 4, where ν_s and ν_0 correspond to the frequency of the scattered and incident radiation respectively, and c is the speed of light [9].

$$\omega = \frac{\nu_s}{c} - \frac{\nu_0}{c} \qquad \text{Equation 4}$$

This means that the Raman wavenumber is proportional to the energy or frequency of the molecular vibration. In this work, Raman spectra were attained using a Horiba Lab-RAM HR Raman spectrometer. A laser was operated at a wavelength of 532nm, and the spectrometer was calibrated using a silicon wafer with a wavenumber of 520cm^{-1}. Spectra were measured over a range of wavenumbers from 100cm^{-1} to 4000cm^{-1}. The acquisition time was 6s and 10 accumulations were recorded for each sample. A total of six spectra were acquired from three glass chips of each sample. By comparing the shapes of all spectra from one sample to the metasilicate (50CaO-50SiO_2) spectra reported in the literature [10], the homogeneous nature of the glass samples could be verified. This is

because the vibrational bands in the Raman spectra of a metasilicate are predominantly due to Q^2 tetrahedral units in the silicate network.

3.7 Scanning Electron Microscopy

Scanning electron microscopy (SEM) can be used to image the surface of a glass sample. One component of the scanning electron microscope is the electron source which emits a beam of electrons via thermionic emission (section 3.2). The electrons get focussed by a series of electron lenses, and the electron beam at the sample surface typically has a spot size of less than 10nm [11]. Scanning coils raster the electron beam on the sample [12]. The signals from the detection of secondary or backscattered electrons can be used to construct images of the sample surface. Secondary electrons are electrons that have been dislodged from the sample by the incident electrons. Backscattered electrons are incident electrons that have been elastically scattered by the sample and are less numerous. In this work, a Hitachi S3400N scanning electron microscope was used to attain SEM images from the detection of secondary electrons.

3.8 Introduction to Diffraction

Neutron and X-ray diffraction are often complimentary techniques used to characterise the structure of glass. Neutrons are scattered by nuclei via the short-ranged nuclear force. As the size of a nucleus is small in comparison to the wavelength of the incident neutrons, the probability of a neutron being scattered is also small and is independent of the magnitude of the scattering vector, Q. This enables neutrons to penetrate the bulk of a sample. The strength of the nuclear interaction is characterised by the neutron scattering length, b, which varies haphazardly across the periodic table [13]. This can enable the contributions of elements that are close together in the periodic table to be distinguished. In addition, the contribution of light elements can be detected amongst the presence of heavy elements.

Instead, X-rays interact with electrons via the long-range electromagnetic interaction. The wavelength of the incident X-rays is comparable to that of the separation distances between electrons. As a consequence, the atomic scattering amplitude described using the form factor, $f(Q)$, diminishes with increasing values of Q. This limits the maximum value of Q attainable experimentally [14]. As the strength of the X-ray scattering is proportional to the atomic number Z, X-rays are strongly scattered by heavy elements and are scattered very little by light elements. X-ray scattering is therefore sensitive to heavy elements, although it is challenging to distinguish elements that are close together in the periodic table.

3.8.1 Theory of Diffraction

The following introduction to diffraction theory is based on [15] and [16]. An incident neutron or X-ray of wavevector $|\mathbf{k_i}| = \frac{2\pi}{\lambda_i}$ that gets scattered by an angle of 2θ from a sample will have a final wavevector of $|\mathbf{k_f}| = \frac{2\pi}{\lambda_f}$. The momentum transfer, $\mathbf{Q}$, during this scattering event is illustrated in figure 1 and defined in equation 5. In neutron and X-ray diffraction experiments, it is of interest to investigate elastic scattering events. During an elastic scattering event, $|\mathbf{k_f}| = |\mathbf{k_i}|$ and so the magnitude of the scattering vector, Q, can be described using equation 6.

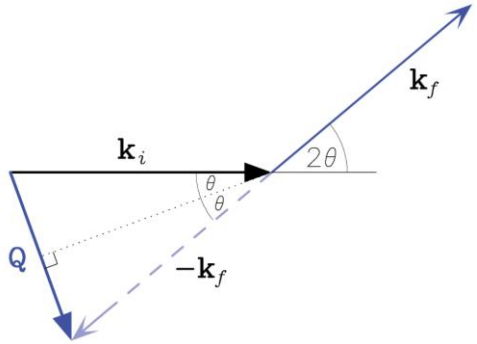

Figure 1: Illustration of elastic scattering from [17].

$$\hbar\mathbf{Q} = \hbar\mathbf{k_i} - \hbar\mathbf{k_f} \qquad \text{Equation 5}$$

$$Q = \frac{4\pi \sin\theta}{\lambda} \qquad \text{Equation 6}$$

When a beam of neutrons or X-rays comes into contact with a monatomic sample, the scattering amplitude of the diffracted beam, $A(\mathbf{Q})$, can be described using equation 7. In the equation, the term $\mathbf{r_a}$ corresponds to the position of the monatomic atoms which are indexed by the symbol a. The term f_a represents the X-ray scattering factor or the neutron scattering length depending on the type of incident radiation used in the experiment.

$$A(\mathbf{Q}) = \sum_a f_a \exp(i\mathbf{Q}\cdot\mathbf{r_a}) \qquad \text{Equation 7}$$

As the scattering amplitude is unattainable experimentally, the differential cross-section, $\left(\frac{d\sigma}{d\Omega}\right)_{tot}$, is measured instead. This is illustrated in figure 2 and defined in equation 8, where R_{tot} is the rate at which neutrons or X-rays of wavelength λ are scattered into the solid angle $d\Omega$ in the direction $(2\theta, \phi)$, regardless of whether they are scattered elastically. Any inelastic scattering contributions need to be corrected for in the data analysis. The term N is the number of atoms in the sample, and Φ is the flux of neutrons or X-rays of wavelength λ that are incident on the sample. The differential cross-section can be written in terms of the scattering intensity, $I(\mathbf{Q})$, [14] as shown in equation 8.

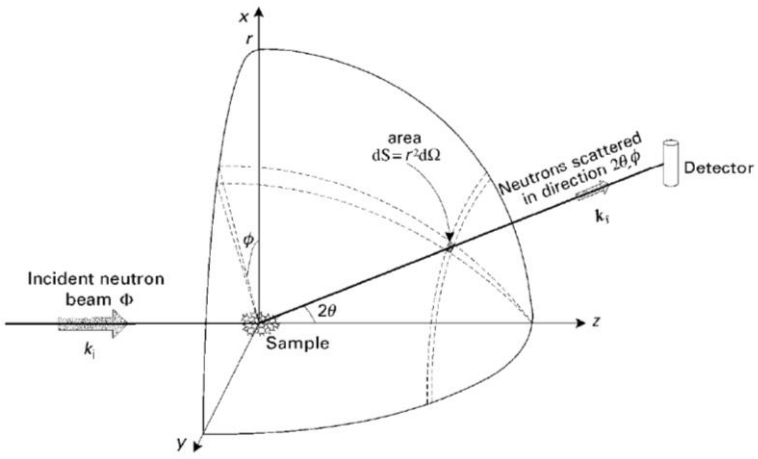

Figure 2: The geometry of a neutron diffraction experiment from [18].

$$\left(\frac{d\sigma}{d\Omega}\right)_{tot} = \frac{R_{tot}}{N\Phi d\Omega} = I(\mathbf{Q}) \qquad \text{Equation 8}$$

The scattering intensity can be calculated by multiplying the scattering amplitude, $A(\mathbf{Q})$, by its complex conjugate as shown in equation 9, where a and b are atoms in the monatomic system. Equation 9 can then be rewritten to form equation 10.

$$I(\mathbf{Q}) = A(\mathbf{Q})A(\mathbf{Q})^* = \sum_a f_a \exp(i\mathbf{Q}\cdot\mathbf{r_a}) \sum_b f_b \exp(-i\mathbf{Q}\cdot\mathbf{r_b}) \qquad \text{Equation 9}$$

$$I(\mathbf{Q}) = \sum_a \sum_b f_a f_b \exp[i\mathbf{Q}\cdot(\mathbf{r_a} - \mathbf{r_b})] \qquad \text{Equation 10}$$

Glasses are isotropic meaning their properties are the same in all directions. Consequently, the scattering intensity can be averaged over all orientations of the scattering vector as defined by the angles φ and ϑ [15]. This enables the $\exp[i\mathbf{Q}\cdot(\mathbf{r_a} - \mathbf{r_b})]$ term in equation 10 to be rewritten using the derivation in [19] which is outlined below. In the derivation, the relation $|\mathbf{r_a} - \mathbf{r_b}| = r_{ab}$ is used, and the integration is simplified by changing the variable of the integration using $\cos(\vartheta) = x$.

$$\langle \exp(i\mathbf{Q}\cdot|\mathbf{r_a} - \mathbf{r_b}|)\rangle = \frac{1}{4\pi}\int_0^{2\pi} d\varphi \int_0^{\pi} \sin(\vartheta)\, d\vartheta \exp(iQr_{ab}\cos(\vartheta)) \qquad \text{Equation 11}$$

$$\langle \exp(i\mathbf{Q}\cdot|\mathbf{r_a} - \mathbf{r_b}|)\rangle = \frac{1}{2}\int_{-1}^{+1} \exp(iQr_{ab}x)\, dx \qquad \text{Equation 12}$$

$$\langle \exp(i\mathbf{Q}\cdot|\mathbf{r_a} - \mathbf{r_b}|)\rangle = \frac{\sin(Qr_{ab})}{Qr_{ab}} \qquad \text{Equation 13}$$

Hence, by substituting equation 13 into equation 10, equation 14 is obtained.

$$I(Q) = \sum_a \sum_b f_a f_b \frac{\sin(Qr_{ab})}{Qr_{ab}} \qquad \text{Equation 14}$$

If there are N atoms in the monatomic sample where $f_a = f_b = f$ then the Debye scattering equation given in equation 15 is obtained.

$$I(Q) = Nf^2\left(1 + \sum_a \sum_{b\neq a} \frac{\sin(Qr_{ab})}{Qr_{ab}}\right)$$ Equation 15

The Debye scattering equation can be rewritten to include the radial density function $\rho(r)$ as shown in equation 16, which is equivalent to equation 17.

$$I(Q) = Nf^2\left(1 + \int_0^\infty \frac{4\pi r^2 \rho(r)\sin(Qr)dr}{Qr}\right)$$ Equation 16

$$I(Q) = Nf^2\left(1 + \int_0^\infty 4\pi r(\rho(r) - \rho^0)\frac{\sin(Qr)}{Q}\,dr + \int_0^\infty 4\pi r\rho^0 \frac{\sin(Qr)}{Q}dr\right)$$ Equation 17

The first term to the right of equation 17 corresponds to self-scattering. The second integral to the right of the equation corresponds to the average scattering from a uniform distribution of atoms such as those in a gas. As this is a background that contains no structural information, it is subtracted to give equation 18. The first integral to the right of equation 18 is known as distinct scattering, and corresponds to the deviations from the continuous distribution that provides insight into the interatomic correlations of a sample.

$$I(Q) = Nf^2\left(1 + \int_0^\infty 4\pi r\,(\rho(r) - \rho^0)\frac{\sin(Qr)}{Q}dr\right)$$ Equation 18

Using the relation $g_{tot}(r) = 4\pi r\rho(r)$ yields equation 19.

$$I(Q) = Nf^2\left(1 + \int_0^\infty (g_{tot}(r) - 4\pi r\rho_0)\frac{\sin(Qr)}{Q}dr\right)$$ Equation 19

The structure factor, $S(Q)$, is defined in equation 20.

$$S(Q) = \frac{I(Q)}{Nf^2} = 1 + \int_0^\infty (g_{tot}(r) - 4\pi r\rho^0)\frac{\sin(Qr)}{Q}dr$$ Equation 20

The Fourier transform of the structure factor leads to the total correlation function, $g_{tot}(r)$, as shown in equation 21.

$$g_{tot}(r) = 4\pi r\rho^0 + \frac{2}{\pi}\int_0^\infty Q(S(Q) - 1)\sin(Qr)\,dQ$$ Equation 21

For a multicomponent system, the total structure factor can be considered as a weighted sum of the partial Faber-Ziman structure factors, $S_{ij}^{FZ}(Q)$, as shown in equation 22. Analogously, the total correlation function can be considered as a weighted sum of the pair correlation functions, $g_{ij}(r)$, as shown in equation 23. The Faber-Ziman partial structure factors and the pair correlation functions are defined in equations 24 and 25 respectively. The weighting factor, ω_{ij}, has been defined in terms of the neutron scattering length, b, and the atomic number, Z, in equations 26 and 27 to correspond with neutron and X-ray diffraction experiments respectively. In equations 26 and 27, the term δ_{ij} is a Kronecker delta function, and the term c_i is the concentration of atom type i.

$$S(Q) = \sum_{ij} \omega_{ij}\ S_{ij}^{FZ}(Q) \qquad \text{Equation 22}$$

$$g_{tot}(r) = \sum_{ij} \frac{\omega_{ij}}{c_j} g_{ij}(r) \qquad \text{Equation 23}$$

$$S_{ij}^{FZ}(Q) = 1 + \int_0^{\infty} \frac{1}{c_j}\left(g_{ij}(r) - 4\pi r\rho_j\right)\frac{\sin(Qr)}{Q}\,dr \qquad \text{Equation 24}$$

$$g_{ij}(r) = 4\pi r\rho_j + \frac{2c_j}{\pi}\int_0^{\infty} Q\left(S_{ij}^{FZ}(Q) - 1\right)\sin(Qr)\,dQ \qquad \text{Equation 25}$$

$$\omega_{ij} = \frac{(2-\delta_{ij})c_i c_j b_i b_j}{[\bar{b}]^2} \qquad \text{Equation 26}$$

$$\omega_{ij} = \frac{(2-\delta_{ij})c_i c_j Z_i Z_j}{[\bar{Z}]^2} \qquad \text{Equation 27}$$

The diffraction theory aforementioned assumes that diffraction data is obtained over an infinite Q-range. In practise however, it only extends to Q_{max}, (where Q_{max} is the maximum momentum transfer available in an experiment). When Fourier transforming diffraction data with a sharp cut-off at Q_{max}, termination ripples emerge in the total correlation function. These can be mistaken for real structural features. To minimise these termination ripples, it is appropriate to multiply the structure factor by a modification function, $M(Q)$, although this can lead to some loss of resolution. Examples of modification functions include the Lorch, the Hanning, and the Step modification functions. These are described mathematically in equations 28-30 (where $\Delta r = \pi/Q_{max}$) and are illustrated in figure 3.

Lorch: $M(Q) = \frac{\sin(Q\Delta r)}{Q\Delta r}$ $\quad Q \leq Q_{max}$ Equation 28

Hanning: $M(Q) = 0.5 + 0.5\cos(Q\Delta r)$ $\quad Q \leq Q_{max}$ Equation 29

Step: $M(Q) = 1$ $\quad Q \leq Q_{max}$ Equation 30

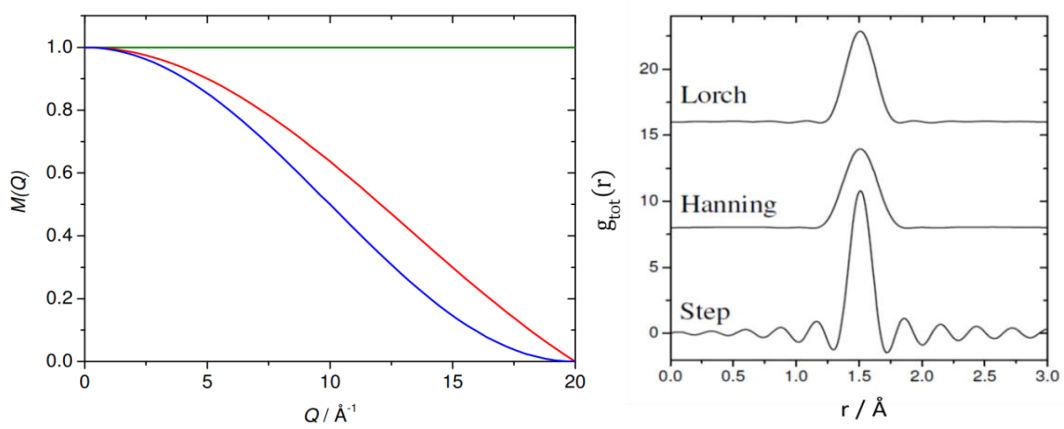

Figure 3: To the left, examples of the Lorch (red), the Hanning (blue), and the Step (green) modification functions, M(Q) from [32]. To the right, the $g_{tot}(r)$ of a single peak following the application of these modification functions from [33].

3.8.2 Neutron Diffraction Experiment

The neutron diffraction experiments in this work were carried out using the GEneral Materials (GEM) diffractometer at the ISIS neutron spallation source. This is located at the Rutherford Appleton Laboratory (RAL) in Oxfordshire and is used to study the structure of disordered materials. As shown in figure 4, the GEM diffractometer (figure 4) has a series of detector banks located at different angles. This is to increase the count rate and extend the measurable Q-range [14]. A detailed description of the GEM diffractometer can be found in [20]. During the ND experiments in this work, coarse glass chips were used to fill thin cylindrical vanadium containers. Measurements were then performed, and in addition to sample measurements, data was also collected for an empty vanadium container, a vanadium niobium rod, and for the empty GEM diffractometer.

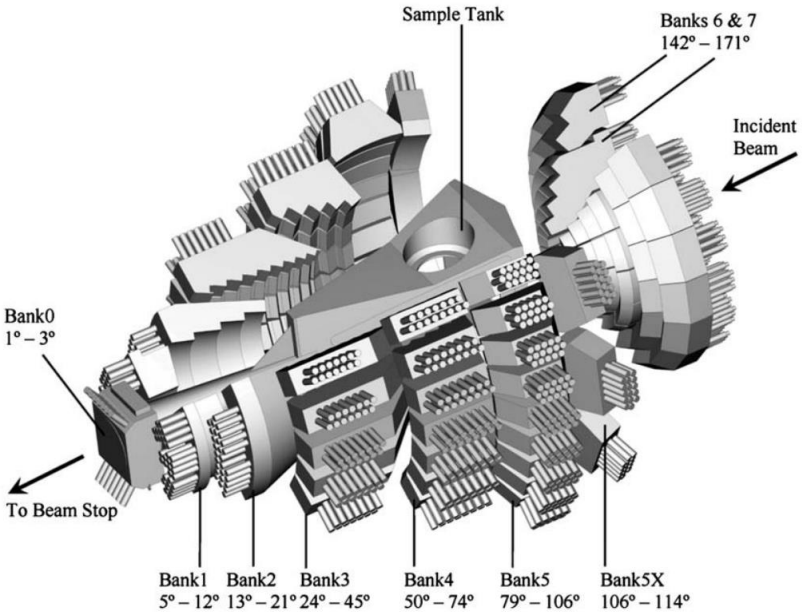

Figure 4: The detector banks in the GEM diffractometer from [20].

3.8.3 Neutron Diffraction Data Analysis

The additional neutron diffraction measurements mentioned in section 3.8.2 complimented the sample measurements and enabled a number of corrections to be applied to the sample data after the experiment as detailed in [14]. One of these corrections is for the detector dead-time. While a detector is counting a neutron, it is unable to count any other neutrons. This can cause more intense signals to be suppressed. Another correction is the background subtraction. Any general background and the background contribution from the sample container need to be removed. The incident neutrons absorbed by a nucleus also need to be corrected for, as does the attenuation of the incident and scattered flux of neutrons due to further scattering events. The detection

of neutrons that have undergone multiple scattering events would cause additional background and so also need to be removed. These corrections depend on the packing fractions of sample in the sample cans. They are also very complex because they are interrelated. For example, a neutron scattered from the sample container may undergo multiple scattering. In this work the above corrections were made using the program Gudrun [21]. Further data processing involved calculating and subtracting the self-scattering contribution using Open GENIE [22], as well as appropriately merging the detector bank contributions from the GEM diffractometer to attain the total structure factor. The total structure factor, $S(Q)$, can be Fourier transformed to obtain the total correlation function, $g_{tot}(r)$, as shown in equation 21.

Contributions from different pair correlation functions are often overlapping in the total correlation function. It is therefore necessary to fit the experimental diffraction data in order to obtain structural information. This was achieved using the program NXFit [23]. NXFit utilises three input parameters to model the contribution of each peak in the pair correlation function in Q-space, $p(Q)$, according to equation 31. In the equation, N is the coordination number, R is the nearest neighbour distance, and σ is a disorder parameter used to calculate the Debye-Waller Factor ($2\sigma^2$). The contributions of different peaks in the pair correlation functions in Q-space are summed and Fourier transformed before being compared to the experimental total correlation function, $g_{tot}(r)$. A Nelder-Mead algorithm is employed to vary the fit parameters to minimise the least squares fit index, given in equation 32 [23]. In the equation, R_{min} and R_{max} define the range over which the data is modelled. The terms $g_{tot}^{E}(r)$ and $g_{tot}^{S}(r)$ represent the experimental and simulated total correlation functions respectively. In order to avoid obtaining fits with unrealistic parameter values, the parameters must be constrained within a given range. The uncertainty in a given parameter is dependent on how much a change in the parameter causes a change in the fit index.

$$p(Q) = \frac{N\omega_{ij}(Q)}{c_j}\frac{\sin(QR)}{QR}\exp\left[\frac{-Q^2\sigma^2}{2}\right] \qquad \text{Equation 31}$$

$$\text{Fit index} = \sum_{r=R_{min}}^{r=R_{max}}\left[g_{tot}^{E}(r) - g_{tot}^{S}(r)\right]^2 \qquad \text{Equation 32}$$

3.9 X-ray Absorption Spectroscopy

3.9.1 Introduction

X-ray absorption spectroscopy (XAS) enables the local environment around particular atomic species to be investigated. The technique involves irradiating a sample with X-rays from a synchrotron source. The intensity of the X-rays absorbed can be measured as a

function of energy, and plotted to form a XAS spectrum. The absorption of X-rays follows the Beer-Lambert law given in equation 33 which can be rearranged in terms of the absorbance, A, as shown in equation 34. The term I_0 is the intensity of the incident X-ray beam, I is the intensity of the beam transmitted through the sample, μ is the linear X-ray absorption coefficient, E is the X-ray energy, and x is the sample thickness.

$$I = I_0 \exp(-\mu(E)x) \qquad \text{Equation 33}$$

$$A = \mu(E)x = \ln\left(\frac{I_0}{I}\right) \qquad \text{Equation 34}$$

The absorption coefficient, $\mu(E)$, determines the probability of X-rays being absorbed and generally declines with increasing incident X-ray energy until the energy of the incident X-rays, E, is approximately equivalent to the binding energy, E_0, of inner shell electrons. When this happens, there is a sharp increase in the absorption due to the X-ray energy being sufficient to excite inner-shell electrons to unbound states (photoelectrons). When this transition involves a 1s electron, a K-edge in the XAS spectrum is generated, and when the transition involves 2s, $2p_{1/2}$, and $2p_{3/2}$ electrons, L_1, L_2, and L_3 edges are generated respectively and so on (figure 5). Any excess energy $(E - E_0)$ from the incident X-rays is acquired by the photoelectrons as kinetic energy. The propagation of a photoelectron is considered to be a spherical wave which scatters off surrounding atoms, hence it interferes with itself. This scattering causes oscillations in $\mu(E)$ beyond the absorption edge E_0. The region around the absorption edge in the XAS spectrum is referred to as the X-ray absorption near-edge structure (XANES) region, while the fine structure oscillations are referred to as the extended X-ray absorption fine structure (EXAFS) region. These are illustrated in figure 6.

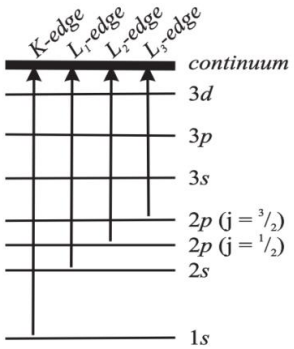

Figure 5: Examples of electron transitions caused by the absorption of an X-ray by inner-shell electrons from [24].

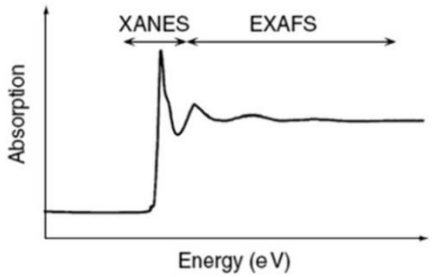

Figure 6: Example of an XAS spectrum from [25].

3.9.2 X-ray Absorption Near-Edge Structure

The X-ray absorption near-edge structure (XANES) region of the XAS spectrum typically starts a few eV before the absorption edge and extends to tens of eV beyond the edge. In the XANES region, the photoelectrons undergo multiple scattering events which are illustrated in figure 7. As the energy of the incident X-rays increases towards that of the EXAFS region, the scattering of photoelectrons becomes increasingly dominated by single scattering events [26]. The complex multiple scattering events of the XANES region are based on complex quantum mechanical equations [27]. Despite this, qualitative analysis of XANES spectra can still provide insight into the oxidation state and the local coordination environment by making comparisons with the XANES spectra of known standard compounds [28].

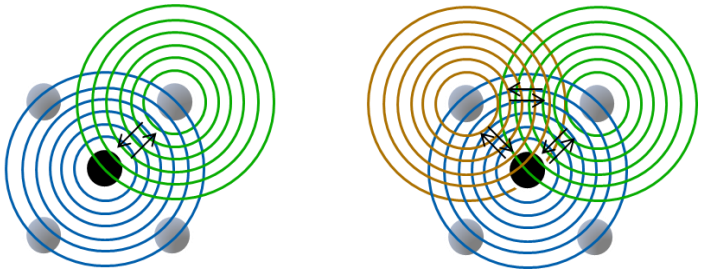

Figure 7: An illustration of single and multiple scattering.

3.9.3 Extended X-ray Absorption Fine Structure

The extended X-ray absorption fine structure (EXAFS) region is illustrated in figure 6 and typically starts tens of eV beyond the edge and extends to over 1000eV beyond the edge [14]. The photoelectron waves propagating from the absorbing atom get scattered by neighbouring atoms. Hence, the amplitudes of these photoelectron waves are influenced by the environment of the absorbing atom. The constructive and destructive interference of these photoelectron waves causes oscillations in the EXAFS region of the XAS spectrum. By studying these oscillations, information about the environment of the absorbing atom

can be obtained. This includes nearest neighbour distances, R, coordination numbers, N, and values of σ^2 which are used to determine the XAS Debye-Waller factors ($2\sigma^2$).

3.9.4 X-ray Absorption Spectroscopy Experiment

The X-ray absorption spectroscopy experiments in this work were carried out using the general purpose beamline B18 at the Diamond Light Source synchrotron facility. This is located at the Rutherford Appleton Laboratory (RAL) in Oxfordshire. The beamline has a wide energy range of 2-35keV, enabling access to elements beyond phosphorus and up to the actinides in the periodic table. A detailed description of B18 is provided in [29]. The specific details of how the samples were prepared and how the measurements were performed are detailed in the relevant results chapters.

Transmission mode and fluorescence mode are the two most common setups for a XAS experiment. Transmission mode involves determining the X-ray absorption coefficient, $\mu(E)$, directly. This is done by measuring the intensity of the X-ray beam incident on the sample, I_0, as well as the intensity of the X-ray beam that gets transmitted though the sample, I, using ionisation chambers. This enables the X-ray absorption to be established using equation 34. To supplement these measurements, the intensity of the X-ray beam that transmits through a standard sample, I_S, can also be detected. This can be used to help calibrate the X-ray energy E [14]. An illustration of the transmission mode experimental setup is shown in figure 8. The difficulty with measuring samples in transmission mode is that the difference between I_0 and I needs to be large while keeping the thickness of the sample small. Additionally, the samples need to be homogeneous and of uniform thickness [27].

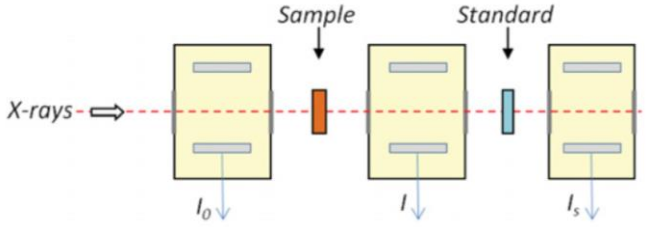

Figure 8: Schematic of the XAS transmission mode experimental setup from [14].

Fluorescence mode is often used when samples cannot be measured in transmission mode, and involves determining the X-ray absorption coefficient indirectly. This is achieved by measuring the intensity of the X-ray beam incident on the sample, as well as the intensity of fluorescent X-rays created through X-ray absorption, I_F (figure 9). This enables the X-ray absorption coefficient to be calculated using equation 35. The samples used in fluorescence measurements can be dilute or inhomogeneous. Germanium solid state detectors can be used for energy discrimination to help ensure that the fluorescent X-rays detected are all

from the element of interest. However, some X-rays that have been scattered elastically or inelastically may also be detected [14]. In addition, corrections for self-absorption often need to be considered following the experiment as some of the fluorescent X-rays could have been absorbed by the sample before reaching the detector [27].

$$\mu(\mathrm{E}) = \frac{\mathrm{I_F}}{\mathrm{I_0}} \qquad \text{Equation 35}$$

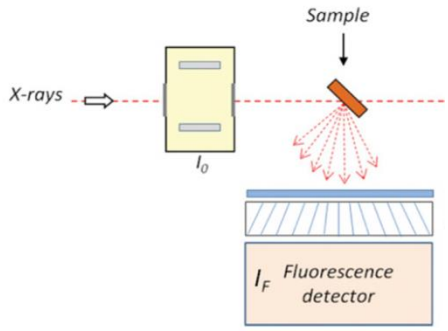

Figure 9: Schematic of the XAS fluorescence mode experimental setup from [14].

3.9.5 X-ray Absorption Spectroscopy Data Analysis

Using the program Athena [30], the analysis of raw XAS data begins by removing any spikes in the data called glitches which are caused by imperfections in the monochromator. This can be achieved by interpolating the XAS spectrum from just before to just after the glitch using a polynomial spline [14]. For measurements performed in fluorescence mode, it is important to consider self-absorption. Algorithms in the Athena program [30] use tables of x-ray absorption coefficients to approximate the self-absorption correction. The binding energy of the inner shell electrons, $\mathrm{E_0}$, is often referred to as the threshold energy. This threshold energy can be identified using the inflection point in the first derivative of $\mu(\mathrm{E})$. The next stage of the analysis involves fitting the pre-edge region using a polynomial spline which extrapolates throughout the EXAFS region. This pre-edge background is then subtracted. A post-edge region is fitted using a further polynomial spline as shown in figure 10. This enables the background X-ray absorption coefficient, $\mu_0(\mathrm{E})$, (corresponding to the X-ray absorption that would occur when the atom is isolated) to be approximated. Following the subtraction of this post-edge spline, the height of the absorption edge at $\mathrm{E_0}$ can be established as the difference between the pre-edge and the post-edge lines, $\Delta\mu_0(\mathrm{E})$ [27]. The XAS spectrum can then be normalised using equation 36 to remove the effects of sample thickness and concentration [27]. At this stage, the XANES region can be studied and compared to those of known standards.

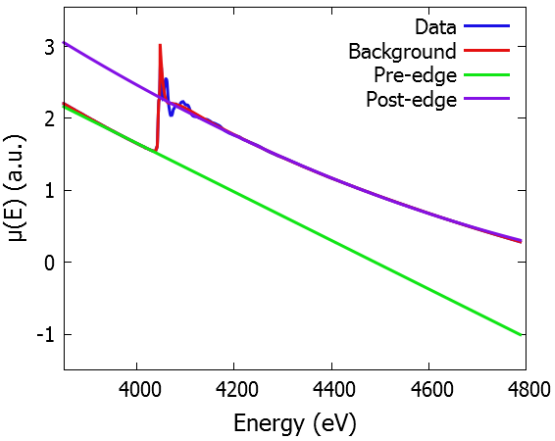

Figure 10: Example of raw μ(E) data for $CaCO_3$, together with the fitted pre-edge and post-edge splines and the background function.

$$1 + \chi(E) = \frac{\mu(E) - \mu_0(E)}{\Delta\mu_0(E)} \qquad \text{Equation 36}$$

To study the EXAFS region of the XAS spectra, the program Artemis [30] can be used. It is convenient to consider the XAS spectra in terms of photoelectron wavenumber, k, rather than the X-ray energy, E. This is because the XAS spectrum is the result of interference effects between photoelectron waves. The photoelectron wavenumber can be related to the kinetic energy of the photoelectron, $(E - E_0)$, using equation 37, where m_e is the electron mass. The EXAFS function, $\chi(k)$, can be weighted by k^n, where n is an integer between 1 and 3. This amplifies the oscillations at higher values of k where the signal strength is reduced [14].

$$k = \sqrt{\frac{2m_e}{\hbar^2}(E - E_0)} \qquad \text{Equation 37}$$

The parameterised form of the EXAFS equation is given in equation 38, where the index i refers to coordination shells of nearest neighbour atoms around the absorbing atom. This can be used to approximate the oscillations in the EXAFS region. As detailed in [27], ${S_0}^2$ is the amplitude reduction factor. This accounts for a small fraction of absorption events in which the energy of the incident X-ray is transferred to more than one electron. The magnitude of the EXAFS is determined by the number and the type of scattering atoms. The terms relating to this are the coordination number, N_i, and the modulus of the atomic scattering amplitude, $|f_i(k)|$. The $\sin[2kR_i]$ term describes the oscillatory nature of the EXAFS due to constructive and destructive interference and depends on the photoelectron wavenumber, k, and the nearest neighbour distances between the absorbing and the scattering atoms, R_i. The terms δ_c and δ_i represent the phase shift of the photoelectron wave caused by the absorbing atom and the scattering atom respectively. Thermal and structural disorder can cause the atoms in a coordination shell to be at different distances to the absorbing atom. This causes phase differences in the scattered photoelectron waves

which increasingly dampens the oscillations in the EXAFS signal with increasing values of k. This is represented by the $\mathrm{e}^{-2\sigma_i{}^2\mathrm{k}^2}$ term, where $2\sigma_i{}^2$ is the XAS Debye-Waller factor. The decay of the photoelectron wave increases with increasing values of $\mathrm{R_i}$. This is considered in the term $\mathrm{e}^{-2\mathrm{R_i}/\lambda(\mathrm{k})}$, where the mean-free path, λ, corresponds to how far the photoelectron wave can travel while still contributing to the EXAFS signal.

$$\chi(\mathrm{k}) = \sum_i \mathrm{S_0}{}^2 \mathrm{N_i} \frac{|\mathrm{f_i(k)}|}{\mathrm{kR_i}{}^2} \sin[2\mathrm{kR_i} + 2\delta_c(\mathrm{k}) + \delta_i(\mathrm{k})]\, \mathrm{e}^{-2\mathrm{R_i}/\lambda(\mathrm{k})} \mathrm{e}^{-2\sigma_i{}^2\mathrm{k}^2} \qquad \text{Equation 38}$$

By Fourier transforming the k^n weighted $\chi(\mathrm{k})$ into r-space, a pseudo-radial distribution function can be attained. To minimise termination ripples, the k^n weighted $\chi(\mathrm{k})$ is often multiplied by a modification function, $\mathrm{M(k)}$, prior to being Fourier transformed. In this work, a Hanning modification function was used. In order to attain structural information from the Fourier transform of the k^n weighted $\chi(\mathrm{k})$ function, a path fitting technique can be used. This involves using relevant reference structures where the type and position of atoms are well-defined. The FEFF code [31] within Artemis [30] then calculates the $|\mathrm{f_i(k)}|\mathrm{e}^{-2\mathrm{R_i}/\lambda(\mathrm{k})}$, the $2\delta_c(k)$, and the $\delta_i(k)$ terms in the parameterised EXAFS equation for the single scattering paths and for the multiple scattering paths which are longer. The single-scattering paths involving nearest neighbour atoms dominate over the multiple-scattering paths. The paths that suitably represent nearest neighbour atoms are selected and used to fit the experimental spectrum using a least-squares fitting algorithm [14]. This minimises the difference between the experimental EXAFS spectra and the modelled EXAFS spectra. During the analysis of the EXAFS region, values of R_i, N_i, and $\sigma_i{}^2$ can be attained using equation 38. An example of this path fitting technique is shown in figure 11 for a crystalline calcite ($CaCO_3$) structure which has well-defined shells and known parameters.

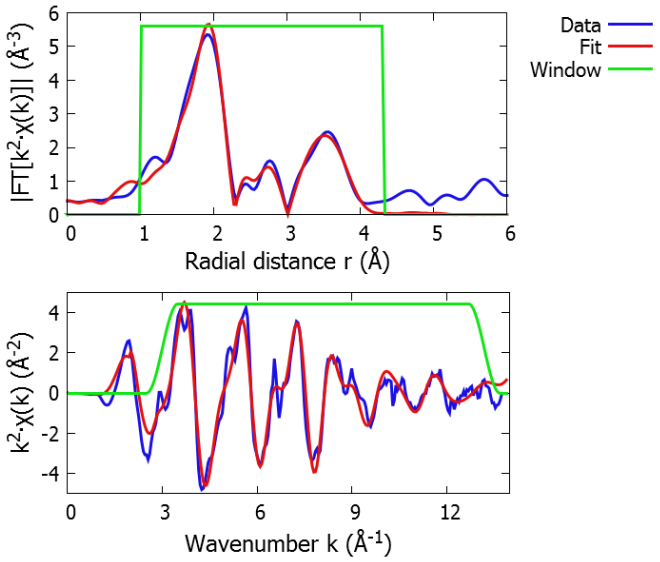

Figure 11: Example of fitting Ca K-edge k^2 weighted $\chi(k)$ experimental crystalline $CaCO_3$ data to a reference crystalline $CaCO_3$ structure.

3.10 References

[1] X. Chen, “Novel Halide Containing Bioactive Glasses,” Queen Mary University of London, 2015.

[2] L. Forto Chungong, L. A. Swansbury, G. Mountjoy, A. C. Hannon, A. F. Lee, and R. A. Martin, “Atomic structure of chlorine containing calcium silicate glasses by neutron diffraction and ^{29}Si solid-state NMR,” *Int. J. Appl. Glas. Sci.*, 2017.

[3] V. K. Pecharsky and P. Y. Zavalij, *Fundamentals of powder diffraction and structural characterization of materials*. New York: Springer, 2009.

[4] S. M. Shackley, *X-Ray Fluorescense Spectometry (XRF) in Geoarchaeology*. Springer, 2012.

[5] J. W. Robinson, E. S. Frame, and G. M. Frame II, *Undergraduate instrumental analysis*. CRC Press, 2014.

[6] A. C. Hannon, “Measuring the Density of Solid and Powder Samples: Instructions for using the Quantachrome Micropycnometer,” *Priv. Commun.*, 2002.

[7] Y. Leng, *Materials characterization: introduction to microscopic and spectroscopic methods*. John Wiley & Sons, 2009.

[8] E. Smith and G. Dent, *Modern Raman spectroscopy: a practical approach*. John Wiley & Sons, 2013.

[9] P. Vandenabeele, *Practical Raman spectroscopy: an introduction*. John Wiley & Sons, 2013.

[10] R. W. Luth, “Raman spectroscopic study of the solubility mechanisms of F in glasses in the system CaO-CaF_2-SiO_2,” *Am. Mineral.*, vol. 73, pp. 297–305, 1988.

[11] J. Goldstein *et al.*, *Scanning electron microscopy and X-ray microanalysis: a text for biologists, materials scientists, and geologists*. Springer Science & Business Media, 2012.

[12] P. J. Goodhew, J. Humphreys, and R. Beanland, *Electron microscopy and analysis*, Third edit. CRC Press, 2000.

[13] I. S. Anderson, A. J. Hurd, and R. . McGreevy, *Neutron Scattering Applications and Techniques*. Springer, 2008.

[14] M. Affatigato, *Modern glass characterization*. John Wiley & Sons, 2015.

[15] M. De Graef and M. E. McHenry, *Structure of materials: an introduction to crystallography, diffraction and symmetry*. Cambridge University Press, 2012.

[16] R. N. Mead, “Molecular dynamics modelling of the amorphous calcium silicate and titania silicate atomic-scale structure,” University of Kent, 2006.

[17] D. S. Sivia, *Elementary scattering theory: for X-ray and neutron users*. Oxford University Press, 2011.

[18] J. C. Lindon, G. E. Tranter, and J. L. Holmes, *Encyclopedia of spectroscopy and spectrometry*. London: Academic Press, 2000.

[19] C. M. Gramaccioli, *Energy Modelling in Minerals*. Gramaccioli, Carlo Maria. Energy Modelling in Minerals. Vol. 4. The Mineralogical Society of Great Britain and Ireland, 2002.

[20] A. C. Hannon, "Results on disordered materials from the GEneral Materials," *Nucl. Instruments Methods Phys. Res. A*, vol. 551, pp. 88–107, 2005.

[21] A. K. Soper, "GudrunN and GudrunX: programs for correcting raw neutron and X-ray diffraction data to differential scattering cross section," *Sci. Technol. Facil. Counc.*, 2011.

[22] C. M. Moreton-Smith, S. D. Johnston, and F. A. Akeroyd, "Open GENIE—a generic multi-platform program for the analysis of neutron scattering data," *J. Neutron Res.*, vol. 4, pp. 41–47, 1996.

[23] D. Pickup, R. Moss, and R. Newport, "NXFit : a program for simultaneously fitting X-ray and neutron diffraction pair-distribution functions to provide optimized structural parameters," *J. Appl. Crystallogr.*, vol. 47, pp. 1790–1796, 2014.

[24] D. L. Tierney and G. Schenk, "X-ray absorption spectroscopy of dinuclear metallohydrolases," *Biophys. J.*, vol. 107, no. 6, pp. 1263–1272, 2014.

[25] R. E. Medjo, *Physical and Chemical Properties of Carbon Nanotubes*. InTech, 2013.

[26] W. Gawelda, "Time-resolved x-ray absorption spectroscopy of transition metal complexes," Adam Mickiewicz University, 2006.

[27] C. S. Schnohr and M. C. Ridgway, Eds., *X-ray absorption spectroscopy of semiconductors*. Springer-Verlag Berlin Heidelberg, 2015.

[28] J. G. Parsons, M. V. Aldrich, and J. L. Gardea-Torresdey, "Environmental and biological applications of extended X-ray absorption fine structure (EXAFS) and X-ray absorption near edge structure (XANES) spectroscopies," *Appl. Spectrosc. Rev.*, vol. 37, no. 2, pp. 187–222, 2002.

[29] A. J. Dent *et al.*, "B18: A core XAS spectroscopy beamline for Diamond," *J. Phys. Conf. Ser.*, vol. 190, p. 12039, 2009.

[30] B. Ravel and M. Newville, "ATHENA, ARTEMIS, HEPHAESTUS: data analysis for X-ray absorption spectroscopy using IFEFFIT," pp. 537–541, 2005.

[31] J. J. Rehr, J. J. Kas, M. P. Prange, A. P. Sorini, and Y. Takimoto, "Ab initio theory and calculations of X-ray spectra," *C. R. Phys.*, vol. 10, no. 6, pp. 548–559, 2009.

[32] R. M. Moss, "Structural Studies of Metal Doped Phosphate Glasses and Computational Developments in Diffraction Analysis," Ph.D. thesis, University of Kent, 2009.

[33] K. M. Wetherall, "The Structure of Amorphous Calcium Phosphate and Other Phosphate Materials," Ph.D. thesis, University of Kent, 2009.

4. A Computational Investigation of the Structure of $ZnCl_2$ glass

4.1 Introduction

Zinc chloride glass, $ZnCl_2$, is a halide system which comprises of Zn^{4+} and Cl^{2-} ions. These interact to form tetrahedral $ZnCl_4$ structural units. In a strong glass former like SiO_2, the corner-sharing SiO_4 tetrahedral units form a rigid three-dimensional network. In a fragile glass former like $BeCl_2$ [1], the $BeCl_4$ edge-sharing tetrahedral units join to form chains. The $ZnCl_2$ glass network is intermediate between the two (figure 1). It has a combination of edge-sharing and corner-sharing tetrahedral structural units as permitted by the polarisability of the chlorine anions, and the Zn-Cl-Zn bond angle of approximately 110° [1].

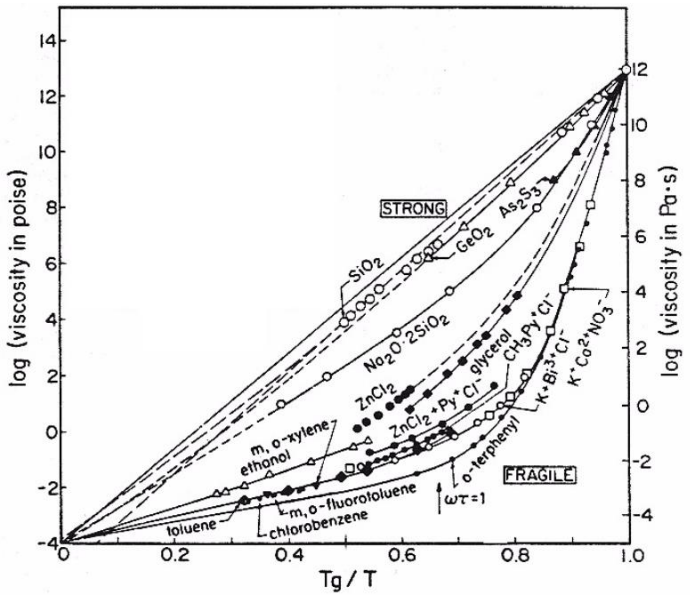

Figure 1: Scaled Arrhenius plots from Angell [2] for a number of strong and fragile glass-forming compositions which illustrates the intermediate glass-forming nature of $ZnCl_2$.

Although a number of experimental studies have probed the crystalline state (e.g. [3]–[5]), the molten state (e.g. [6]–[11]), and the glassy state (e.g. [8]–[12]) of $ZnCl_2$, comparatively few computational studies on $ZnCl_2$ glass have been conducted. This is despite $ZnCl_2$ exhibiting interesting properties, such as a high tendency towards glass formation [13]. The cause is likely to be the complexity of accounting for chlorine anion polarisability, together with the shortage of suitable interatomic potential parameters available in the literature [8], [13].

First principles computational simulation considers the electronic configuration of atoms. However, the computational expense limits the simulation size and timescale. Alsayoud *et al.* [14] has modelled liquid $ZnCl_2$ using first principles simulation. Although the model only contained 108 atoms and was quenched from 2000K to 600K at a rate of 1.8×10^{14}K/s, the model overwhelmingly comprised of $ZnCl_4$ tetrahedral units. Only 5% of the Zn ions were involved in $ZnCl_3$ or $ZnCl_5$ structural units, which could be attributed to the temperature of the system. Although Alsayoud *et al.* [14] did not produce a $ZnCl_2$ glass model, it can be anticipated that the proportion of $ZnCl_4$ tetrahedral units in a glass model would be at least 95%.

Classical molecular dynamics (MD) is a different type of computational simulation that does not consider the electronic configuration of atoms. This enables larger system sizes to be modelled over relatively long timescales. MD simulations are often run using rigid-ion (RI) interatomic potential parameters. These treat the atoms as solid spheres and fail to account for ion polarisability. Kumta *et al.* [15] modelled a $ZnCl_2$ glass using RI interatomic potential parameters, although the model only contained 324 atoms. In addition, the Zn-Cl coordination number of 4.96 was significantly higher than the value of 4.00 expected. This was because 40% of the structural units were reported to be $ZnCl_6$ structural units, casting doubt over the interatomic potential parameters used.

In order to compromise between first principles and classical molecular dynamics, classical molecular dynamics simulations can be made to consider ion polarisability. One approach is the addition of the polarisable ion model (PIM). This reproduces polarisability through enabling the dipole strength and orientation to fluctuate throughout the simulation. It was used by Sharma and Wilson [1] to generate a model of $ZnCl_2$ melt that was consistent with experimental findings [16]–[22]. The addition of the core-shell model is an alternative approach. In this, the atom is split into a separate core and shell unit. The core and the shell are connected by a harmonic spring of spring constant K_{cs}. The shell can either be massless (dynamic core-shell model), or have an assigned mass (adiabatic core-shell model). Since the charge is divided between the core and the shell, the shell can move with respect to the ion core. This reproduces dipole induction, and hence the polarisable nature of the ion. The core-shell model is typically only applied to the anions in a simulation because they are generally more susceptible to polarisation. The adiabatic core-shell model was used by Huang *et al.* [13] to model $ZnCl_2$ melt. The study involved melting a crystalline $ZnCl_2$ structure at 2000K for 2ps to attain results consistent with experimental findings [23]–[26]. However, it is conceivable that the low melting temperature and the short simulation timescale may not have been adequate in allowing a representative melt structure to develop, making the results biased towards the input crystal structure.

A different type of computational simulation is reverse Monte Carlo (RMC) modelling. This involves the atoms in an input configuration being successively moved to reproduce

experimental diffraction results as closely as possible. Pusztai and McGreevy [27] have modelled $ZnCl_2$ glass using RMC. The model comprised of distorted tetrahedral units that were of trigonal planar symmetry. In addition, the Zn-Zn coordination number of ~5.3 was significantly higher than the value of 4.0 expected for a system comprising entirely of tetrahedral units. Zeidler *et al.* [9], [10] has also modelled $ZnCl_2$ glass using RMC modelling. Average Zn and Cl coordination numbers of ~4.0 and ~2.0 respectively were attained and indicated consistency with tetrahedral units. However, in one of the studies [9], it was reported that 41% of the Cl ions did not have a coordination number of 2.0. In the later study [10], 9.8% of the structural units were found to either be $ZnCl_3$ or $ZnCl_5$ structural units. This could be due to a lot of the disorder present in the initial random configuration of atoms being retained throughout the RMC modelling process.

In this chapter, $ZnCl_2$ glass was modelled computationally without bias towards an input crystalline structure or experimental diffraction results. This was achieved using MD with the addition of the adiabatic core-shell model. The structural effects of anion polarisability in $ZnCl_2$ glass were explored by performing nearest neighbour distance, coordination number, bond angle, and structure factor calculations. As mentioned, the strong glass former SiO_2 also comprises of tetrahedral structural units and shares the same stoichiometry as $ZnCl_2$. Since SiO_2 glass has been well studied both experimentally and computationally, the structural effects of anion polarisability in the intermediate and strong glass formers were compared.

4.2 Computational Modelling Methodology

4.2.1 Interatomic Potential Parameters

Throughout this chapter, the atomic correlations refer to the core atomic correlations unless clearly stated otherwise. For example, Cl-Cl refers to the chlorine cores, while Cl_s-Cl_s refers to the chlorine shells. Core-shell model interatomic potential parameters for modelling $ZnCl_2$ have been reported by Binks [28] (table 1). An additional three-body interatomic potential parameter of truncated harmonic form was fitted in this work to encourage the four-fold coordination of Zn ions, and hence maintain tetrahedral structural units. It was important to test these interatomic potential parameters on crystalline structures using the General Utility Lattice Program (GULP) [29] to ensure their suitability in this modelling study.

Table 1: The two-body Buckingham and three-body screened harmonic potential parameters used to model $ZnCl_2$ glass. The two-body interatomic potential parameters were obtained from Binks [28], whilst the three-body interatomic potential was fitted in this work. The chlorine shell mass was 0.450u.

	Two body $V_{ij}(r) = A_{ij}\exp\left(\frac{-r}{\rho_{ij}}\right) - \frac{C_{ij}}{r^6}$		
	A_{ij} (eV)	ρ_{ij} (Å)	C_{ij} (eV Å^6)
$Zn - Zn$	0.0000000	0.0000000	0.000000
$Zn - Cl_s$	9704.8900	0.2320000	0.000000
$Cl_s - Cl_s$	3296.5700	0.3289000	107.2000
	Three body $V(\theta_{jik}) = \frac{k_3}{2}(\theta_{jik} - \theta_0)^2 \exp\left[-\left(\frac{r_{ij}}{\rho} + \frac{r_{ik}}{\rho}\right)\right]$		
	k_3 (eV rad^{-2})	θ_0 (°)	ρ (Å)
$Cl - Zn - Cl$	1.5	109.47	3.0
	Core-shell potential $V = \frac{1}{2}K_{cs}r^2$		
	K_{cs} (eV Å^{-2})	Q (core) (e)	q (shell) (e)
$Cl - Cl_s$	17.25	0.984	-1.984
$Zn - Zn$		2.000	

There are four crystalline polymorphs of $ZnCl_2$ [3]. They are referred to as α, β, γ, and δ and are illustrated in figure 2. It is known that the α, β, and γ polymorphs occur with some water absorption [3], leaving orthorhombic δ-$ZnCl_2$ as the only pure polymorph. The δ-$ZnCl_2$ crystal structure of space group 33 was therefore used to test the interatomic potentials in table 1.

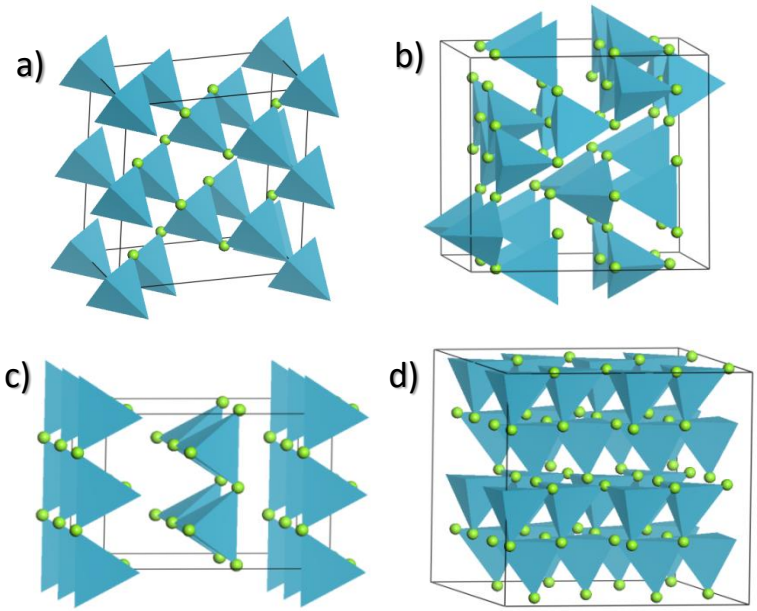

Figure 2: The crystalline structures of a) α-$ZnCl_2$ b) β-$ZnCl_2$ c) γ-$ZnCl_2$ d) δ-$ZnCl_2$ reproduced from [5], [30]. The blue tetrahedra represent zinc ions and the light green spheres correspond to the chlorine ions. In this figure, the chlorine ions have not been split into core-shell units.

It can be seen in table 2 that upon energy minimisation, the unit cell volume of δ-$ZnCl_2$ increased by 6.80%, but its orientation remained intact. The Zn-Cl, Cl-Cl, and Zn-Zn nearest neighbour distances increased from 2.27Å, 3.77Å, and 3.76Å to 2.30Å, 3.88Å, and 3.85Å respectively. The coordination numbers of 4.00, 12.00, and 4.00 respectively were unchanged. Taking into account the shortage of alternative published interatomic potentials for $ZnCl_2$ [8], [13], the interatomic potentials derived by Binks [28] were deemed adequate as a starting point to model $ZnCl_2$ glass in this study.

Table 2: The initial δ-$ZnCl_2$ crystalline lattice parameters, and the corresponding percentage changes following GULP energy minimisation.

Parameter	Unit	Initial value	Percent Change (%)
Volume	$Å^3$	303.59	6.80
a	Å	6.44	-1.34
b	Å	7.69	9.04
c	Å	6.13	-0.72
α	°	90.00	0.00
β	°	90.00	0.00
γ	°	90.00	0.00

4.2.2 Molecular Dynamics Simulations

An initial δ-$ZnCl_2$ starting configuration containing 1280 atomic constituents was prepared using the program DL_FIELD [31]. This configuration included 256 Zn cores, 512 Cl cores, and 512 corresponding Cl shells (to account for anion polarisability). Of the atomic mass of chlorine (35.003u), a mass of 0.450u was assigned to the shell. The remaining mass was assigned to the chlorine core. The simulation cell side lengths of a=28.37Å, b=33.87Å, and c=26.97Å corresponded to the experimental density of the glass ($0.0359Å^{-3}$ [9]). The core-shell model molecular dynamics simulation was then run using the program DLPOLY [32] with the interatomic potential parameters in table 1. A universal cut-off of 7.5Å, a primary cut-off of 6.5Å, and a van der Waals cut-off of 5.5Å were applied.

The simulation began at a temperature of 6000K to ensure a random distribution of ions. The simulation temperature was then successively reduced to 3000K, then 1000K. At this point, the system was still liquid as it was comfortably above its melting temperature of 593K [3]. To produce a glass model, it is necessary to quench the system quickly to prevent crystallisation. The system was quenched from 1000K to 300K at a rate of 10^{13}K/s. To ensure a solid glass model, a further stage at 300K was run and used for analysis. The results of this stage were also used to initiate further sampling runs at 600K and 1000K. All

stages of the simulation ran for 800,000 time-steps, other than the quench stage which required 350,000 time-steps because the time-step was 0.2fs. To make sure the system maintained the correct density, an NVT Berendsen thermostat was used throughout the simulation. To help conserve stability, all simulation stages were fully equilibrated. The glass model of SiO_2 later used for structural comparison with $ZnCl_2$ was obtained using the computational method denoted as SM1 by Tilocca *et al.* [33].

4.3 Results

4.3.1 Images of Models

Figure 3 compares the δ-$ZnCl_2$ crystalline structure to the glass model at 300K. While the δ-$ZnCl_2$ crystalline structure to the left comprises solely of corner-sharing tetrahedra, the glass model to the right contains some edge-sharing tetrahedral units which have been highlighted in dark green. The chlorine shells (in brown) are closer to zinc than the chlorine cores (in bright green) in both the crystalline and glass models. This is due to the charges assigned to the cores and shells (table 1).

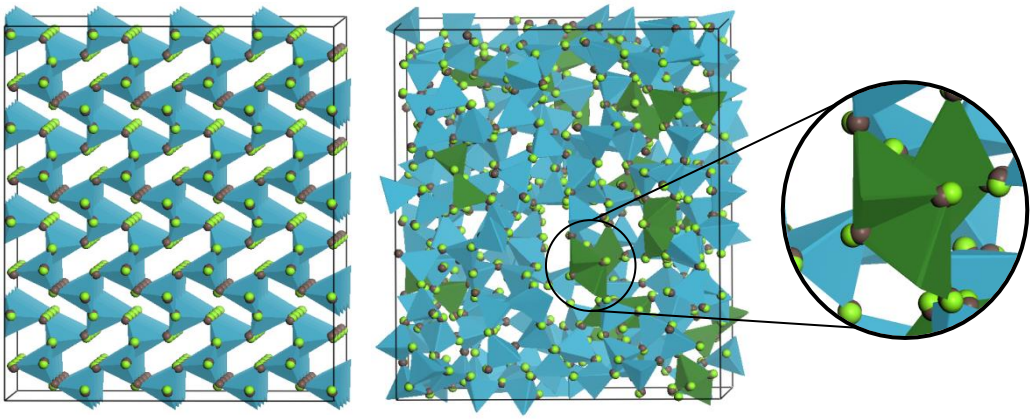

Figure 3: To the left, the original δ-$ZnCl_2$ crystal structure and to the right, the $ZnCl_2$ glass model. The blue tetrahedra are zinc tetrahedra, the light green and brown spheres are the chlorine cores and shells respectively.

4.3.2 Pair Correlation Functions and Cumulative Coordination Numbers

As shown in figure 4, the pair correlation functions of $ZnCl_2$ glass involving shells have smaller nearest neighbour distances than the corresponding correlations involving cores. This could be visualised in the crystalline and glass models of $ZnCl_2$ in figure 3, and occurs because the chlorine shells were assigned a negative charge (table 1). Small pre-peaks

consistent with a minority of edge-sharing tetrahedra in the $ZnCl_2$ glass model are also visible in the Zn-Zn and Cl_s-Cl_s pair correlation functions.

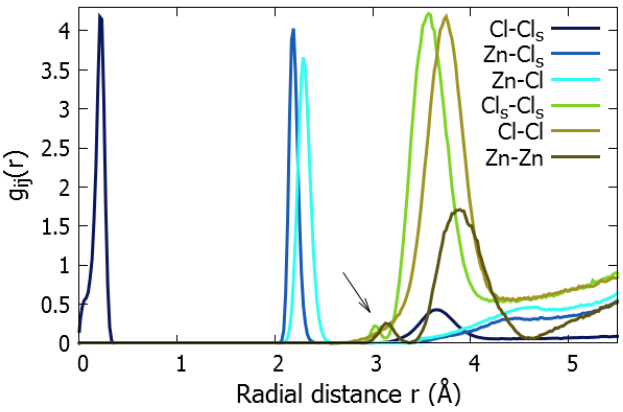

Figure 4: Core and shell pair correlation functions, $g_{ij}(r)$, for the $ZnCl_2$ glass model. The amplitudes of the Cl-Cl_s, Zn-Cl_s, and Zn-Cl correlations were reduced by factors of 10, 4, and 3 respectively. This enabled the lower amplitude distributions to be seen more clearly.

The pair correlation functions of $ZnCl_2$ glass from this work (labelled MD) were then compared with experimental neutron diffraction (ND) results [9] in figure 5. The Zn-Cl and Cl-Cl pair correlation functions agreed well with the ND findings. There was some discrepancy between the Zn-Zn pair correlation functions because while two peaks were identified from computational simulation, only one broad peak was observed experimentally.

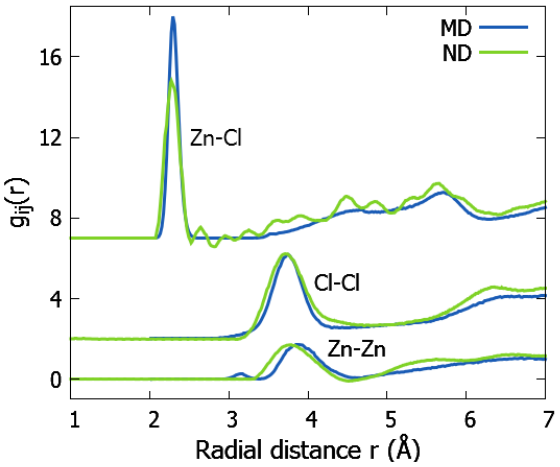

Figure 5: The Zn-Cl, Cl-Cl, and Zn-Zn pair correlation functions, $g_{ij}(r)$, obtained computationally in this work (MD) and experimentally using ND by Zeidler *et al.* [9]. The Cl-Cl and Zn-Cl pair correlation functions have offsets of 2.0 and 7.0 respectively.

The nearest neighbour distances and coordination numbers attained in this study are summarised in table 3. Values from other studies are also reported to enable comparisons. The Zn-Cl nearest neighbour distance of 2.30Å was in good agreement with other studies.

The corresponding coordination number of 4.00 was expected for a tetrahedral structural unit. The Cl-Cl nearest neighbour distance of 3.76Å was in line with other studies, but there was obvious disagreement between the corresponding coordination number values. This is due to the cumulative coordination number plot (figure 6) being very steep, placing a high sensitivity on the cut-off distance applied.

Table 3: The nearest neighbour distances, R_{ij}, coordination numbers, $N_{ij}(r)$, and coordination number cut-off distances from this work and a number of experimental studies. These include neutron diffraction (ND) [9], [10], [34] , X-ray diffraction (XRD) [9], and extended X-ray absorption fine structure (EXAFS) [11], [4]. A reverse Monte Carlo (RMC) computational study is also included [9]. The uncertainty in measurement is given in brackets.

Ref.	Method	Zn-Cl			Cl-Cl			Zn-Zn		
		R_{ij} (Å)	$N_{ij}(r)$	Cut-off (Å)	R_{ij} (Å)	$N_{ij}(r)$	Cut-off (Å)	R_{ij} (Å)	$N_{ij}(r)$	Cut-off (Å)
This work	MD	2.30(1)	4.00(2)	3.0	3.76(5)	10.07(5)	5.0	3.89(5)	3.62(5)	4.3
[9]	ND	2.27(1)	3.8(3)	2.52	3.68(1)	11.0(4)	4.66	3.74(1)	3.8(2)	4.42
[9]	ND/RMC	2.29(5)	3.99(1)	3.0	3.69(5)	12.2(1)	5.0	3.67(5)	4.16(1)	4.3
[9]	XRD	2.27(2)	4.0(1)	2.47						
[10]	ND	2.27(2)	4.04(5)							
[34]	ND	2.29(1)	3.8		3.72(1)	9.5				
[11]	EXAFS	2.34(1)	5.1(8)							
[4]	EXAFS	2.30(4)								

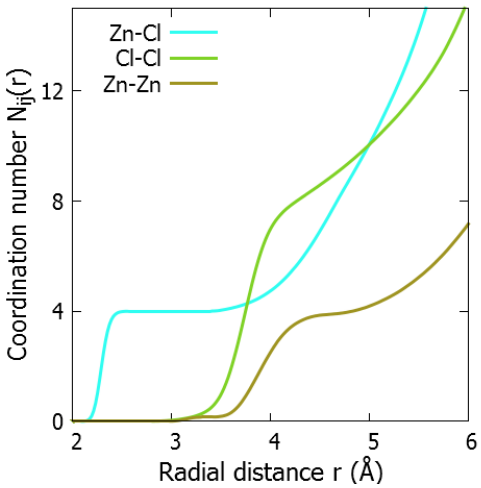

Figure 6: Cumulative coordination number plots for Zn-Zn, Zn-Cl and Cl-Cl correlations.

4.3.3 Structure Factors

The calculated Faber-Ziman (FZ) partial structure factors from the computational model of $ZnCl_2$ glass (labelled MD) were in good agreement with experimental ND results [9] (figure 7). The very marginal phase shift in $S^{FZ}_{ClCl}(Q)$ was caused by the Cl-Cl nearest neighbour

distance in the computational model being slightly greater than that determined from the ND results (table 3). The noise in $S^{FZ}_{ZnZn}(Q)$ from ND illustrates its weak weighting factor, ω_{ZnZn}, of 0.05. The total neutron and X-ray structure factors in figure 8 were in good agreement with experimental findings [9], [10].

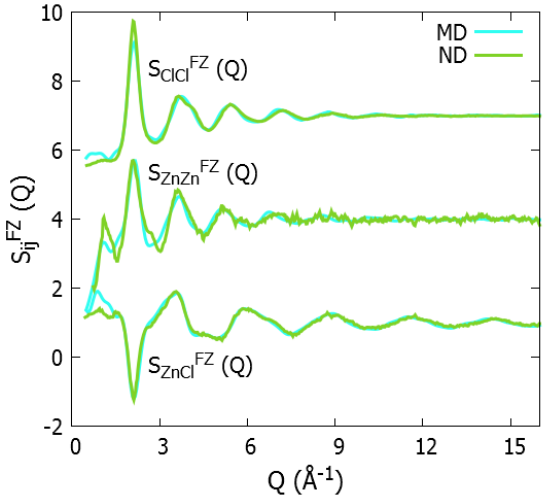

Figure 7: The Faber-Ziman partial structure factors calculated in this work (MD) compared with those obtained from neutron diffraction (ND) [9]. The $S^{FZ}_{ZnZn}(Q)$ and $S^{FZ}_{ClCl}(Q)$ plots have vertical offsets of 3.0 and 6.0 respectively.

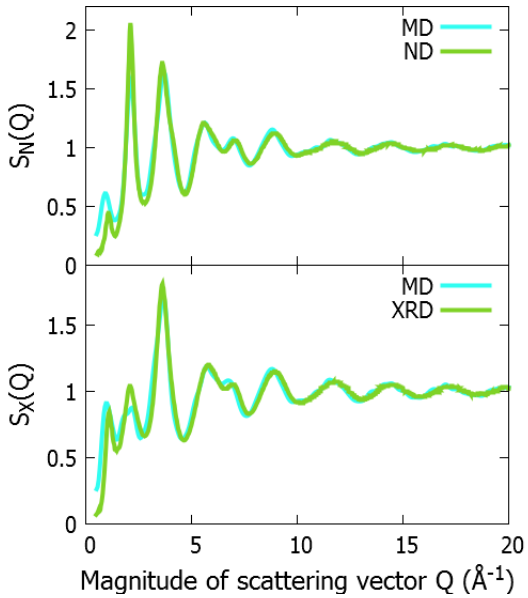

Figure 8: The total neutron and X-ray structure factors ($S_N(Q)$ and $S_X(Q)$ respectively) from this work (MD) compared to those obtained experimentally (ND) [9], [10].

4.3.4 Bond Angle Distributions

The Zn-Cl-Zn bond angle distribution in figure 9 shows two distinct peaks centred around angles of 83° and 113°. These correspond to edge-sharing and corner-sharing tetrahedra

respectively [35]. While 14% of the tetrahedral structural units were edge-sharing, 86% were corner-sharing. Sharma and Wilson [1] state that a Zn-Cl-Zn bond angle of ~110° permits the formation of edge-sharing or corner-sharing tetrahedra. The Cl-Zn-Cl bond angle distribution was centred around an angle of 109°, matching the ideal tetrahedral angle [9].

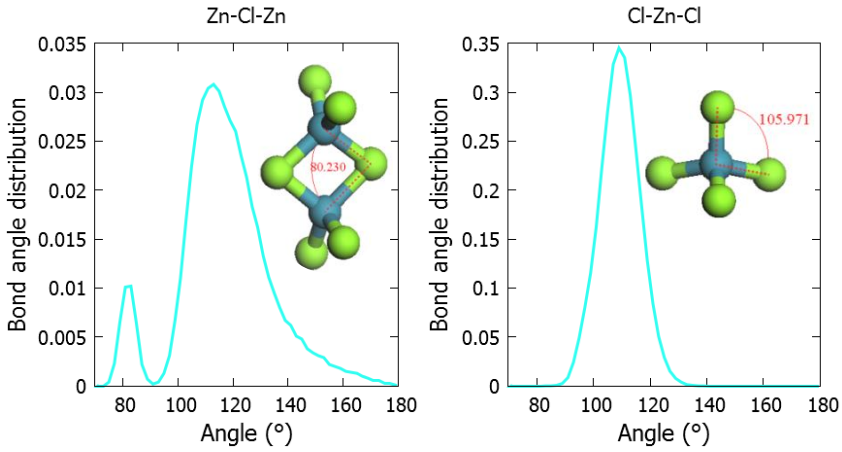

Figure 9: The Zn-Cl-Zn bond angle distribution to the left, and the Cl-Zn-Cl bond angle distribution to the right for $ZnCl_2$ glass. Images of tetrahedra are included to help visualise the bond angles where the blue and green atoms represent Zn and Cl atoms respectively.

4.3.5 Comparing $ZnCl_2$ and SiO_2

It was of interest to compare the structural effects of anion polarisability in the intermediate glass former $ZnCl_2$ to those in the well-established strong glass-former SiO_2. Table 4 details the positions of the first three peaks in total correlation functions of $ZnCl_2$ and SiO_2 glass (corresponding to the cation-anion, the anion-anion, and the cation-cation nearest neighbour distances and labelled as R_1, R_2, and R_3 respectively). The first three peak positions in the total neutron structure factors (labelled Q_1, Q_2, and Q_3 respectively where the Q-scale is conceptually reciprocal to the r-scale) are also included. The R_1 ratio compares the Zn-Cl and Si-O nearest neighbour distances. Since both have tetrahedral structural units ($ZnCl_4$ and SiO_4), it can be seen that those in $ZnCl_2$ are 1.42 times larger than those in SiO_2. The R_2 ratio compares the edge lengths of the $ZnCl_4$ and the SiO_4 tetrahedral structural units, hence the R_2 ratio matches the R_1 ratio. The R_3 ratio of 1.25 is smaller than the R_1 ratio of 1.42. The average Zn-Cl-Zn bond angle of ~110° is smaller than the average Si-O-Si bond angle of ~150° [36]. This has the effect of lowering the Zn-Zn nearest neighbour distance (R_3), and in turn reducing the R_3 ratio. Although comparable to the Q_2 and Q_3 ratios, the R_1 ratio is in poor agreement with the Q_1 ratio.

Table 4: The terms R_1, R_2, and R_3 denote the cation-anion, anion-anion, and cation-cation nearest neighbour distances respectively. The terms Q_1, Q_2 and Q_3 denote the first three peak positions in the total neutron structure factors. The uncertainty in the R and Q values was ±0.01Å and ±0.05Å^{-1} respectively.

	R_1 (Å)	R_2 (Å)	R_3 (Å)	Q_1 (Å^{-1})	Q_2 (Å^{-1})	Q_3 (Å^{-1})
$ZnCl_2$	2.30	3.76	3.89	0.88	2.11	3.69
SiO_2	1.62	2.64	3.11	1.53	2.91	5.19
Ratio	1.42	1.42	1.25	1.74	1.38	1.41

The Q_1 values compare the first sharp diffraction peak (FSDP) positions in the total neutron structure factors of $ZnCl_2$ and SiO_2. The FSDP's from the computational models in this work (labelled MD) are compared to experimental ND results [9], [37], [38] in figure 10. An important consideration in these comparisons is the weighting factor of each contribution. In $ZnCl_2$ glass, the Zn-Cl, Cl-Cl, and Zn-Zn weighting factors are 0.35, 0.59, and 0.05 respectively. The corresponding weighing factors in SiO_2 glass are similar with values of 0.39, 0.54, and 0.07 for Si-O, O-O, and Si-Si respectively. The $S^{FZ}_{ZnZn}(Q)$ and $S^{FZ}_{SiSi}(Q)$ Faber-Ziman (FZ) partial structure factors have low weighting and reveal that the higher-weighted cation-anion contributions are most significant in the FSDP.

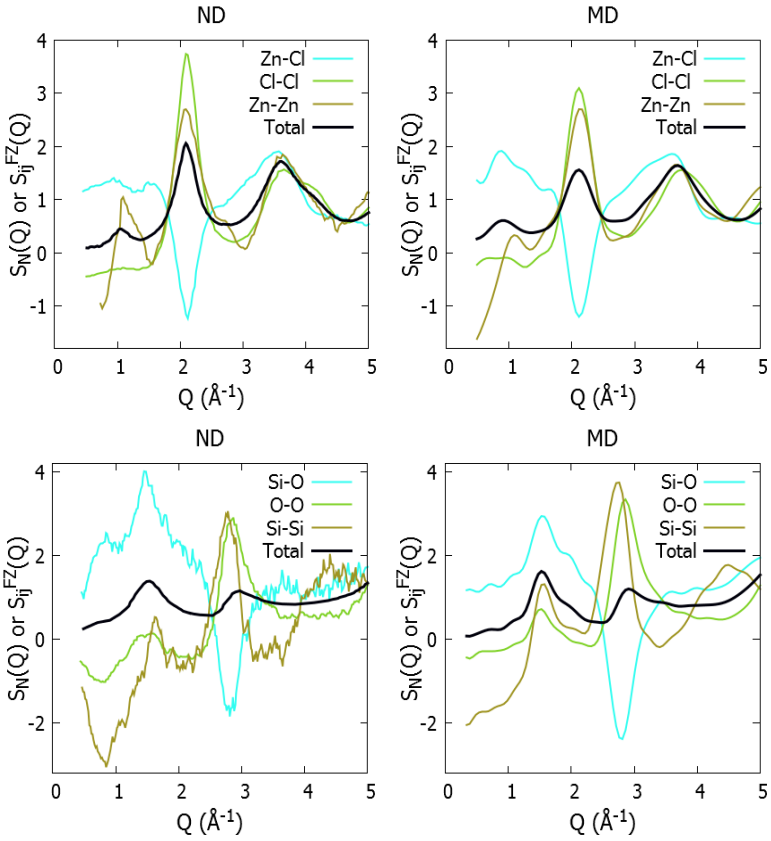

Figure 10: Total neutron structure factors and unweighted Faber-Ziman partial structure factors for $ZnCl_2$ and SiO_2. The plots to the left were obtained from neutron diffraction (ND) experiments [9], [37], [38] and the plots to the right were from this molecular dynamics (MD) study.

To compare the partial Faber-Ziman structure factors of $ZnCl_2$ and SiO_2, it is necessary to account for the different Q ratios and scale the partial Faber-Ziman structure factors accordingly. This was achieved using the equation $Q'=Q\times R_{ij}$, where R_{ij} is the i-j nearest neighbour distance. As shown in figure 11, differences between the FSDP's of the scaled partial Faber-Ziman structure factors are observed. However, beyond the FSDP's, good agreement can be seen.

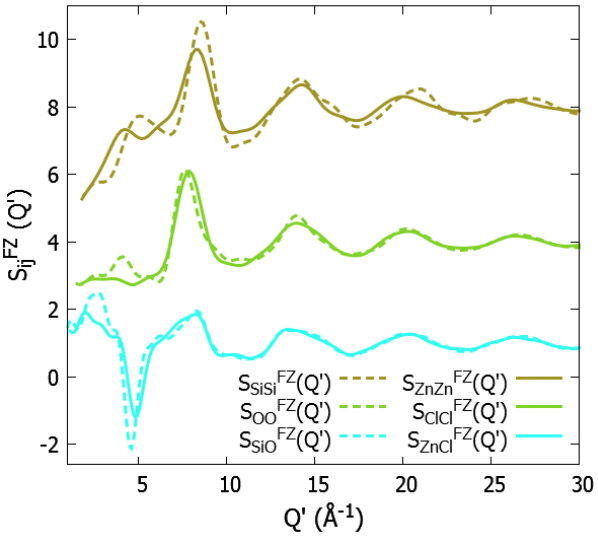

Figure 11: A Faber-Ziman partial structure factor comparison between $ZnCl_2$ and SiO_2 glass. The $\mathbf{S_{ZnZn}^{FZ}(Q')}$ and $\mathbf{S_{SiSi}^{FZ}(Q')}$ plots have a vertical offset of 7.0. The $\mathbf{S_{ClCl}^{FZ}(Q')}$ and $\mathbf{S_{OO}^{FZ}(Q')}$ plots have a vertical offset of 3.0.

Packing fraction calculations of $ZnCl_2$ and SiO_2 formed the final comparison between the intermediate and the strong glass formers. The packing fraction (PF) is a measure of the occupancy of a given atom type within a system volume. It is defined using equation 1, where ρ^0 is the atomic number density, and R_i is the packing radius attributed to the atom. In this work, the packing radius of the atom was assumed to be equivalent to half of its nearest neighbour distance. The atomic number density could be calculated since the number of each atom type, and the size of the simulation cell was known. The packing fractions for the atomic constituents of $ZnCl_2$ and SiO_2 are shown in table 5. While the packing fractions of Zn and Si were similar, the packing fractions of Cl and O were significantly different.

$$PF = \rho^0 \frac{4\pi}{3} {R_i}^3 \qquad \text{Equation 1}$$

Table 5: The parameters needed to calculate the packing fractions, and the packing fraction values attained for the anions and cations in $ZnCl_2$ and SiO_2 glass. The packing radius R_i of an atom was assumed to be half of its nearest neighbour distance.

Atom type i	No. atoms	Volume (Å^3)	$2 \times R_i$ (Å)	PF
Zn	256	25915	3.89	0.30
Cl	512	25915	3.76	0.55
Si	500	22675	3.11	0.35
O	1000	22675	2.64	0.42

4.4 Discussion

Classical molecular dynamics with the addition of the adiabatic core-shell model was used to model $ZnCl_2$ glass. The input δ-$ZnCl_2$ crystalline structure comprised entirely of corner-sharing tetrahedral units, but in the glass model, 14% of these tetrahedral units had become edge-sharing (figure 3). The formation of edge-sharing tetrahedral units has been explained by Madden and Wilson [35]. When bond bending induces a dipole in the chlorine anions, the Zn-Zn separation distance is reduced. This causes cation-cation repulsion to occur. It then becomes possible to make the transition from corner-sharing to edge-sharing if the Cl_s-Cl_s separation distance reduces in order to screen the cation-cation repulsion as illustrated in figure 12.

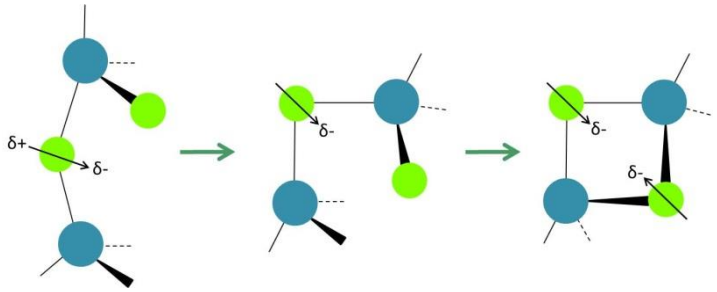

Figure 12: The formation of edge-sharing zinc tetrahedral structural units, where the blue circles represent zinc ions and the green circles represent the chlorine ions. This diagram was reproduced from [35].

Zeidler *et al.* [10] noticed that the proportion of edge-sharing tetrahedra increases with increasing system temperature. This seemed intuitive because at higher temperatures, there would be more energy to permit bond breaking and making, promoting the formation of edge-sharing tetrahedra. This prompted simulations to be run when the system was around its melting temperature (of 593K [3]) at 600K, and when the system was a melt at 1000K. Illustrations of the $ZnCl_2$ models at 600K and 1000K are shown alongside the 300K model in figure 13. Blue lines were added to show Cl_s-Cl_s separation distances of less than 3.1Å. Distances lower than 3.1Å in the Cl_s-Cl_s pair correlation function (figure 4) had been attributed to edge-sharing tetrahedra. At 300K, the reduced Cl_s-Cl_s

distances almost exclusively only occurred in edge-sharing tetrahedra, but as the system temperature increased, the shorter Cl_s-Cl_s separation distances began to occur elsewhere in the model and in greater numbers. This confirmed that the formation of edge-sharing tetrahedra becomes more favourable with increasing system temperatures.

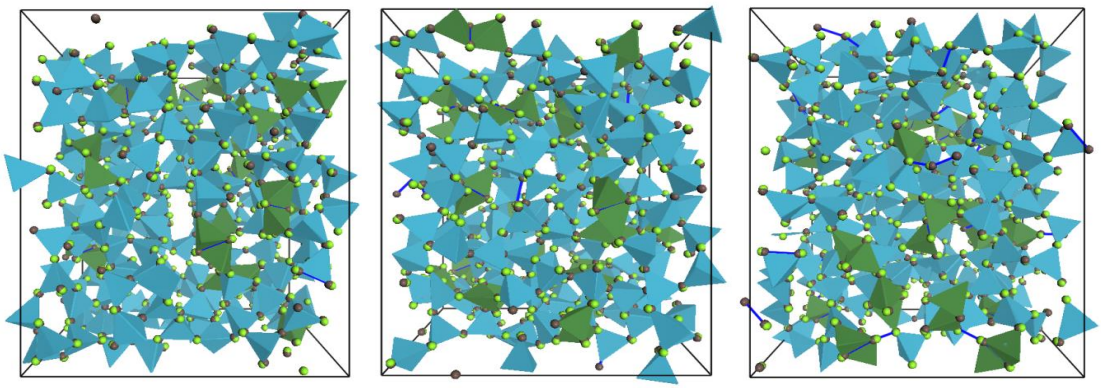

Figure 13: A perspective view of the $ZnCl_2$ glass at 300K (left), $ZnCl_2$ at around its melting temperature at 600K (middle) and molten $ZnCl_2$ at 1000K (right). The blue tetrahedra represent Zn atoms, and the light green and brown spheres are Cl cores and shells respectively. Edge-sharing tetrahedra have been highlighted in dark green. The dark blue lines correspond to Cl_s-Cl_s separation distances of less than 3.1Å.

Although the number of edge-sharing tetrahedral structural units in this study did rise with system temperature, it was to a far lesser extent than in the RMC models reported by Zeidler *et al.* [10]. In this study, the proportion of edge-sharing tetrahedra increased from 14% at 300K, to 17% at 600K, and then to 19% at 1000K. Zeidler *et al.* [10] reported proportions of 8%, 37%, and 55% at temperatures of 300K, 600K and around 1000K respectively. Despite the very close agreement with experimental diffraction data [10], part of this significant inconsistency is likely to be caused by structural units other than tetrahedra being present in the RMC models. The number of these defects, such as Zn cations not having a coordination number of 4.00, was also seen to increase with increasing system temperature (figure 14). It is likely that these defects were caused by the retention of some disorder present in initial random distribution of atoms. If RMC had instead been used to refine an existing $ZnCl_2$ glass model, from MD for example, instead of using a random initial configuration, it is likely that the same level of defects would not have been observed. Another source of the significant discrepancy between the two studies could be the strength of the three-body interatomic potential used in this work. A weaker three-body interatomic potential parameter could have led to higher proportions of edge-sharing tetrahedra at higher temperatures.

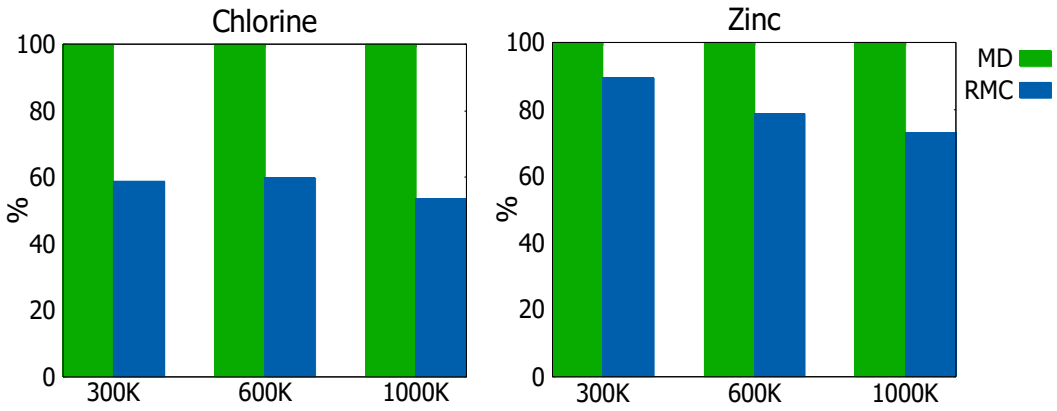

Figure 14: To the left, a plot comparing the proportion of two-coordinated chlorine; and to the right, a plot comparing the proportion of four-fold coordinated zinc ions between this MD study and an RMC study [10] at temperatures of 300K, 600K, and 1000K.

Upon further examination of the pair correlation functions in figure 4, it can be seen that the correlations involving anion shells have smaller nearest neighbour distances compared to the corresponding correlations involving anion cores. This is due to the charges assigned to the core and shell units (table 1). The positively charged zinc ions are attracted to the negatively charged chlorine ions, and repelled by the positively charged chlorine cores. This reduces the separation between the zinc cores and the chlorine shells in tetrahedral structural units, and reduces the separation distance between two chlorine shells.

When the pair correlation functions from this work were compared with experimental ND results [9] (figure 5), noticeable differences between the Zn-Zn pair correlation functions were observed. While two peaks distinguishing edge-sharing and corner-sharing contributions were observed in this study, only a single peak was observed experimentally. This was because the Zn-Zn partial structure factor only contributes a weighting factor, ω_{ZnZn}, of 0.05 to the total neutron structure factor, as highlighted by Soper [7] in an earlier $ZnCl_2$ study. This generates significant uncertainty in the Zn-Zn pair correlation function, making it challenging to determine the Zn-Zn nearest neighbour distance and coordination number experimentally (table 4). Furthermore, since RMC modelling reproduces experimental diffraction data, the Zn-Zn pair correlation function reported by Zeidler *et al.* [9], [10] also only displayed one broad peak as opposed to two separate peaks. This may have led to the formation of defects (figure 14), and highlights the current importance of modelling $ZnCl_2$ glass without bias towards experimental diffraction data.

Since SiO_2 glass has been well studied both experimentally and computationally, it was of interest to explore how the structural effects of anion polarisability differ between intermediate and strong glass formers. One difference noticed in table 4 was the R_3 ratio which compares the cation-cation nearest neighbour distances. The ratio was lower than the ratio for R_1 and R_2 because the average Zn-Cl-Zn bond angle of ~110° (figure 9) is noticeably smaller than the average Si-O-Si bond angle of ~150° [36]. This brings the Zn

cations in closer proximity to each other, reducing the R_3 value for $ZnCl_2$, and hence lowering the R_3 ratio. The other difference in table 4 was the higher than anticipated Q_1 ratio of 1.74. A Q_1 value corresponds to the position of the FSDP, and it was established in figure 10 that the main contributors to the FSDP in $ZnCl_2$ and SiO_2 are $S^{FZ}_{ZnCl}(Q)$ and $S^{FZ}_{SiO}(Q)$ respectively. This contradicts Madden and Wilson [12] who reported that the FSDP was almost exclusively caused by the $S^{FZ}_{ZnZn}(Q)$ contribution in $ZnCl_2$ glass. This cannot be the case due to its weak weighting. Since the Zn-Cl nearest neighbour distance was greater than the Si-O nearest neighbour distance (table 4), it was anticipated that the Q_1 value for $ZnCl_2$ would be smaller than that of SiO_2 since the Q-scale is reciprocal to the r-scale. However, it still remains unclear why the Q_1 ratio is higher than the Q_2 and Q_3 ratios.

When the $ZnCl_2$ and SiO_2 partial Faber-Ziman structure factors were compared in figure 11, the partial Faber-Ziman structure factors were in good agreement beyond the FSDP. This was because both $ZnCl_2$ and SiO_2 largely comprise of corner-sharing tetrahedral structural units. The difference in phase between $S^{FZ}_{ZnZn}(Q)$ and $S^{FZ}_{SiSi}(Q)$ was caused by the different average Zn-Cl-Zn and Si-O-Si bond angles as previously discussed.

Packing fraction calculations of $ZnCl_2$ and SiO_2 formed the final comparison between the intermediate and strong glass formers. It was seen in table 5 that the packing fraction of O was noticeably less than that of Cl. Since all of the tetrahedral structural units in SiO_2 are corner-sharing, larger ring sizes can form, reducing the O packing fraction. In contrast, $ZnCl_2$ glass contains some edge-sharing tetrahedral units which leads to smaller ring sizes, and ultimately to a higher Cl packing fraction. Although it is a reasonable approximation to use half of the anion-anion nearest neighbour distance as the packing radius in equation 1, it is less reasonable to use half of the cation-cation nearest neighbour distance. This is because the typical cation ionic radius is significantly less than half of its nearest neighbour distance.

4.5 Conclusion

In this chapter, the first fully tetrahedral model of $ZnCl_2$ glass was obtained. This was achieved using classical molecular dynamics with the addition of the adiabatic core-shell model. While 86% of the $ZnCl_4$ tetrahedral units were found to be corner-sharing, 14% were found to be edge-sharing. The calculated total neutron and X-ray structure factors were in very good agreement with those obtained experimentally. Clear details in the Zn-Zn pair correlation function were attained which are unobtainable experimentally due to the weak weighting of the Zn-Zn correlation in comparison to the total structure factor.

The latter part of this chapter concerned making comparisons between the intermediate glass former $ZnCl_2$ and the strong glass former SiO_2. Since both comprise of tetrahedral structural units, there were similarities in the cation-anion and anion-anion Faber-Ziman

partial structure factors. Although the most significant contribution to the FSDPs of $ZnCl_2$ and SiO_2 glass came from the cation-anion contributions, there were differences between the positions of the FSDPs that could not be comprehended. Studying other intermediate and strong glass forming systems with tetrahedral networks may help elucidate this finding.

4.6 References

[1] B. K. Sharma and M. Wilson, "Polyamorphism and the evolution of intermediate-range order in molten $ZnCl_2$," *J. Phys. Condens. Matter*, vol. 20, pp. 244123–244132, 2008.

[2] C. A. Angell, *Strong and fragile liquids*. National Technical Information Service, U.S. Department of Commerce, Springfield, VA 22161, 1985.

[3] A. Sen, M. N. Rao, R. Mittal, and S. L. Chaplot, "Collective dynamics in crystalline polymorphs of $ZnCl_2$: potential modelling and inelastic neutron scattering study," *J. Phys. Condens. Matter*, vol. 17, pp. 6179–6192, 2005.

[4] C. Fillaux, B. Couzinet, C. Dreyfus, J. P. Itié, and A. Polian, "Determination of the Short Range Structure of $ZnCl_2$ in its Liquid, Vitreous and Crystalline Phases by XAS, at High Pressure and High Temperature," *Phys. Scr.*, vol. 115, pp. 339–341, 2005.

[5] H. L. Yakel and J. Brynestad, "Refinement of the crystal structure of orthorhombic zinc chloride," *Inorg. Chem.*, vol. 17, no. 11, pp. 3294–3296, 1978.

[6] S. Biggin and J. E. Enderby, "The structure of molten zinc chloride," *J. Phys. C Solid State Phys.*, vol. 14, pp. 3129–3136, 1981.

[7] A. K. Soper, "The structure of molten $ZnCl_2$: A new analysis of some old data," *Pramana - J. Phys.*, vol. 63, no. 1, pp. 41–50, 2004.

[8] S. N. Yannopoulos, A. G. Kalampounias, A. Chrissanthopoulos, and G. N. Papatheodorou, "Temperature induced changes on the structure and the dynamics of the 'tetrahedral' glasses and melts of $ZnCl_2$ and $ZnBr_2$," *J. Chem. Phys.*, vol. 118, no. 7, pp. 3197–3214, 2003.

[9] A. Zeidler *et al.*, "Structure of liquid and glassy $ZnCl_2$," *Phys. Rev. B - Condens. Matter Mater. Phys.*, vol. 82, pp. 1–17, 2010.

[10] A. Zeidler *et al.*, "Structure of the network glass-former $ZnCl_2$: From the boiling point to the glass," *J. Non. Cryst. Solids*, vol. 407, pp. 235–245, 2015.

[11] J. Wong and F. W. Lytle, "EXAFS studies of glassy and liquid $ZnCl_2$: A comparison with vitreous GeO_2," *J. Non. Cryst. Solids*, vol. 37, no. 2, pp. 273–284, Apr. 1980.

[12] M. Wilson and P. Madden, "Voids, Layers, and the First Sharp Diffraction Peak in $ZnCl_2$," *Phys. Rev. Lett.*, vol. 80, no. 3, pp. 532–535, 1998.

[13] S. Huang, F. Yoshida, and W. Wang, "The structural and dynamical properties of $ZnCl_2$ melt—a molecular dynamics simulation study," *J. Mol. Liq.*, vol. 115, pp. 81–88, 2004.

[14] A. Q. Alsayoud *et al.*, "Structure of $ZnCl_2$ melt. Part I: Raman spectroscopy analysis driven by Ab initio methods," *J. Phys. Chem. B*, vol. 120, no. 17, pp. 4174–4181, 2016.

[15] P. N. Kumta, P. A. Deymier, and S. H. Risbud, "Improved Rigid Ion Model of Molten Zinc Chloride," *Phys. B Condens. Matter*, vol. 153, pp. 85–92, 1988.

[16] G. Heusel, H. Bertagnolli, M. Kreitmeir, J. Neuefeind, and A. Lemke, "High pressure studies on molten zinc chloride," *Phys. Chem. Chem. Phys.*, vol. 4, no. 17, pp. 4155–4160, 2002.

[17] D. A. Allen, R. A. Howe, N. D. Wood, and W. S. Howells, "Tetrahedral coordination of Zn ions in molten zinc halides," *J. Chem. Phys.*, vol. 94, no. 7, pp. 5071–5076, 1991.

[18] V. V Brazhkin, a G. Lyapin, S. V Popova, Y. Katayama, H. Saitoh, and W. Utsumi, "Molecular-network-ionic structure transitions in liquid AlCl3 and ZnCl2 halogenides under pressure.," *J. Phys. Condens. Matter*, vol. 19, no. 24, pp. 246104–246114, 2007.

[19] T. Pfleiderer, I. Waldner, H. Bertagnolli, K. Tödheide, and H. E. Fischer, "High temperature-high pressure apparatus for neutron diffraction on molten salts: Structure factors of molten zinc chloride," *Phys. Chem. Chem. Phys.*, vol. 5, no. 23, pp. 5313–5318, 2003.

[20] J. Neuefeind, K. Tödheide, A. Lemke, and H. Bertagnolli, "The structure of molten $ZnCl_2$," *J. Non. Cryst. Solids*, vol. 224, no. 3, pp. 205–215, 1998.

[21] W. Klemm, "Dichtemessungen an geschmolzenen Chloriden," *Zeitschrift für Anorg. Chemie*, vol. 152, no. 1, pp. 235–251, 1926.

[22] R. A. Duke, F. R. Fleming, "Density and Electrical Conductance in the System KCl-$ZnCl_2$," *J. Electrochem. Soc.*, vol. 104, no. 4, pp. 251–254, 1957.

[23] J. P. Hansen and I. R. McDonald, *Theory of simple liquids*, 2nd ed. London: Academic Press, 1986.

[24] A. Gray-Weale, P. A. Madden, and M. Wilson, "Induced-dipole contributions to the conductivity and dielectric response of molten $ZnCl_2$," *J. Chem. Phys.*, vol. 113, no. 16, pp. 6782–6787, 2000.

[25] C. A. Angell and J. Wong, "Structure and glass transition thermodynamics of liquid zinc chloride from far-infrared, raman, and probe ion electronic and vibrational spectra," *J. Chem. Phys.*, vol. 53, no. 5, pp. 2053–2066, 1970.

[26] D. A. Allen, R. A. Howe, N. D. Wood, and W. S. Howells, "Tetrahedral coordination of Zn ions in molten zinc halides," *J. Chem. Phys.*, vol. 94, no. 7, pp. 5071–5076, 1991.

[27] L. Pusztai and R. L. McGreevy, "The Structure of Glassy Zinc Chloride: A Reverse Monte Carlo Study," *J. Non. Cryst. Solids*, vol. 117/118, pp. 627–630, 1990.

[28] D. J. Binks, "Computational Modelling of Zinc Oxide and Related Oxide Ceramics," 1994.

[29] J. D. Gale and A. L. Rohl, "The General Utility Lattice Program (GULP)," *Mol. Simul.*, vol. 29, no. 5, pp. 291–341, 2003.

[30] B. Brehler, “Kristallstrukturuntersuchungen an $ZnCl_2$,” *Zeitschrift für Krist. Mater.*, vol. 115, pp. 373–402, 1961.

[31] C. W. Wong, “DL_FIELD - A force field and model development tool for DL_POLY.” R Blake, Ed., CSE Frontier, STFC Computational Science and Engineering, Daresbury Laboratory, pp. 38–40, 2010.

[32] W. Smith and T. R. Forester, “DL_POLY_2. 0: A general-purpose parallel molecular dynamics simulation package,” *J. Mol. Graph.*, vol. 14, no. 3, pp. 136–141, 1996.

[33] A. Tilocca, N. H. De Leeuw, and A. N. Cormack, “Shell-model molecular dynamics calculations of modified silicate glasses,” *Phys. Rev. B - Condens. Matter Mater. Phys.*, vol. 73, pp. 1–14, 2006.

[34] J. A. E. Desa, A. C. Wright, J. Wong, and R. N. Sinclair, “A neutron-diffraction investigation of the structure of vitreous zinc-chloride,” *J. Non. Cryst. Solids*, vol. 51, pp. 57–86, 1982.

[35] P. A. Madden and M. Wilson, “‘Covalent’ effects in ‘ionic’ liquids,” *J. Phys. Condens. Matter*, vol. 12, pp. 95–108, 2000.

[36] D. L. Price, M. L. Saboungi, S. Susman, K. J. Volin, and A. C. Wright, “Dynamics of vitreous and molten zinc chloride,” *J., Non-Cryst. Solids*, vol. 150, pp. 287–291, 1992.

[37] Q. Mei, C. J. Benmore, S. Sen, R. Sharma, and J. L. Yarger, “Intermediate range order in vitreous silica from a partial structure factor analysis,” *Phys. Rev. B - Condens. Matter Mater. Phys.*, vol. 78, no. 14, pp. 144204–144211, 2008.

[38] D. I. Grimley, A. C. Wright, and R. N. Sinclair, “Neutron scattering from vitreous silica IV. Time-of-flight diffraction,” *J. Non. Cryst. Solids*, vol. 119, no. 1, pp. 49–64, 1990.

5. An Experimental Investigation of the Structure of $CaO\text{-}SiO_2\text{-}CaCl_2$ Glasses

5.1 Introduction

The ubiquitous bioactive glass, 45S5, is a soda-lime-phosphosilicate glass ($Na_2O\text{-}CaO\text{-}P_2O_5\text{-}SiO_2$) used for a number of orthopaedic and dental applications [1]. One of these applications is in toothpastes to help reduce dentine hypersensitivity [1]. Fluoride is known to inhibit dentine and enamel demineralisation and to encourage remineralisation [2]–[4]. Consequently, fluorine-containing bioactive glasses are of interest for dental applications (e.g. [5]–[7]). While most bioactive glass compositions form a hydroxycarbonate apatite (HCA) layer on their surface following exposure to body fluids, fluorine-containing bioactive glasses form a fluorapatite layer. Fluorapatite is known to be more chemically stable than HCA, making it more appropriate for the acidic conditions present in the mouth. However, the formation of fluorite (CaF_2) is possible [5]. This can result in the bioactive glass being less resorbable, hindering enamel regeneration. An excess of fluorine can also result in dental fluorosis [8], a condition that causes visual defects in tooth enamel.

Due to some of the limitations of fluorine-containing bioactive glasses, attention has recently turned to the possibility of using chlorine-containing bioactive glasses as an alternative [8], [9]. Not only is chlorine chemically similar to fluorine, but the larger ionic radius of chlorine is expected to expand the glass network, making the glass less abrasive and able to dissolve more readily in the body [8], [9]. This would enable an apatite layer to form more quickly, and hence reduce the time required for bone regeneration [8], [9]. These characteristics make chlorine-containing bioactive glasses particularly appealing for dental applications such as toothpastes. However, studies on chlorine-containing bioactive glasses are currently scarce.

Chen *et al.* [8], [9] synthesised a series of $CaO\text{-}SiO_2\text{-}P_2O_5\text{-}CaCl_2$ chlorine-containing bioactive glass compositions that contained approximately 6mol% P_2O_5. Although the thermal properties of the glasses were studied in addition to apatite formation, there was an absence of glass structure characterisation. Understanding the structure of chlorine-containing bioactive glasses is fundamental for understanding the degradation mechanisms of the glass, and for being able to realise their applications.

It is therefore intuitive to begin structural investigations on simpler systems. Recently, Chen *et al.* [9], [10] synthesised a less complex ternary chlorine-containing silicate glass series (CaO-SiO_2-$CaCl_2$) to help elucidate the structural role of chlorine in chlorine-containing bioactive glasses. However, the glass structure was only investigated using ^{29}Si MAS-NMR. The chemical shift positions were centred around -80ppm. This indicated a dominance of Q^2 silicate species and an absence of detectable Si-Cl bonding which would have depolymerised the silicate network.

An investigation of the structural role of chlorine in chlorine-containing silicate glasses may also be beneficial for understanding the structural role of chlorine in borosilicate glasses. Radioactive waste (which commonly contains chlorine) is often immobilised by vitrification to form a borosilicate glass [11]. The vitrification process involves melting the radioactive waste with glass-forming additives to form a vitreous product that contains the radioactive waste [12]. Borosilicate glasses are commonly used because of their good glass-forming ability, their chemical durability, and their excellent thermal and radiation stability [12]. The difficulty with immobilising nuclear waste containing chlorine is that chlorine has a limited solubility in borosilicate glass [11]. Therefore, an understanding of the structural role of chlorine in borosilicate glass could lead to modified borosilicate glass compositions that have improved levels of chlorine solubility.

In this chapter, the CaO-SiO_2-$CaCl_2$ glass structure was investigated experimentally to help elucidate the structural role of chlorine. Using glass samples supplied by collaborators, this was achieved using central facility techniques including neutron diffraction (ND) and X-ray absorption spectroscopy (XAS). This was the first time CaO-SiO_2-$CaCl_2$ glasses have been studied using these techniques. In addition, the determination of the glass compositions and density values would later enable the glasses to be modelled computationally for further structural insight, as detailed in the following chapter.

5.2 Glass Synthesis

The nominal CaO-SiO_2-$CaCl_2$ chlorine-containing silicate glass series is shown in table 1. The series maintains a constant SiO_2 to CaO ratio corresponding to a calcium metasilicate, whilst the $CaCl_2$ content is allowed to vary. It was therefore anticipated that $CaCl_2$ would not behave as a network modifier. This glass series was synthesised both by Xiaojing Chen at Queen Mary University of London (denoted as the QCl series) and later by Louis Chungong at Aston University (denoted as the ACl series), although different approaches were used. The QCl glass series had been synthesised by initially mixing 200g of SiO_2, $CaCO_3$, and $CaCl_2{\cdot}2H_2O$ reagents according to the molar concentration of each nominal composition. The mixed reagents were then placed into a platinum-rhodium crucible and melted in a pre-heated furnace at between 1320°C and 1550°C for 1 hour. The melt was

quenched into deionised water to form a glass. The present work took place around two years after the original synthesis, and by then only the first six QCl samples in table 1 were available from the collaborators.

The ACl glass series had been synthesised by initially mixing 25g of SiO_2, $CaCO_3$, and $CaCl_2 \cdot 2H_2O$ reagents according to the molar concentration of each nominal composition. The mixed reagents were then placed into a platinum-rhodium crucible and heated from room temperature to a final temperature of between 1445°C and 1530°C at a rate of 10°C/min, before being heated for a further hour at the desired temperature. Heating was performed under an inert flowing argon atmosphere. The melt was subsequently splash-quenched between two graphite blocks to form a glass.

Table 1: The nominal CaO-SiO_2-$CaCl_2$ glass series (in mol%).

CaO	SiO_2	$CaCl_2$
48.4	48.4	3.3
46.7	46.7	6.6
45.3	45.3	9.3
44.1	44.1	11.9
41.9	41.9	16.1
36.3	36.3	27.4
33.3	33.3	33.5
28.5	28.5	43.0
23.5	23.5	53.1

5.3 Compositional Analysis

Halogen losses in glasses are generally reported to be between 10% and 95% depending on the chemical composition and the synthesis conditions [13]. It is therefore important to carefully study the composition of the CaO-SiO_2-$CaCl_2$ glasses experimentally. Compositional analysis was performed using X-ray fluorescence spectroscopy (XRF) which is described in section 3.3. As a flat distribution of sample material is necessary for quantitative compositional analysis [14], fusion beads were prepared prior to the quantitative XRF measurements.

The production of a fusion bead began by mixing 0.6g of finely powdered glass sample with 6.0g of a lithium borate flux using an agate pestle and mortar. The mixture was placed into a platinum/rhodium crucible and inserted into an Eagon 2 fusion bead maker with a platinum/rhodium dish beneath it. Within the Eagon 2 instrument, the crucible and dish would then enter the furnace which was preheated to a temperature of 1050°C to melt the flux. The powdered glass sample would get dissolved into the molten flux during this

melting stage which lasted for 180s before the mixing stage began. Mixing involved tilting the crucible by 45° from one side to the other repeatedly for 480s to obtain a homogeneous liquid. A de-wetting agent was added 280s into this stage to dissolve and mix with the melt. After mixing, the molten liquid was poured into the dish. The iodine-based de-wetting agent assisted in the pouring of the molten mixture and helped prevent the fusion bead from sticking to the platinum dish. The time allowed for pouring was 15s. Once the crucible and dish came out of the furnace, the cooling phase began. Assisted cooling was initially delayed by 60s to help prevent the fusion bead from cracking. Cool air was then blown onto the platinum dish for 240s. Once the fusion bead and the platinum dish had cooled, the fusion bead could be carefully extracted from the dish.

In addition to preparing fusion beads containing the glass samples, a number of fusion beads containing standard mixtures were also prepared using the same technique. The standard mixtures were combinations of crystalline $CaSiO_3$ and $CaCl_2{\cdot}4H_2O$ reagents. The SiO_2, CaO, and $CaCl_2$ molar concentrations of these standard mixtures are given in table 2. By using the calibration feature of the Epsilon 3 software, measurements on the fusion beads containing known standard mixtures were used to calibrate the XRF measurements on the fusion beads containing the glass samples. To achieve good calibration, the fusion beads containing standard mixtures were each measured for 2.5 hours. During a measurement on a fusion bead containing a glass sample, the regression lines calculated during calibration enabled mathematical models to convert the fluorescent X-ray intensities into SiO_2, CaO, and $CaCl_2$ molar concentrations. Each measurement on a fusion bead containing a glass sample lasted approximately 15 minutes. The calibration and sample measurements were performed separately for both the top and the bottom sides of the fusion beads.

Table 2: The SiO_2, CaO, and $CaCl_2$ combinations (in mol%) used in fusion beads to calibrate XRF measurements.

Mixture	CaO	SiO_2	$CaCl_2$
a	50.0	50.0	0.0
b	48.5	48.5	3.1
c	46.8	46.8	6.3
d	45.2	45.2	9.7
e	43.4	43.4	13.2
f	41.6	41.6	16.8
g	39.7	39.7	20.6
h	37.7	37.7	24.6

Chen *et al.* [8] synthesised a $CaO\text{-}SiO_2\text{-}P_2O_5\text{-}CaCl_2$ bioactive glass series and reported that losses via chlorine volatilisation were probably as $CaCl_2$ or HCl. If chlorine losses occurred as

$CaCl_2$, then the SiO_2 and CaO content would not vary from the nominal content. If instead losses due to chlorine volatilisation occurred as HCl, then the CaO content would be expected to exceed the nominal CaO content. For the QCl glass series in this work, the SiO_2 and CaO contributions from XRF did not vary significantly from the nominal contributions. The $CaCl_2$ contributions were also in good agreement with the nominal contributions as shown in figure 1. It was therefore established that little, if any, chlorine loss had occurred and so the nominal glass compositions could be used to describe the QCl glass series. In contrast, the CaO contributions in the ACl glass series persistently exceeded the nominal CaO contributions. The $CaCl_2$ contributions were also lower than expected (figure 1), indicating chlorine losses via HCl.

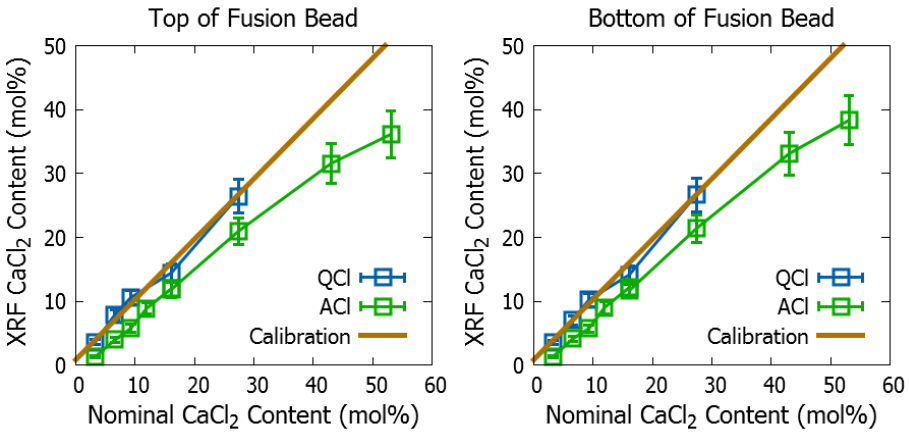

Figure 1: The $CaCl_2$ content relative to the calibration line measured using XRF on the top (left) and on the bottom (right) of each fusion bead containing a glass sample. The calibration line is a linear extrapolation based on the XRF measurements of the standard mixtures. The uncertainty is ±10% of the measured $CaCl_2$ content.

Figure 2 shows a number of Raman spectra obtained for the ACl glass series. These include the spectra for the end member compositions and two of the middle compositions (ACl3.3, ACl16.1, ACl27.4, and ACl53.1). These are compared with the Raman spectra of calcium silicate glasses reported by Luth *et al.* [15] labelled WL37.5 glass (of composition $43.67SiO_2$-$56.33CaO$ which is CaO rich), Wo glass (of composition $50SiO_2$-$50CaO$ which has equal proportions of SiO_2 and CaO), and SW84 glass (of composition $54.29SiO_2$-$45.71CaO$ which is SiO_2 rich). Rather than maintaining a spectrum similar to the Wo spectrum (as expected for equal proportions of SiO_2 and CaO), the ACl spectra progressively became more similar to the WL37.5 (i.e. CaO rich) spectrum, as seen by the growth of a small peak at $920cm^{-1}$. Excess CaO provides further evidence for chlorine losses via HCl. It was therefore necessary to adjust the nominal ACl compositions (table 1) to account for these losses.

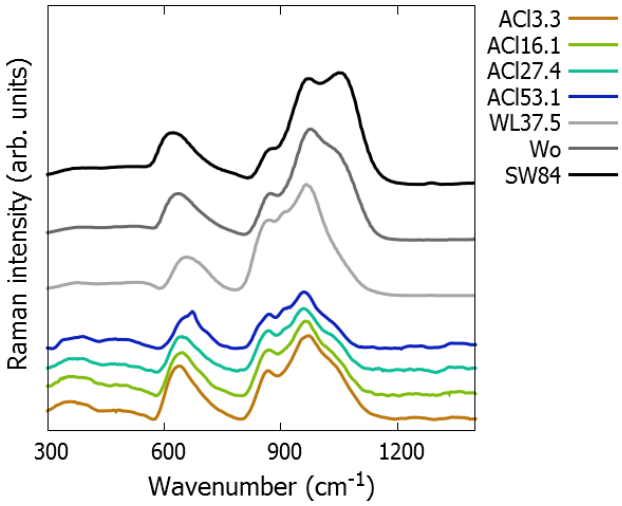

Figure 2: A comparison of Raman spectra between the ACl3.3, ACl16.1, ACl27.4, and ACl53.1 spectra from this work and the WL37.5, Wo, and SW84 spectra of CaO-SiO_2 glasses reported by Luth *et al.* [15]. The WL37.5 composition is CaO rich, the Wo composition contains equal proportions of SiO_2 and CaO, and the SW84 composition is SiO_2 rich. Beyond ACl3.3, each plot has been progressively offset.

The $CaCl_2$ content in each ACl sample was obtained by averaging the results from the two sides of the fusion beads. This enabled the average chlorine losses to be established. The proportion of chlorine losses in the ACl series is shown in figure 3, where the furnace temperatures used to melt the reagents are also shown for comparison. In general, higher furnace temperatures coincide with higher chlorine losses via HCl. By maintaining the nominal SiO_2 contributions, and treating the excess calcium contribution from chlorine volatilisation as CaO (i.e. $CaCl_2+H_2O \rightarrow 2HCl+CaO$), the revised ACl compositions in table 3 could be established. The differences between the nominal and the revised ACl compositions are illustrated on the ternary plot in figure 4. If chlorine losses in the ACl series had occurred as $CaCl_2$, then the green points would have followed the same tie line as the blue points.

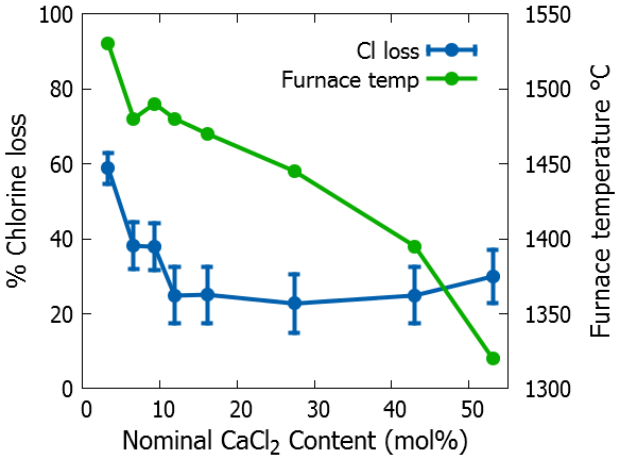

Figure 3: The furnace temperatures used during glass synthesis, and the proportion of chlorine losses deduced from XRF measurements as a function of nominal $CaCl_2$ content. The uncertainty in the chlorine losses is ±10% of the measured $CaCl_2$ content.

Table 3: The revised ACl glass series based on calibrated XRF measurements (in mol%).

Sample	$CaCl_2$	CaO	SiO_2
ACl1.3	1.3	50.3	48.4
ACl4.0	4.0	49.3	46.7
ACl5.6	5.6	49.1	45.3
ACl8.9	8.9	47.0	44.1
ACl12.1	12.1	46.0	41.9
ACl20.6	20.6	43.1	36.3
ACl25.1	25.1	41.6	33.3
ACl32.2	32.3	39.2	28.5
ACl39.8	39.8	36.7	23.5

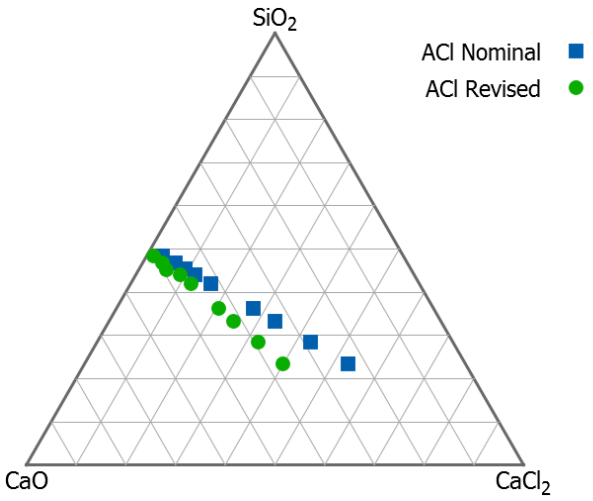

Figure 4: A ternary diagram of the nominal and revised ACl compositions based on XRF measurements. The QCl series maintained the nominal compositions and so is the same as the nominal ACl series.

5.4 Glass Characterisation

5.4.1 Density

Density measurements using helium pycnometry were performed on the QCl and the ACl glass series both by collaborators and also in this work. As shown to the left of figure 5, the ACl density values measured by collaborators were generally higher than those measured in this work, although the density values for each sample were generally within the uncertainty range of two standard deviations. The uncertainties in the ACl density values obtained by collaborators were larger than those in this work. This was because the collaborators performed three density measurements on each sample to obtain an average, while in this work ten density measurements of each sample were averaged to

obtain density values. As the ACl density values from this work were better defined, they were chosen to represent the density of the ACl glasses.

The QCl density values from collaborators were also obtained by averaging ten density measurements for each sample. Good agreement between the density values from this work and those from collaborators can be seen to the right of figure 5 for $CaCl_2$ concentrations below 10mol%. Beyond 10mol% $CaCl_2$, the agreement declines with increasing $CaCl_2$ content. This can be attributed to the glass samples of higher $CaCl_2$ content being more susceptible to atmospheric moisture. While the collaborators performed density measurements immediately after the samples were synthesised, the density measurements in this work were performed approximately two years later. It was therefore appropriate to use the original density values measured by the collaborators.

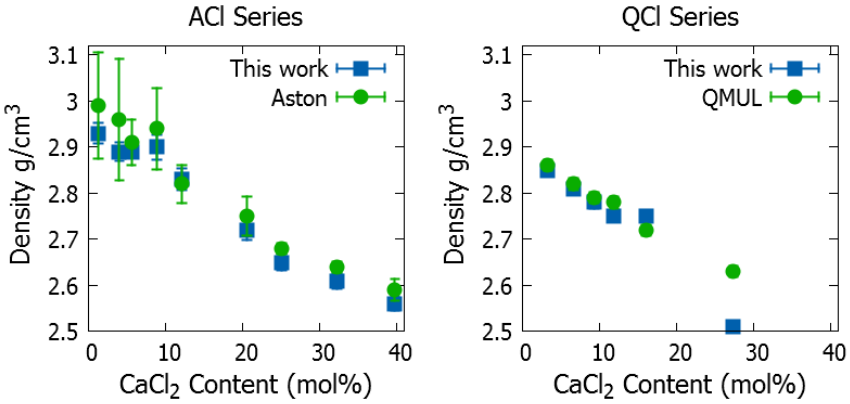

Figure 5: Density values for the ACl and QCl glass series (to the left and right respectively) from collaborators and from this work as a function of increasing $CaCl_2$ content. The uncertainty is two standard deviations. Error bars that are not observed are smaller than the symbol size.

5.4.2 Neutron Diffraction

Neutron diffraction measurements were carried out on the ACl glass series. In preparation, approximately 5g of each sample was ground into coarse glass chips before being used to fill cylindrical vanadium cans. The cans had an internal diameter of 8.3mm and were made of vanadium foil which was 40µm thick. Measurements were then performed using the GEM diffractometer at the ISIS neutron spallation source at the Rutherford Appleton Laboratory in Oxfordshire. In addition to the sample measurements, data was also collected for an empty 8.3mm vanadium can, for an 8mm vanadium niobium rod (94.86% V: 5.14% Nb), and for the empty GEM diffractometer. This was to enable a number of corrections to be made to the sample data following the experiment using the programs Gudrun [16] and Open GENIE [17].

After correcting the experimental data, the total neutron structure factors shown in figure 6 were obtained. It can be seen that the ACl glasses of lower $CaCl_2$ content follow a similar

trend up until the ACl12.1 composition. Between the ACl12.1 and the ACl20.6 compositions, the total neutron structure factors change significantly. Beyond the ACl20.6 composition, the remaining compositions again follow a trend. As shown to the right of figure 8, the signal to noise ratio decreases with increasing $CaCl_2$ content.

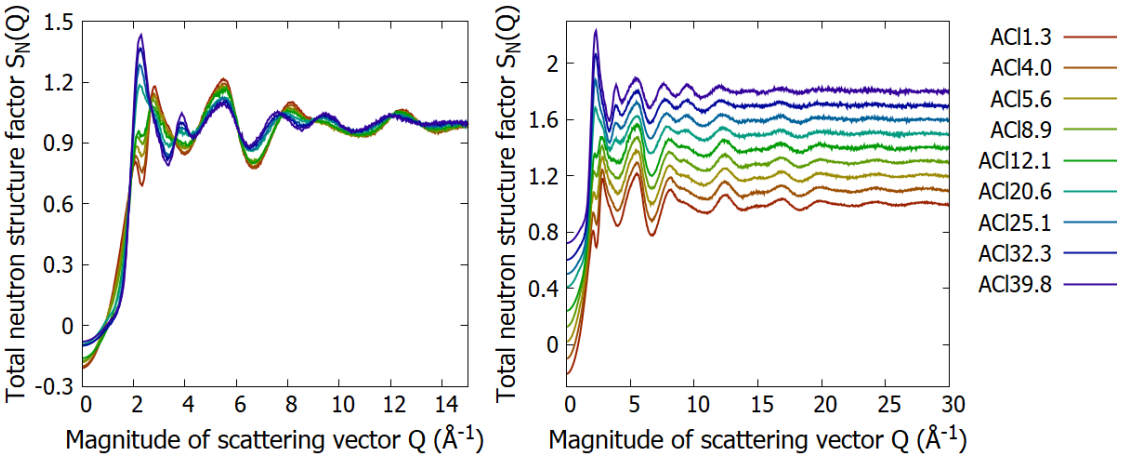

Figure 6: The total neutron structure factors for the ACl glass series. The plots to the right have been progressively offset by 0.1. Although the data range extends to 50Å^{-1}, the plot to the left and right extends to 15Å^{-1} and 30Å^{-1} respectively so differing features of the structure factors can be identified.

Following the Fourier transformation of the total neutron structure factors using a Lorch window function with a maximum Q value of 50Å^{-1}, the total correlation functions in figure 7 were obtained. The presence of termination ripples is evident. These are more noticeable for compositions of higher $CaCl_2$ content due to the declining peak amplitudes below 3Å. A small contribution around 1.9Å was also present for each sample and can be seen more easily in the plot to the right of figure 7. Following XRF measurements on the ACl glass chips, the small contribution was assumed to be an Al_2O_3 impurity from the SiO_2 reagent used to synthesise the glasses.

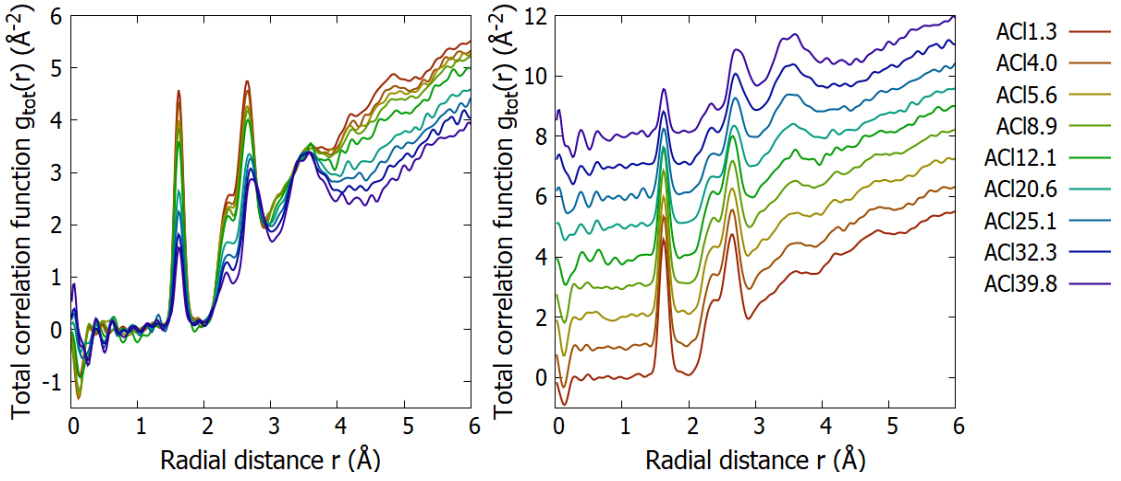

Figure 7: The total correlation functions for the GCl glass series where the plots to the right have been progressively offset by 1Å^{-2}.

In order to acquire structural information from the total correlation functions in figure 7 including nearest neighbour distances, R_{ij}, coordination numbers, N_{ij}, and values of σ_{ij} which are used to determine the Debye-Waller factors ($2\sigma_{ij}^2$), the program NXFit [18] was used. This involved fitting peaks to the data in accordance with the input and restraint parameters specified. Initially, the uniform input parameters in table 4 were used. In order to account for the Al_2O_3 impurity, it was assumed that Al_2O_3 made up 1mol% of the SiO_2 contribution. The local environment around aluminium ions is poorly understood [19]. However, based on the ^{27}Al MQ-MAS NMR (Multiple Quantum Magic Angle Spinning Nuclear Magnetic Resonance) measurements performed by Neuville *et al.* [19] on calcium aluminosilicate glasses of low Al_2O_3 content, it was reasonable to assume that the aluminium ions were six-fold coordinated with oxygen ions.

Table 4: The uniform input and restraint parameters used to fit the ND data. The fitting range was 1.50Å to 2.85Å and 10,000 iterations were used.

	Input parameters			Restraint parameters		
	R_{ij} (Å)	N_{ij}	σ_{ij} (Å)	R_{ij} (Å)	N_{ij}	σ_{ij} (Å)
Si-O	1.62	4.00	0.06	0.01	0.05	0.01
Al-O	1.88	6.00	0.06	0.03	0.10	0.01
Ca-O	2.36	4.50	0.15	0.03	2.10	0.02
O-O	2.66	4.00	0.09	0.03	0.85	0.02
Ca-Cl	2.78	2.50	0.18	0.03	2.30	0.04

Examples of peak fitting using the starting parameters in table 4 are shown in figure 8. These include the fits for the end-member compositions and a middle composition (ACl1.3, ACl39.8, and ACl12.1). These have been plotted on the same scale to emphasise the declining peak amplitudes below 2.7Å with increasing $CaCl_2$ content. This can make peak fitting increasingly problematic due to the deteriorating signal to noise ratio.

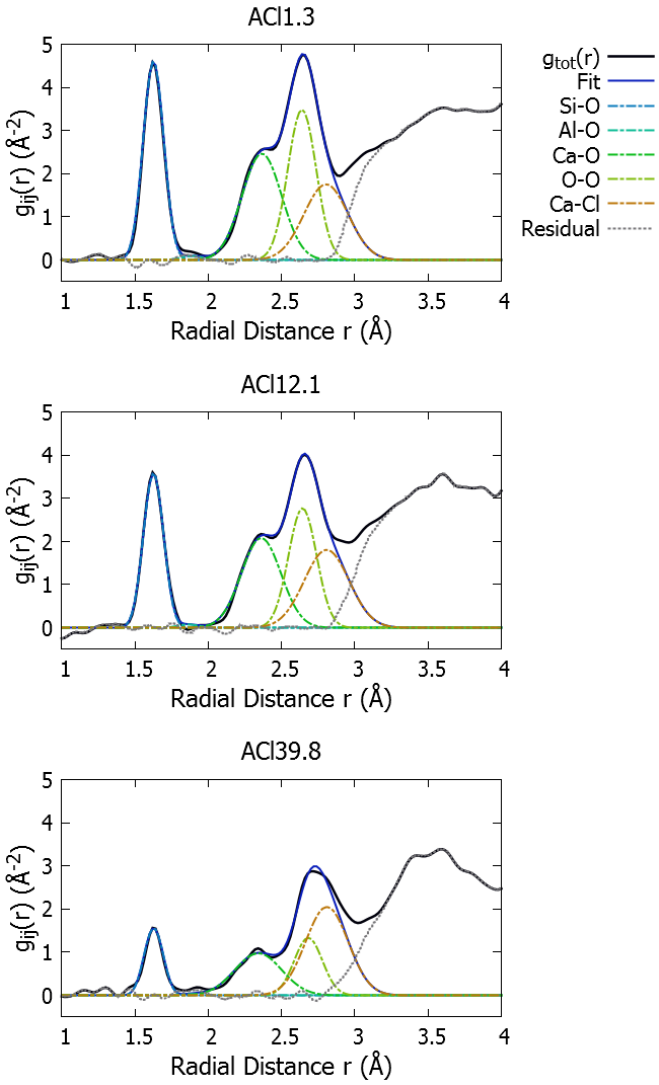

Figure 8: Examples of fits to experimental neutron diffraction data following the refinement of the uniform input parameters in table 4.

The output parameters attained from fitting the experimental data using the uniform input and restraint parameters in table 4 are given in table 5. Details for the Si-O and Al-O correlations are not included since they underwent minimal change. The Si-O nearest neighbour distance was 1.62-1.63Å (±0.01Å), the coordination number was 3.95-4.03 (±0.10), and the value of σ_{ij} was 0.06±0.01Å. The Al-O nearest neighbour distance was 1.86-1.90Å (±0.05Å), and the coordination number and σ_{ij} values were 5.95-6.08 (±1.00) and 0.06-0.07Å (±0.02Å) respectively. It can be seen in table 5 that the Ca-O, O-O, and Ca-Cl nearest neighbour distances underwent minimal change. The Ca-O coordination numbers declined markedly with increasing $CaCl_2$ content as expected due to the reduction in oxygen content. However, the O-O coordination numbers increased slightly despite a reduction being anticipated. In addition, the Ca-Cl coordination numbers did not follow an obvious trend despite an increase being expected. This revealed the challenging nature of obtaining coordination numbers from overlapping O-O and Ca-Cl peaks.

Table 5: The output fit parameters for the ACl series following the use of the uniform input parameters and restraints in table 4. The uncertainty in R_{Ca-O}, R_{O-O}, and R_{Ca-Cl} is ±0.01Å, ±0.01Å, and ±0.02Å respectively. The uncertainty in N_{Ca-O}, N_{O-O}, and N_{Ca-Cl} is ±1.00, ±1.00, and ±1.00 respectively. The uncertainty in σ_{Ca-O}, σ_{O-O}, and σ_{Ca-Cl} is ±0.01Å, ±0.01Å, and ±0.02Å respectively.

Sample	Fit index	Correlation	R_{ij} (Å)	N_{ij}	σ_{ij} (Å)
ACl1.3	0.30	Ca-O	2.37	4.88	0.13
		O-O	2.64	3.16	0.09
		Ca-Cl	2.80	2.78	0.15
ACl4.0	0.26	Ca-O	2.36	4.42	0.13
		O-O	2.65	3.28	0.09
		Ca-Cl	2.81	3.19	0.20
ACl5.6	0.51	Ca-O	2.35	4.16	0.13
		O-O	2.65	3.45	0.10
		Ca-Cl	2.81	3.01	0.20
ACl8.9	0.21	Ca-O	2.35	4.15	0.13
		O-O	2.65	3.15	0.09
		Ca-Cl	2.80	3.53	0.19
ACl12.1	0.19	Ca-O	2.36	4.21	0.13
		O-O	2.64	3.25	0.09
		Ca-Cl	2.81	2.98	0.15
ACl20.6	0.23	Ca-O	2.34	3.15	0.13
		O-O	2.67	3.75	0.11
		Ca-Cl	2.81	3.09	0.18
ACl25.1	0.14	Ca-O	2.34	2.57	0.13
		O-O	2.69	3.54	0.10
		Ca-Cl	2.81	3.44	0.20
ACl32.3	0.22	Ca-O	2.34	2.46	0.13
		O-O	2.68	4.20	0.11
		Ca-Cl	2.81	2.91	0.16
ACl39.8	0.35	Ca-O	2.34	2.40	0.16
		O-O	2.68	3.38	0.09
		Ca-Cl	2.81	3.34	0.14

In an attempt to overcome the difficulty of establishing the areas of overlapping O-O and Ca-Cl peaks, the input parameters and restraints for the O-O, Ca-O, and Ca-Cl coordination numbers were varied for each composition. These changing input parameters were based on the results of computational modelling as detailed in the following chapter. The restraint on the O-O coordination number was 0.2, and the restraints on the Ca-O and Ca-Cl coordination numbers were set to 5% and 10% respectively.

By applying these non-uniform fitting parameters, it can be seen in figure 9 that the Ca-O and O-O coordination numbers decrease while the Ca-Cl coordination number increases as expected. However, as quantified in table 6, the fit indexes are generally not as good as those in table 5 (where uniform input and restraint parameters were used). The output parameters for the Si-O and Al-O correlations were not provided in table 6 as variation was minimal. The Si-O nearest neighbour distance was maintained at 1.63±0.01Å, and the

corresponding coordination number and σ_{ij} values were 3.95-4.04 (±0.10) and 0.05-0.06Å (±0.01Å) respectively. The Al-O nearest neighbour distances, coordination numbers, and σ_{ij} values were 1.85-1.91Å (±0.05Å), 5.90-6.10 (±1.00), and 0.05-0.07Å (±0.02Å) respectively. These values did not differ significantly from those obtained in the previous fitting.

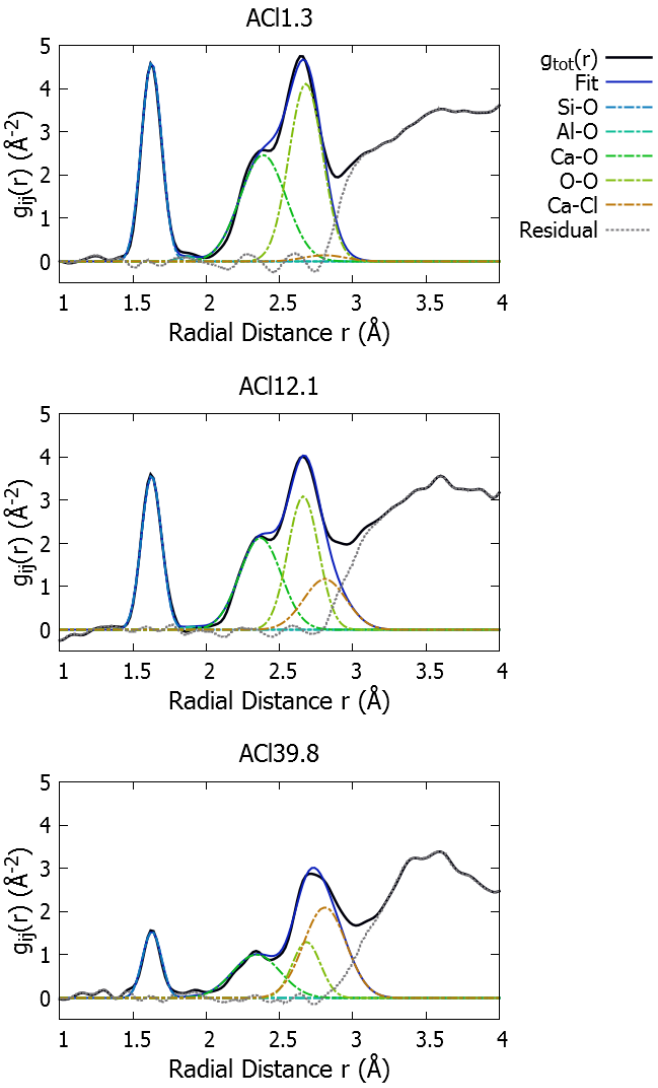

Figure 9: Examples of fits to experimental neutron diffraction data following the refinement of non-uniform input parameters.

Table 6: The output fit parameters for the ACl series following the use of the non-uniform input parameters and restraints. The uncertainty in R_{Ca-O}, R_{O-O}, and R_{Ca-Cl} is ±0.01Å, ±0.01Å, and ±0.02Å respectively. The uncertainty in N_{Ca-O}, N_{O-O}, and N_{Ca-Cl} is ±1.00, ±1.00, and ±1.00 respectively. The uncertainty in σ_{Ca-O}, σ_{O-O}, and σ_{Ca-Cl} is ±0.01Å, ±0.01Å, and ±0.02Å respectively.

Sample	Fit index	Correlation	R_{ij} (Å)	N_{ij}	σ_{ij} (Å)
ACl1.3	1.21	Ca-O	2.39	5.70	0.15
		O-O	2.68	4.49	0.11
		Ca-Cl	2.81	0.22	0.14
ACl4.0	0.98	Ca-O	2.38	5.38	0.15
		O-O	2.67	4.26	0.10
		Ca-Cl	2.81	0.70	0.14
ACl5.6	1.08	Ca-O	2.38	5.21	0.15
		O-O	2.68	4.20	0.11
		Ca-Cl	2.81	0.94	0.14
ACl8.9	0.68	Ca-O	2.37	4.94	0.15
		O-O	2.67	4.13	0.10
		Ca-Cl	2.81	1.43	0.14
ACl12.1	0.49	Ca-O	2.37	4.53	0.14
		O-O	2.66	4.00	0.10
		Ca-Cl	2.81	1.83	0.14
ACl20.6	0.31	Ca-O	2.36	3.79	0.15
		O-O	2.68	3.81	0.10
		Ca-Cl	2.81	2.30	0.15
ACl25.1	0.25	Ca-O	2.37	3.42	0.16
		O-O	2.69	3.70	0.10
		Ca-Cl	2.81	2.52	0.15
ACl32.3	0.31	Ca-O	2.36	2.97	0.16
		O-O	2.69	3.54	0.10
		Ca-Cl	2.81	2.97	0.15
ACl39.8	0.39	Ca-O	2.34	2.52	0.16
		O-O	2.68	3.30	0.09
		Ca-Cl	2.81	3.41	0.14

5.4.3 X-ray Absorption Spectroscopy

An X-ray absorption spectroscopy (XAS) experiment was carried out on the ACl glass series using beamline B18 at the Diamond Light Source synchrotron facility at the Rutherford Appleton Laboratory in Oxfordshire. A solid glass chip for each ACl composition was chosen. In addition, a number of crystalline systems including $CaCl_2{\cdot}4H_2O$, $CaCO_3$, $CaSiO_3$, and NaCl were selected to be standard samples. Approximately 3-4mg of each crystalline standard was then mixed with 50mg of powdered polyvinylpyrrolidone (PVP) using an agate pestle and mortar before being pressed into a 13mm pellet. XAS measurements on the glass chips and the pellets containing crystalline standards were carried out in fluorescence mode around the calcium K-edge (at 4038eV [20]) and around the chlorine K-edge (at 2822eV [20]) under vacuum using a double crystal Si(111) monochromator. An ionisation chamber measured the incident X-ray intensity which was calibrated using

titanium foil (4966eV [20]), and a 9-element monolithic germanium solid-state detector [21] was used to measure the intensity of fluorescent X-rays. The pellets containing crystalline standard samples were measured throughout the experiment in order to detect any drift in beam energy. Following the experiment, the programs Athena [22] and Artemis [22] were used to analyse the data.

5.4.3.1 X-ray Absorption Near-Edge Structure

The X-ray absorption near-edge structure (XANES) spectra in this work were obtained by using a pre-edge range of -109eV to -10eV, a normalisation range of 50eV to 355eV, and an Rbkg value of 1.0. In order to help validate the experimental results, it is common to compare the XANES spectra of known crystalline standards to those reported in the literature. To the left of figure 10, the crystalline calcite ($CaCO_3$) XANES spectrum from this work (where the value of E_0 is 4047.98eV) is compared with the spectrum reported by Hormes *et al.* [23] around the Ca K-edge (4038eV [20]). To the right of figure 10, the crystalline sodium chlorine (NaCl) XANES spectrum from this work (where the value of E_0 is 2827.22eV) is compared to the spectrum reported by Szilagyi *et al.* [24] around the Cl K-edge (2822eV [20]). For both comparisons, good agreement can be seen.

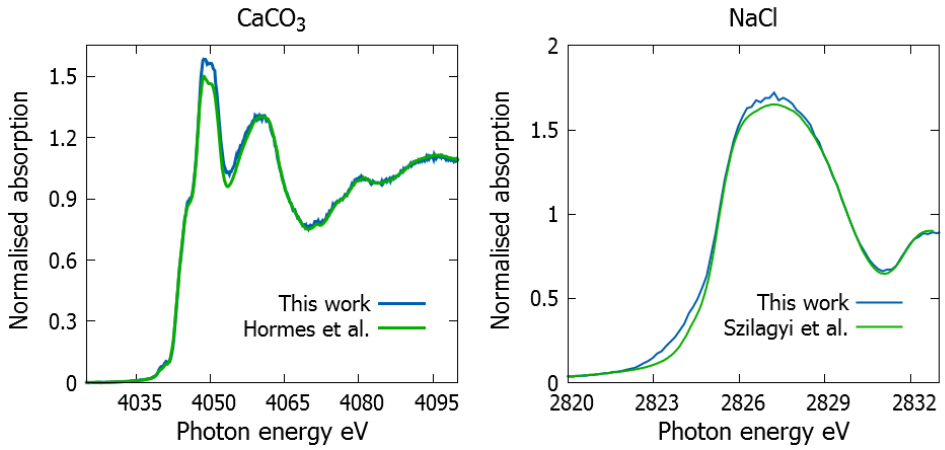

Figure 10: To the left, the crystalline $CaCO_3$ XANES spectra around Ca K-edge from this work and from Hormes *et al.* [23]. To the right, the crystalline NaCl XANES spectra around Cl K-edge from this work and from Szilagyi *et al.* [24].

The XANES spectra for the ACl glass series around the Cl K-edge (where E_0 is 2825eV) are shown to the left of figure 11. A decrease in intensity and a marginal shift towards lower energies can be seen in the main absorption edge peak with increasing $CaCl_2$ content. In addition, the shoulder of the absorption edge around 2831eV exhibits a distinct change in position between the ACl12.1 and ACl20.6 compositions. By comparing the XANES spectra around the Cl K-edge to the crystalline $CaCl_2{\cdot}4H_2O$ standard XANES spectra, a difference in edge position of around 1eV can be seen. The XANES spectra for the ACl glass series around

the Ca K-edge (where E_0 is 4043eV) is shown to the right of figure 11. Around the Ca K-edge, the main absorption edge peak exhibits a more obvious shift towards lower energies with increasing $CaCl_2$ content, as can be seen in the inset of the figure. By comparing the XANES spectra around the Ca K-edge to the crystalline $CaCl_2{\cdot}4H_2O$ standard XANES spectra, it became apparent that the calcium environment becomes more like the crystalline $CaCl_2$ environment with increasing $CaCl_2$ content.

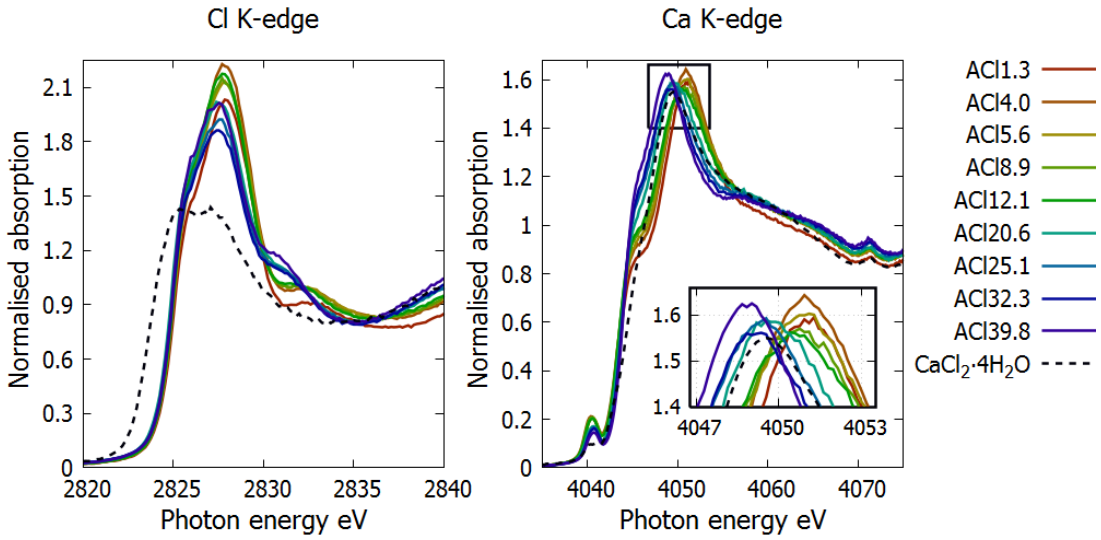

Figure 11: To the left, the XANES spectra for the ACl glass series around the Cl K-edge. To the right, the XANES spectra for the ACl glass series around the Ca K-edge. XANES spectra for the $CaCl_2{\cdot}4H_2O$ crystalline standard have been added for comparison.

5.4.3.2 Extended X-ray Absorption Fine Structure

The extended X-ray absorption fine structure (EXAFS) spectra for the ACl glass series were obtained using a pre-edge range of -100eV to -30eV, a normalisation range of 155eV to 560eV, and an Rbkg value of 1.0 for all samples. The Ca K-edge k^2 weighted EXAFS spectra in k-space and the modulus of the Fourier transforms in r-space are shown in figure 12. The first peak of the EXAFS spectra in k-space declines in amplitude with increasing $CaCl_2$ content. In addition, the third peak shifts towards a lower wavenumber, and a smaller peak emerges to the right of the third peak (around k~6.5 $Å^{-1}$). Arguably, the forth peak shifts towards a higher wavenumber with increasing $CaCl_2$ content although the signal-to-noise ratio is low. The modulus of the Fourier transformed EXAFS spectra in r-space show a prominent Ca-O peak and follow the same trend up until the ACl12.1 composition. For compositions beyond ACl12.1, a significant Ca-Cl peak emerges at a larger distance than the Ca-O peak. The Ca-Cl peak then continues to gain dominance and first supersedes the Ca-O peak in the ACl32.3 sample.

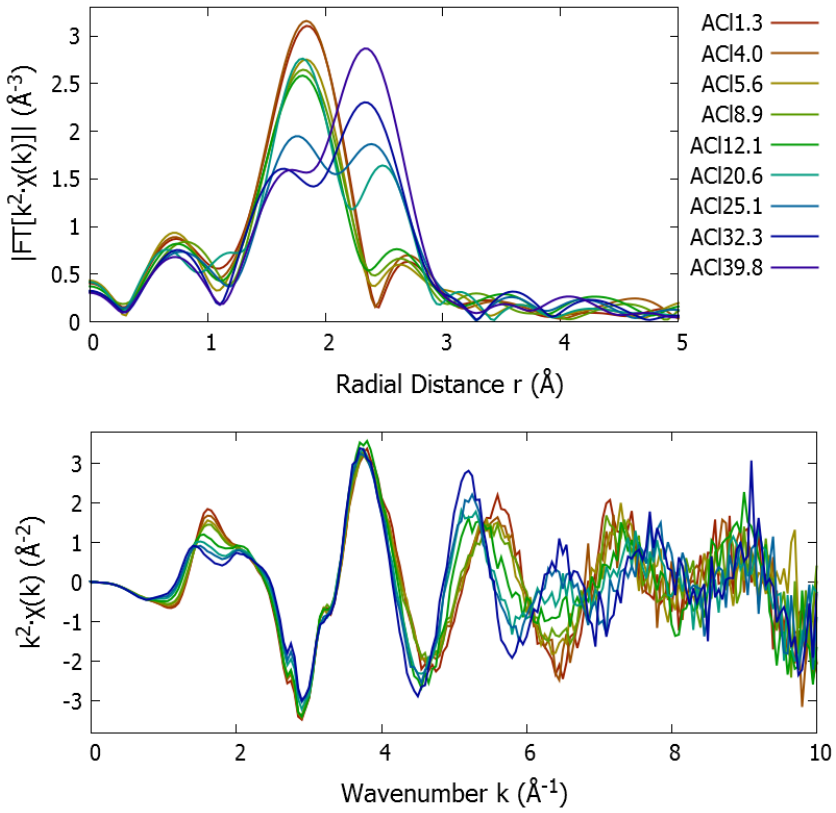

Figure 12: The Ca K-edge k^2 weighted EXAFS spectra (bottom) and the modulus of their Fourier transforms (top) for the ACl glass series.

The $CaCl_2{\cdot}4H_2O$ crystalline reference structure was used to create a modelled EXAFS spectrum around the Ca K-edge using the FEFF code [25]. Single-scattering Ca-O and Ca-Cl FEFF paths were then chosen to fit the experimental EXAFS spectra for the ACl glass series. This was to attain structural information on the Ca-O and Ca-Cl correlations including nearest neighbour distances (R_{ij}), coordination numbers (N_{ij}), and values of $\sigma_{ij}{}^2$ which are used to determine the XAFS Debye-Waller factors ($2\sigma_{ij}{}^2$). The input parameters used for fitting in Artemis [22] are given in table 7. A k-range of 3.0Å^{-1} to 9.0Å^{-1} and an r-range of 1.0Å to 4.0Å was considered appropriate for fitting. The fits to the k^2 weighted experimental EXAFS spectra and to their Fourier transforms are shown in figures 13 and 14 respectively, where good agreement over the fitting ranges can be seen.

Table 7: The input parameters for the Ca-O and Ca-Cl FEFF paths used to fit the experimental EXAFS spectra of the ACl glass series around the Ca K-edge.

	R_{ij} (Å)	N_{ij}	$\sigma_{ij}{}^2$ (Å^2)
Ca-O	2.36	4.5	0.01
Ca-Cl	2.79	2.0	0.01

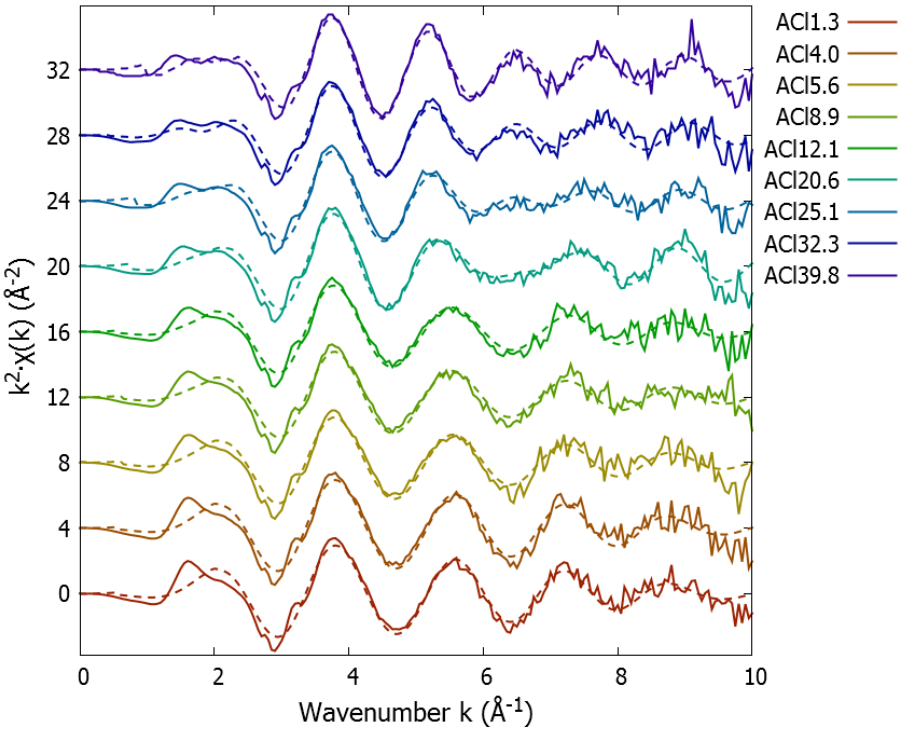

Figure 13: The experimental (solid lines) and fitted (dashed lines) Ca K-edge k^2 weighted EXAFS spectra for the ACl glass series. The plots have been progressively offset by 4.0Å^{-2}.

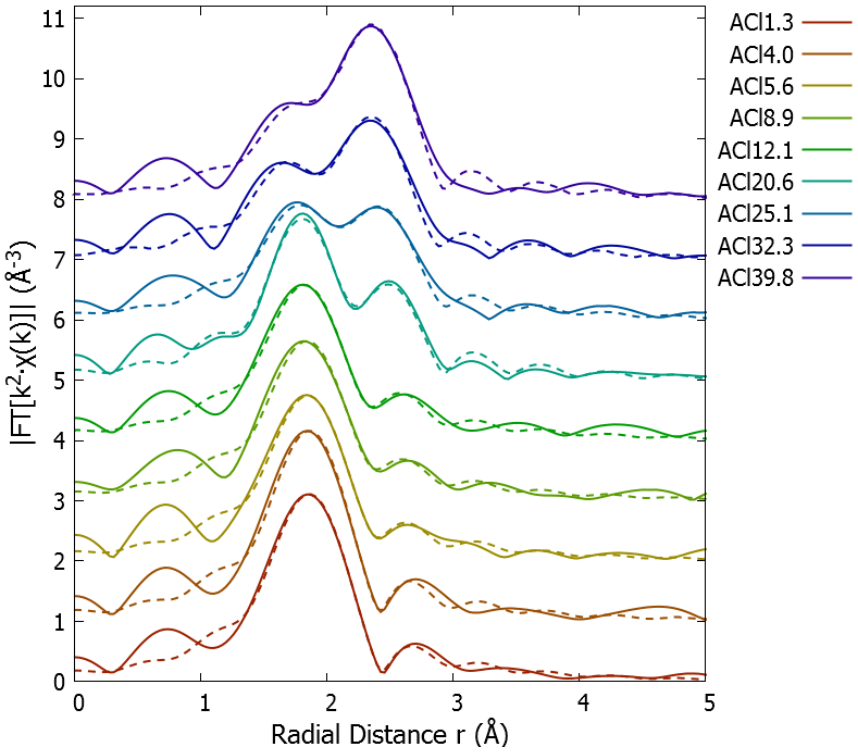

Figure 14: The modulus of the Fourier transformed experimental (solid lines) and fitted (dashed lines) Ca K-edge k^2 weighted EXAFS spectra for the ACl glass series. The plots have been progressively offset by 1.0Å^{-3}.

The parameters attained from fitting the experimental Ca K-edge EXAFS spectra are given in table 8. To ensure the values of σ_{ij}^2 were not unphysically small, the fits were restrained to encourage $0.01Å^2 \leq \sigma_{ij}^2 \leq 0.03Å^2$ which is appropriate for a glass. In addition, to obtain the coordination numbers, a suitable amplitude reduction factor of 0.7 [26] was used. The Ca-O nearest neighbour distance did not exhibit a clear trend, but the Ca-Cl nearest neighbour distance reduced with increasing $CaCl_2$ content. The Ca-O coordination numbers declined significantly while the Ca-Cl coordination numbers increased significantly with increasing $CaCl_2$ content as expected.

Table 8: The output structural parameters for the Ca-O and Ca-Cl correlations from fitting the k^2 weighted EXAFS spectra for the ACl glass series.

	$R_{Ca\text{-}O}$ (Å)	$N_{Ca\text{-}O}$	σ_{Ca-O}^2 ($Å^2$)	$R_{Ca\text{-}Cl}$ (Å)	$N_{Ca\text{-}Cl}$	σ_{Ca-Cl}^2 ($Å^2$)
ACl1.3	2.34±0.01	5.23±0.36	0.013±0.002	2.97±0.05	0.40±0.17	0.010±0.001
ACl4.0	2.34±0.01	5.04±0.41	0.012±0.002	2.94±0.06	0.43±0.20	0.010±0.002
ACl5.6	2.34±0.03	4.63±1.02	0.013±0.005	2.89±0.11	0.90±1.93	0.024±0.060
ACl8.9	2.34±0.02	4.20±0.65	0.012±0.004	2.84±0.09	1.51±0.61	0.030±0.001
ACl12.1	2.34±0.04	4.50±1.32	0.013±0.006	2.84±0.09	1.36±2.27	0.023±0.042
ACl20.6	2.35±0.02	3.88±0.23	0.010±0.001	2.80±0.02	1.63±0.19	0.010±0.001
ACl25.1	2.36±0.11	3.43±2.22	0.011±0.013	2.80±0.07	2.47±2.56	0.015±0.017
ACl32.2	2.31±0.11	2.21±1.87	0.014±0.016	2.76±0.05	3.90±2.64	0.013±0.012
ACl39.8	2.35±0.04	2.04±0.34	0.010±0.001	2.78±0.02	3.71±0.73	0.012±0.004

The Cl K-edge k^2 weighted EXAFS spectra in k-space and the modulus of their Fourier transforms in r-space are shown in figure 15. The first two peaks of the EXAFS spectra in k-space display a marginal shift towards lower wavenumbers and decline in amplitude with increasing $CaCl_2$ content. The shoulder of the first peak also exhibits a distinct change in shape between the ACl12.1 and the ACl20.6 compositions. Although slight, it is arguable that the Fourier transformed EXAFS spectra in r-space displays a reduction in the Ca-Cl nearest neighbour distance with increasing $CaCl_2$ concentrations.

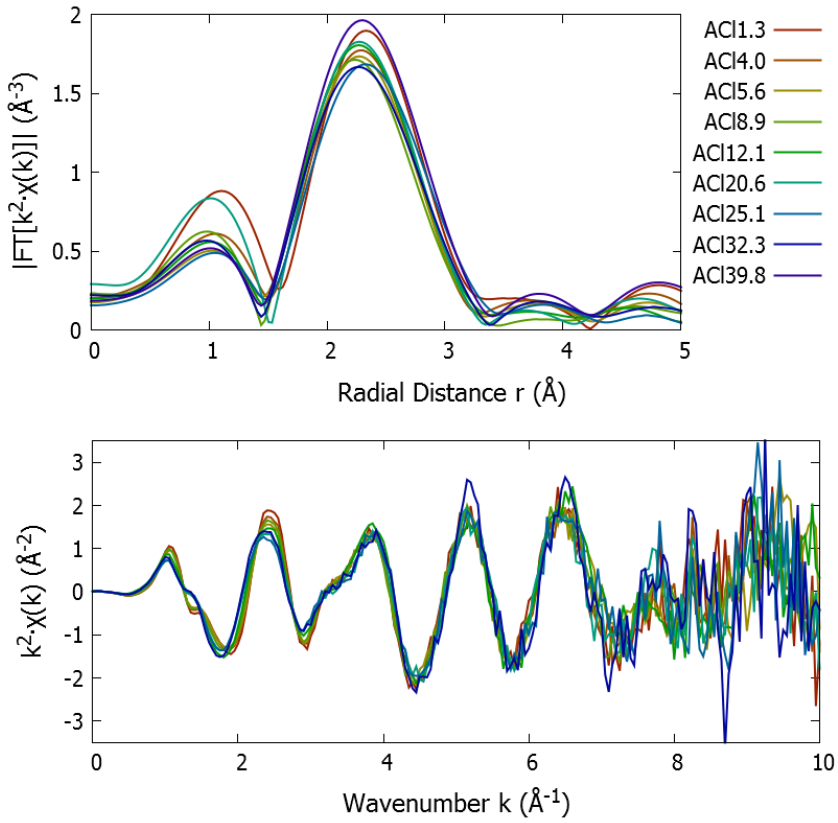

Figure 15: The Cl K-edge k^2 weighted EXAFS spectra (bottom) and the modulus of their Fourier transforms (top) for the ACl glass series.

The $CaCl_2 \cdot 4H_2O$ crystalline reference structure was also used to create a modelled EXAFS spectrum around the Cl K-edge using the FEFF code [25]. A single-scattering Ca-Cl FEFF path was chosen to fit the experimental EXAFS spectra of the ACl glass series. This was to attain values of R_{ij}, N_{ij}, and σ_{ij}^2 for each glass sample. The input parameters used for fitting in Artemis [22] are given in table 9. A k-range of 3.0Å^{-1} to 7.0Å^{-1} and an r-range of 1.0Å to 3.7Å was appropriate for fitting. The fits to the k^2 weighted experimental EXAFS spectra and to the modulus of their Fourier transforms are shown in figures 16 and 17 respectively. Although the data is noticeably noisier than that for the Ca K-edge, fair agreement over the fitting ranges can still be seen.

Table 9: The input parameters for the Ca-Cl FEFF path used to fit the experimental EXAFS spectra of the ACl glass series around the Cl K-edge.

	R_{ij} (Å)	N_{ij}	σ_{ij}^2 (Å^2)
Ca-Cl	2.79	4.0	0.01

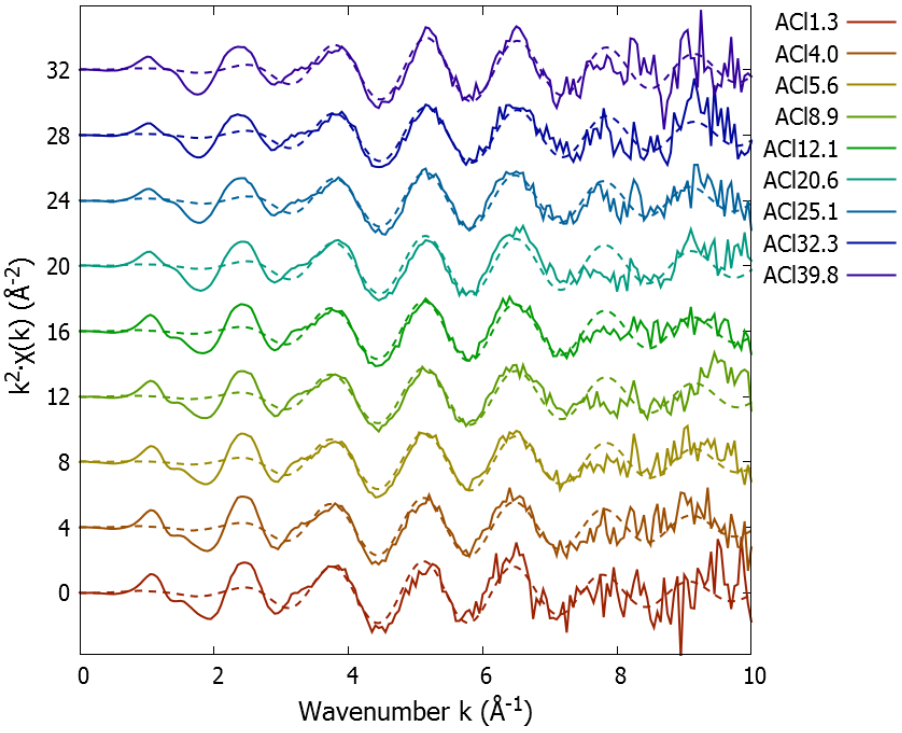

Figure 16: The experimental (solid lines) and fitted (dashed lines) Cl K-edge k^2 weighted EXAFS spectra for the ACl glass series. The plots have been progressively offset by 4.0Å^{-2}.

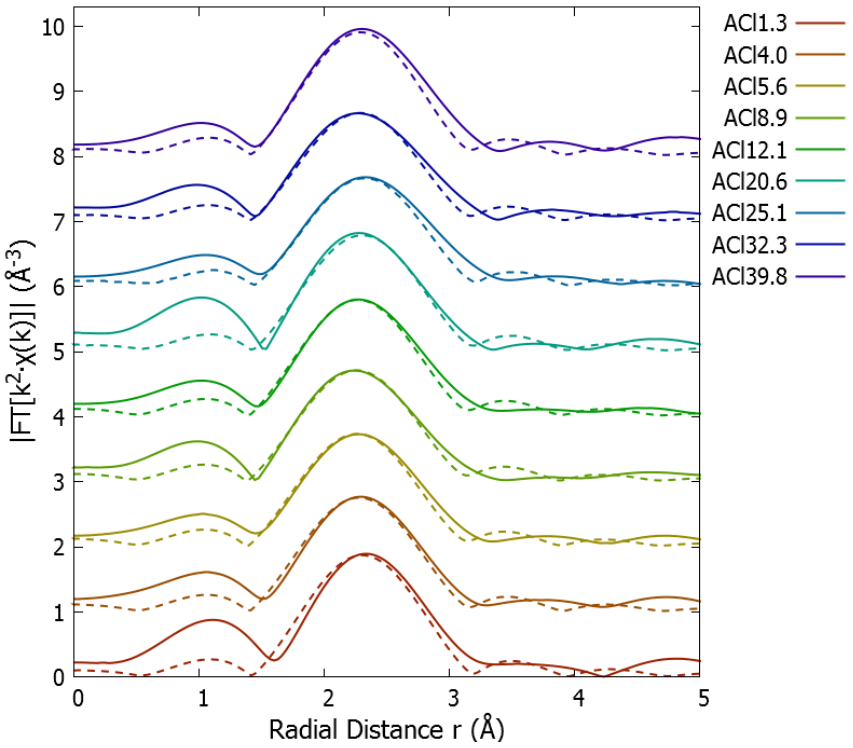

Figure 17: The modulus of the Fourier transformed experimental (solid lines) and fitted (dashed lines) Cl K-edge k^2 weighted EXAFS spectra for the ACl glass series. The plots have been progressively offset by 1.0Å^{-3}.

The parameters acquired from fitting the experimental Cl K-edge EXAFS spectra are given in table 10. Like the Ca K-edge fits, the Cl K-edge fits were also restrained to encourage $0.01Å^2 \leq \sigma_{ij}{}^2 \leq 0.03Å^2$ and an amplitude reduction factor of 0.7 was used. Since the relative concentrations of calcium and chlorine ions were known, the Ca-Cl coordination numbers could be calculated using the Cl-Ca coordination numbers obtained from the fits. As shown in table 10, the Ca-Cl nearest neighbour distances did not exhibit a clear trend but the Ca-Cl coordination numbers increased with increasing $CaCl_2$ concentrations as expected.

Table 10: The output structural parameters for the Ca-Cl correlation from fitting the k^2 weighted EXAFS spectra for the ACl glass series.

	$R_{Ca\text{-}Cl}$ (Å)	$N_{Cl\text{-}Ca}$	$N_{Ca\text{-}Cl}$	$\sigma_{Ca-Cl}{}^2$ ($Å^2$)
ACl1.3	2.78±0.04	2.66±0.80	0.13±0.04	0.011±0.008
ACl4.0	2.77±0.03	2.52±0.62	0.38±0.09	0.011±0.007
ACl5.6	2.76±0.03	2.34±0.55	0.48±0.11	0.010±0.006
ACl8.9	2.75±0.03	2.25±0.25	0.72±0.08	0.010±0.002
ACl12.1	2.76±0.03	2.37±0.28	0.99±0.12	0.010±0.002
ACl20.6	2.77±0.03	2.28±0.30	1.48±0.19	0.010±0.003
ACl25.1	2.78±0.04	2.15±0.30	1.62±0.23	0.010±0.003
ACl32.2	2.76±0.04	2.14±0.27	1.93±0.24	0.010±0.002
ACl39.8	2.76±0.04	2.40±0.34	2.50±0.35	0.009±0.003

5.5 Discussion

Losses via chlorine volatilisation have seldom been investigated [8], although halide losses in glasses are typically reported to be between 10% and 95% depending on the synthesis method used [13]. It was therefore important to study the compositions of the QCl and the ACl glass samples. This was achieved using calibrated XRF measurements. Fusion beads containing known combinations of crystalline $CaSiO_3$ and $CaCl_2{\cdot}4H_2O$ reagents were used to calibrate measurements on fusion beads containing glass samples. The calibration and sample measurements were performed on both sides of the fusion beads (apart from the fusion beads containing the nominal QCl11.9 and the ACl33.5 samples which shattered before they could be measured). This was because the raw XRF spectra revealed that the chlorine concentration on the bottom side of each fusion bead was persistently higher than the top side of each fusion bead. This finding was interpreted as being due to a chlorine-rich phase forming above the alkali borate melt when the fusion bead precursors (dominantly lithium borate flux) were heated in the Eagon 2 furnace during fusion bead production. When the molten precursors contained within the platinum crucible were poured into the platinum dish below, the chlorine rich phase would have left the crucible first, entering the bottom of the dish.

Scanning electron microscopy (SEM) was used to image the surfaces of fusion bead fragments to examine this further. The SEM images from both sides of the fusion bead containing the ACl25.1 glass sample are shown in figure 18 as an example. While the top of the fusion bead fragment does not contain small bubbles, the bottom side of the fusion bead fragment does. This could be associated with the formation of a chlorine-rich phase. Examining both sides of the ACl glass chips did not reveal noticeable differences, despite the limited solubility of chlorine in silicate melt [27], [28]. A significant difference between the fusion beads and the glass samples was that the fusion beads were based on a lithium borate system, while the glass samples were based on a calcium silicate system. In addition, the quenching procedures used to prepare the fusion beads and the glass samples were different. The melt used to prepare the fusion beads was poured into a relatively small dish, while the melt used to prepare glass samples for analysis was either splash-quenched between graphite plates or poured into water. The melt therefore covered a much larger area and so the glass samples were thin in comparison to the fusion beads. Another difference was the cooling rate. The melt used to prepare the fusion beads was cooled slowly relative to the melt used to prepare the glass samples.

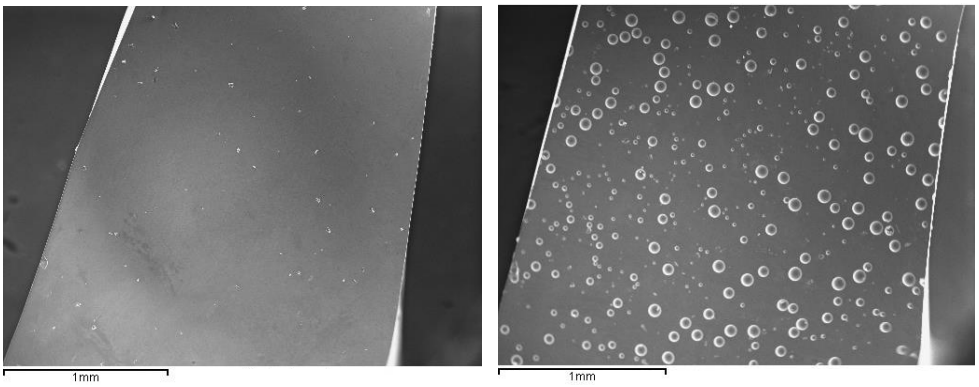

Figure 18: SEM images of the top and bottom side of a fusion bead fragment containing the ACl25.1 glass sample, as shown to the left and right respectively.

Following the analysis of the calibrated XRF measurements, it was found that the QCl series underwent insignificant losses. It was therefore assumed that the QCl glasses maintained their nominal compositions. Conversely, the ACl glasses exhibited chlorine losses of between 23% and 59%. While the percentage of chlorine loss in the ACl glasses generally reduced with increasing $CaCl_2$ content (figure 3), the absolute chlorine losses increased (figure 1). This finding was consistent with that of Kiprianov *et al.* [29] who studied chlorine loss in a number of $27Na_2O$-$73SiO_2$ glasses to which chlorine had been added. The XRF measurements on the ACl series did not reveal SiO_2 losses, but did show CaO contributions that were persistently higher than the nominal contributions. Losses via chlorine volatilisation therefore occurred as HCl. Raman spectra comparisons between a number of the ACl glasses and the spectra reported by Luth *et al.* [15] for CaO-SiO_2 glasses that were

CaO-rich, equimolar, and SiO_2-rich, confirmed this finding (figure 2). Density measurements of the QCl and ACl glass samples (figure 5) provided further evidence that the two glass series were not equivalent. The ACl densities were higher than the corresponding QCl densities which also suggested losses via chlorine volatilisation in the ACl series. This was because the mass per unit volume of chlorine is low in comparison to oxygen because of its larger size.

The ACl glass series had undergone significant losses via chlorine volatilisation while the QCl series exhibited negligible losses despite the two series having the same nominal compositions. It was therefore apparent that the scale of chlorine loss was highly dependent on the synthesis conditions used. Although the QCl and the ACl reagents were melted at temperature for one hour, the ACl reagents were also heated from room temperature to a final temperature of between 1445°C and 1530°C at a rate of 10°C/min prior to this, increasing the likelihood of chlorine volatilisation. In addition, the ACl samples were melted in an argon atmosphere where argon flowed over the melt. If chlorine volatilisation did occur above the melt, it is possible that using an argon flow would have removed more chlorine compared to using atmospheric conditions without a flow of gas. The batch size is another important consideration. The QCl glasses were synthesised from a 200g batch, while the ACl glasses were synthesised using a batch size of ~25g. Using a smaller batch size would have increased the surface area of the melt relative to the bulk, exposing a higher proportion of chlorine to the atmosphere and making the ACl glasses more susceptible to chlorine loss. It was therefore necessary to adjust the ACl compositions accordingly.

The structure of the ACl glass series was investigated using neutron diffraction (ND) and X-ray absorption spectroscopy (XAS). The same characterisation was not performed for the QCl glass series. In addition to not having a complete set of samples for the QCl glass series, the QCl samples had originally been prepared by quenching the melt in water. For a ND experiment, this would be problematic not only due to the large incoherent cross-section of hydrogen which would cause a large incoherent background, but also due to the prevalence of inelastic scattering events associated with hydrogen [30]. During the limited beamtime allocated for the XAS experiment, measurements on the ACl glass series were prioritised. This was to enable the XAS and ND results from the same samples to be compared.

The total neutron structure factors for the ACl glass series exhibited a distinct change of shape between the ACl12.1 and the ACl20.6 compositions as shown in figure 6. To investigate this further, peaks were fitted to the total correlation functions that had been obtained by Fourier transforming the total neutron structure factors using the program NXFit [18]. This was challenging because the signal to noise ratio deteriorated with increasing $CaCl_2$ concentrations, as shown in figures 8 and 9. This made termination ripples

increasingly prominent, and the ability to distinguish structural features more challenging. The reduction in signal to noise ratio was caused by chlorine ions having a notably higher neutron absorption cross section compared to the other ions in the glass series. For incident thermal neutrons (i.e. neutrons travelling at 2200ms^{-1}), the absorption cross section for chlorine is 33.5 barns [31]. In comparison, the absorption cross sections for oxygen, silicon, and calcium ions are 0.0001 barns, 0.41 barns, and 0.177 barns respectively [31]. Consequently, chlorine ions are considerably more likely to absorb neutrons, lowering the signal to noise ratio with increasing $CaCl_2$ content.

Another challenge with fitting peaks to the total correlation functions was the overlapping O-O and Ca-Cl peaks. Smaller peak contributions such as the ACl1.3 Ca-Cl peak for example were particularly difficult to fit. It was therefore necessary to use non-uniform input parameters for these peaks. The Ca-O and Ca-Cl coordination number parameters were restrained to be within 5% and 10% of their input values respectively while the restraint on the O-O coordination number was 0.20. By fitting the Ca-O, O-O, and Ca-Cl peaks of the total correlation function using the non-uniform fitting parameters, it was found by that the Ca-O and O-O coordination numbers decreased, while the Ca-Cl coordination number increased as shown in table 6. These trends were expected due to the decreasing oxygen contributions and the increasing chlorine contributions with increasing $CaCl_2$ content. As peak fitting was restrained in this way, it was necessary to account for systematic errors in addition to statistical errors. This explains why the uncertainty in the Ca-O and Ca-Cl coordination numbers is noticeably larger than those for the other correlations. From the structural parameters attained (table 6), an explanation for the distinct shape change in the total neutron structure factors between the ACl12.1 and the ACl20.6 compositions was not clear.

By considering the Si^{4+} and Cl^- effective ionic radii of 0.4Å and 1.67Å respectively [32], the presence of any Si-Cl bonding would be expected to result in a nearest neighbour distance contribution around 2.1Å, although Si-Cl nearest neighbour distances in $SiCl_4$ molecules have been reported to be 2.01Å [33]. A contribution around this distance in the total correlation functions was not obvious, indicating an absence of detectable amounts of Si-Cl bonding in the ACl glass series.

XAS data was collected for the ACl glass series around the Ca K-edge and around the Cl K-edge. It would have been challenging to investigate the silicon or oxygen environment using XAS due to the low absorption edge energies of 1.839keV and 0.543keV respectively [20]. To perform XAS experiments on elements lighter than phosphorus (including silicon and oxygen), the samples would need to be contained under vacuum to help minimise the attenuation of the incident X-ray beam [34]. The accessible X-ray energy range for beamline B18 was 2-35keV [21].

The Cl K-edge X-ray absorption near-edge structure (XANES) spectra for the ACl series displayed a marginal shift towards lower energies with increasing $CaCl_2$ content (figure 11). When these spectra were compared to the crystalline $CaCl_2 \cdot 4H_2O$ XANES spectra measured in this work, there was a noticeable difference in edge position. The edge positions in metal chlorides around the Cl K-edge have been reported to differ by around 1eV, even though the formal oxidation state of chlorine remains 1^- [35]–[37]. Szilagyi *et al.* [24] attributed this finding to differences in the ionicity of the cation-chlorine bond. The Ca K-edge XANES spectra also revealed a shift towards lower energies with increasing $CaCl_2$ content. By making comparisons with the crystalline $CaCl_2 \cdot 4H_2O$ XANES spectra, it was evident that the calcium environment became increasingly similar to the crystalline $CaCl_2$ environment with increasing $CaCl_2$ content.

The modulus of the Fourier transformed Ca K-edge k^2 weighted EXAFS spectra in r-space shown in figures 12 and 14 displayed a distinct change in shape between the ACl12.1 and the ACl20.6 compositions. The Ca-O and Ca-Cl paths became distinguishable beyond the ACl12.1 composition. This could be indicative of phase separation, where the Ca-O and Ca-Cl paths are prevalent in different regions of the sample. However, this cannot be established using XAS. Small angle neutron scattering (SANS) or small angle X-ray scattering (SAXS) would be useful to investigate the occurrence and scale of phase separation experimentally.

The Cl K-edge k^2 weighted EXAFS spectra (figure 16) were noticeably noisier than the Ca K-edge k^2 weighted EXAFS spectra (figure 13). This was due to the lower energy of the Cl K-edge (2822eV [20]) compared to the Ca K-edge (4038eV [20]). The flux of incident X-rays from the Si(111) monochromator would therefore have been lower, and X-ray attenuation due to the absorption of X-rays by elements other than chlorine would have increased. It was therefore necessary to fit the Cl K-edge k^2 weighted EXAFS spectra in Artemis [22] using a smaller fitting range (k=3.0-7.0Å^{-1}, r=1.0-3.7Å) compared to the fitting range used for the Ca K-edge k^2 weighted EXAFS spectra (k=3.0-9.0Å^{-1}, r=1.0-4.0Å).

By comparing the structural parameters attained from fitting the Ca K-edge and the Cl K-edge k^2 weighted EXAFS spectra (tables 8 and 10), it can be seen that the Ca-Cl nearest neighbour distances and coordination numbers from the Ca K-edge are generally larger than those from the Cl K-edge. This can be attributed to the poorer signal at the Cl K-edge as previously discussed. The structural parameters obtained from the Ca K-edge k^2 weighted EXAFS spectra are compared to those from neutron diffraction (where non-uniform fitting parameters were required due to the overlapping Ca-O, O-O, and Ca-Cl contributions) in figure 19. The coordination numbers from the two techniques displayed the same trends and were in reasonable agreement. The values of $\sigma_{ij}{}^2$ from neutron diffraction were generally higher, particularly for Ca-O, while the values from EXAFS analysis displayed more variation. The discrepancy in nearest neighbour distance for low

$CaCl_2$ concentrations was due to the difficulty of distinguishing the Ca-O and Ca-Cl contributions.

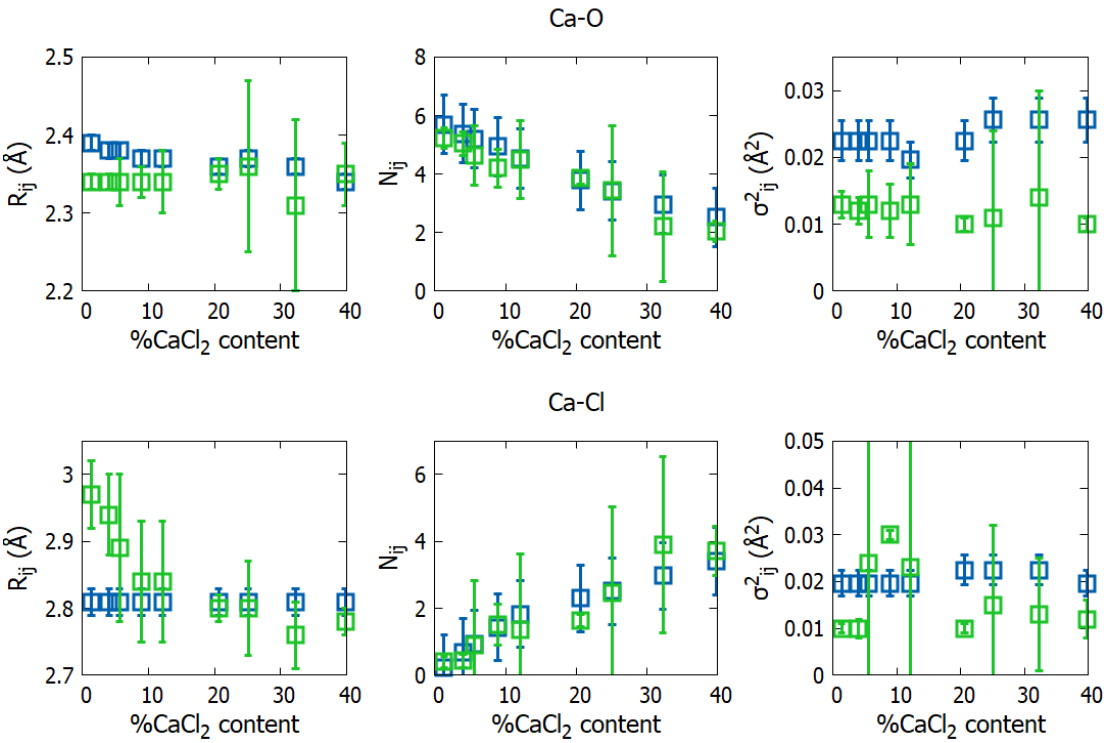

Figure 19: The nearest neighbour distances, R_{ij}, coordination numbers, N_{ij}, and values of σ_{ij}^2 obtained for the Ca-O (top) and Ca-Cl (bottom) correlations from Ca K-edge k^2 weighted EXAFS spectra (green squares) and neutron diffraction (blue squares).

5.6 Conclusion

In addition to the limited solubility of chlorine in silicate melts, chlorine is also susceptible to volatilisation. This makes the retention of chlorine in CaO-SiO_2-$CaCl_2$ glass challenging. Compositional analysis involved performing calibrated XRF measurements on the two CaO-SiO_2-$CaCl_2$ glass series that had been synthesised by collaborators using different approaches. Losses via chlorine volatilisation were found to occur as HCl, and the scale of these losses was highly dependent on the synthesis conditions used. In order to help minimise losses via chlorine volatilisation, it is important to ensure that the reagents are not melted any longer than necessary at a sufficient temperature for a sufficient time. If melting under an argon atmosphere, the use of a flow of argon gas should be avoided. In addition, the use of larger batch sizes (~200g) is also preferable.

Structural characterisation of the CaO-SiO_2-$CaCl_2$ glasses was performed using neutron diffraction and X-ray absorption spectroscopy. Both techniques were capable of probing the calcium and chlorine environments, although probing the chlorine environment was challenging due to the attenuation of incident radiation. The total neutron structure factors

and the modulus of the Fourier transformed Ca K-edge k^2 weighted EXAFS spectra both exhibited a distinct change in shape between the ACl12.1 and the ACl20.6 compositions. It is possible that this change was caused by phase separation. Small angle neutron scattering (SANS) or small angle X-ray scattering (SAXS) measurements would be useful to investigate the occurrence and scale of phase separation experimentally. Although the Ca-O and Ca-Cl contributions overlapped in the experimental data, reasonable agreement between the Ca-O and Ca-Cl nearest neighbour distances and coordination numbers could be achieved using the two techniques. The Ca-O coordination number was found to decrease with increasing $CaCl_2$ content, while the Ca-Cl coordination number increased as expected. Detectable amounts of Si-Cl bonding were not observed using neutron diffraction, although a complete absence of Si-Cl bonding could not be assumed. Having established the glass compositions and densities, the CaO-SiO_2-$CaCl_2$ glasses could be modelled computationally for the first time to further elucidate the structural role of chlorine. The occurrence of any phase separation could also be investigated computationally.

5.7 References

[1] J. Jones and A. Clare, *Bio-Glasses: An Introduction*. John Wiley & Sons, 2012.

[2] J. D. Featherstone, "The science and practice of caries prevention.," *J. Am. Dent. Assoc.*, vol. 131, no. 7, pp. 887–899, 2000.

[3] T. T. Thuy *et al.*, "Effect of strontium in combination with fluoride on enamel remineralisation in vitro," *Arch. Oral Biol.*, vol. 53, no. 11, pp. 1017–1022, 2008.

[4] S. E. Jabbarifar, S. Salavati, A. Akhavan, K. Khosravi, N. Tavakoli, and F. Nilchian, "Effect of fluoridated dentifrices on surface microhardness of the enamel of deciduous teeth," *Dent. Res. J. (Isfahan).*, vol. 8, no. 3, p. 113, 2011.

[5] X. Chen, X. Chen, D. S. Brauer, R. M. Wilson, R. G. Hill, and N. Karpukhina, "Novel alkali free bioactive fluorapatite glass ceramics," *J. Non. Cryst. Solids*, vol. 402, pp. 172–177, 2014.

[6] M. Mneimne, R. G. Hill, A. J. Bushby, and D. S. Brauer, "High phosphate content significantly increases apatite formation of fluoride-containing bioactive glasses," *Acta Biomater.*, vol. 7, no. 4, pp. 1827–1834, 2011.

[7] D. S. Brauer, N. Karpukhina, M. D. O'Donnell, R. V. Law, and R. G. Hill, "Fluoride-containing bioactive glasses: Effect of glass design and structure on degradation, pH and apatite formation in simulated body fluid," *Acta Biomater.*, vol. 6, no. 8, pp. 3275–3282, 2010.

[8] X. Chen, N. Karpukhina, D. S. Brauer, and R. G. Hill, "Novel Highly Degradable Chloride Containing Bioactive Glasses," *Biomed. Glas.*, vol. 1, no. 1, pp. 108–118, 2015.

[9] X. Chen, "Novel Halide Containing Bioactive Glasses," Queen Mary University of

London, 2015.

[10] X. Chen, N. Karpukhina, D. S. Brauer, and R. G. Hill, “High Chloride Content Calcium Silicate Glasses,” *Phys. Chem. Chem. Phys.*, vol. 19, pp. 7078–7085, 2017.

[11] D. A. McKeown, H. Gan, I. L. Pegg, W. C. Stolte, and I. N. Demchenko, “X-ray absorption studies of chlorine valence and local environments in borosilicate waste glasses,” *J. Nucl. Mater.*, vol. 408, no. 3, pp. 236–245, 2011.

[12] M. I. Ojovan and W. E. Lee, *An introduction to nuclear waste immobilisation*. Newnes, 2013.

[13] A. A. Kiprianov and N. G. Karpukhina, “Oxyhalide silicate glasses,” *Glas. Phys. Chem.*, vol. 32, no. 1, pp. 1–27, 2006.

[14] J. W. Robinson, E. S. Frame, and G. M. Frame II, *Undergraduate instrumental analysis*. CRC Press, 2014.

[15] R. W. Luth, “Raman spectroscopic study of the solubility mechanisms of F in glasses in the system CaO-CaF_2-SiO_2,” *Am. Mineral.*, vol. 73, pp. 297–305, 1988.

[16] A. K. Soper, “GudrunN and GudrunX: programs for correcting raw neutron and X-ray diffraction data to differential scattering cross section,” *Sci. Technol. Facil. Counc.*, 2011.

[17] C. M. Moreton-Smith, S. D. Johnston, and F. A. Akeroyd, “Open GENIE—a generic multi-platform program for the analysis of neutron scattering data,” *J. Neutron Res.*, vol. 4, pp. 41–47, 1996.

[18] D. Pickup, R. Moss, and R. Newport, “NXFit : a program for simultaneously fitting X-ray and neutron diffraction pair-distribution functions to provide optimized structural parameters,” *J. Appl. Crystallogr.*, vol. 47, pp. 1790–1796, 2014.

[19] D. R. Neuville, L. Cormier, and D. Massiot, “Al coordination and speciation in calcium aluminosilicate glasses: Effects of composition determined by ^{27}Al MQ-MAS NMR and Raman spectroscopy,” *Chem. Geol.*, vol. 229, no. 1–3, pp. 173–185, 2006.

[20] W. T. Elam, B. D. Ravel, and J. R. Sieber, “A new atomic database for X-ray spectroscopic calculations,” *Radiat. Phys. Chem.*, vol. 63, pp. 121–128, 2002.

[21] A. J. Dent *et al.*, “B18: A core XAS spectroscopy beamline for Diamond,” *J. Phys. Conf. Ser.*, vol. 190, p. 12039, 2009.

[22] B. Ravel and M. Newville, “ATHENA, ARTEMIS, HEPHAESTUS: data analysis for X-ray absorption spectroscopy using IFEFFIT,” pp. 537–541, 2005.

[23] J. Hormes, A. Diekamp, W. Klysubun, G. L. Bovenkamp, and N. Börste, “The characterization of historic mortars: A comparison between powder diffraction and synchrotron radiation based X-ray absorption and X-ray fluorescence spectroscopy,” *Microchem. J.*, vol. 125, pp. 190–195, 2016.

[24] R. K. Szilagyi, S. Mori, K. Hara, T. Iwai, and M. Sawamura, “ELECTRONIC STRUCTURE OF Ir-HALIDES FROM CHLORINE K-EDGE X-RAY ABSORPTION SPECTROSCOPIC MEASUREMENTS,” *Phot. Fact. Act. Rep.*, 2014.

[25] J. J. Rehr, J. J. Kas, M. P. Prange, A. P. Sorini, and Y. Takimoto, “Ab initio theory and

calculations of X-ray spectra," *C. R. Phys.*, vol. 10, no. 6, pp. 548–559, 2009.

[26] S. Calvin, *XAFS for Everyone*. CRC Press, 2013.

[27] S. Tanimoto and T. Rehren, "Interactions between silicate and salt melts in LBA glassmaking," *J. Archaeol. Sci.*, vol. 35, no. 9, pp. 2566–2573, 2008.

[28] I. V. Veksler *et al.*, "Partitioning of elements between silicate melt and immiscible fluoride, chloride, carbonate, phosphate and sulfate melts, with implications to the origin of natrocarbonatite," *Geochim. Cosmochim. Acta*, vol. 79, no. June, pp. 20–40, 2012.

[29] A. A. Kiprianov, N. G. Karpukhina, and V. A. Molodozhen, "Investigation into the Influence of Chloride Additives on the Properties of Alkali Silicate Glasses," vol. 30, no. 4, pp. 325–332, 2004.

[30] M. Affatigato, *Modern glass characterization*. John Wiley & Sons, 2015.

[31] V. F. Sears, "Neutron scattering lengths and cross sections," *Neutron News*, vol. 3, no. 3, pp. 26–37, 1992.

[32] R. D. Shannon, "Revised Effective Ionic Radii and Systematic Studies of Interatomic Distances in Halides and Chalcogenides," *Acta Crystallogr.*, no. A32, p. 751, 1976.

[33] L. N. Zakharov, M. Y. Antipin, Y. T. Struchkov, A. V. Gusev, A. M. Gibin, and N. V. Zhernenkov, "Molecular and crystal structures of $SiCl_4$ at 163 K," *Kristallografiya*, vol. 31, pp. 171–172, 1986.

[34] J. A. McCleverty and T. J. Meyer, *Comprehensive coordination chemistry II*. Elsevier Ltd, 2004.

[35] H. Konishi, M. Yamashita, H. Uchida, and J. Mizuki, "Cl K-Edge XANES Spectra of Atmospheric Rust on Fe , Fe-Cr and Fe-Ni Alloys Exposed to Saline Environment," *Mater. Trans.*, vol. 45, no. 12, pp. 3356–3359, 2004.

[36] K. A. Evans, J. A. Mavrogenes, H. S. O'Neill, N. S. Keller, and L. Y. Jang, "A preliminary investigation of chlorine XANES in silicate glasses," *Geochemistry, Geophys. Geosystems*, vol. 9, no. 10, 2008.

[37] F. Zhu, M. Takoaka, K. Oshita, S. Morisawa, H. Tsuno, and Y. Kitajima, "CHLORIDE SPECIATION IN WASHED RESIDUE OF TWO KINDS OF FLY ASH WITH DIFFERENT NEUTRALIZATION REAGENT," *Proc. Annu. Conf. Japan Soc. Waste Manag. Expert.*, vol. 19, 2008.

6. A Computational Investigation of the Structure of $CaO\text{-}SiO_2\text{-}CaCl_2$ Glasses

6.1 Introduction

As mentioned in the previous chapter, Chen [1], [2] was able to synthesise a series of $CaO\text{-}SiO_2\text{-}P_2O_5\text{-}CaCl_2$ chlorine-containing bioactive glass compositions which contained approximately 6mol% P_2O_5. Chen [1] reported that these glasses have 'outstanding' potential for remineralising toothpastes. To assist in characterising the glass system, Chen [1], [2] also synthesised a series of less complex $CaO\text{-}SiO_2\text{-}CaCl_2$ chlorine-containing silicate glasses where an equal SiO_2:CaO ratio was maintained.

During the experimental examination of the $SiO_2\text{-}CaO\text{-}CaCl_2$ glass samples [1], [2], a linear reduction in the glass transition temperature, the first crystallisation temperature, and the density of the samples was observed up until the 16.1mol% $CaCl_2$ composition. Beyond this composition a new linear trend formed, leaving a distinct break between the 16.1mol% $CaCl_2$ and 27.4mol% $CaCl_2$ compositions. Although a range of experimental techniques (including powder X-ray diffraction (PXRD) and Fourier transform infrared spectroscopy (FTIR)) were used to test for apatite formation, only ^{29}Si MAS-NMR spectroscopy was used to characterise the glass structure. The chemical shift positions in the ^{29}Si MAS-NMR spectra were centred around -80ppm. This indicated a dominantly Q^2 silicate network and an absence of detectable amounts of Si-Cl bonding. Understanding the $CaO\text{-}SiO_2\text{-}CaCl_2$ glass structure more closely is fundamental for being able to elucidate the structure of more complex $CaO\text{-}SiO_2\text{-}P_2O_5\text{-}CaCl_2$ chlorine-containing bioactive glass.

Since determining structural features such bond lengths, coordination numbers, and phase separation can be challenging experimentally, the use of computational modelling can be appealing. Currently, there is scant information on $CaO\text{-}SiO_2\text{-}CaCl_2$ glass in the literature and no computational modelling work has been undertaken. This chapter therefore investigates the $CaO\text{-}SiO_2\text{-}CaCl_2$ glass structure computationally. This was achieved using classical molecular dynamics with the addition of the adiabatic core-shell model. Results including glass model images, pair correlation functions, cumulative coordination number plots, structure factors, and silicon network connectivity distributions were attained. The aim was to characterise the structure of $CaO\text{-}SiO_2\text{-}CaCl_2$ glass, and provide insight into the structural role of chlorine in these chlorine-containing silicate glasses.

6.2 Computational Modelling Methodology

In order to model a glass computationally, the glass composition and density needs to be established. As mentioned in section 5.2, a nominal $CaO\text{-}SiO_2\text{-}CaCl_2$ glass series was synthesised both by collaborators at Queen Mary University of London (denoted as the QCl glass series), and later by other collaborators at Aston University (denoted as the ACl glass series). Based on the results of compositional analysis detailed in section 5.3, the nominal glass compositions were adjusted as necessary. Density values were determined using helium pycnometry as covered in section 5.4.1. Additionally, it is important to ensure that simulations of the basic glass components are stable prior to performing simulations of multicomponent systems. The first component to be considered in this work was the archetypal glass SiO_2 due to it being a simple oxide glass which has been well-studied experimentally. Throughout this chapter, the atomic correlations refer to the core atomic correlations unless explicitly stated otherwise. For example, O-O corresponds to oxygen cores, while $O_s\text{-}O_s$ corresponds to oxygen shells.

6.2.1 SiO_2 System

Interatomic potential parameters for modelling SiO_2 had been reported by Malavasi *et al.* [3] (table 1). These were tested on an $\alpha\text{-}SiO_2$ crystal structure [4] using the General Utility Lattice Program (GULP) [5] to assess their suitability for modelling glass in this study. Following GULP energy minimisation, the input $\alpha\text{-}SiO_2$ crystalline structure [4] of space group 154 underwent a volume change of -2.21%. The Si-O and O-O nearest neighbour distances of 1.61Å and 2.62Å, and coordination numbers of 4.00 and 6.00 respectively were unchanged.

Table 1: The two-body and three-body interatomic potential parameters of Buckingham and screened harmonic form respectively for modelling SiO_2 as reported by Malavasi *et al.* [3]. The inner cut-offs for the O_s-O_s and Si-O_s interatomic potential parameters were 1.7Å and 1.2Å respectively during simulations.

	Two-body $V_{ij}(r) = A_{ij}\exp\left(\frac{-r}{\rho_{ij}}\right) - \frac{C_{ij}}{r^6}$		
	A_{ij} (eV)	ρ_{ij} (Å)	C_{ij} (eV Å^6)
$O_s - O_s$	22764.30	0.1490	27.88
$Si - O_s$	1283.91	0.32052	10.66158
	Three-body $V(\theta_{jik}) = \frac{k_3}{2}(\theta_{jik} - \theta_0)^2\exp\left[-\left(\frac{r_{ij}}{\rho} + \frac{r_{ik}}{\rho}\right)\right]$		
	k_3 (eV rad^{-2})	θ_0 (°)	ρ (Å)
$O_s - Si - O_s$	100	109.47	1.0
	Core-shell potential $V = \frac{1}{2}K_{cs}r^2$		
	K_{cs} (eV Å^{-2})	Q (core) (e)	q (shell) (e)
$O - O_s$	74.92	0.8482	-2.8482
Si		4.000	

A random SiO_2 starting configuration of experimental density (2.2g/cm^3 [4]) was then prepared. The configuration contained 1296 oxygen ion cores, 1296 corresponding oxygen ion shells, and 648 silicon ions within a box of side length 30.86Å. From the atomic mass of an oxygen ion (15.9994u), 0.2u was assigned to the ion shell. The interatomic potential parameters in table 1 were used. An NVT Berendsen thermostat was chosen, and all simulation stages were to be fully equilibrated. A universal cut-off of 12.0Å, a primary cut-off of 10.0Å, and a van der Waals cut-off of 8.0Å were applied. To ensure a random distribution of ions, the simulation began at a temperature of 6000K and was supposed to run for 800,000 time-steps where each time-step was 0.1fs. However, the simulation was unstable. Through increasing the mass assigned to the shell from 0.2u to 0.4u to reduce the vibration of the harmonic spring, by reducing the simulation time-step of 0.1fs by orders of magnitude to monitor the trajectory of the shell more closely, by accounting for thermal expansion, and by lowering the system temperature, the simulation still failed to stabilise and maintain realistic temperatures.

It has been reported that the application of frictional damping to the harmonic spring connecting the core and the shell improves simulation stability [6], [7]. This can be implemented by adding a damping term to the force equation for the core-shell harmonic spring as shown in equation 1. In the equation, m_s is the shell mass, r is the displacement of the shell from the core, t is the time, c is the damping coefficient, and K_{cs} is the spring constant between the core and the shell units. Based on expert advice [8] and testing, a damping coefficient of c=100kgs^{-1} seemed to thermally stabilise the SiO_2 core-shell model simulations up to a temperature of 2000K.

$$m_s \frac{d^2r}{dt^2} = -c\frac{dr}{dt} - K_{cs}r \qquad \text{Equation 1}$$

Although rigid-ion simulations fail to account for ion polarisability, they do have improved stability at higher temperatures. The rigid-ion interatomic potential parameters reported by Teter [9] (table 2) were therefore tested on the α-SiO_2 crystalline structure [4] as well. The total volume change following GULP energy minimisation was 1.63%. The Si-O and O-O separation distances of 1.61Å and 2.62Å reduced to 1.59Å and 2.60Å respectively, and the coordination numbers of 4.00 and 6.00 respectively were unchanged.

Table 2: The rigid-ion two-body Buckingham interatomic potential parameters for modelling SiO_2 as stated by Teter [9]. The inner cut-offs for the O-O and Si-O interatomic potential parameters were 1.7Å and 1.2Å respectively during simulations.

	Two-body $V_{ij}(r) = A_{ij}\exp\left(\frac{-r}{\rho_{ij}}\right) - \frac{C_{ij}}{r^6}$		
	A_{ij} (eV)	ρ_{ij} (Å)	C_{ij} (eV Å^6)
$O-O$	1844.7458	0.343645	192.58
$Si-O$	13702.905	0.193817	54.681

After removing the oxygen shells from the input configuration of atoms and reinstating the oxygen mass of 15.9994u, rigid-ion simulations could be run from a molten liquid to a solid glass using the interatomic potential parameters in table 2. A universal cut-off of 12.0Å, a primary cut-off of 10.0Å, and a van der Waals cut-off of 8.0Å were used as before. The simulation temperature began at 6000K before it was reduced to 3000K and then 2000K. The system was then quenched from 2000K to 300K at a rate of 10^{13} K/s and a further stage at 300K followed. Each temperature stage comprised of 400,000 time-steps where each time-step was 1fs apart from the quench stage which required 170,000 time-steps. The system pressure at 300K was ~-30kbar. The REVCON file from the 300K sampling stage (which contained the final configuration of the atoms in the simulation cell) was used as the starting configuration for core-shell model runs once the oxygen shells had been added. The ion cores and corresponding shells were connected by a harmonic spring which was frictionally damped using a damping coefficient, c, of 100kgs^{-1}. The core-shell model runs used the interatomic potential parameters given in table 1.

Since Tilocca *et al.* [6] had only run a core-shell model simulation at 300K, and temperature stability up to 2000K had been achieved in this study, it was of interest to run and compare two core-shell model simulations. The first was only run at 300K, as had been done in the Tilocca *et al.* [6] study. The second was run from a temperature of 2000K before being quenched to 300K at a rate of 10^{13}K/s, where a further run at 300K followed. Sampling runs at 300K were then run for each set and used for data analysis. The core-shell model stages

used 800,000 time-steps, apart from the quench stage which needed 1,700,000 time-steps. The time-step was 0.1fs.

It was anticipated that applying the core-shell model from 2000K instead of 300K would have caused better agreement with experimental findings since the atoms would have more time to reproduce the effects of polarisation. However, by applying the core-shell model from 2000K, the total structure factor results failed to reproduce the first sharp diffraction peaks (FSDP's) seen experimentally [10], [11] (figure 1). The O-O coordination number of 6.19 (±0.03) was higher than the value of 6.0 attained experimentally using neutron diffraction [12] (table 3). Applying the core-shell model from 300K therefore produced a model more consistent with experimental findings. This was despite substantially lower system pressures being exhibited. The system pressures at 300K were -3.5±0.5kbar and -53.0±0.5kbar when the core-shell model had been applied from 2000K and 300K respectively. Tilocca *et al.* [6] failed to report any system pressure values in their study.

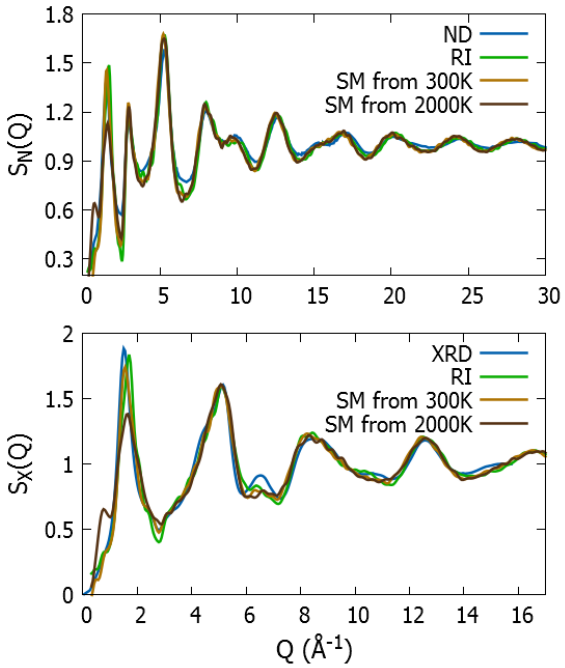

Figure 1: Total neutron ($S_N(Q)$) and X-ray ($S_X(Q)$) structure factor comparison at 300K for SiO_2 where the rigid-ion (RI) and core-shell model (SM) simulation results (from 300K and 2000K) are compared with the experimental diffraction results (labelled ND [10] and XRD [11]).

Table 3: The nearest neighbour distance, R_{ij}, and coordination number, $N_{ij}(r)$, values for SiO_2 glass determined experimentally by Johnson *et al.* [12] using neutron diffraction, and computationally in this work by applying the core-shell model (SM) from 300K or 2000K. Cut-off distances of 2.00Å, 2.85Å, and 3.40Å were used to determine the Si-O, O-O, and Si-Si coordination numbers respectively in this work.

	Si-O		O-O		Si-Si	
	R_{ij} (Å)	$N_{ij}(r)$	R_{ij} (Å)	$N_{ij}(r)$	R_{ij} (Å)	$N_{ij}(r)$
ND [12]	1.610	3.9	2.632	6.0	3.080	4.0
SM from 300K	1.63±0.01	4.00±0.01	2.65±0.01	6.03±0.03	3.03±0.01	4.00±0.02
SM from 2000K	1.63±0.01	4.00±0.01	2.63±0.01	6.19±0.03	3.03±0.01	4.02±0.02

Treating the atoms in the higher temperature simulation stages as rigid ions allows stable core-shell model simulations to run at lower temperatures. However, rigid-ion interatomic potentials are not available for the all of the correlations in the QCl and ACl glass compositions. It therefore became of interest to test whether core-shell model interatomic potentials (table 1) could be used as a viable estimate for rigid-ion potentials (table 2) in the higher temperature stages. To test this, rigid-ion simulations were run as before, but rather than using dedicated rigid-ion interatomic potentials, core-shell model interatomic potentials were used to estimate rigid-ion interatomic potential parameters instead (table 4). Shells were therefore not included and the atoms were considered to be solid, rigid spheres. In the core-shell model stages that followed at lower temperatures, shells were included and core-shell model interatomic potentials were used as per table 1.

Table 4: The two-body and three-body rigid-ion interatomic potential parameters of Buckingham and screened harmonic form respectively based on the core-shell model interatomic potential parameters reported by Malavasi *et al.* [3] in table 1. The inner cut-offs for the O-O and Si-O interatomic potential parameters were 1.7Å and 1.2Å respectively during simulations.

	Two-body $V_{ij}(r) = A_{ij}\exp\left(\frac{-r}{\rho_{ij}}\right) - \frac{C_{ij}}{r^6}$		
	A_{ij} (eV)	ρ_{ij} (Å)	C_{ij} (eV Å^6)
$O-O$	22764.30	0.1490	27.88
$Si-O$	1283.91	0.32052	10.66158
	Three-body $V(\theta_{jik}) = \frac{k_3}{2}(\theta_{jik} - \theta_0)^2 \exp\left[-\left(\frac{r_{ij}}{\rho} + \frac{r_{ik}}{\rho}\right)\right]$		
	k_3 (eV rad^{-2})	θ_0 (°)	ρ (Å)
$O-Si-O$	100	109.47	1.0
	Q (core) (e)		
O	-2.000		
Si	4.000		

It was found that regardless of whether the rigid-ion interatomic potentials from table 2 or from table 4 were used, nearest neighbour distances and coordination numbers equivalent to those in table 3 were obtained. Furthermore, total structure factors in fair agreement with experimental results could still be achieved (figure 2). This was despite the system

pressures becoming positive and very large when core-shell model interatomic potentials were used as estimates in the rigid-ion stages (24.5±0.5kbar at 300K). The system pressures returned to being negative in the core-shell model stages that ensued. The system pressures at 300K were -51.5±0.5kbar and -10.9±0.5kbar when the core-shell model had been applied from 300K and 2000K respectively.

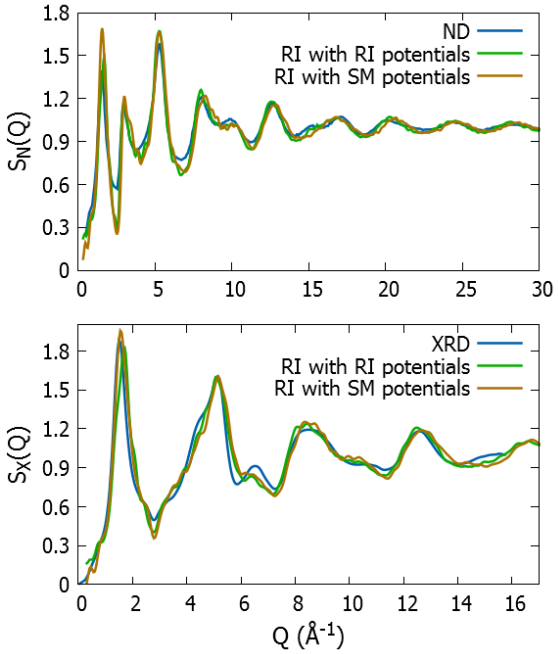

Figure 2: Total neutron ($S_N(Q)$) and X-ray ($S_X(Q)$) structure factor comparison at 300K for SiO_2. The results of running rigid-ion (RI) stages using the interatomic potentials from table 2 or table 4 prior to applying the core-shell model from 300K (table 1) are compared with results from neutron diffraction (ND) [10] and X-ray diffraction (XRD) [11] experiments.

To summarise, due to temperature instabilities it is necessary to treat the higher temperature stages of a SiO_2 simulation as being rigid-ion. The rigid-ion stages can be run using dedicated rigid-ion interatomic potentials (table 2), or estimates from core-shell model interatomic potentials (table 4). However, using estimates from core-shell model interatomic potentials significantly lowers the system pressure. It was also noticed that results more consistent with experimental findings were achieved by applying the core-shell model from 300K rather than from 2000K.

6.2.2 CaO-SiO_2 System

A marginally more complex system to model in the build up to the QCl and ACl glass series is CaO-SiO_2 glass. Before running simulations, it was necessary to obtain a Ca-O_s core-shell model interatomic potential parameter to compliment those in table 1. Both Malavasi *et al.* [3] and Rabone and De Leeuw [13] have reported Ca-O_s interatomic potential parameters (table 5). These were tested on CaO [14] and $CaSiO_3$ [15] crystalline structures using GULP

[5]. As shown in table 6, the one reported by Malavasi *et al.* [3] (labelled (1)) could reproduce the crystalline structures more closely. The core-shell model interatomic potentials used to model CaO-SiO_2 glass are presented in table 7.

Table 5: The two-body Ca-O_s Buckingham interatomic potentials obtained from Malavasi *et al.* [3] and Rabone and De Leeuw [13]. Labels 1, 2, and 3 are for reference.

			Two-body $V_{ij}(r) = A_{ij}\exp\left(\frac{-r}{\rho_{ij}}\right) - \frac{C_{ij}}{r^6}$		
			A_{ij} (eV)	ρ_{ij} (Å)	C_{ij} (eV Å^6)
(1)	[3]	$Ca - O_s$	2152.3566	0.309227	0.09944
(2)	[13]	$Ca - O_s$	1279.32	0.317201	0.00000
(3)	[13]	$Ca - O_s$	1250.00	0.343700	0.00000

Table 6: The GULP energy minimisation results comparing the performance of the Ca-O_s interatomic potentials in table 5 (labelled as (1), (2), and (3)) using crystalline CaO [14] and $CaSiO_3$ [15] structures. The terms R_{ij} and N_{ij} denote the nearest neighbour distances and coordination numbers respectively.

	CaO [14]				$CaSiO_3$ [15]			
	Input	(1) [3]	(2) [13]	(3) [13]	Input	(1) [3]	(2) [13]	(3) [13]
R_{Ca-O} (Å)/N_{Ca-O}	2.42/ 6.00	2.40/ 6.00	2.25/ 6.00	2.47/ 6.00	2.41/ 6.00	2.43/ 6.00	2.30/ 6.00	2.48/ 5.66
R_{O-O} (Å)/N_{O-O}	3.42/ 12.00	3.40/ 12.00	3.18/ 12.00	3.49/ 12.00	2.69/ 4.00	2.65/ 4.00	2.63/ 3.77	2.66/ 4.00
R_{Si-O} (Å)/N_{Si-O}					1.64/ 4.00	1.62/ 4.00	1.62/ 4.00	1.63/ 4.00
Volume (Å^3)	28.27	27.75	22.77	30.10	823.73	816.02	728.45	869.81

Table 7: The two-body and three-body interatomic potential parameters of Buckingham and screened harmonic form respectively for modelling CaO-SiO_2 as reported by Malavasi *et al.* [3]. An oxygen shell mass of 0.2u was used. The inner cut-offs for the O_s-O_s, Si-O_s, and Ca-O_s interatomic potential parameters were 1.7Å, 1.2Å, and 1.5Å respectively.

	Two-body $V_{ij}(r) = A_{ij}\exp\left(\frac{-r}{\rho_{ij}}\right) - \frac{C_{ij}}{r^6}$		
	A_{ij} (eV)	ρ_{ij} (Å)	C_{ij} (eV Å^6)
$O_s - O_s$	22764.30	0.1490	27.88
$Si - O_s$	1283.91	0.32052	10.66158
$Ca - O_s$	2152.3566	0.309227	0.09944
	Three-body $V(\theta_{jik}) = \frac{k_3}{2}(\theta_{jik} - \theta_0)^2 \exp\left[-\left(\frac{r_{ij}}{\rho} + \frac{r_{ik}}{\rho}\right)\right]$		
	k_3 (eV rad^{-2})	θ_0 (°)	ρ (Å)
$O_s - Si - O_s$	100	109.47	1.0
	Core-shell potential $V = \frac{1}{2}K_{cs}r^2$		
	K_{cs} (eV Å^{-2})	Q (core) (e)	q (shell) (e)
$O - O_s$	74.92	0.8482	-2.8482
Si		4.000	
Ca		2.000	

As in section 6.2.1, temperature instabilities meant that it was necessary to treat the higher temperature stages of a simulation as being rigid-ion. Core-shell model stages could then run with the application of frictional damping at lower temperatures. This scenario provided the opportunity to carry out similar tests to those detailed in section 6.2.1 on a different glass system. First however, it was necessary to test the Ca-O rigid-ion interatomic potential stated by Teter [9] (table 8) on CaO [14] and $CaSiO_3$ [15] crystalline structures using GULP [5]. The results of GULP energy minimisation are shown in table 9. By comparing the GULP results in tables 6 and 9, it can be seen that using core-shell model interatomic potential parameters instead of rigid-ion interatomic potential parameters enables the CaO [14] and $CaSiO_3$ [15] crystalline structures to be reproduced more closely.

Table 8: Rigid-ion two-body Buckingham interatomic potential parameters for modelling CaO-SiO_2 as stated by Teter [9]. The inner cut-offs for the O-O, Si-O, and Ca-O interatomic potential parameters were 1.7Å, 1.2Å, and 1.5Å respectively.

	Two-body $V_{ij}(r) = A_{ij}\exp\left(\frac{-r}{\rho_{ij}}\right) - \frac{C_{ij}}{r^6}$		
	A_{ij} (eV)	ρ_{ij} (Å)	C_{ij} (eV Å^6)
$O - O$	1844.7458	0.343645	192.58
$Si - O$	13702.905	0.193817	54.681
$Ca - O$	7747.1834	0.252623	93.109

Table 9: The GULP energy minimisation results testing the performance of the rigid-ion interatomic potentials in table 8 using crystalline CaO [14] and $CaSiO_3$ [15] structures. The terms R_{ij} and N_{ij} denote the nearest neighbour distances and coordination numbers respectively.

	CaO [14]		$CaSiO_3$ [15]	
	Input	Output	Input	Output
R_{Ca-O} (Å)/N_{Ca-O}	2.42/ 6.00	2.39/ 6.00	2.41/ 6.00	2.42/ 6.00
R_{O-O} (Å)/N_{O-O}	3.42/ 12.00	3.38/ 12.00	2.69/ 4.00	2.59/ 4.00
R_{Si-O} (Å)/N_{Si-O}			1.64/ 4.00	1.59/ 4.00
Volume ($Å^3$)	28.27	27.19	823.73	785.99

Models of $50CaO\text{-}50SiO_2$ glass were simulated in the same manner as the SiO_2 glass models in section 6.2.1. An initial random configuration of 384 silicon ions, 384 calcium ions, and 1152 oxygen ions contained within a cubic box of side length of $29.45Å^3$ corresponding to the experimental density of $2.9g/cm^3$ [16] was prepared. A universal cut-off of 12.0Å, a primary cut-off of 10.0Å, and a van der Waals cut-off of 8.0Å were applied. Dedicated rigid-ion interatomic potential parameters (table 8) were used in the rigid-ion stages. The initial rigid-ion simulation stages ran at temperatures of 6000K, 3000K, and 2000K. The system was then quenched at a rate of 10^{13}K/s to 300K, and a stage at 300K ensured a solid glass model. A sampling stage at 300K was then run and used for analysis. The single temperature rigid-ion stages ran for 400,000 time-steps. The quench stage ran for 170,000 time-steps and the time-step was 1fs. The final configuration of atoms from the rigid-ion stages was used as the starting configuration for the core-shell model stages that followed.

For the core-shell model atomic configuration, 1152 oxygen shells were added. While most of the oxygen atomic mass was assigned to the oxygen cores (15.7994u), 0.2u was allocated to the oxygen shells. The core and shell units were connected by a harmonic spring of spring constant K_{cs} which was frictionally damped using a damping coefficient, c, of $100kgs^{-1}$. The core-shell model interatomic potentials in table 7 were used, and two sets of core-shell model simulations were run. One began at 2000K before being quenched from 2000K to 300K at a rate of 10^{13}K/s. A stage at 300K followed afterwards. The other core-shell model simulation was only run at 300K. Sampling runs of both simulations were then run and used for data analysis. Each single temperature stage ran for 800,000 time-steps. The quench stage ran for 1,700,000 time-steps and the time-step was 0.1fs. Throughout the entire simulation (both the rigid-ion and core-shell model stages), an NVT Berendsen thermostat was used and all simulation stages were fully equilibrated. The system pressures exhibited at 300K were ~-12kbar in the rigid-ion stage, and ~26kbar and ~29kbar when the core-shell model had been applied from 300K and 2000K respectively.

It was also of interest to further test whether core-shell model interatomic potential parameters could be used to estimate rigid-ion interatomic potentials. This prompted simulations to be run as described above, but rather than using the dedicated rigid-ion interatomic potential parameters in table 8 for the rigid-ion stages of the simulation, core-shell model interatomic potential parameters were used to estimate the rigid-ion interatomic potential parameters (table 10) instead. Anion shells were therefore not included and the atoms were treated as being rigid spheres. In the core-shell model stages that ensued, dedicated core-shell model interatomic potential parameters were used (table 7), and the anion shells were included. The system pressures exhibited at 300K were ~28kbar in the rigid-ion stage, and ~20kbar and ~32kbar in the core-shell model stages that had been applied from 300K and 2000K respectively.

Table 10: The two-body and three-body rigid-ion interatomic potential parameters of Buckingham and screened harmonic form respectively based on the core-shell model interatomic potential parameters reported by Malavasi *et al.* [3] in table 7. The inner cut-offs for the O-O, Si-O, and Ca-O interatomic potential parameters were 1.7Å, 1.2Å, and 1.5Å respectively during simulations.

	Two-body $V_{ij}(r) = A_{ij}\exp\left(\frac{-r}{\rho_{ij}}\right) - \frac{C_{ij}}{r^6}$		
	A_{ij} (eV)	ρ_{ij} (Å)	C_{ij} (eV Å^6)
$O-O$	22764.30	0.1490	27.88
$Si-O$	1283.91	0.32052	10.66158
$Ca-O$	2152.3566	0.309227	0.09944
	Three-body $V(\theta_{jik}) = \frac{k_3}{2}(\theta_{jik} - \theta_0)^2 \exp\left[-\left(\frac{r_{ij}}{\rho} + \frac{r_{ik}}{\rho}\right)\right]$		
	k_3 (eV rad^{-2})	θ_0 (°)	ρ (Å)
$O-Si-O$	100	109.47	1.0
	Q (core) (e)		
O	-2.000		
Si	4.000		
Ca	2.000		

Due to the high system pressures being exhibited, it was necessary to compromise between having a system of the correct experimental density (2.9g/cm^3 [16]), and having one of a more physical pressure. The system density was therefore reduced to 2.84g/cm^3, 98% of the experimental density. The simulations described above were rerun, and lower system pressures were achieved. For example, when using core-shell model interatomic potentials to estimate rigid-ion interatomic potentials in the rigid-ion stages, pressures of ~19kbar in the rigid-ion stage, and ~12kbar and ~21kbar in the following core-shell model stages from 300K and 2000K respectively were achieved. Furthermore, table 11 shows that reducing the system density yields a Ca-O nearest neighbour distance that is more consistent with experimental results.

Table 11: A comparison of Ca-O nearest neighbour distances, R_{ij}, and coordination numbers, $N_{ij}(r)$ in 50CaO-50SiO_2 glass. The values were obtained computationally in this work (MD) using the experimental density (2.9g/cm^3 [16]) or a reduced density (2.84g/cm^3). A cut-off of 3.1Å was used to identify the coordination numbers. Experimental extended absorption fine structure (EXAFS) [17], [18] and neutron diffraction (ND) [19] results are included for comparison.

Ref.	Method	R_{Ca-O} (Å)	$N_{Ca-O}(r)$
This work	MD exp. density	2.31±0.01 Å	6.11±0.03
This work	MD 98% exp. density	2.33±0.01 Å	6.00±0.03
[17]	EXAFS	2.49	5.6
[18]	EXAFS	2.36(1)	6.0(3)
[19]	ND	2.37(6)	6.15(17)

The silicon network connectivity distributions from the 50CaO-50SiO_2 glass models of reduced density (98% of the experimental density) are compared with experimental NMR data [20] in figure 3. Both plots in figure 3 reveal that results most consistent with experimental NMR data are achieved by applying the core-shell model from 2000K instead of 300K. Interestingly, the model in best agreement with the NMR data was attained using core-shell model interatomic potential parameters (to estimate rigid-ion interatomic potential parameters) in the rigid-ion stages before the core-shell model was applied from 2000K.

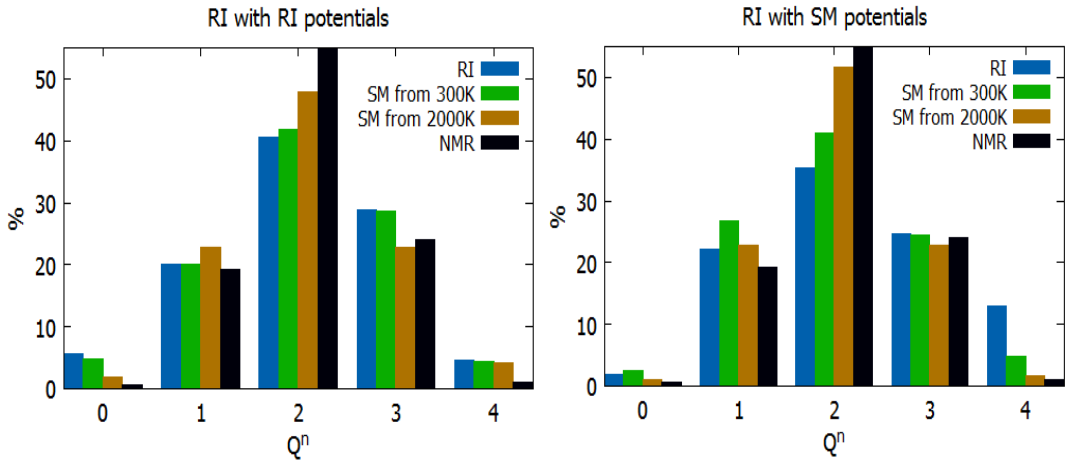

Figure 3: Silicon network connectivity distributions in 50CaO-50SiO_2 glass at 300K obtained experimentally using NMR [20], and computationally in this work using densities equivalent to 98% of the experimental density. In the plot to the left, the dedicated rigid-ion (RI) interatomic potentials in table 8 were used in the RI stages. In the plot to the right, core-shell model (SM) interatomic potentials were used to estimate RI interatomic potentials (table 10) in the RI stages.

To enable further comparisons with experimental data, models of 42CaO-58SiO_2 glass were prepared. The models contained 336 calcium ions, 464 silicon ions, and 1264 oxygen ions (as well as 1264 oxygen ion shells in the core-shell model stages) within a cubic simulation cell. The models were either of experimental density (2.78g/cm^3 [16]) and had a simulation

cell side length of 30.33Å, or were of a reduced density of 2.72g/cm^3 (98% of the experimental density) and had a simulation cell side length of 30.55Å. Core-shell model interatomic potentials were used to estimate rigid-ion interatomic potentials in the rigid-ion stages (table 10). In the core-shell model stages from either 2000K or 300K that followed, dedicated core-shell model interatomic potentials were used (table 7). A universal cut-off of 12.0Å, a primary cut-off of 10.0Å, and a van der Waals cut-off of 8.0Å were applied.

The calculated total structure factors obtained using the experimental and reduced system densities (where the core-shell model had been applied from 2000K) are compared with experimental diffraction results in figure 4. Good agreement between the two sets of computational results and the experimental results is seen. Arguably, the model of reduced density agrees with the experimental results more closely, most noticeably for Q~2Å^{-1}.

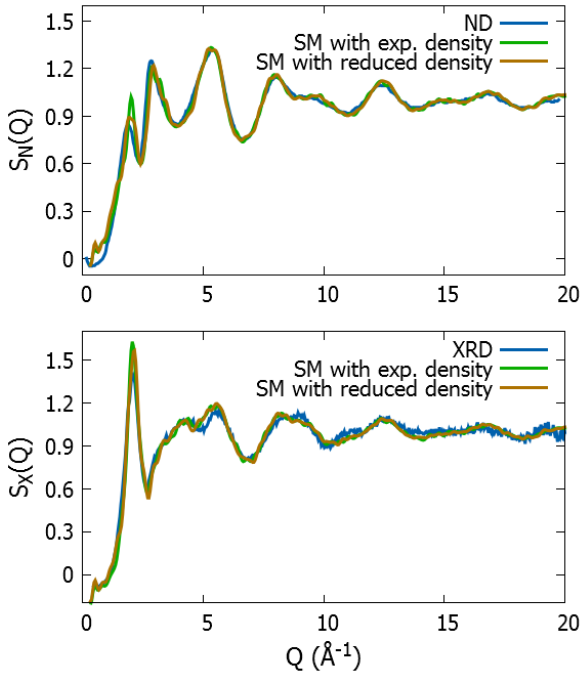

Figure 4: A comparison of total neutron ($S_N(Q)$) and X-ray ($S_X(Q)$) structure factors for 42CaO-58SiO$_2$ glass at 300K obtained experimentally [32] and computationally. The computational results were attained using the experimental density or a reduced density equivalent to 98% of the experimental density. Core-shell model (SM) interatomic potentials were used to estimate RI interatomic potentials (table 10).

Considering SiO_2 corresponds to a fully Q^4 environment, while orthosilicate compositions with SiO_4 are fully Q^0, the equation n=-2a+8, where 'n' is the silicon network connectivity and 'a' is the O:Si ratio can be used to predict average silicon network connectivity value. By assuming that just two different Q^n groups are present, it is possible to determine the Q^n distribution. Therefore, by assuming the 42CaO-58SiO$_2$ system

comprises of Q^2 and Q^3 species, the system should contain 45% Q^2 species and 55% Q^3 species. By considering the model of experimental density, it can be seen in figure 5 that the application of the core-shell model from 2000K rather than 300K yields a silicon network connectivity distribution that is more similar to the expected distribution. It was also found that the Q^n distribution was not affected by reducing the system density to 98% of the experimental density.

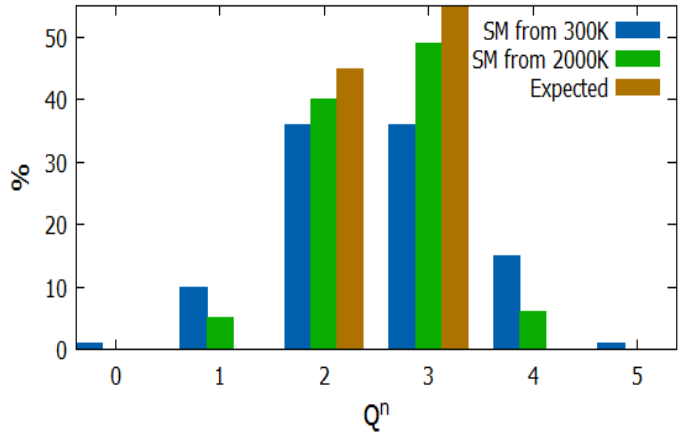

Figure 5: The expected silicon network connectivity distribution in 42CaO-58SiO_2 glass compared with the distributions in the computational models. The models were of experimental density, and core-shell model interatomic potentials were used to estimate rigid-ion interatomic potentials in the rigid-ion stages (table 10). The core-shell model (SM) was applied from 300K or 2000K.

To summarise, as with the SiO_2 simulations in section 6.2.1, temperature instabilities meant it was necessary to treat the higher temperatures stages of a CaO-SiO_2 simulation as being rigid-ion. The core-shell model stages could then run at lower temperatures with the application of frictional damping. The highly positive system pressures were reduced by lowering the system density by 2%. This also caused the agreement with experimental results to be improved. In contrast to the SiO_2 simulations, it was preferable to apply the core-shell model from 2000K. It has therefore become apparent that choosing the temperature at which the core-shell model is applied from in more complex systems such as the QCl and ACl series requires consideration.

6.2.3 SiO_2-CaO-$CaCl_2$ System - Fitting Interatomic Potential Parameters

Having worked on stabilising SiO_2 and CaO-SiO_2 simulations and achieved results consistent with experimental findings, more complex systems could be modelled. This involved the addition of $CaCl_2$ to the CaO-SiO_2 system to form the ACl and QCl glass compositions in the CaO-SiO_2-$CaCl_2$ system. A number of interatomic potentials were needed to compliment

those in table 7 (Cl_s-Cl_s, Ca-Cl_s, Cl_s-O_s, and Si-Cl_s), and most had been reported by Rabone and De Leeuw [13] (table 12).

Table 12: Two-body Buckingham interatomic potential parameters reported by Rabone and De Leeuw [13] in an apatite study. In [13], $O_{(P)}$ was used to denote oxygen in PO_4^{3-}, CO_3^{2-}, SiO_4^{4-}, while $O_{(H)}$ was used to denote oxygen in OH^-.

	Two body $V_{ij}(r) = A_{ij}\exp\left(\frac{-r}{\rho_{ij}}\right) - \frac{C_{ij}}{r^6}$		
	A_{ij} (eV)	ρ_{ij} (Å)	C_{ij} (eV Å^6)
$Cl_s - Cl_s$	49039.26	0.243207	16.05
$Cl_s - O_{s\,(H)}$	71379.71	0.227705	0.13
$Cl_s - O_{s\,(P)}$	68297092.09	0.153267	15.16
$O_{s\,(H)} - O_{s\,(H)}$	22764.0	0.149000	6.97
$O_{s\,(P)} - O_{s\,(P)}$	16372.00	0.213000	3.47
$Ca - O_{s\,(H)}$	1279.32	0.317201	0.00
$Ca - O_{s\,(H)}$	1250.00	0.343700	0.00
$Ca - Cl_s$	1220.80	0.35300	0.00
$Ca - Cl_s$	1285.14	0.348729	0.00
	Core-shell potential $V = \frac{1}{2}K_{cs}r^2$		
	K_{cs} (eV Å^{-2})	Q (core) (e)	q (shell) (e)
$Cl - Cl_s$	54.41	1.650	-2.650
$O_{(H)} - O_{s\,(H)}$	74.92	0.900	-2.300
$O_{(P)} - O_{s\,(P)}$	507.40	0.587	-1.632
Ca		2.000	

The interatomic potential parameters involving oxygen ions in table 12 fail to maintain charge neutrality. It was therefore intuitive to continue using the ones reported by Malavasi *et al.* [3] (table 7). The Cl_s-Cl_s and Ca-Cl_s interatomic potentials in table 12 do maintain charge neutrality, but since two Ca-Cl_s interatomic potentials had been reported, the most suitable needed to be identified. A $CaCl_2$ crystal structure [21] underwent GULP energy minimisation, and volume changes of 0.26% and -1.18% were attained using the first and second Ca-Cl_s interatomic potentials respectively. While both GULP output structures maintained the Ca-Cl coordination number of 6.00, only the one obtained using the first Ca-Cl_s interatomic potential was also able to reproduce the Ca-Cl nearest neighbour distance of 2.74Å. It was therefore favorable to use the first Ca-Cl_s interatomic potential listed in table 12.

Two more interatomic potential parameters still needed to be established; Si-Cl_s and Cl_s-O_s. There are no reports of a Si-Cl_s interatomic potential in the literature, and neither of the two Cl_s-O_s interatomic potentials in table 12 uphold charge neutrality on oxygen. It would have been challenging to fit both the Si-Cl_s and Cl_s-O_s interatomic potentials simultaneously

due to the number of parameters being involved. Consequently, the Cl_s-$O_{s(H)}$ interatomic potential (table 12) was chosen over the Cl_s-$O_{s(P)}$ one because the charges were closer to neutrality. For consistency with the other interatomic potential parameters involving oxygen, the ion core and shell charges for oxygen reported by Malavasi *et al.* [3] (which are charge neutral) were assigned to the Cl_s-$O_{s(H)}$ interatomic potential. The Si-Cl_s interatomic potential could then be fitted.

The A_{ij}, ρ_{ij}, and C_{ij} parameters of the Si-Cl_s Buckingham interatomic potential were fitted one at a time manually using $SiCl_4$ [22], $(SiCl_3)O(SiCl_2)O(SiCl_3)$ [23], $Si_6O_7Cl_{10}$ [24], $(Cl_2SiO)_3$ [25], and $(Cl_2SiO)_4$ [25] crystalline structures (figure 6) in GULP. The Si-Cl input and output separation distances were monitored throughout the fitting procedure to see whether a change in interatomic potential yielded better agreement with the input crystalline structures. A final interatomic potential of A_{ij}=1063eV, ρ_{ij}=0.3352Å and C_{ij}=17eVÅ^6 was attained for the Si-Cl_s potential. The set of interatomic potentials for modelling the QCl and ACl glass series are presented in table 13, and the final GULP energy minimisation results which show reasonable performance are shown in table 14.

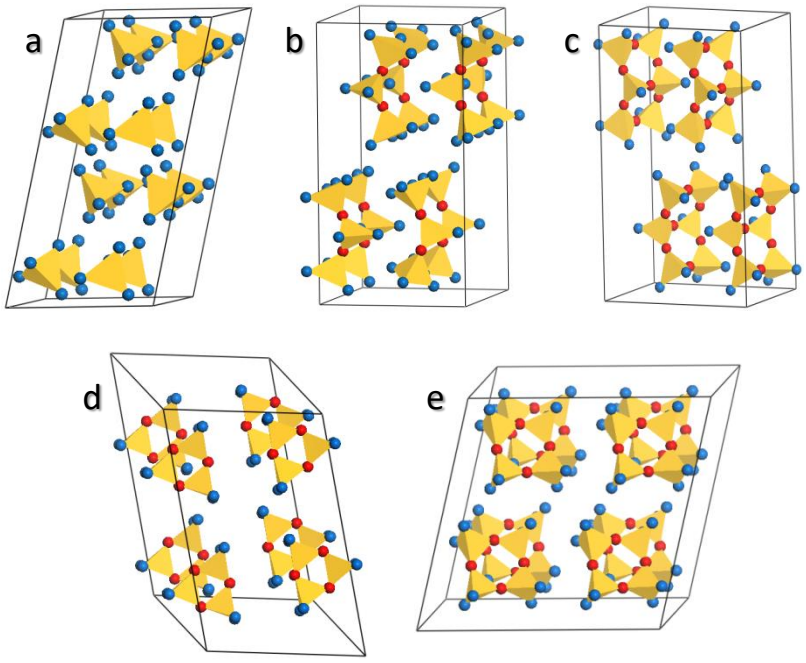

Figure 6: The $SiCl_4$ [22], $(SiCl_3)O(SiCl_2)O(SiCl_3)$ [23], $Si_6O_7Cl_{10}$ [24], $(Cl_2SiO)_3$ [25], and $(Cl_2SiO)_4$ [25] crystalline structures used to fit the Si-Cl_s interatomic potential. They are labelled labeled from 'a' to 'e' respectively. The red and blue spheres represent oxygen and chlorine ions respectively, and the yellow tetrahedra represent silicon ions.

Table 13: The two-body and three-body interatomic potential parameters of Buckingham and screened harmonic form respectively for modelling the QCl and ACl glass series. The oxygen and chlorine shell masses used were 0.2u and 1.5u respectively. The inner cut-offs for the O_s-O_s, Cl_s-Cl_s, Cl_s-O_s, and Ca-Cl_s interatomic potentials were 1.7Å. The Ca-O_s, Si-Cl_s, and Si-O_s interatomic potentials had inner cut-offs of 1.5Å, 1.3Å, and 1.2Å respectively.

	Two body $V_{ij}(r) = A_{ij}\exp\left(\frac{-r}{\rho_{ij}}\right) - \frac{C_{ij}}{r^6}$		
	A_{ij} (eV)	ρ_{ij} (Å)	C_{ij} (eV Å^6)
$O_s - O_s$	22764.30	0.1490	27.88
$Si - O_s$	1283.91	0.32052	10.66158
$Cl_s - Cl_s$	49039.26	0.243207	16.05
$Si - Cl_s$	1063.00	0.3352	17.00
$Cl_s - O_s$	71379.71	0.227705	0.13
$Ca - Cl_s$	1220.80	0.35300	0.00
$Ca - O_s$	2152.3566	0.309227	0.09944
	Three body $V(\theta_{jik}) = \frac{k_3}{2}(\theta_{jik} - \theta_0)^2 \exp\left[-\left(\frac{r_{ij}}{\rho} + \frac{r_{ik}}{\rho}\right)\right]$		
	k_3 (eV rad^{-2})	θ_0 (°)	ρ (Å)
$O_s - Si - O_s$	100	109.47	1.0
	Core-shell potential $V = \frac{1}{2}K_{cs}r^2$		
	K_{cs} (eV Å^{-2})	Q (core) (e)	q (shell) (e)
$O - O_s$	74.92	0.8482	-2.8482
$Cl - Cl_s$	54.41	1.650	-2.650
Si		4.000	
Ca		2.000	

Table 14: The GULP energy minimisation results testing the performance of the interatomic potentials in table 13 on the crystal structures used to fit the Si-Cl_s interatomic potential. The terms R_{ij} and N_{ij} denote the nearest neighbour distances and coordination numbers respectively. All of the coordination number values were unchanged.

	$SiCl_4$ [22]	$(SiCl_3)O(SiCl_2)O(SiCl_3)$ [23]	$Si_6O_7Cl_{10}$ [24]	$(Cl_2SiO)_3$ [25]	$(Cl_2SiO)_4$ [25]
	In/out	In/out	In/out	In/out	In/out
R_{Si-O} (Å)		1.60/1.66	1.60/1.63	1.62/1.66	1.58/1.64
N_{Si-O}		1.33	2.33	2.00	2.00
R_{Si-Cl} (Å)	2.01/1.98	2.01/2.01	2.01/2.01	2.00/2.00	1.99/2.01
N_{Si-Cl}	4.00	2.67	1.66	2.00	2.00
R_{O-O} (Å)		2.58/2.48	2.63/2.54	2.61/2.52	2.58/2.50
N_{O-O}		1.00	2.86	2.00	2.00
R_{Cl-O} (Å)		2.96/3.02	2.95/3.03	2.97/3.04	2.93/3.03
N_{Cl-O}		1.25	2.20	2.00	2.00
R_{Cl-Cl} (Å)	3.28/3.24	3.29/3.28	3.27/3.27	3.27/3.27	3.24/3.27
N_{Cl-Cl}	3.00	1.75	0.80	1.00	1.00
R_{Si-Si} (Å)	5.08/5.22	3.10/3.32	3.12/3.21	2.96/3.14	3.12/3.26
N_{Si-Si}	1.00	1.33	2.33	2.00	2.00
Volume (Å^3)	575.73/ 584.26	1340.36/ 1768.65	1030.92/ 1170.62	570.25/ 667.31	392.81/ 418.78

The neutron diffraction and reverse Monte Carlo (RMC) modelling study of liquid $SiCl_4$ by Jóvári *et al.* [26] prompted a liquid $SiCl_4$ simulation in this work to further test the fitted Si-Cl_s interatomic potential parameter. A random starting configuration containing 3000 atoms (600 silicon and 2400 chlorine ions) within a simulation box of side length 48.50Å and so of atomic number density 0.0263$Å^{-3}$ [26] was prepared. Core-shell model interatomic potential parameters were used to estimate rigid-ion interatomic potentials. The rigid-ion stages were run at 6000K, 3000K, 2000K, 1000K, 500K, and then 300K. Each stage comprised of 400,000 time-steps and the time-step was 1fs. A core-shell model stage was then run with the addition of chlorine shells (of mass 1.5u) at 300K. This was above the melting temperature (203K [27]) and ran for 400,000 time-steps where each time-step was 0.1fs. An NVT Berendsen thermostat was used throughout and all stages were fully equilibrated. A universal cut-off of 12.0Å, a primary cut-off of 10.0Å, and a van der Waals cut-off of 8.0Å were applied.

From using RMC modelling, Jóvári *et al.* [26] reports Si-Cl and Cl-Cl nearest neighbour distances of 2.02Å and 3.28Å respectively. Corresponding distances of 2.01Å and 3.27Å respectively were attained in this study. Furthermore, with application of a 3.82Å cut-off distance, Jóvári *et al.* [26] reports a Cl-Cl coordination number of 4.97. By using the same cut-off distance, a Cl-Cl coordination number of 5.02 was achieved in this work. The two sets of computational modelling results were therefore in good agreement.

Since the QCl and ACl glass series also contained calcium, it was important to test the performance of the interatomic potentials in table 13 on crystalline structures containing silicon, oxygen, calcium and chlorine ions. Crystalline $Ca_3Cl_2(SiO_4)$ [28] and $Ca_2(SiO_3Cl_2)$ [29] structures (figure 7) were chosen, and the reasonable results attained following GULP energy minimisation are presented in table 15.

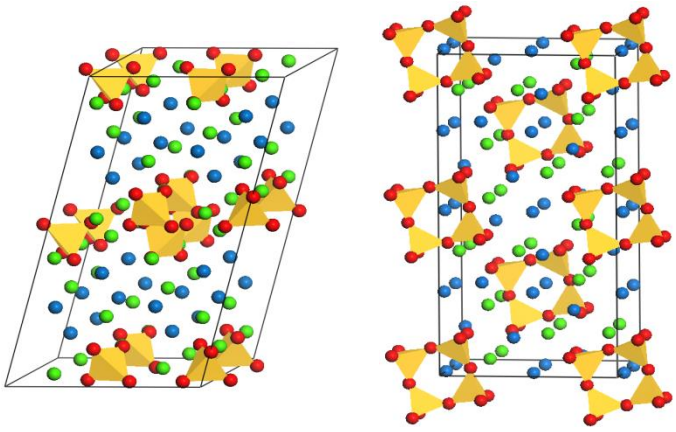

Figure 7: Crystalline structures of $Ca_3Cl_2(SiO_4)$ [28] and $Ca_2(SiO_3Cl_2)$ [29] to the left and right respectively. The yellow tetrahedra represent silicon atoms and the red, green, and blue spheres represent oxygen, calcium, and chlorine ions respectively.

Table 15: GULP energy minimisation results for the $Ca_3Cl_2(SiO_4)$ [28] and $Ca_2(SiO_3Cl_2)$ [29] crystal structures from using the interatomic potential parameters in table 13. The terms R_{ij} and N_{ij} denote the nearest neighbour distances and coordination numbers respectively.

	$Ca_3Cl_2(SiO_4)$ [28]	$Ca_2(SiO_3Cl_2)$ [29]
	In/out	In/out
R_{Si-O} (Å)	1.64/1.63	1.63/1.62
N_{Si-O}	4.00/4.00	4.00/4.00
R_{Ca-O} (Å)	2.39/2.35	2.49/2.51
N_{Ca-O}	4.00/3.33	4.00/4.00
R_{Si-Cl} (Å)	4.36/4.57	3.42/3.63
N_{Si-Cl}	4.00/4.00	1.00/1.00
R_{O-O} (Å)	2.61/2.63	2.65/2.64
N_{O-O}	2.00/2.00	4.00/4.00
R_{Ca-Cl} (Å)	2.93/2.93	2.81/2.87
N_{Ca-Cl}	2.33/2.33	3.00/3.00
R_{Cl-O} (Å)	3.44/3.54	3.29/3.10
N_{Cl-O}	4.00/4.00	5.50/5.50
R_{Cl-Cl} (Å)	3.51/3.52	3.55/3.83
N_{Cl-Cl}	2.00/2.00	4.00/4.00
R_{Si-Ca} (Å)	3.02/3.21	3.21/3.26
N_{Si-Ca}	4.00/4.00	4.00/4.00
R_{Si-Si} (Å)	4.16/4.08	3.23/3.24
N_{Si-Si}	2.00/2.00	2.00/2.00
R_{Ca-Ca} (Å)	3.82/3.80	3.64/3.62
N_{Ca-Ca}	4.00/4.00	1.00/1.00
Volume ($Å^3$)	699.29/749.09	1069.51/1068.23

6.2.4 CaO-SiO_2-$CaCl_2$ System – Glass Modelling

Satisfied with the performance of the interatomic potentials in table 13, attention could turn to modelling the QCl and ACl glasses. As discussed in the previous chapter (section 5.2), the QCl series was able to maintain the equal CaO:SiO_2 ratio in the $(50\text{-}x/2)CaO\text{-}(50\text{-}x/2)SiO_2\text{-}xCaCl_2$ compositions with increasing $CaCl_2$ contributions. The ACl series experienced losses via chlorine volatilisation and the compositions were revised. For simplicity, specific glasses in each series are referred to by their $CaCl_2$ content. For the QCl glasses, the $CaCl_2$ content is denoted as 'x', and for the ACl glasses, the $CaCl_2$ content is denoted as 'y' (tables 16 and 17 respectively).

Table 16: The $CaCl_2$ content (x) in the (50-x/2)CaO-(50-x/2)SiO_2-x$CaCl_2$ compositions as well as the density, number of atoms, and simulation box side lengths used to the model the QCl glass series.

x	CaO	SiO_2	$CaCl_2$	ρ (g/cm^3)	Atoms	Length (Å)
0.0	50.0	50.0	0.0	2.75	10000	51.96
2.2	48.9	48.9	2.2	2.74	10044	52.37
3.3	48.4	48.4	3.3	2.72	10076	52.68
4.3	47.8	47.8	4.3	2.70	10076	52.94
6.6	46.7	46.7	6.6	2.68	10132	53.44
9.3	45.3	45.3	9.3	2.65	10176	54.03
11.9	44.1	44.1	11.9	2.64	10248	54.53
16.1	41.9	41.9	16.1	2.58	10312	55.54
27.4	36.3	36.3	27.4	2.58	10548	57.17
33.5	33.3	33.3	33.5	2.55	10680	58.25
43.1	28.5	28.5	43.1	2.39	10860	60.79

Table 17: The $CaCl_2$ content (y), composition, density, number of atoms, and simulation box side lengths used to the model the ACl glass series.

y	CaO	SiO_2	$CaCl_2$	ρ (g/cm^3)	Atoms	Length (Å)
1.3	50.3	48.4	1.3	2.78	9988	51.96
4.0	49.3	46.7	4.0	2.75	10028	52.57
5.6	49.1	45.3	5.6	2.75	10036	52.81
8.9	47.0	44.1	8.9	2.76	10120	53.25
12.1	46.0	41.9	12.1	2.69	10160	54.18
20.6	43.1	36.3	20.6	2.58	10276	56.17
25.1	41.6	33.3	25.1	2.52	10336	57.25
32.3	39.2	28.5	32.3	2.48	10432	58.55
39.8	36.7	23.5	39.8	2.43	10532	59.96

The QCl and ACl simulations were run in a similar manner to the SiO_2 and CaO-SiO_2 simulations (in sections 6.2.1 and 6.2.2 respectively), with rigid-ion stages being run prior to the core-shell model stages at lower temperatures. Core-shell model interatomic potential parameters (table 13) were used to estimate the rigid-ion interatomic potential parameters. The RI stages included a 6000K stage, a 3000K stage, and a 2000K stage, a quench stage from 2000K to 300K at a rate of 10^{13}K/s, a 300K stage, and a final sampling stage at 300K. The single temperature rigid-ion stages ran for 400,000 time-steps. The quench stage ran for 170,000 time-steps and the time-step was 1fs. Oxygen and chlorine shells were then added to the final configuration of atoms to form the input configuration of atoms for the core-shell model stages.

From the atomic mass of oxygen (15.9994u) and chlorine (35.453u), shell masses of 0.20u and 1.50u respectively were assigned. The core and corresponding shell units were connected by a harmonic spring of spring constant K_{cs} which was frictionally damped using a damping coefficient, c, of 100kgs^{-1} (section 6.2.1). The core-shell model stages began at 2000K. The system was then quenched to 300K at a rate of 10^{13}K/s. A stage at 300K

followed before a sampling stage at 300K was run and used for analysis. The time-step was 0.1fs. To help compensate for the smaller time-step, 800,000 time-steps were used in the single temperature stages. The quench stage required 1,700,000 time-steps. An NVT Berendsen thermostat was used throughout, and all simulation stages were fully equilibrated. A universal cut-off of 12.0Å, a primary cut-off of 10.0Å, and a van der Waals cut-off of 8.0Å were applied.

As with the SiO_2 and $CaO\text{-}SiO_2$ simulations, the system pressures exhibited were problematic. Pressures of around 30kbar were experienced up to x=16.1 in the QCl series, before the pressures declined to 21kbar, 14kbar, and 4kbar in the x=27.4, x=33.5, and x=43.1 compositions respectively. The system densities were subsequently reduced by 5% up to x=16.1, by 2% for x=27.4, and the remaining two compositions (x=33.5, x=43.1) were run using the experimental densities. As the experimental densities of the ACl series were slightly higher, it was appropriate to reduce all composition densities by 5%. The sample compositions, densities, atom numbers, and simulation box side lengths used for modelling the QCl and ACl glasses are detailed in tables 16 and 17 respectively.

6.3 QCl Glass Series Results

6.3.1 Images of Models

The QCl $(50\text{-}x/2)CaO\text{-}(50\text{-}x/2)SiO_2\text{-}xCaCl_2$ glass model images are shown in figure 8. Phase separation appears to begin around x=16.1 (labelled c) and becomes more prevalent with increasing $CaCl_2$ contributions. It can be seen that the models become biphasic, with the two phases being $CaSiO_3$ and $CaCl_2$. Separating the atoms out into their elemental constituents (figure 9) confirms that phase separation occurs by the x=27.4 composition.

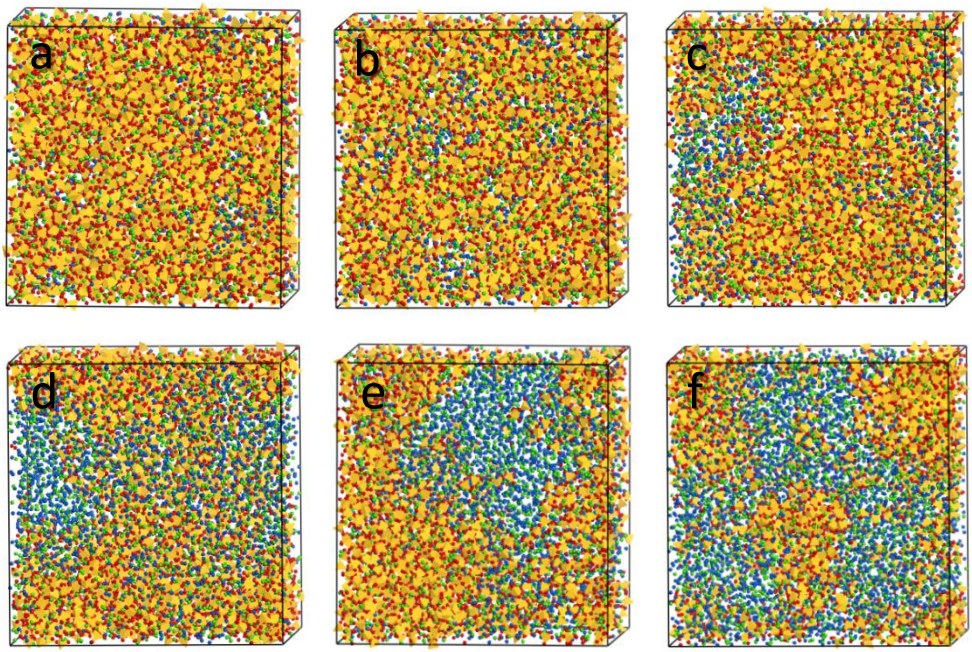

Figure 8: The x=9.3, 11.9, 16.1, 27.4, 33.5, and 43.1 QCl models labelled from 'a' to 'f' respectively. The green, blue, and red spheres represent calcium, chlorine, and oxygen ions respectively. The yellow tetrahedra correspond to silicon ions. Anion shells have not been included.

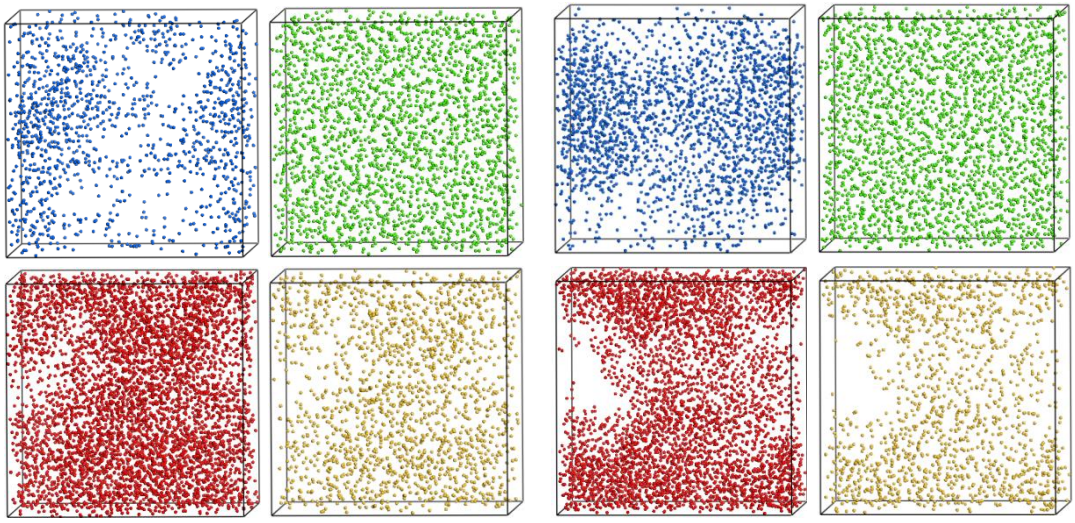

Figure 9: The distribution of chlorine (blue), calcium (green), oxygen (red), and silicon (yellow) ions in the x=16.1 and x=27.4 QCl compositions respectively. Anion shells have not been included.

6.3.2 Pair Correlation Functions

The Si-O, O-O, Si-Si, and Si-Ca pair correlation functions (figure 10) permit the short-range order in the $CaSiO_3$ components of the models to be explored. The Si-O and O-O correlations relate to SiO_4 tetrahedral structural units. The Si-Si correlation relates to the corner-linking of these tetrahedral units. All four pair correlation functions show minimal

change with increasing $CaCl_2$ concentrations, consistent with minimal change to the silicate network. The four pair correlation functions are also consistent with a pure $CaSiO_3$ glass [30].

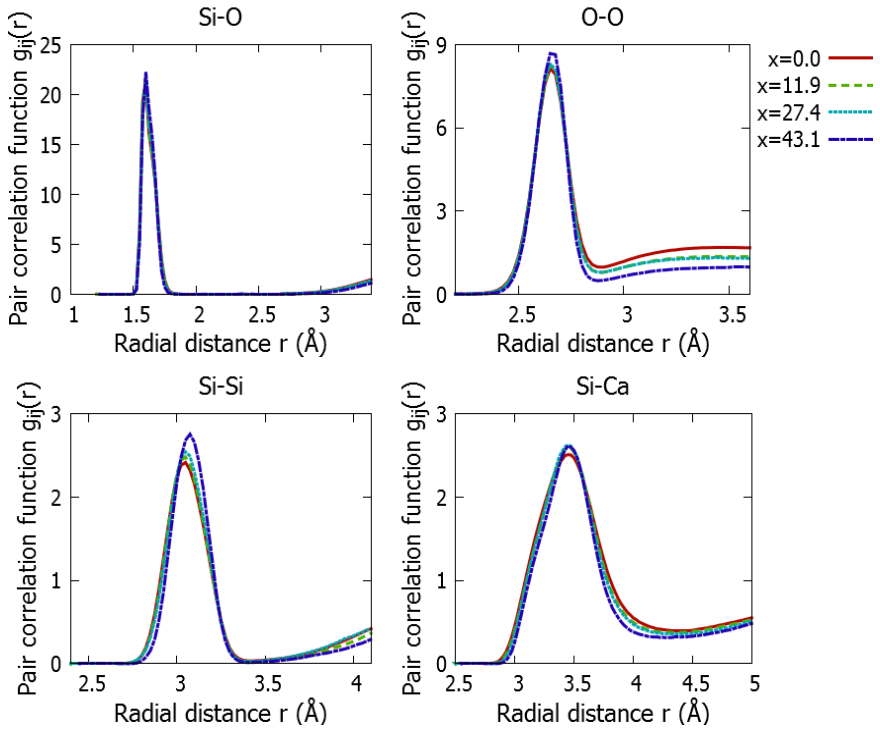

Figure 10: The Si-O, O-O, Si-Si, and Si-Ca pair correlation functions for the x=0.0, 11.9, 27.4, and 43.1 QCl compositions.

The nearest neighbour distances for the Si-O, Si-Si, O-O, Si-Ca, and Ca-O correlations in the QCl series were 1.62±0.01Å, 3.05-3.07Å (±0.01Å), 2.66±0.01Å, 3.44±0.01Å, and 2.36-2.37Å (±0.03Å) respectively. The Si-O coordination number of 4.00±0.01 was maintained using a cut-off distance of 2.00Å. The Si-Si coordination numbers increased from 2.01 to 2.06 (±0.02) with increasing $CaCl_2$ content when a cut-off distance of 3.40Å was used. Conversely, the O-O, Si-Ca, and Ca-O coordination numbers were seen to decrease from 4.37 to 4.19 (±0.03), 6.12 to 5.39 (±0.03), and 6.14 to 2.24 (±0.03) when using cut-off distances of 2.85Å, 4.35Å, and 3.10Å respectively. Details of the other correlations are given in table 18. The large Si-Cl separation distance shows a lack of Si-Cl bonding. Instead, the shorter Ca-Cl distances show that chlorine ions bond with calcium ions. When the Ca-Ca pair correlation functions are plotted (figure 11), a distinct shape change is observed, most notably between the x=16.1 and the x=27.4 plots.

Table 18: Nearest neighbour distance, R_{ij}, and coordination number, $N_{ij}(r)$, values for the Ca-Cl, Cl-Cl, Cl-O, Ca-Ca, and Si-Cl correlations. Cut-off distances of 3.70Å, 4.90Å, 4.70Å, 5.25Å, and 5.65Å were applied respectively to attain the coordination numbers.

	Ca-Cl		Cl-Cl		O-Cl		Ca-Ca		Si-Cl	
x	R_{ij} (Å) ±0.01	$N_{ij}(r)$ ±0.05	R_{ij} (Å) ±0.05	$N_{ij}(r)$ ±0.10	R_{ij} (Å) ±0.10	$N_{ij}(r)$ ±0.10	R_{ij} (Å) ±0.05	$N_{ij}(r)$ ±0.05	R_{ij} (Å) ±0.10	$N_{ij}(r)$ ±0.10
0.0							3.90	7.47		
2.2	2.81	0.36	3.55	1.04	3.78	0.45	3.93	7.55	4.59	0.87
3.3	2.81	0.52	3.54	1.85	3.79	0.63	3.97	7.63	4.60	1.22
4.3	2.81	0.67	3.57	2.50	3.79	0.78	4.05	7.61	4.61	1.52
6.6	2.80	0.99	3.59	3.54	3.80	1.08	4.11	7.63	4.63	2.10
9.3	2.79	1.33	3.61	4.84	3.79	1.31	4.20	7.63	4.65	2.58
11.9	2.78	1.62	3.63	5.72	3.77	1.51	4.37	7.72	4.62	2.96
16.1	2.78	2.08	3.65	6.97	3.78	1.68	4.48	7.72	4.63	3.44
27.4	2.77	3.20	3.61	9.40	3.77	1.83	4.56	8.25	4.61	3.70
33.5	2.77	3.68	3.62	9.88	3.75	2.01	4.60	8.41	4.63	3.75
43.0	2.77	4.22	3.73	9.52	3.79	3.01	4.69	8.08	4.67	5.72

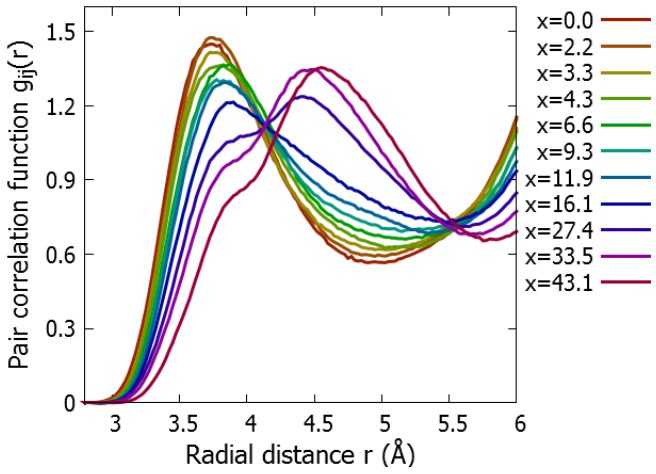

Figure 11: The Ca-Ca pair correlation functions for the QCl series.

6.3.3 Structure Factors

The changes in the calculated total neutron and X-ray structure factors with increasing $CaCl_2$ content are shown for the QCl series in figure 12. These changes occur because as the chlorine and calcium concentration increases, the silicon and oxygen concentrations decrease. As shown in figure 13, the changes are predominantly brought about by changes in the O-O, Cl-O, and Cl-Cl partial structure factors. The sharp vertical lines illustrated to the right of figure 12 at low values of Q indicate phase separation, and occur in and beyond the x=16.1 composition.

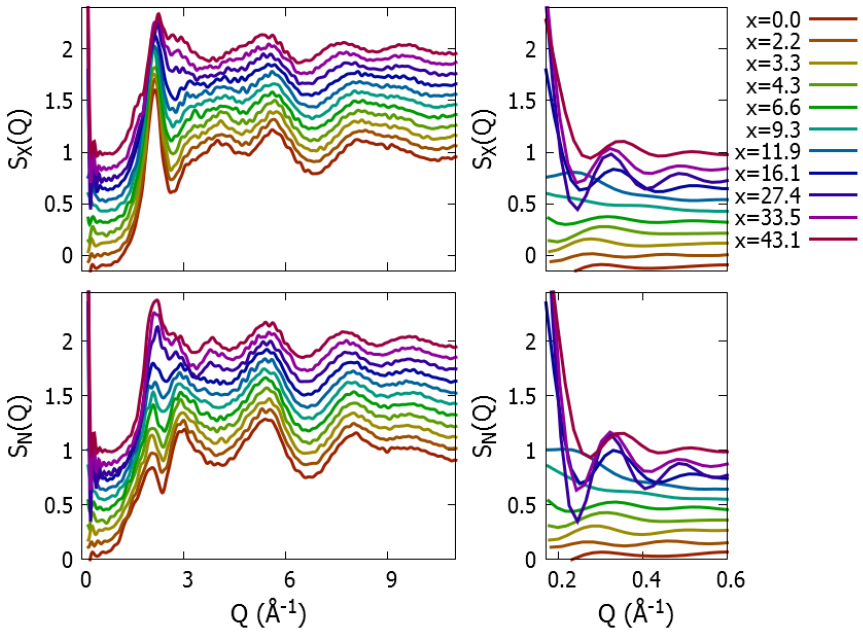

Figure 12: Simulated total X-ray ($S_X(Q)$) and neutron ($S_N(Q)$) structure factor spectra for the QCl compositions in table 16. The plots to the left cover scattering vector (Q) magnitudes from 0Å^{-1} to 10Å^{-1}, while the plots to the right cover Q values from 0.17Å^{-1} to 0.60Å^{-1}. The plots are progressively offset from x=0.0 by 0.1 upwards.

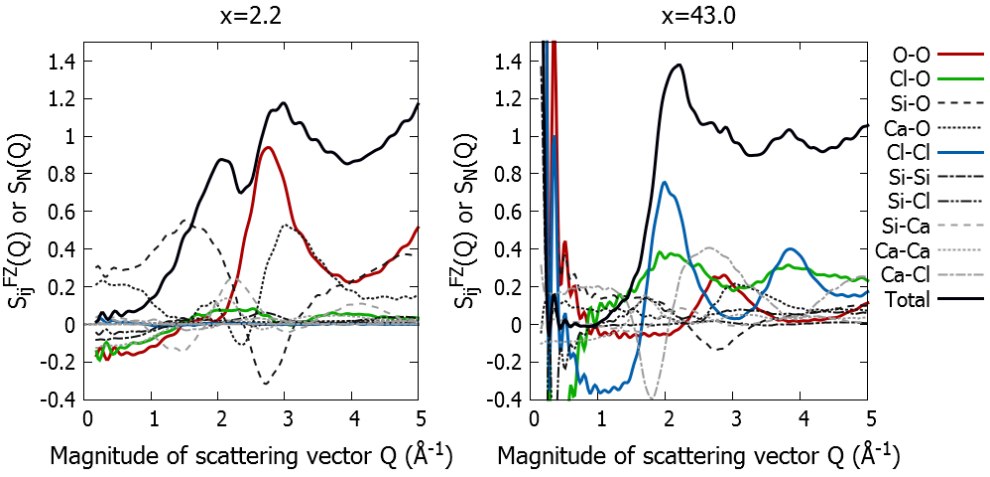

Figure 13: Partial Faber-Ziman neutron structure factors ($S_{ij}^{FZ}(Q)$) and total neutron structure factors ($S_N(Q)$) for the x=2.2 (left) and x=43.0 (right) QCl glass models.

6.3.4 Silicon Network Connectivity

The average silicon network connectivity values, Q^n, for the QCl series are shown in table 19. The Q^n values were also predicted using the equation n=-2a+8, where the terms 'n' and 'a' refer to the connectivity, and to O:Si ratio excluding free oxygens respectively. Free oxygens are oxygen ions that are neither bridging nor non-bridging. As shown in table 19, the actual and predicted Q^n values were in good agreement, and a connectivity of 2.00 corresponds to a metasilicate glass with an equal $CaO:SiO_2$ ratio. The x=27.4, x=33.5, and

x=43.1 models have average silicon network connectivity values that are greater than 2.00 due to the presence of free oxygens. The reason for this is unclear.

Table 19: The Q^n distributions for each of the QCl glass compositions. The average and predicted Q^n values are also stated. The uncertainty in the average Q^n values was ±2%.

x	Si atoms	Q^0 (%)	Q^1 (%)	Q^2 (%)	Q^3 (%)	Q^4 (%)	Average Q^n	Predicted Q^n
0.0	2000	1.55	22.90	50.80	23.45	1.30	2.00	2.00
2.2	1956	1.64	23.01	50.41	23.47	1.48	2.00	2.00
3.3	1936	1.19	22.52	52.89	21.59	1.81	2.00	2.00
4.3	1912	1.52	23.27	50.58	22.75	1.88	2.00	2.00
6.6	1868	1.50	22.16	53.05	21.47	1.82	2.00	2.00
9.3	1812	1.60	22.41	51.43	23.29	1.27	2.00	2.00
11.9	1764	1.53	22.11	52.78	21.66	1.93	2.00	2.00
16.1	1676	2.09	22.26	50.89	22.55	2.21	2.00	2.00
27.4	1452	2.89	21.49	48.07	25.21	2.34	2.03	2.02
33.5	1332	2.63	22.45	45.12	27.40	2.40	2.05	2.04
43.0	1140	3.77	20.00	47.02	26.58	2.63	2.04	2.04

6.4 ACl Glass Series Results

6.4.1 Images of Models

Images of the last six ACl computational models (y=8.9 onwards) are shown in figure 14. The models indicate that phase separation first occurs between the y=12.1 and y=20.6 models (labelled b and c respectively). This result is consistent with phase separation occurring around x=16.1 in the QCl series. The distribution of atomic constituents in figure 15 corroborates with this finding.

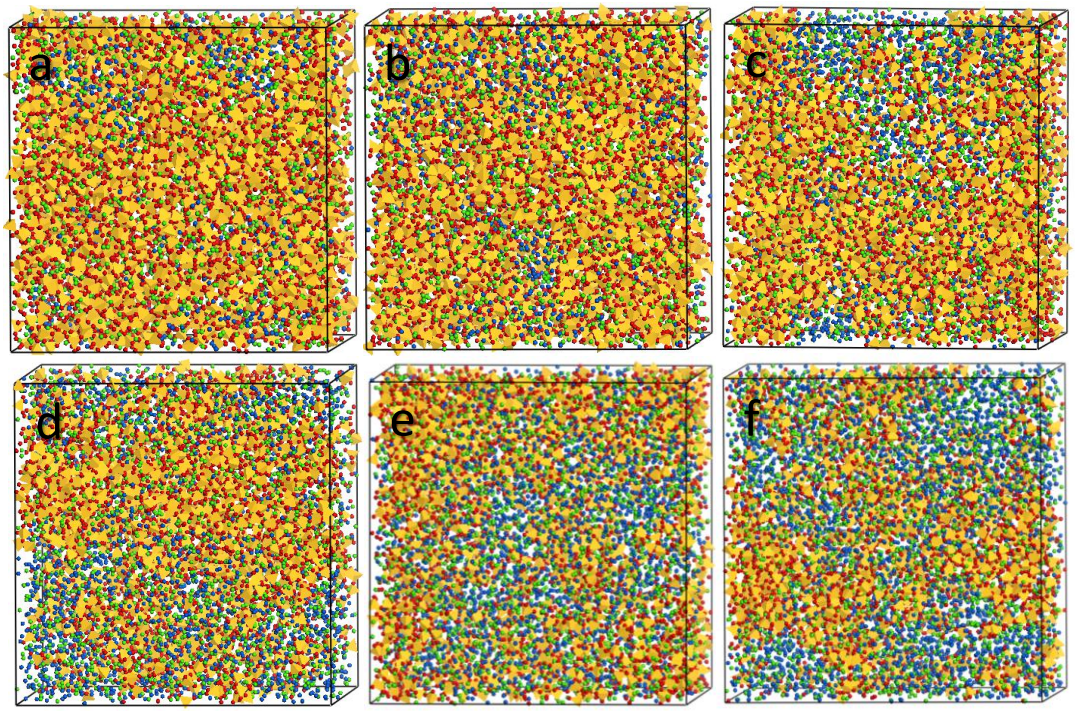

Figure 14: The y=8.9, 12.1, 20.6, 25.1, 32.3, and 39.8 ACl models labelled from 'a' to 'f' respectively. The green, blue, and red spheres represent calcium, chlorine, and oxygen ions respectively. The yellow tetrahedra correspond to silicon ions. Anion shells have not been included.

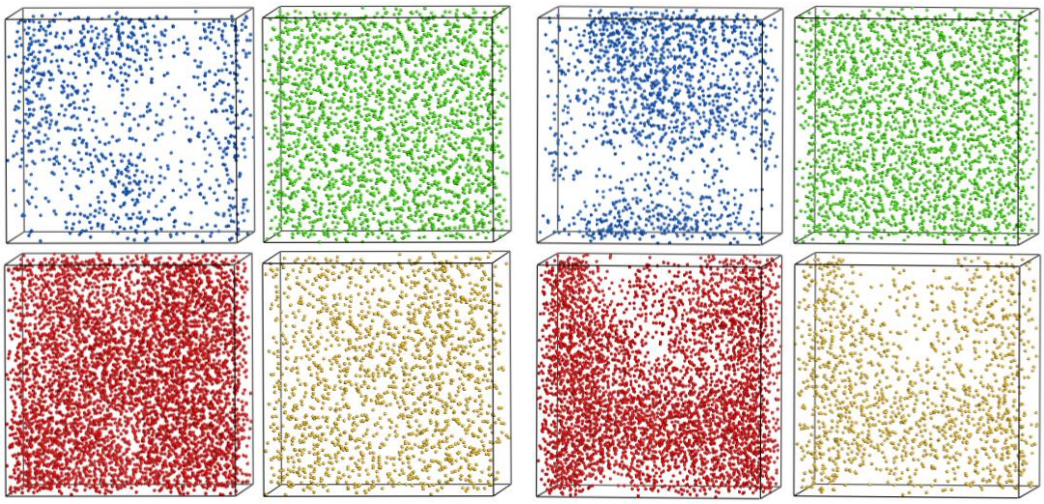

Figure 15: The distribution of chlorine (blue), calcium (green), oxygen (red), and silicon (yellow) ions in the y=12.1 and y=20.6 ACl compositions respectively. Anion shells have not been included.

6.4.2 Pair Correlation Functions

The Si-O and O-O pair correlation functions help describe SiO_4 tetrahedral structural units. It can be seen in figure 16 that these structural units were maintained, and that the Si-O and O-O nearest neighbour distances of 1.62±0.01Å and 2.66±0.01Å respectively were unchanged. However, changes in the Si-Si and Si-Ca pair correlation functions with increasing $CaCl_2$ contributions (figure 16) were consistent with disruption to the silicate network. The Si-Si separation distance increased from 3.06Å to 3.09Å (±0.01Å), and the Si-Ca nearest neighbour distances reduced from 3.44Å to 3.40Å (±0.01Å) with increasing $CaCl_2$ content. Small reductions in the Ca-O nearest neighbour distances from 2.37Å to 2.34Å (±0.01Å) were also observed.

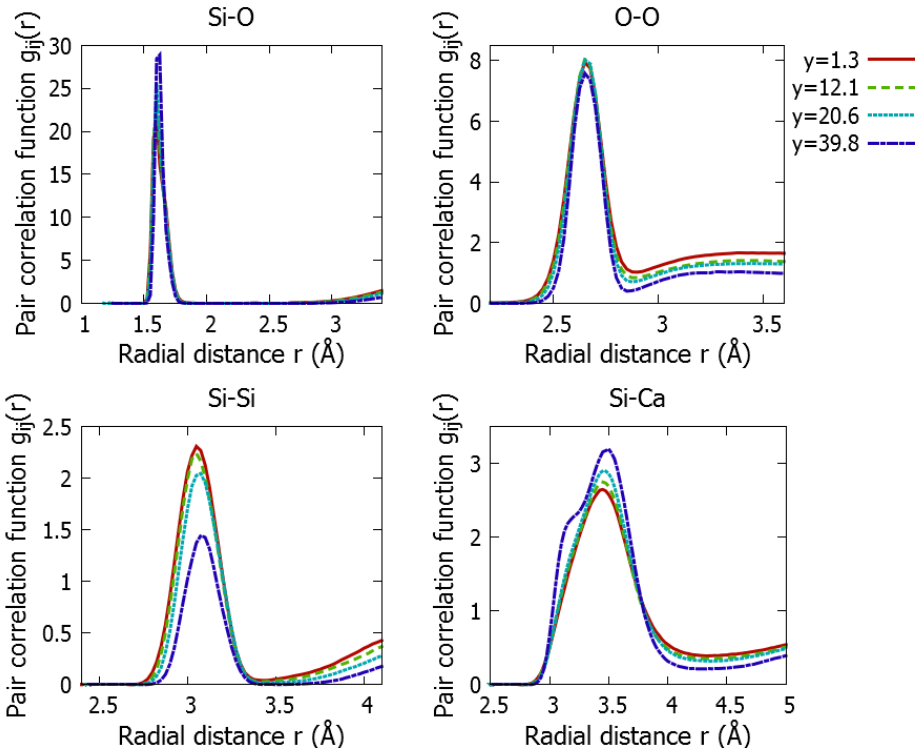

Figure 16: The Si-O, O-O, Si-Si, and Si-Ca pair correlation functions for the y=1.3, 12.1, 20.6, and 39.8 ACl compositions.

As expected, the Si-O coordination numbers were unchanged with values of 4.00±0.01 when a 2.00Å cut-off distance was used, consistent with tetrahedral structural units. The O-O and Si-Si coordination numbers declined markedly with increasing $CaCl_2$ content from 4.34 to 3.50 (±0.03) and from 1.94 to 1.07 (±0.02) when using 2.85Å and 3.40Å cut-off distances respectively. The Si-Ca coordination number increased from 6.33 to 7.03 (±0.03) using a 4.35Å cut-off, and the Ca-O coordination numbers decreased from 6.01 to 2.66 (±0.03) using a 3.10Å cut-off. Details of the other correlations in the ACl glass models are provided in table 20. The large Si-Cl nearest neighbour distances showed a lack of Si-Cl

bonding. The shorter Ca-Cl nearest neighbour distances revealed that chlorine ions bond with calcium ions. The changing shape of the Ca-Ca pair correlation function (figure 17) with increasing $CaCl_2$ contributions helps visualise the significant changes in Ca-Ca nearest neighbour distance.

Table 20: Nearest neighbour distance (R_{ij}) and coordination number ($N_{ij}(r)$) values for the Ca-Cl, Cl-Cl, Cl-O, Ca-Ca, and Si-Cl correlations in the ACl models. Cut-off distances of 3.70Å, 4.90Å, 4.70Å, 5.25Å, and 5.65Å were applied to obtain the coordination number values respectively.

	Ca-Cl		Cl-Cl		Cl-O		Ca-Ca		Si-Cl	
y	R_{ij} (Å) ±0.01	$N_{ij}(r)$ ±0.05	R_{ij} (Å) ±0.05	$N_{ij}(r)$ ±0.10	R_{ij} (Å) ±0.10	$N_{ij}(r)$ ±0.10	R_{ij} (Å) ±0.05	$N_{ij}(r)$ ±0.05	R_{ij} (Å) ±0.10	$N_{ij}(r)$ ±0.10
1.3	2.82	0.22	3.38	0.67	3.76	15.66	3.90	7.73	4.54	0.54
4.0	2.80	0.64	3.46	1.89	3.77	13.94	3.96	7.84	4.58	1.53
5.6	2.79	0.86	3.55	3.01	3.75	12.51	4.01	8.04	4.60	1.95
8.9	2.78	1.30	3.57	5.11	3.75	9.63	4.13	8.12	4.58	2.47
12.1	2.78	1.66	3.59	5.81	3.77	8.43	4.37	8.17	4.59	3.05
20.6	2.78	2.43	3.64	7.80	3.77	5.46	4.48	8.36	4.58	3.78
25.1	2.78	2.79	3.68	7.89	3.79	5.22	4.51	8.41	4.66	4.81
32.3	2.78	3.30	3.68	8.66	3.79	4.15	4.56	8.61	4.68	5.55
39.8	2.77	3.79	3.68	8.89	3.80	3.76	4.60	8.76	4.68	7.10

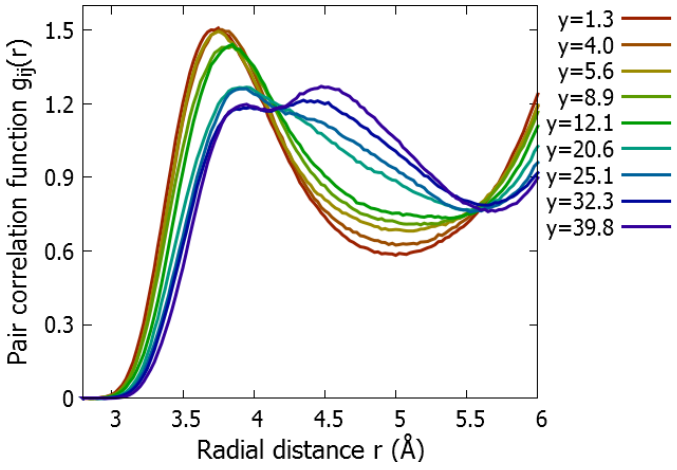

Figure 17: The Ca-Ca pair correlation functions for the ACl glass models.

6.4.3 Structure Factors

As shown in figure 18, the calculated total neutron and X-ray structure factors for the ACl glass series exhibited distinct changes in shape with increasing $CaCl_2$ content. This was predominantly caused by changes in the O-O, Cl-O, and Cl-Cl partial structure factors. The sharp vertical lines at low values of Q (illustrated to the right of figure 18) were indicative of phase separation and were first observed around y=12.1.

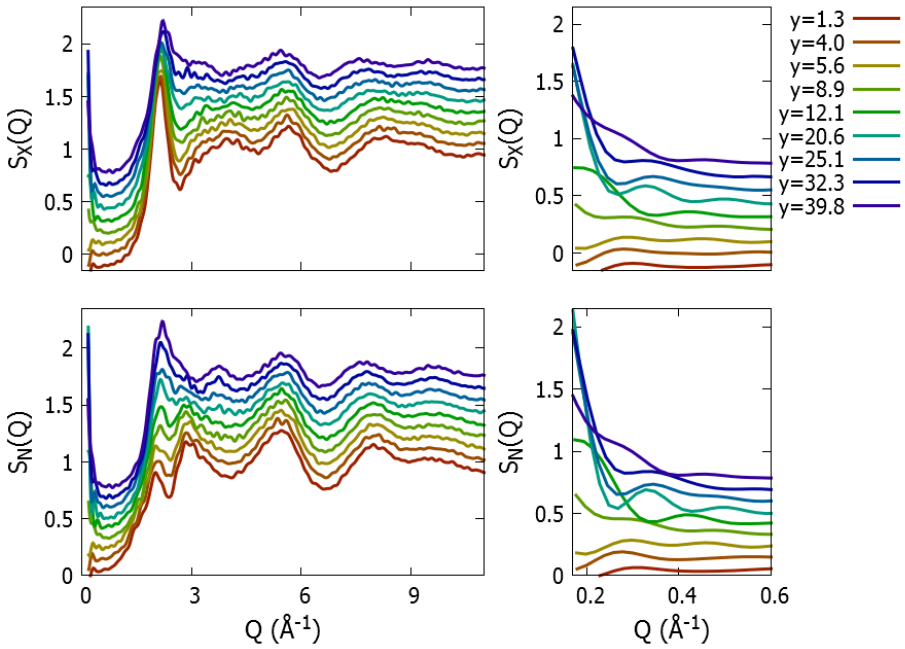

Figure 18: Simulated total X-ray ($S_x(Q)$) and neutron ($S_N(Q)$) structure factor spectra for the ACl compositions in table 17. The plots to the left cover scattering vector magnitudes (Q) from 0Å^{-1} to 10Å^{-1}, while the plots to the right cover Q values from 0.17Å^{-1} to 0.60Å^{-1}. The plots are progressively offset from y=1.3 by 0.1 upwards.

6.4.4 Silicon Network Connectivity

The silicon network connectivity (Q^n) distributions for the ACl series are quantified in table 21. A rise in the number of Q^0 and Q^1 species, and fall in the number of Q^2, Q^3, and Q^4 species (as illustrated in figure 19) caused the average Q^n values in the glass models to decline. The average Q^n values were also predicted using the equation n=-2a+8, where the terms 'n' and 'a' are the connectivity and O:Si ratio (excluding free oxygens) respectively. The average and predicted Q^n values were in close agreement. The most noticeable change in Q^n occurred between the y=12.1 and the y=20.6 compositions.

Table 21: The Q^n distributions for each of the ACl glass compositions. The average and predicted Q^n values are also stated. The uncertainty in the average Q^n values was ±2%.

y	Si atoms	Q^0 (%)	Q^1 (%)	Q^2 (%)	Q^3 (%)	Q^4 (%)	Average Q^n	Predicted Q^n
1.3	1936	1.96	25.57	52.17	18.44	1.86	1.93	1.92
4.0	1868	2.52	26.55	50.96	19.06	0.91	1.89	1.89
5.6	1812	2.43	31.51	48.12	16.11	1.82	1.83	1.83
8.9	1764	2.95	27.66	49.60	18.82	0.96	1.87	1.87
12.1	1676	3.34	31.38	47.20	16.59	1.49	1.82	1.81
20.6	1452	5.72	38.09	42.70	12.74	0.76	1.65	1.65
25.1	1332	8.48	39.64	42.12	9.23	0.53	1.54	1.54
32.3	1140	14.30	44.39	36.32	4.74	0.26	1.32	1.32
39.8	940	24.79	48.30	22.45	4.47	0.00	1.07	1.07

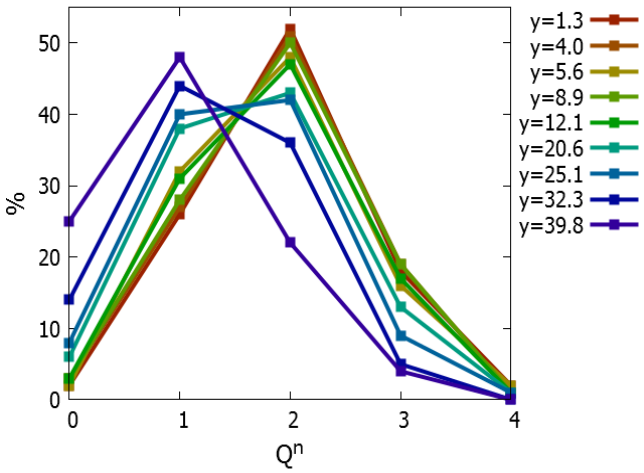

Figure 19: The Q^n distribution for the ACl glass series.

6.5 Discussion

In this chapter, the QCl and ACl glass compositions were modelled computationally using classical molecular dynamics with the addition of the adiabatic core-shell model. The Si-Cl nearest neighbour distances of ~4.6Å established an absence of Si-Cl bonding. The shorter Ca-Cl nearest neighbour distances of ~2.8Å (tables 18 and 20) elucidated that chlorine ions bond with calcium ions. Both the QCl and ACl glass models (figures 8 and 14) were seen to become phase separated with increasing $CaCl_2$ content to form biphasic systems. For the QCl series, these two phases were $CaSiO_3$ and $CaCl_2$. As discussed in the previous chapter, the ACl series contained excess CaO (figure 20). This was because the ACl series had exhibited losses due to chlorine volatilisation as HCl. As a consequence, the two phases were a calcium silicate phase and a $CaCl_2$ phase. Phase separation was first identified between x=16.1 and x=27.4 in the QCl series, and between y=12.1 and y=20.6 in the ACl series. Experimentally, Chen [1] observed a change in the linear relationship of density, molar volume, and first crystallisation temperature with increasing $CaCl_2$ content between x=16.1 and x=27.4 in the QCl series.

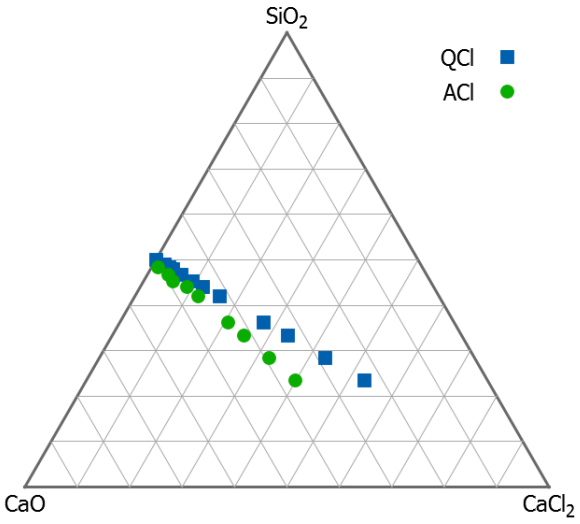

Figure 20: Ternary plot showing the QCl and ACl glass compositions.

Not only was phase separation evident in the glass model images, but it was also apparent in the pair correlation functions. The Ca-Ca pair correlation functions exhibited a distinct change in shape with increasing $CaCl_2$ content (figures 11 and 17). This was because calcium was present in both phases of the QCl glass series, and in both phases of the ACl glass series. When the glasses contained small amounts of $CaCl_2$, the calcium silicate phase dominated. This caused the Ca-Ca nearest neighbour distances (3.90Å) to be comparable to those in crystalline $CaSiO_3$ (3.65Å [15]). As the $CaCl_2$ contribution increased (4.60Å), the $CaCl_2$ phase gained dominance. Consequently, the Ca-Ca nearest neighbour distances increased to become more comparable to those in crystalline $CaCl_2$ (4.20Å [31]). The difference in Ca-Ca nearest neighbour distance between the crystal structures and the glass models was in part caused by the structural disorder in the glasses. Further differences were caused by accounting for the asymmetry in the Ca-Ca pair correlation functions when determining the values of nearest neighbour distance. The differences would have been reduced by not taking the asymmetry of the Ca-Ca pair correlation function into account.

In addition to the Ca-Ca nearest neighbour distances increasing with growing $CaCl_2$ contributions, the Cl-Cl nearest neighbour distances also increased. This was despite the increasing proportion of calcium and chlorine ions. This was indicative of a tendency towards phase separation, even in the glass models containing small amounts of $CaCl_2$. Figures 21 and 22 below show the pair correlation functions involving chlorine ions in the QCl and ACl series respectively. The corresponding average pair correlation function values expected at a relatively large distance of 10Å have been added as dots for reference. Each of the Ca-Cl pair correlation functions passes through the corresponding dot because calcium is present in both phases of the glass. However, while the Cl-Cl pair correlation functions have an increasing tendency to surpass the expected average pair correlation function values, the Si-Cl and O-Cl pair correlation functions seem to increasingly

underestimate the expected average pair correlation function values. This is due to chlorine ions becoming increasingly concentrated in the $CaCl_2$ phase, while the silicon and oxygen ions become increasingly concentrated in the calcium silicate phase. Therefore, the pair correlation functions involving chlorine can be used to more closely identify when phase separation first occurs. For the QCl and ACl series, deviations from the expected average pair correlation function values were first observed in the x=6.6 and y=8.9 models respectively. This finding indicates that the higher proportion of CaO in the ACl glasses slows the proliferation of phase separation.

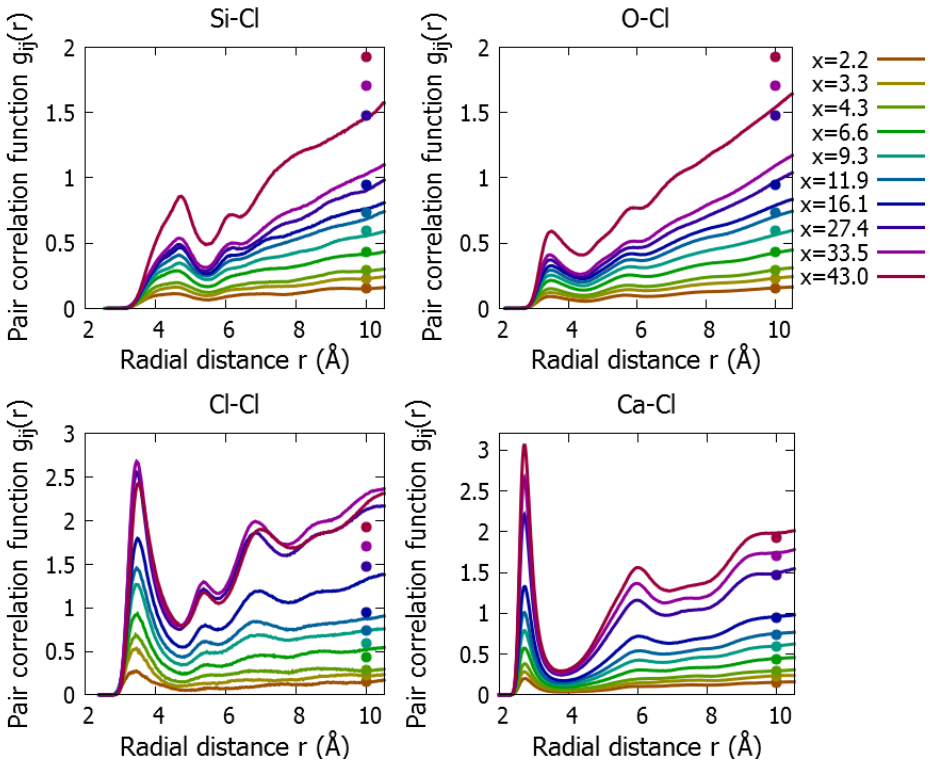

Figure 21: The Si-Cl, O-Cl, Cl-Cl, and Ca-Cl pair correlation functions for the QCl series. Dots corresponding to the expected average pair correlation function values at a distance of 10Å have been added.

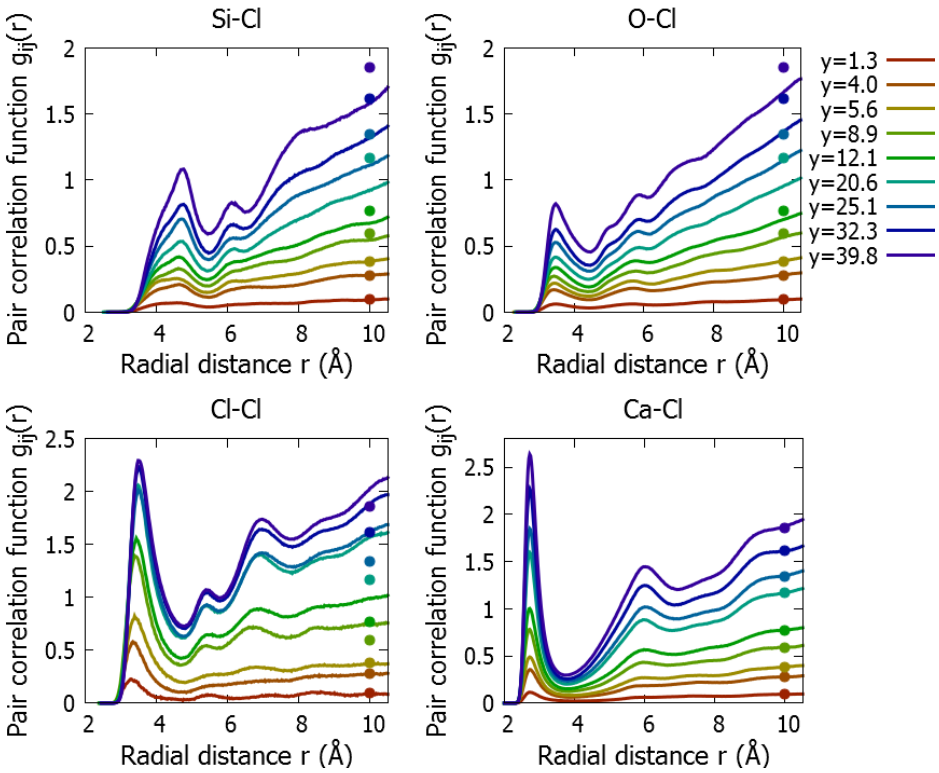

Figure 22: The Si-Cl, O-Cl, Cl-Cl, and Ca-Cl pair correlation functions for the ACl series. Dots corresponding to the expected average pair correlation function values at a distance of 10Å have been added.

The x=33.5 and y=32.3 phase separated models provide a point of close comparison between the two glass series. Through comparing their Ca-Ca pair correlation functions in figures 11 and 17 respectively, it can be seen that the x=33.5 model is more phase separated than the y=32.3 model. The x=33.5 model is also more phase separated than the y=39.8 model (which contains more $CaCl_2$). This confirms that the higher CaO content in the ACl glass series slows the proliferation of phase separation. This is caused by the excess CaO disrupting the silicate network. As shown in figure 23, the silicon network connectivity (Q^n) distributions differed greatly between the QCl and ACl series. While the average Q^n values in the QCl series were close to 2.00, the average Q^n values in the ACl series continually declined with increasing $CaCl_2$ content. Furthermore, the Si-Si coordination numbers (which relate to the corner sharing of SiO_4 tetrahedra) for the QCl series increased modestly from 2.01 to 2.06 (±0.02), while a sharp decrease from 1.94 to 1.07 (±0.02) was observed in the ACl series with increasing $CaCl_2$ content.

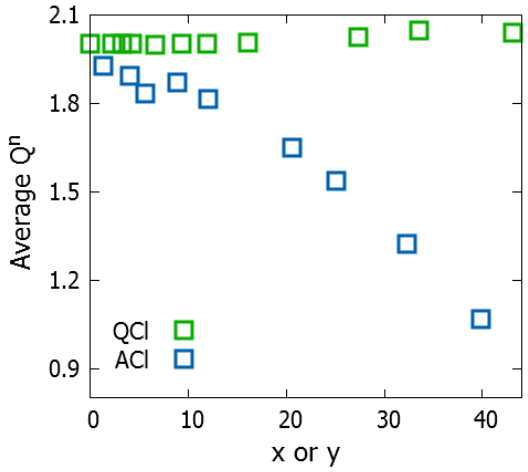

Figure 23: A comparison of the average Q^n values in the ACl and QCl glass models. The uncertainty in the average Q^n values is ±2%.

After identifying the presence of phase separation in the computational models, it is of interest to quantify its scale. The scale of the phase separated regions in the QCl and ACl glass models can be approximated from the computed total structure factors according to $\frac{2\pi}{Q}$, where Q is the magnitude of the scattering vector. Based on the Q range of 0.2Å^{-1} to 0.6Å^{-1} in the total structure factors (vertical lines shown to the right of figures 12 and 18), the scale of phase separation was on the order of 10Å to 30Å. However, simulation cell side lengths of up to only 60Å were used in this work. The limited system sizes that can be modelled computationally are insufficient to determine the actual scale of phase separation. Small angle neutron or small angle X-ray scattering experiments (SANS and SAXS respectively) may be appropriate for determining the scale of phase separation.

6.6 Conclusion

To help elucidate the structure of complex chlorine-containing bioactive glasses, it is first important to comprehend less complex systems. This chapter investigated the structure of CaO-SiO_2-$CaCl_2$ glasses computationally using classical molecular dynamics with the addition of the adiabatic core-shell model for the first time. Chlorine ions were found to bond with calcium ions and no Si-Cl bonding was observed. By increasing the $CaCl_2$ content in the glass models, the models became phase separated to form biphasic systems. The two phases included a calcium silicate phase and a $CaCl_2$ phase. By studying the pair correlation functions involving chlorine ions, it was evident that there was a tendency towards phase separation, even in models containing small amounts of $CaCl_2$. The excess CaO in the ACl glass series disrupted the silicate network and slowed the proliferation of phase separation.

6.7 References

[1] X. Chen, “Novel Halide Containing Bioactive Glasses,” Queen Mary University of London, 2015.

[2] X. Chen, N. Karpukhina, D. S. Brauer, and R. G. Hill, “Novel Highly Degradable Chloride Containing Bioactive Glasses,” *Biomed. Glas.*, vol. 1, no. 1, pp. 108–118, 2015.

[3] G. Malavasi, A. Pedone, and M. C. Menziani, “Study of the Structural Role of Gallium and Aluminum in 45S5 Bioactive Glasses by Molecular Dynamics Simulations,” *J. Phys. Chem. B*, vol. 117, no. 15, pp. 4142–4150, 2013.

[4] G. S. Smith and L. E. Alexander, “Refinement of the atomic parameters of α-quartz,” *Acta Crystallogr.*, vol. 16, no. 6, pp. 462–471, 1963.

[5] J. D. Gale, “GULP: A computer program for the symmetry-adapted simulation of solids,” *J. Chem. Soc. Faraday Trans.*, vol. 93, no. 4, pp. 629–637, 1997.

[6] A. Tilocca, N. H. De Leeuw, and A. N. Cormack, “Shell-model molecular dynamics calculations of modified silicate glasses,” *Phys. Rev. B - Condens. Matter Mater. Phys.*, vol. 73, pp. 1–14, 2006.

[7] R. I. Ainsworth, D. Di Tommaso, J. K. Christie, and N. H. de Leeuw, “Polarizable force field development and molecular dynamics study of phosphate-based glasses.,” *J. Chem. Phys.*, vol. 137, p. 234502, 2012.

[8] A. Tilocca, “Private communication.” 2015.

[9] D. Teter, “Private communication.” 2004.

[10] D. I. Grimley, A. C. Wright, and R. N. Sinclair, “Neutron scattering from vitreous silica IV. Time-of-flight diffraction,” *J. Non. Cryst. Solids*, vol. 119, no. 1, pp. 49–64, 1990.

[11] J. Neuefeind and K. D. Liss, “Bond angle distribution in amorphous germania and silica,” *Ber. Bunsenges. Phys. Chem.*, vol. 100, p. 1341, 1996.

[12] P. Johnson, A. Wright, and R. Sinclair, “Neutron scattering from vitreous silica II. Twin-axis diffraction experiments,” *J. Non. Cryst. Solids*, vol. 58, pp. 109–130, 1983.

[13] J. A. L. Rabone and N. H. De Leeuw, “Interatomic potential models for natural apatite crystals: incorporating strontium and the lanthanides,” *J. Comput. Chem.*, vol. 27, no. 2, pp. 253–266, 2006.

[14] C. H. Shen, R. S. Liu, J. G. Lin, and C. Y. Huang, “Phase stability study of $La_{1.2}Ca_{1.8}Mn_2O_7$,” *Mater. Res. Bull.*, vol. 36, pp. 1139–1148, 2001.

[15] Y. Ohashi, “Polysynthetically-twinned structures of enstatite and wollastonite,” *Phys. Chem. Miner.*, vol. 10, pp. 217–229, 1984.

[16] H. Doweidar, “Density-structure correlations in silicate glasses,” *J. Non. Cryst. Solids*, vol. 249, no. 2–3, pp. 194–200, 1999.

[17] T. Taniguchi, M. Okuno, and T. Matsumoto, “X-ray diffraction and EXAFS studies of silicate glasses containing Mg, Ca and Ba atoms,” *J. Non. Cryst. Solids*, vol. 211, no.

1–2, pp. 56–63, 1997.

[18] V. R. Mastelaro, E. D. Zanotto, N. Lequeux, and R. Cortès, “Relationship between short-range order and ease of nucleation in $Na_2Ca_2Si_3O_9$, $CaSiO_3$ and $PbSiO_3$ glasses,” *J. Non. Cryst. Solids*, vol. 262, no. 1, pp. 191–199, 2000.

[19] P. H. Gaskell, M. C. Eckersley, A. C. Barnes, and P. Chieux, “Medium-range order in the cation distribution of a calcium silicate glass,” *Nature*, vol. 350, no. 6320, pp. 675–677, 1991.

[20] P. Zhang, P. J. Grandinetti, and J. F. Stebbins, “Anionic Species Determination in $CaSiO_3$ Glass Using Two-Dimensional ^{29}Si NMR,” *J. Phys. Chem. B*, vol. 101, no. 20, pp. 4004–4008, 1997.

[21] K. W. Toernroos, G. Calzaferri, and R. Imhof, “Octachlorosilasesquioxane, $Cl_8Si_8O_{12}$,” *Acta Crystallogr. Sect. C Cryst. Struct. Commun.*, vol. 51, pp. 1732–1735, 1995.

[22] L. N. Zakharov, M. Y. Antipin, Y. T. Struchkov, A. V. Gusev, A. M. Gibin, and N. V. Zhernenkov, “Molecular and crystal structures of $SiCl_4$ at 163 K,” *Kristallografiya*, vol. 31, pp. 171–172, 1986.

[23] K. M. Jöllenbeck and J. U. Weidner, “Rontgenstrukturuntersuchung des flussigen Silicium- , Germanium- und Zinntetrachlorids . Ein Beitrag zur Frage einer gemeinsamen Fliissigkeitsstruktur . II . Bestimmung der individuellen partiellen Paarkorrelationsfunktionen. Vorschlag eines einheitlichen,” *Berichte der Bunsengesellschaft für Phys. Chemie*, vol. 91, no. 17, pp. 17–24, 1987.

[24] M. Binnewies and J. Magull, “Crystal structure of decachloro-bicyclo(5.5.1) heptaoxatridecasilane, $Si_6O_7Cl_{10}$,” *Zeitschrift fuer Krist. - New Cryst. Struct.*, vol. 217, pp. 325–326, 2002.

[25] U. Wannagat *et al.*, “Das Isosterenpaar SiO/PN,I. Zur Isosterie von Perchlorcyclophosphaze Schwingungsspektren und Roentgenstruktrukturanalyse von $(Cl_2SiO)_3$ und $(Cl_2SiO)_4$,” *Zeitschrift fuer Naturforschung, B Chem. Sci.*, vol. 46, pp. 931–940, 1991.

[26] P. Jóvári, G. Mészáros, L. Pusztai, and E. Sváb, “The structure of liquid tetrachlorides CCl_4, $SiCl_4$, $GeCl_4$, $TiCl_4$, VCl_4, and $SnCl_4$,” *J. Chem. Phys.*, vol. 114, no. 18, pp. 8082–8090, 2001.

[27] S. Budavari, *The Merck Index - An Encyclopedia of Chemicals, Drugs, and Biologicals*. Whitehouse Station, NJ: Merck and Co., 1996.

[28] E. N. Treushnikov, V. V. Ilyukhin, and N. V. Belov, “Crystal structure of metastable phase of cement clinker of Ca-chloride orthosilicate $Ca_3(SiO_4)$ Cl_2,” *Dokl. Akad. Nauk SSSR*, vol. 193, pp. 1048–1051, 1970.

[29] N. I. Golovastikov and V. F. Kazak, “Crystal-Structure of Calcium Chlorosilicate $Ca_2SiO_3Cl_2$,” *Kristallografiya*, vol. 22, no. 5, pp. 962–965, 1977.

[30] Y. Ohashi, “Polysynthetically-twinned structures of enstatite and wollastonite,” *Phys. Chem. Miner.*, vol. 10, no. 5, pp. 217–229, 1984.

[31] W. R. Busing, “An interpretation of the structures of alkaline earth chlorides in terms

of interionic forces," *Trans. Am. Crystallogr. Assoc.*, vol. 6, pp. 57–72, 1970.

[32] G. Mountjoy, "No Title," *SRS Experimental Reports; Daresbury Laboratory: Warrington; RB42218*. 2005.

7. An Experimental Investigation of the Structure of $CaO\text{-}SiO_2\text{-}CaF_2$ Glasses

7.1 Introduction

The archetypal bioactive glass 45S5 ($26.91CaO\text{-}46.13SiO_2\text{-}24.35Na_2O\text{-}2.60P_2O_5$ in mol%) was developed by Larry Hench in the 1960's [1]. Since then, numerous bioactive glass compositions have been synthesised to fulfil a number of applications. More recently, the addition of CaF_2 into a bioactive glass composition has been found to be beneficial for dental applications. Through inhibiting both bacterial enzymes and demineralisation, and encouraging remineralisation, fluorine-containing bioactive glasses help prevent tooth decay and dentine hypersensitivity [2]–[6]. The addition of CaF_2 has also been found to increase the bioactivity of the glass and to decrease its hardness [7]. Decreasing the hardness of the glass is crucial for making the glass less abrasive and so more suitable for dental applications.

Currently however, the structure of fluorine-containing bioactive glasses remains controversial, and in particular the structural role of fluorine is unclear. In a ^{19}F and ^{29}Si magic angle spinning nuclear magnetic resonance (MAS-NMR) study by Brauer *et al.* [8], detectable amounts of Si-F bonding were not observed and it was concluded that fluorine ions only bond with calcium ions. However, Pedone *et al.* [9] reported that Si-F bonding cannot be resolved using MAS-NMR experiments. It would be necessary to have a complete structural understanding of fluorine-containing bioactive glasses in order to comprehend both their degradation and ion-release mechanisms, and to ultimately realise their applications [9].

Fluorine-containing bioactive glasses such as those synthesised by Brauer *et al.* (e.g.[8], [10], [11]) are typically quinary $CaO\text{-}SiO_2\text{-}P_2O_5\text{-}Na_2O\text{-}CaF_2$ glasses, although the presence of Na_2O is not essential [12], [13]. In addition, bioactive glasses often only contain small amounts of P_2O_5. Brauer *et al.* [8], [10] for example used between 0.72 and 1.07 mol% P_2O_5. This is because P_2O_5 has a limited solubility in the silicate glass network. Continuing to increase the P_2O_5 concentration would ultimately lead to the devitrification of the glass [14]. Hence, in order to understand the structure of complex $CaO\text{-}SiO_2\text{-}P_2O_5\text{-}Na_2O\text{-}CaF_2$ glasses, it is intuitive to first consider the structure of less complex $SiO_2\text{-}CaO\text{-}CaF_2$ glasses.

Ternary CaO-SiO_2-CaF_2 glasses have predominantly been studied for mould flux applications during the continuous casting of steel. Despite numerous studies, the structure of these SiO_2-CaO-CaF_2 glasses remains unclear, and conclusions on whether fluorine coordinates with silicon are contradictory [15]. Hayashi *et al.* [16] summarises these conflicting conclusions. The first is that Si-F bonding is dependent on the basicity of the glass. For acidic glasses, the addition of CaF_2 causes Si-F bonding, while basic glasses do not contain any Si-F bonding [17], [18]. The second is that fluorine ions preferentially bond with silicon ions when CaF_2 contents are less than around 15mol%, and bonds with calcium ions for higher contents [18], [19]. The last contradiction is that Si-F bonding is not observed [20], [21]. In a later study, Watanabe *et al.* [22] also concluded that Si-F bonding is not observed and suggested the formation of clusters of Ca and F ions.

In this chapter, the structure of ternary CaO-SiO_2-CaF_2 glasses is explored experimentally. This is to help elucidate the structural role of fluorine in both CaO-SiO_2-CaF_2 glasses and in more complex fluorine-containing bioactive glass compositions. The work begins by synthesising a CaO-SiO_2-CaF_2 glass series and characterising the composition and density of the samples. Well-defined CaO-SiO_2-CaF_2 glass compositions and densities are not currently available in the literature and would be essential for modelling CaO-SiO_2-CaF_2 glasses computationally. Further laboratory-based measurements include ^{29}Si and ^{19}F solid-state magic-angle spinning nuclear magnetic resonance spectroscopy (MAS-NMR), and differential scanning calorimetry (DSC) measurements. The results of central facility neutron diffraction (ND) and extended absorption fine structure (EXAFS) experiments are then detailed. To the author's knowledge there are no previous reports of CaO-SiO_2-CaF_2 glasses being studied using ND or EXAFS techniques.

7.2 Glass synthesis

The nominal CaO-SiO_2-CaF_2 glass series (denoted as GF) synthesised in this work is presented in table 1. It was desirable for the nominal compositions to be analogous to the nominal CaO-SiO_2-$CaCl_2$ compositions so comparisons could later be made. However, it was anticipated that the number of samples would not be as extensive as the chlorine-containing samples due to the tendency for CaF_2 to crystallise with increasing CaF_2 content [14]. A GF27.4 composition is therefore not included in table 1, but two further compositions (GF19.0 and GF21.0) are included instead.

Table 1: The nominal GF glass series synthesised in this study (in mol%).

Sample	CaF_2	CaO	SiO_2
GF3.3	3.3	48.4	48.4
GF6.6	6.6	46.7	46.7
GF9.3	9.3	45.3	45.3
GF11.9	11.9	44.1	44.1
GF19.0	19.0	40.5	40.5
GF21.0	21.0	39.5	39.5

The glass series in table 1 is illustrated on a ternary phase diagram in figure 1. According to the molar concentration of each nominal composition, 150g of reagents (SiO_2, CaF_2 and $CaCO_3$) were mixed using an agate pestle and mortar for 30 minutes. The mixed reagents were then placed into a platinum-rhodium crucible and melted in a pre-heated furnace at between 1540°C and 1570°C (table 2) for 1 hour. The furnace temperatures exceeded the melting temperatures reported by Watanabe *et al.* [23] in order to promote melting and mixing. After melting, some of the melt was splash-quenched between steel plates and used for analysis. The excess was quenched in water and used for yield calculations before being discarded. The highly amorphous nature of the samples was verified using powder X-ray diffraction (PXRD), although insignificant peaks around 2θ=27° corresponding to crystalline SiO_2 were observed, as shown in figure 2. To verify the homogeneity of the glass samples, the Raman spectra attained from multiple glass chips of each sample (whose nominal compositions contained equal proportions of SiO_2 and CaO) were compared with the Raman spectra reported by Luth *et al.* [20] for 50SiO_2-50CaO (equal proportions of SiO_2 and CaO), 54.29SiO_2-45.71CaO (SiO_2 rich), and 43.67SiO_2-56.33CaO (CaO rich) glasses.

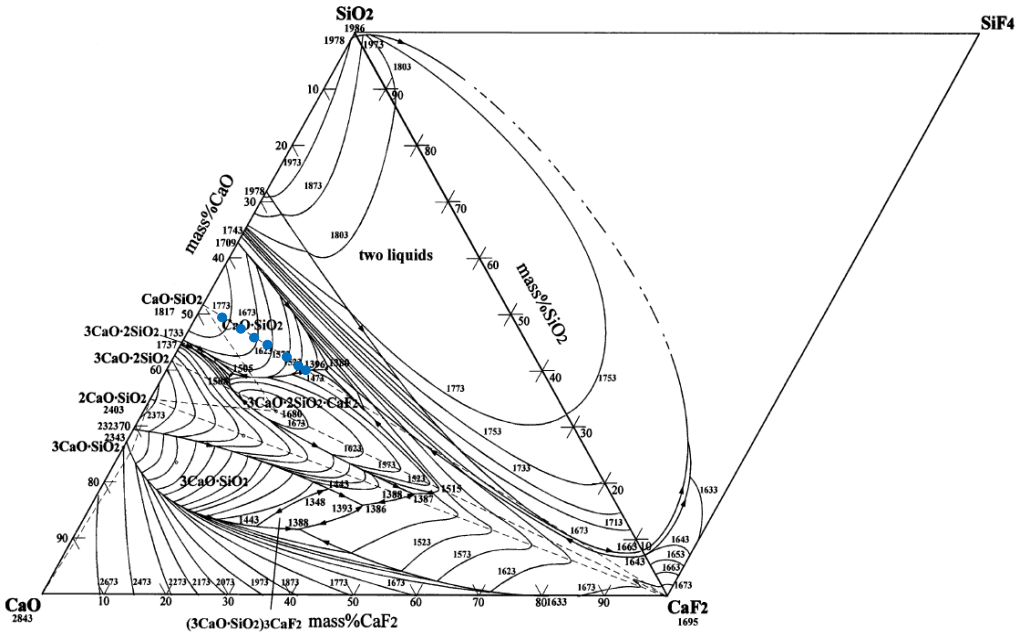

Figure 1: Phase diagram for CaO-SiO_2-CaF_2-SiF_4 systems reported by Watanabe *et al.* [23] with the addition of blue points representing the nominal GF series.

Table 2: The reagent combinations for each GF glass sample along with the corresponding melting temperatures, furnace temperatures, and the percent yields achieved. The errors in the percent yield values were based on 0.5g of unaccounted mass.

	SiO_2 ±0.01(g)	$CaCO_3$ ±0.01(g)	CaF_2 ±0.01(g)	Melting temp (°C)	Furnace temp ±1(°C)	Percent yield (%)
GF3.3	54.46	90.71	4.83	1515	1570	98.96±0.46
GF6.6	52.64	87.69	9.67	1450	1565	99.22±0.45
GF9.3	51.16	85.21	13.63	1400	1560	98.76±0.45
GF11.9	49.72	82.82	17.45	1360	1555	99.25±0.45
GF16.1	47.40	78.96	23.64	1300	1550	98.83±0.43
GF19.0	45.80	76.29	27.92	1250	1545	99.34±0.43
GF21.0	44.69	74.44	30.87	1173	1540	98.60±0.44

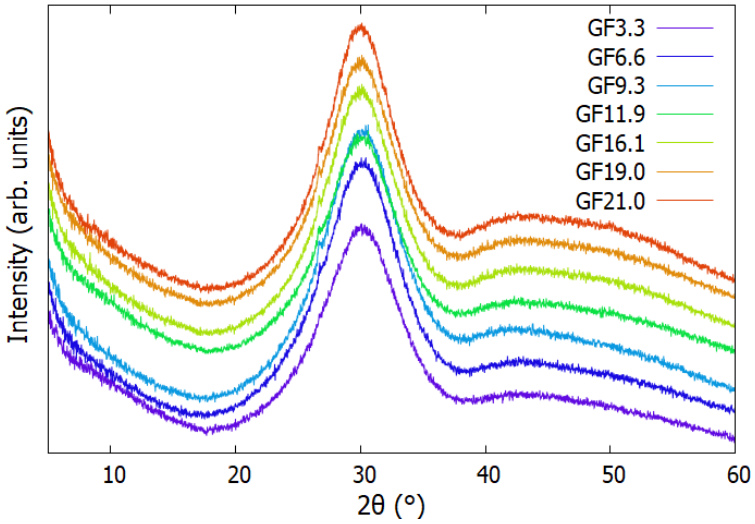

Figure 2: The powder X-ray diffraction spectra for the GF glass series.

7.3 Compositional Analysis

The volatile nature of halides can not only make halide retention challenging, but can also significantly alter the glass composition [24]. It is therefore important that the actual glass compositions are established. A number of compositional analysis techniques for fluorine-containing oxide glasses have been reported in the literature. They include X-ray photoelectron spectroscopy (XPS) (e.g. [21]), scanning electron microscopy with an energy dispersive spectrometer (SEM-EDS) (e.g. [25]), pyrohydrolysis (PH) (e.g. [26]), the use of an ion-selective electrode (ISE) (e.g. [26], [27]), electron probe microanalysis (EPMA) (e.g. [16], [22]), and solid-state MAS-NMR (e.g. [26], [28]–[30]). The latter is the most commonly reported technique.

For this work, ^{19}F MAS-NMR spectra were obtained by Dr David Apperley at the EPSRC UK National Solid-State NMR Service at Durham. Sample preparation involved grinding small

amounts of each sample (~250mg) into a fine powder using an agate pestle and mortar. In order to later quantify the fluorine content of each glass, a number of standard samples were also prepared. These were combinations of SiO_2 and CaF_2 reagents that had been thoroughly mixed using an agate pestle and mortar with ethanol. The spectra were recorded at a frequency of 376.59MHz using a Bruker Avance III HD spectrometer and a 3.2mm magic-angle spinning probe. Measurements were carried out using an ambient probe temperature of 298K. The sample spin rate was 20kHz and a total of 16 scans were collected for each sample using direct excitation where the pulse duration was 2.9µs. The spectral width was 300kHz and the acquisition time was 3.4ms. Chemical shift values are reported with respect to trichlorofluoromethane ($CFCl_3$).

By plotting the intensity of the NMR signal for the standard samples as a function of the number of fluorine atoms per milligram, a calibration line could be set as shown in figure 3. By comparing the GF glass samples to the calibration line, insight into the fluorine losses could be established. While most of the GF glasses were within the uncertainty range of the calibration line (figure 3), it was evident from the lower intensity values that the samples had undergone some losses via fluorine volatilisation. However, determining how these fluorine losses occurred was challenging due to ^{19}F MAS-NMR being sensitive to fluorine only.

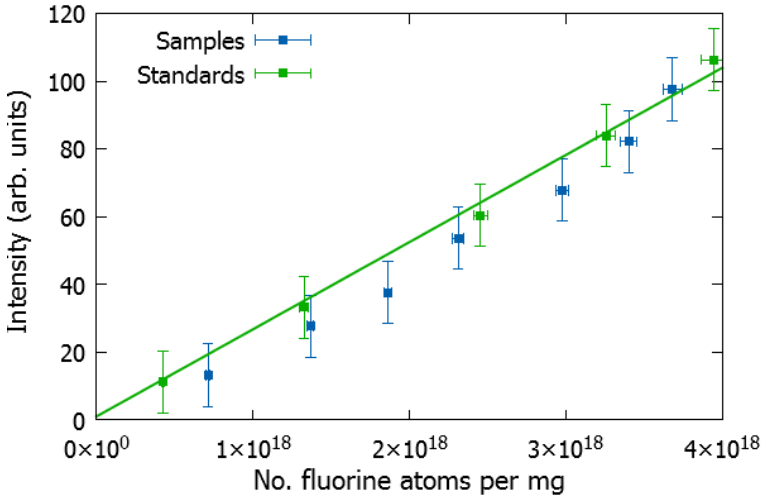

Figure 3: Solid state ^{19}F MAS-NMR results for the GF series and a number of standard SiO_2-CaF_2 mixtures. A linear trend line through the standards forms a calibration line. Uncertainty in the ^{19}F MAS-NMR results was calculated based on the errors in the mass, the intensity, and the reproducibility.

In a study by Watanabe *et al.* [22] where EPMA was used to quantify the composition of a $xCaF_2$-(100-x)($CaO{\cdot}SiO_2$) glass series, it was found that the CaO content was persistently higher than the nominal content. This suggests fluorine loss via HF (as $CaF_2+H_2O \rightarrow 2HF+CaO$). For some compositions in the series, the SiO_2 content was lower than expected, perhaps indicating losses via SiF_4. However, for other compositions, the SiO_2

content was higher than expected. In addition, Brauer *et al.* [27] used an ion selective electrode for the compositional analysis of a fluorine-containing bioactive glass series where the CaF_2 content ranged from 0mol% to 17.76mol%. The measured CaO content was higher than the nominal content, and it was concluded that fluorine losses occurred as HF. It was therefore assumed in this work that fluorine losses via fluorine volatilisation only occur as HF.

To further examine the losses due to fluorine volatilisation, the results of yield calculations (following the synthesis of the glass samples) were considered. It can be seen in table 3 that the fluorine losses based on the ^{19}F MAS-NMR and yield calculations are generally in fair agreement. The exceptions are GF3.3 and GF21.0. This could be because the GF3.3 composition contained the least amount of CaF_2 and so was more susceptible to higher proportions of fluorine loss. Immediately following splash-quenching, all of the glasses underwent some spontaneous glass breakage which may have led to the loss of some glass chips. Since the GF21.0 glass chips were substantially thicker than the others due to the melt being more viscous, the sample was more susceptible to the loss of some glass. Based on the compositional analysis and in particular the assumed F losses, the revised compositions of the GF glass series are presented in table 4. The differences between the nominal and the revised compositions can be visualised in the ternary plot in figure 4.

Table 3: The percentage of fluorine losses as identified from ^{19}F MAS-NMR and from yield calculations where all mass loss was attributed to HF losses. Uncertainty in the NMR results was calculated based on the errors in the mass, the intensity, and the reproducibility. The errors in the %yield calculations were based on 0.5g of losses.

	NMR (%)	Percent yield (%)	Assumed F losses (%)
GF3.3	32 ± 83	63 ± 24	40
GF6.6	24 ± 42	25 ± 11	25
GF9.3	23 ± 31	28 ± 7	25
GF11.9	11 ± 23	13 ± 6	10
GF16.1	13 ± 18	15 ± 5	10
GF19.0	7 ± 15	7 ± 4	10
GF21.0	-2 ± 13	13 ± 3	10

Table 4: The revised compositions for the GF glass series in mol%.

	SiO_2	CaO	CaF_2
GF2.0	48.4	49.7	2.0
GF5.0	46.7	48.3	5.0
GF7.0	45.4	47.7	7.0
GF10.7	44.1	45.3	10.7
GF14.5	42.0	43.6	14.5
GF17.1	40.5	42.4	17.1
GF18.9	39.5	41.6	18.9

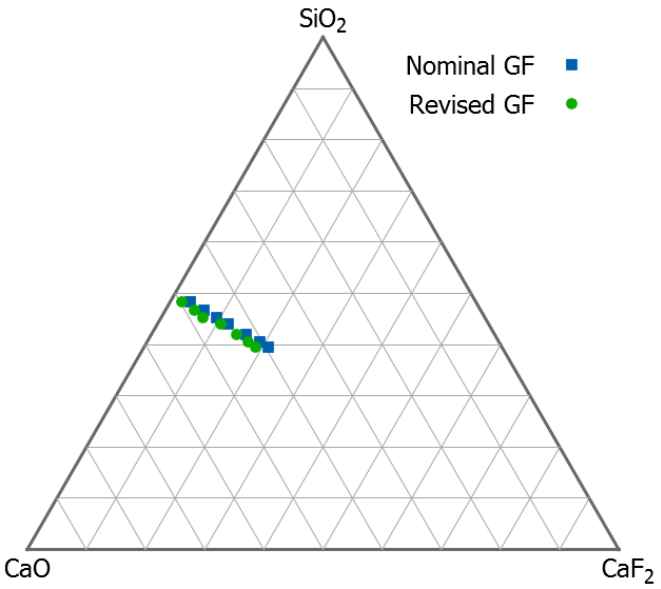

Figure 4: Ternary plot comparing the nominal GF series (blue squares) and the revised GF series (green circles).

7.4 Glass Characterisation

7.4.1 Density

Density measurements were performed using helium pycnometry. As shown in figure 5, the density values form a linear trend and typically have values higher than those reported for the $xCaF_2$-(100-x)($CaO{\cdot}SiO_2$) glass series synthesised by Susa *et al.* [15]. This could be because Susa *et al.* [15] only used the nominal glass compositions and did not take any potential losses into account. Watanabe *et al.* [22] reported inconsistent density values for a $xCaF_2$-(100-x)($CaO{\cdot}SiO_2$) glass series. A $CaSiO_3$ glass density value of 2.895g/cm^3 reported by Fokin *et al.* [31] was in good agreement with the density trend in this study.

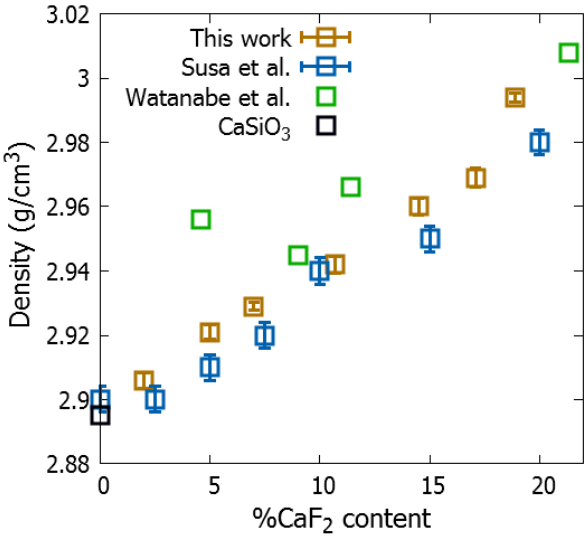

Figure 5: The glass density values attained in this work compared with those reported by Susa *et al.* [15], Watanabe *et al.* [22] ,and Fokin *et al.* [31]. Error bars of ±0.004g/cm^3 were reported by Susa *et al.*, but Watanabe *et al.* and Fokin *et al.* did not specify uncertainties. Two standard deviations were taken to be the uncertainty in this study.

7.4.2 Solid-State MAS-NMR

NMR spectra can contain information regarding the local atomic environment of elements. In addition to the ^{19}F solid-state MAS-NMR spectra detailed in section 7.3, ^{29}Si solid-state MAS-NMR spectra were also collected by Dr. David Apperley at the EPSRC UK National Solid-State NMR service at Durham. The ^{29}Si MAS-NMR spectra were recorded at a frequency of 79.50MHz using a Bruker Avance III HD spectrometer and a 3.2mm magic-angle spinning probe. Measurements were carried out using an ambient probe temperature of 298K. The sample spin rate was 6kHz and direct excitation measurements were recorded. The pulse duration was 6.00µs, the spectral width was 29.8kHz, and the acquisition time was 8.6ms. The number of repeat measurements ranged from 140 to 308. Chemical shift values were reported with respect to neat tetramethylsilane (TMS).

Changes to the ^{29}Si MAS-NMR chemical shift positions were minimal with increasing fluorine concentrations. For example, the chemical shift was 80.2±0.5ppm in GF2.0 and 80.1±0.5ppm in GF18.9. This suggests that the silicon environment does not change with increasing CaF_2 contributions. In contrast, the position of the ^{19}F MAS-NMR chemical shift did become more negative with increasing fluorine contributions as shown in figure 6 and table 5.

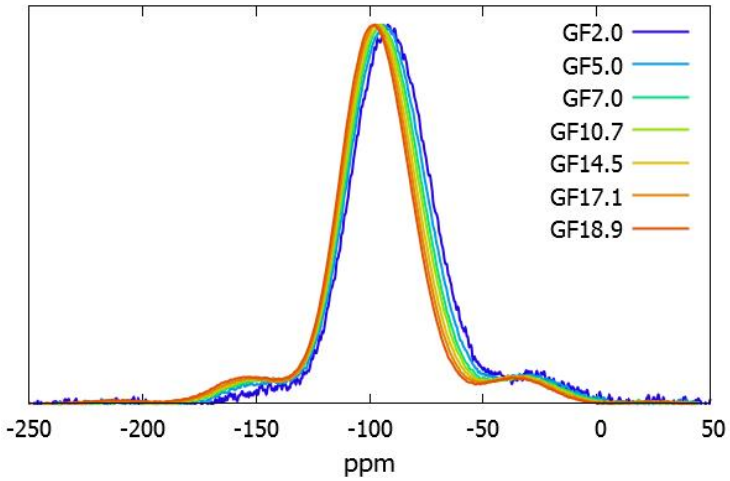

Figure 6: The normalised ^{19}F MAS-NMR spectra for the GF glass series relative to $CFCl_3$.

Table 5: The ^{19}F MAS-NMR chemical shift positions for the GF glass series relative to $CFCl_3$. The uncertainty is ±0.5ppm.

	Chemical Shift (ppm)
GF2.0	-92.0
GF5.0	-93.9
GF7.0	-95.0
GF10.7	-95.1
GF14.5	-97.0
GF17.1	-97.6
GF18.9	-98.0

7.4.3 Differential Scanning Calorimetry

The glass transition temperature, T_g, can provide insight into both the degradation rate [8] and the hardness of a glass [32], and can be established using differential scanning calorimetry (DSC). The DSC measurements were performed by placing around 35mg of powdered glass sample into an alumina crucible which was then heated from room temperature to 1173K at a rate of 10K per minute in air. The onset of deviation in the DSC curve could be used to identify the glass transition temperature. As shown in figure 7, T_g decreased linearly with increasing CaF_2 content.

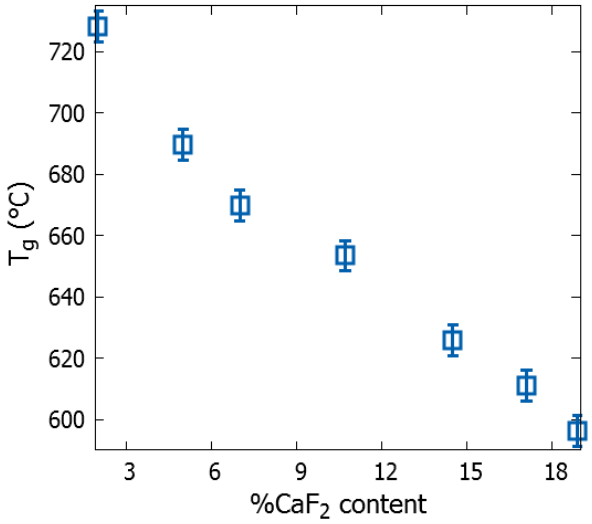

Figure 7: The glass transition temperatures for the GF glass series as a function of increasing CaF_2 content. The uncertainty is ±5°C.

7.4.4 Neutron Diffraction

For neutron diffraction measurements, approximately 9g of each sample was ground into coarse glass chips before being used to fill cylindrical vanadium cans. The cans had an internal diameter of 10.3mm and were made of vanadium foil which was 40µm thick. Measurements were then performed using the GEM diffractometer at the ISIS neutron spallation source at the Rutherford Appleton Laboratory in Oxfordshire. In addition to sample measurements, data was also collected for an empty 10.3mm vanadium can, for an 8mm vanadium niobium rod (94.86% V: 5.14% Nb), and for the empty GEM diffractometer. This was to enable corrections to the sample data following the experiment using the programs Gudrun [33] and Open GENIE [34].

After correcting the experimental data, it can be seen in figure 8 that the total neutron structure factors display subtle changes with increasing fluorine contributions. Similarly, there are subtle changes in the total correlation functions in figure 9 which were attained by Fourier transforming the total neutron structure factors using a Lorch window function with a maximum Q value of 50$Å^{-1}$. Although challenging to see, there is a small non-zero contribution in each of the total correlation functions around 1.9Å, which could only be explained by an Al-O correlation. Following X-ray fluorescence (XRF) measurements on the reagents used to make the glass series, it was established that the SiO_2 reagent contained some Al_2O_3 impurity.

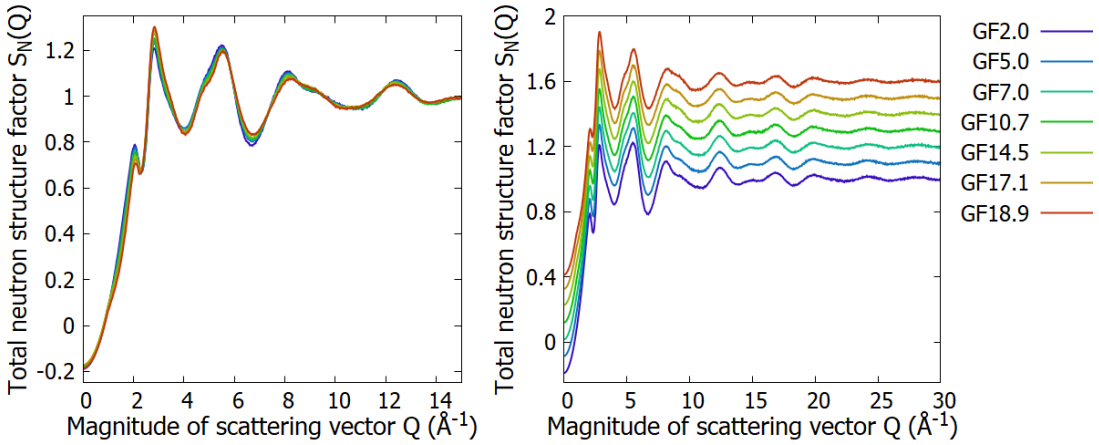

Figure 8: The total neutron structure factors for the GF glass series. The plots to the right have been progressively offset by 0.1. Although the data range extends to 50Å^{-1}, the plot to the left and right extends to 15Å^{-1} and 30Å^{-1} respectively so differing features of the structure factors can be identified.

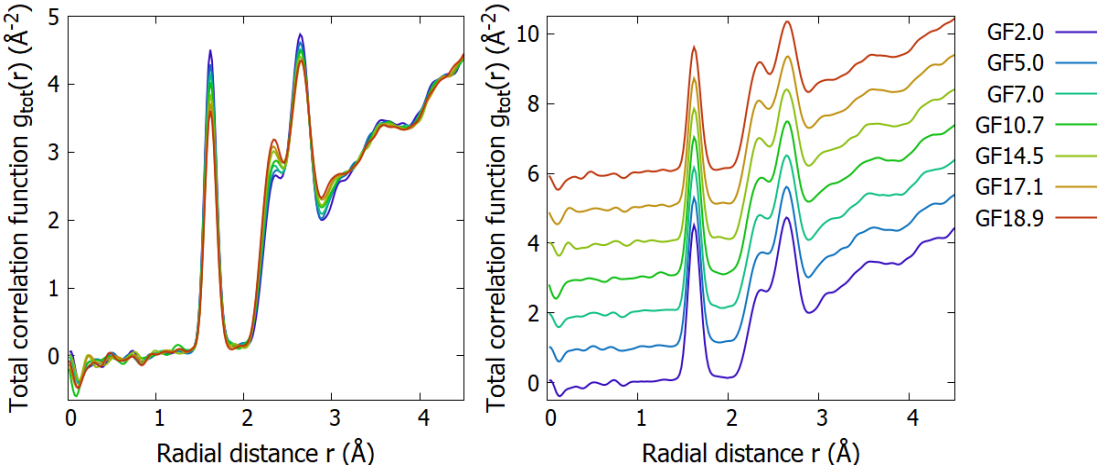

Figure 9: The total correlation functions for the GF glass series where the plots to the right have been progressively offset by 1Å^{-2}. The plots shown only extend to 5Å so differing features of the total correlation functions can be identified.

To obtain structural information from the total correlation functions including nearest neighbour distances, R_{ij}, coordination numbers, N_{ij}, and values of σ_{ij}, the program NXFit [35] was used. This involved fitting peaks to the data in accordance with the input and restraint parameters specified. Initially, the uniform input parameters in table 6 were used. To account for the Al_2O_3 impurity, it was assumed that Al_2O_3 made up 1mol% of the SiO_2 content.

Table 6: The uniform input and restraint parameters used to fit the ND data. The fitting range was 1.50Å to 2.74Å and 10,000 iterations were used.

	Input parameters			Restraint parameters		
	R_{ij} (Å)	N_{ij}	σ_{ij} (Å)	R_{ij} (Å)	N_{ij}	σ_{ij} (Å)
Si-O	1.62	4.00	0.06	0.01	0.05	0.01
Al-O	1.88	6.00	0.07	0.03	0.10	0.01
Ca-F	2.28	1.00	0.11	0.03	1.00	0.02
Ca-O	2.38	5.00	0.15	0.03	1.00	0.02
O-O	2.66	4.05	0.09	0.03	0.20	0.03

Examples of fits to the experimental data based on the parameters in table 6 are shown in figure 10. These include the fits for the end member compositions and a middle composition (GF2.0, GF10.7, and GF18.9). Although the fits appear reasonable, the challenging nature of distinguishing overlapping Ca-F and Ca-O peaks is apparent. For example, it is expected that the Ca-F peak would be small for compositions of low fluorine content, and increase with increasing fluorine content. However, figure 10 shows that the fitting gives Ca-F peaks with similar areas, despite great differences in fluorine content.

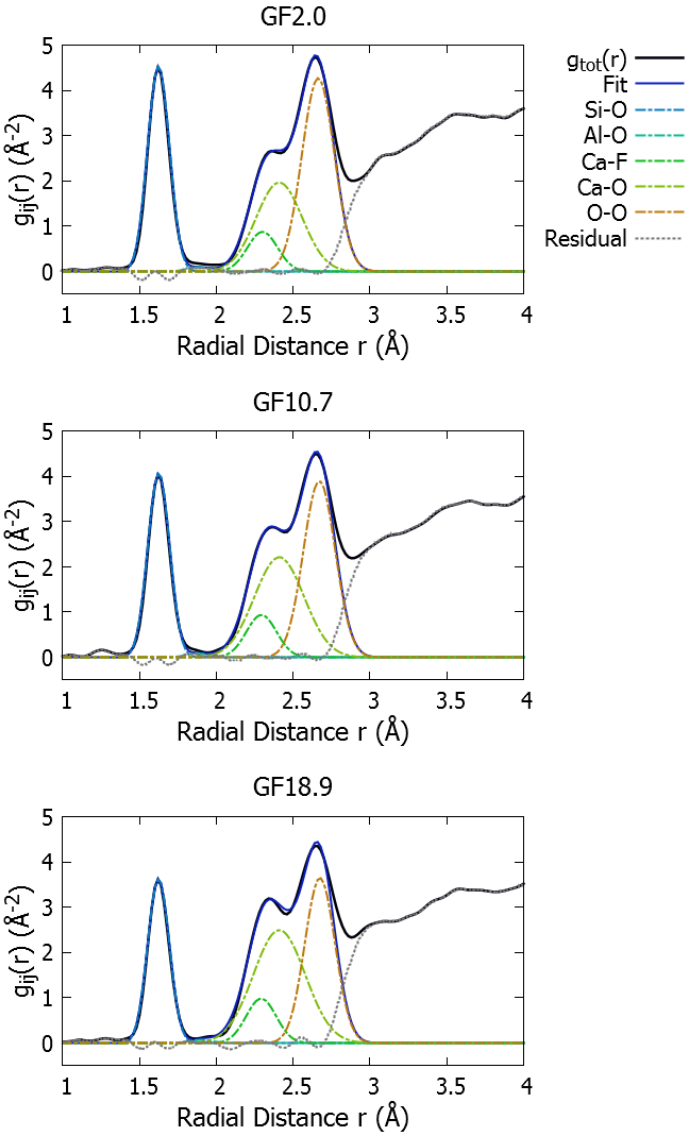

Figure 10: Examples of fits to experimental neutron diffraction data following the refinement of the uniform input parameters in table 6.

The output parameters attained from fitting the experimental data using the input and restraint parameters in table 6 are given in table 7. Details for the Si-O and Al-O correlations are not included since they underwent minimal change. The Si-O nearest neighbour distance was 1.61-1.63Å (±0.01Å), the coordination number was 3.95±0.1, and the value of sigma was 0.06±0.01Å. The Al-O nearest neighbour distance was 1.87-1.90Å (±0.05Å), and the coordination number and sigma values were 5.90-6.09 (±1.00) and 0.06±0.02Å respectively. It can be seen in table 8 that the Ca-O and O-O coordination numbers gradually increased with increasing fluorine contributions, while the Ca-F coordination numbers did not show any consistent trend.

Table 7: The output fit parameters for the GF series following the use of the uniform input and restraint parameters in table 6. The uncertainty in R_{Ca-F}, R_{Ca-O}, and R_{O-O} is ±0.02Å, ±0.01Å, and ±0.01Å respectively. The uncertainty in N_{Ca-F}, N_{Ca-O}, and N_{O-O} is ±1.00, ±1.00, and ±0.20 respectively. The uncertainty in σ_{Ca-F}, σ_{Ca-O}, and σ_{O-O} is ±0.02Å, ±0.01Å, and ±0.01Å respectively.

Sample	Fit index	Correlation	R_{ij} (Å)	N_{ij}	σ_{ij} (Å)
GF2.0	0.37	Ca-F	2.30±0.02	1.24	0.09
		Ca-O	2.41±0.01	4.33	0.15
		O-O	2.66±0.01	4.23	0.10
GF5.0	0.29	Ca-F	2.30±0.02	1.34	0.09
		Ca-O	2.41±0.01	4.47	0.16
		O-O	2.67±0.01	4.24	0.10
GF7.0	0.43	Ca-F	2.28±0.02	1.20	0.09
		Ca-O	2.41±0.01	4.67	0.15
		O-O	2.67±0.01	4.24	0.10
GF10.7	0.30	Ca-F	2.29±0.02	1.24	0.09
		Ca-O	2.41±0.01	4.95	0.16
		O-O	2.67±0.01	4.25	0.10
GF14.5	0.40	Ca-F	2.29±0.02	1.30	0.09
		Ca-O	2.41±0.01	5.00	0.16
		O-O	2.67±0.01	4.25	0.09
GF17.1	0.40	Ca-F	2.29±0.02	1.21	0.09
		Ca-O	2.41±0.01	5.31	0.16
		O-O	2.68±0.01	4.25	0.09
GF18.9	0.39	Ca-F	2.29±0.02	1.22	0.09
		Ca-O	2.41±0.01	5.50	0.16
		O-O	2.67±0.01	4.25	0.09

In an attempt to overcome the difficulty of attaining the areas of the overlapping Ca-F and Ca-O peaks, the input and restraint parameters for the Ca-F, Ca-O, and O-O coordination numbers were varied for each composition. The varying input parameters were based on the computational modelling results for the glass series which are presented in the following chapter. The restraint parameters for the Ca-F and Ca-O coordination numbers were 10% and 5% of the input parameter values respectively. The restraint on the O-O coordination number remained 0.20 as before.

It can be seen in figure 11 that the area of the Ca-F peaks now increases with increasing fluorine content as anticipated. In addition, the area of the Ca-O peak decreases with increasing fluorine contributions due to the reducing oxygen content as expected. However, as quantified in table 8, the fit indexes are generally not as good as those in table 7 (where uniform input and restraint parameters were used). The output parameters for the Si-O and Al-O correlations were not provided in table 8 as variation was minimal. The Si-O nearest neighbour distances, coordination numbers, and sigma values were 1.62±0.01Å, 3.95-3.98 (±0.10), and 0.06±0.01Å respectively. The Al-O nearest neighbour distances, coordination numbers, and sigma values were 1.88-1.90Å (±0.05Å), 5.91-6.10

(±1.00) and 0.06-0.07Å (±0.02Å) respectively. These values did not differ significantly from those obtained in the previous fitting.

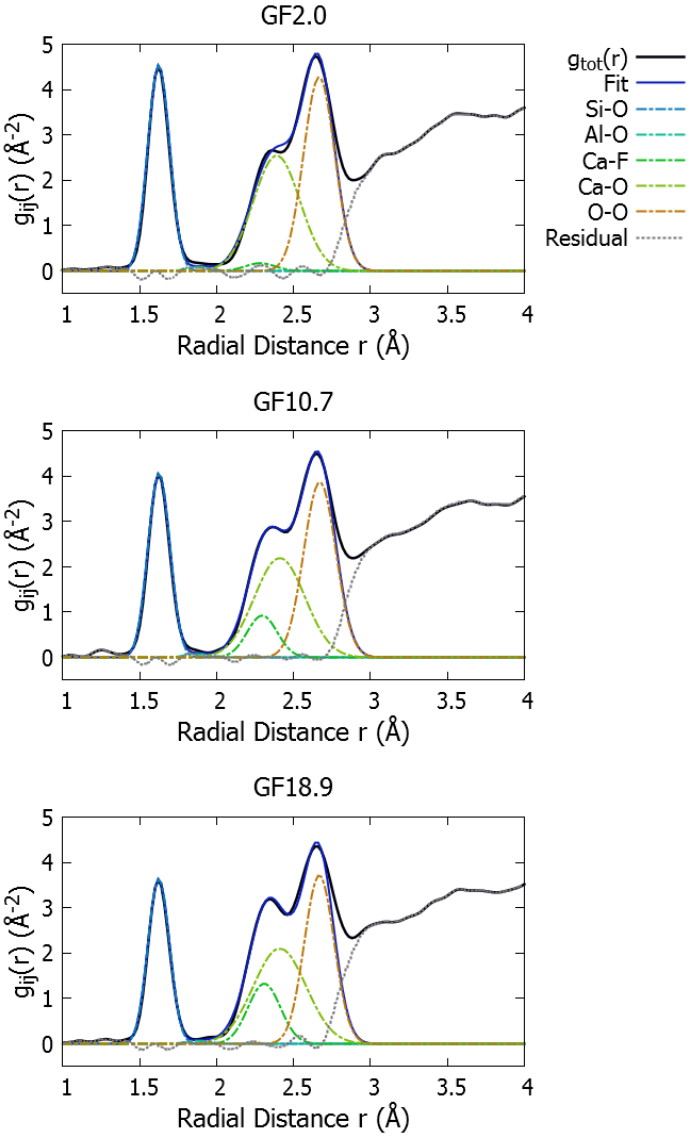

Figure 11: Examples of fits to experimental neutron diffraction data following the refinement of non-uniform input parameters.

Table 8: The output fit parameters for the GF series following the use of the non-uniform input parameters and restraints. The uncertainty in R_{Ca-F}, R_{Ca-O}, and R_{O-O} is ±0.02Å, ±0.01Å, and ±0.01Å respectively. The uncertainty in N_{Ca-F}, N_{Ca-O}, and N_{O-O} is ±1.00, ±1.00, and ±0.20 respectively. The uncertainty in σ_{Ca-F}, σ_{Ca-O}, and σ_{O-O} is ±0.02Å, ±0.01Å, and ±0.01Å respectively.

Sample	Fit index	Correlation	R_{ij} (Å)	N_{ij}	σ_{ij} (Å)
GF2.0	0.60	Ca-F	2.28	0.24	0.09
		Ca-O	2.39	5.63	0.15
		O-O	2.67	4.06	0.09
GF5.0	0.40	Ca-F	2.29	0.62	0.09
		Ca-O	2.40	5.37	0.15
		O-O	2.67	4.10	0.10
GF7.0	0.47	Ca-F	2.29	0.87	0.09
		Ca-O	2.40	5.22	0.16
		O-O	2.67	4.17	0.10
GF10.7	0.30	Ca-F	2.30	1.22	0.09
		Ca-O	2.41	5.01	0.16
		O-O	2.67	4.25	0.10
GF14.5	0.43	Ca-F	2.30	1.46	0.09
		Ca-O	2.41	4.82	0.16
		O-O	2.67	4.25	0.09
GF17.1	0.51	Ca-F	2.31	1.63	0.09
		Ca-O	2.41	4.84	0.17
		O-O	2.67	4.25	0.09
GF18.9	0.57	Ca-F	2.31	1.79	0.10
		Ca-O	2.41	4.70	0.17
		O-O	2.67	4.25	0.09

7.4.5 X-ray Absorption Spectroscopy

An X-ray absorption spectroscopy (XAS) experiment was carried out on the GF glass series using beamline B18 at the Diamond Light Source synchrotron facility at the Rutherford Appleton Laboratory in Oxfordshire. Sample preparation involved finely grinding small amounts of each sample using an agate pestle and mortar. Approximately 4mg of each sample was then mixed with 50mg of powdered polyvinylpyrrolidone (PVP) before being pressed into a 13mm pellet. Crystalline standard samples including CaF_2, $CaCO_3$, and $CaSiO_3$ were also mixed with PVP to form pellets in the same manner. Spectra for all samples were collected around the calcium K-edge at 4038eV [36] in transmission mode using a double crystal Si(111) monochromator. Ionisation chambers measured the incident, the transmitted, and the reference X-ray intensity. The energy of the incident X-ray beam was calibrated using titanium foil (4966eV [36]). A $CaCO_3$ reference pellet was prepared to monitor the energy drift of the beam during the experiment. However, the high level of X-ray absorption meant that the reference spectra were noisy and had an uncertainty of 0.2eV. Instead, the three crystalline standard samples (CaF_2, $CaCO_3$, and $CaSiO_3$) were measured throughout the experiment in order to detect any drift in beam energy with an

uncertainty of 0.02eV. Following the experiment, the programs Athena [37] and Artemis [37] were used to analyse the data.

7.4.5.1 X-ray Absorption Near-Edge Structure

It is often useful to compare the X-ray absorption near-edge structure (XANES) spectra of crystalline standards to those reported in literature to help validate experimental results. By comparing the crystalline calcite ($CaCO_3$) XANES spectra from this work to the spectra reported by Hormes *et al.* [38] in figure 12, very good agreement can be seen. The value of E_0 was 4047.55eV. A pre-edge range of -100eV to -10eV, a normalisation range of 150eV to 650eV, and an Rbkg value of 1.0 was used.

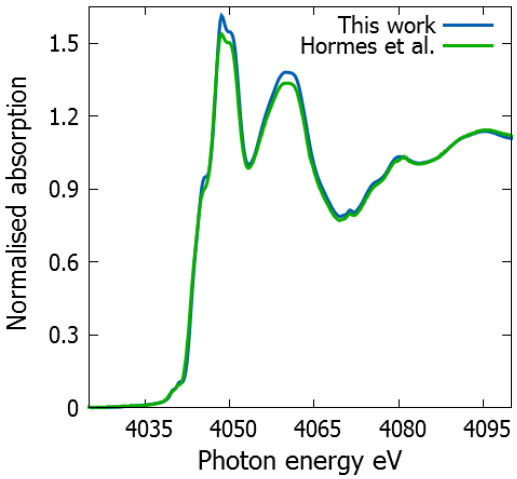

Figure 12: The crystalline $CaCO_3$ XANES spectra around Ca K-edge from this work and from Hormes *et al.* [38].

The XANES spectra for the GF glass series are shown to the left of figure 13, where the value of E_0 is 4043.00eV. A pre-edge range of -100eV to -10eV, a normalisation range of 150eV to 650eV, and an Rbkg value of 1.0 was applied to all samples. In order to examine the possibility of small spectral changes as a function of composition, the derivative of the XANES spectra was calculated. As shown in the insets to the right of figure 13, there are some subtle shifts towards higher energies in the derivative of the XANES spectra as the CaF_2 content increases.

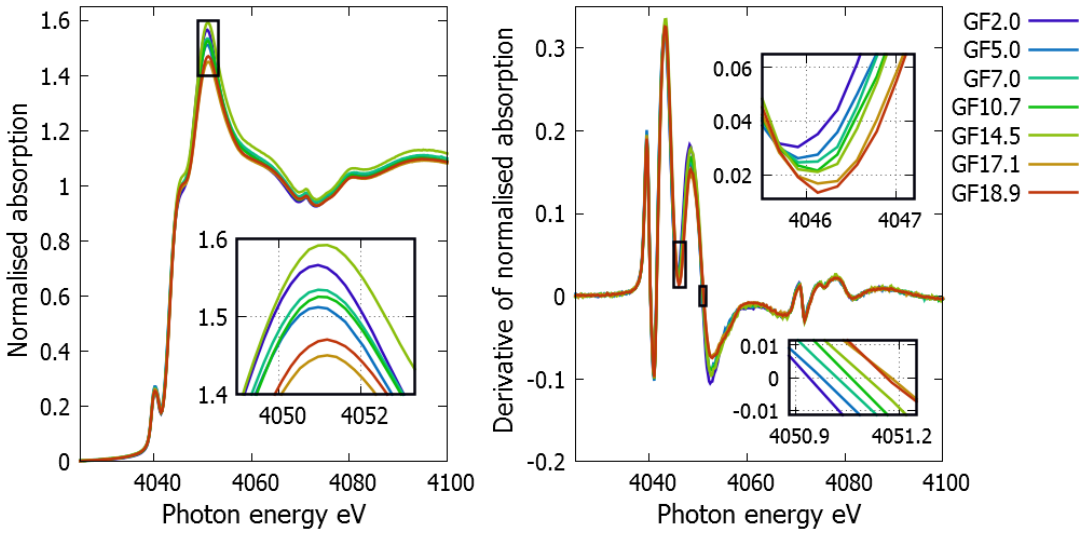

Figure 13: The XANES spectra (left) and the derivative of the XANES spectra (right) for the GF glass series around the Ca K-edge.

7.4.5.2 Extended X-ray Absorption Fine Structure

The k^2 weighted extended X-ray absorption fine structure (EXAFS) spectra in k-space and the modulus of their Fourier transforms in r-space are shown in figure 14. A pre-edge range of -100eV to -10eV, a normalisation range of 150eV to 650eV, and an Rbkg value of 1.0 was applied to all samples. It is clear that the series of GF samples follows a trend, although there is some deviation from the trend in the amplitude of the peaks.

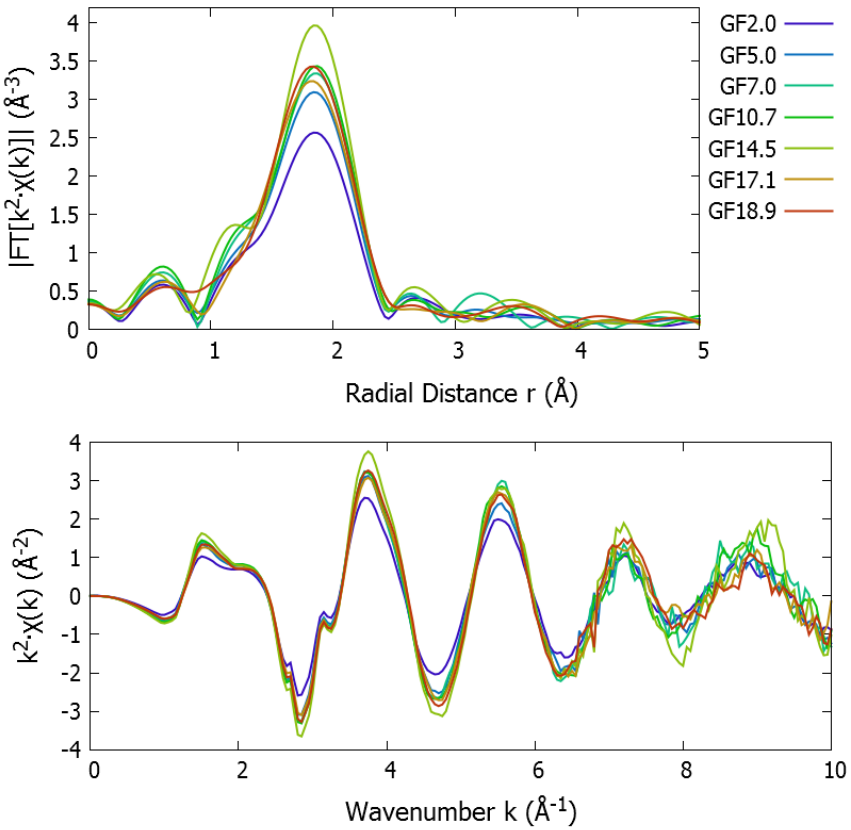

Figure 14: The Ca K-edge k^2 weighted EXAFS spectra (bottom) and the modulus of their Fourier transforms (top) for the GF glass series.

The $CaCO_3$ and CaF_2 crystalline reference structures were used to create a modelled EXAFS spectrum using the FEFF code [39]. The single-scattering Ca-O and Ca-F FEFF paths were then chosen to fit the experimental EXAFS spectra for the GF glasses. This was to attain structural information on the Ca-O and Ca-F correlations including nearest neighbour distances (R_{ij}), coordination numbers (N_{ij}), and values of σ_{ij}^2 which are used to determine the XAS Debye-Waller factors ($2\sigma_{ij}^2$). The input parameters used for fitting in Artemis [37] are given in table 9. A k-range of 3.0Å^{-1} to 9.0Å^{-1} and an r-range of 1.0Å to 4.0Å was considered appropriate for fitting. The fits to the k^2 weighted experimental EXAFS spectra and to the modulus of their Fourier transforms are shown in figures 15 and 16 respectively, where good agreement over the fitting ranges can be seen.

Table 9: The input parameters for the Ca-O and Ca-F FEFF paths used to fit the experimental EXAFS spectra of the GF glass series.

	R_{ij} (Å)	N_{ij}	σ_{ij}^2 (Å^2)
Ca-O	2.38	5.0	0.01
Ca-F	2.27	1.0	0.01

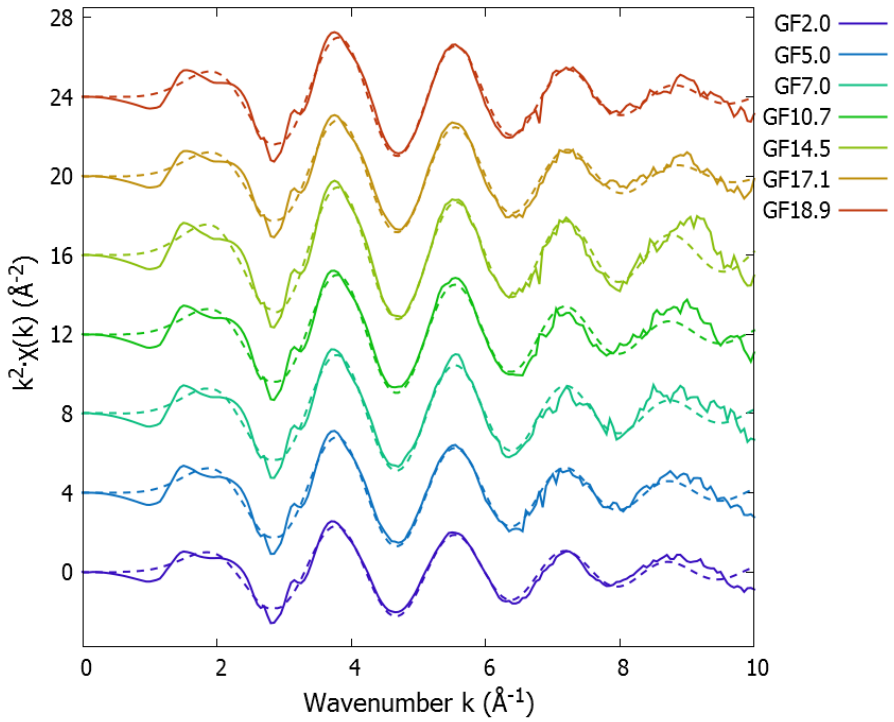

Figure 15: The experimental (solid lines) and fitted (dashed lines) Ca K-edge k^2 weighted EXAFS spectra for the GF glass series. The plots have been progressively offset by 4.0Å^{-2}.

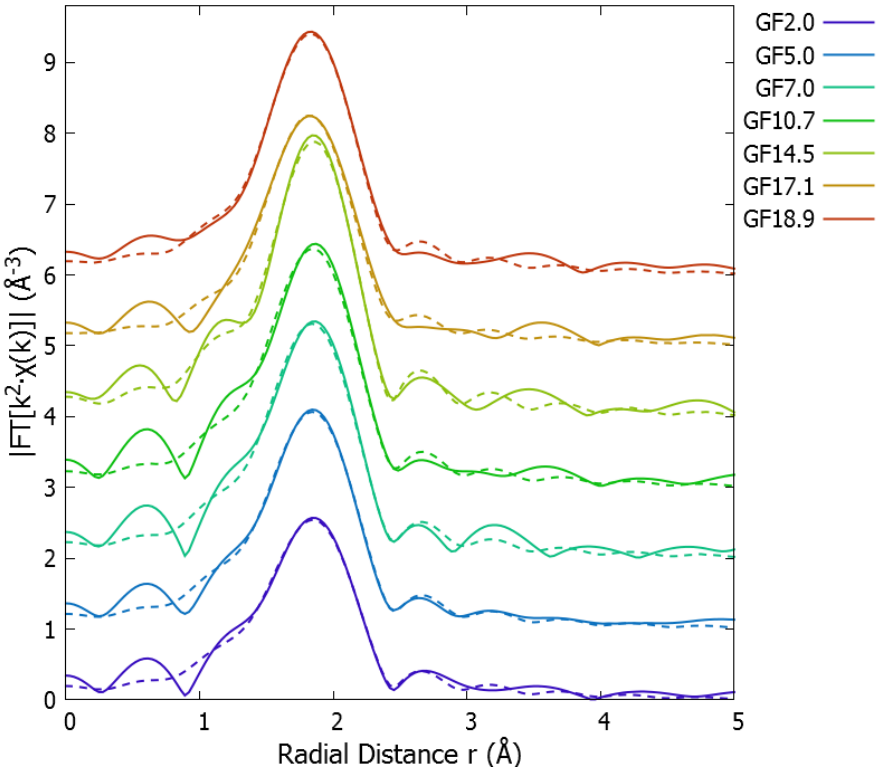

Figure 16: The modulus of the Fourier transformed experimental (solid lines) and fitted (dashed lines) Ca K-edge k^2 weighted EXAFS spectra for the GF glass series. The plots have been progressively offset by 1.0Å^{-3}.

The parameters attained from fitting the experimental EXAFS spectra are given in table 10. To ensure the values of σ^2 were not unphysically small, the fits were restrained to encourage $0.01Å^2 \leq \sigma^2 \leq 0.03Å^2$ which is appropriate for a glass. Both the Ca-O and Ca-F nearest neighbour distances increased as the CaF_2 contribution increased. To obtain the coordination numbers, a suitable amplitude reduction factor of 0.7 [40] was used. The Ca-O coordination number generally declined, while the Ca-F coordination number generally increased with increasing CaF_2 content. This was expected because the oxygen content declines as the fluorine content increases.

Table 10: The output structural parameters for the Ca-O and Ca-F correlations from fitting the k^2 weighted EXAFS spectra for the GF glass series.

	$R_{Ca\text{-}O}$ (Å)	$N_{Ca\text{-}O}$	$\sigma_{Ca-O}{}^2$ ($Å^2$)	$R_{Ca\text{-}F}$ (Å)	$N_{Ca\text{-}F}$	$\sigma_{Ca-F}{}^2$ ($Å^2$)
GF2.0	2.36±0.03	5.02±0.88	0.009±0.002	2.18±0.06	1.61±0.75	0.010±0.003
GF5.0	2.36±0.03	5.71±1.67	0.010±0.001	2.20±0.09	2.30±1.93	0.012±0.010
GF7.0	2.36±0.03	5.40±3.21	0.010±0.002	2.22±0.14	2.71±3.37	0.013±0.016
GF10.7	2.37±0.04	4.68±4.41	0.009±0.002	2.24±0.15	3.48±4.38	0.013±0.020
GF14.5	2.44±0.19	4.72±4.79	0.014±0.002	2.28±0.05	4.70±4.27	0.009±0.003
GF17.1	2.41±0.08	3.13±1.86	0.009±0.003	2.27±0.05	4.06±1.66	0.010±0.003
GF18.9	2.40±0.06	3.38±3.78	0.010±0.002	2.27±0.08	4.26±3.27	0.012±0.010

7.5 Discussion

Following the compositional analysis of the $CaO\text{-}SiO_2\text{-}CaF_2$ glass series, fluorine losses via HF were established. These fluorine losses could have been reduced by reducing the time during which the reagents were melted in the furnace. It was observed that by melting the reagents for 30 minutes instead of 60 minutes, the percent yields improved noticeably. However, powder XRD spectra revealed significant Bragg peaks, and Raman spectra revealed sample inhomogeneity. It was important to ensure amorphous and homogeneous samples by melting the reagents at a sufficient temperature for a sufficient time, meaning some fluorine loss was inevitable. The nominal GF3.3 composition had the highest melting temperature (1515°). Correspondingly, the highest furnace temperature was used (1570°) which caused a noticeably higher proportion of fluorine loss compared to the other samples.

The chemical shift positions in the ^{29}Si solid state MAS-NMR spectra for the GF glasses were centered around -80 ppm. This corresponds to Q^2 species [8] and is expected for a calcium metasilicate composition. As the chemical shift positions did not become less negative (closer to 0 ppm) by a discernible amount with increasing CaF_2 concentrations, the results indicated an absence of detectable amounts of Si-F bonding. This was because any Si-F bonding would have disrupted Si-O-Si linkages in the silicate network, lowering the network connectivity. This is plausible because Si-O bonding is favoured over Si-F bonding since Si^{4+}

ions have a higher affinity for O^{2-} ions compared to F^- ions [41]. Brauer *et al.* [8], [42] also reported an absence of detectable Si-F bonding in fluorine-containing bioactive glasses. However, Pedone *et al.* [9] reported that Si-F bonding cannot be detected using MAS-NMR. This was because a small Si-F contribution would be masked in the broad NMR spectrum. In addition, Zeng and Stebbins [29] commented that the width of the spinning sidebands would obscure any Si-F-Ca contributions in NMR spectra if they were present.

The ^{19}F solid state MAS-NMR chemical shift positions did become more negative with increasing CaF_2 concentrations. The chemical shift position went from -92.0ppm for GF2.0 to -98.0ppm for GF18.9. This suggests an increase in the average fluorine coordination to calcium [43] towards that of crystalline CaF_2 which has a chemical shift position of -109ppm [29]. Watanabe *et al.* [22] studied a (100-x)/2 CaO-(100-x)/2 SiO_2-xCaF_2 glass series where x=5, 10, 15, 20, 25 and reported the same trend. In addition, Watanabe *et al.* [22] also studied a xCaO-xSiO_2-15CaF_2 glass series and found consistent chemical shift positions. Zeng and Stebbins [29] synthesised a glass with a nominal composition of 0.8CaF_2-22.6SiO_2-15.0CaO, although the fluorine loss was reportedly 7.1%. The glass had a ^{19}F MAS-NMR chemical shift position of -89ppm which was comparable to the chemical shift position for GF2.0 in this work.

The glass transition temperatures of the GF glass series in figure 7 were seen to decrease linearly as a function of increasing CaF_2 content. Both Brauer *et al.* [8] and Chen *et al.* [13] reported the same observation for a fluorine-containing bioactive glass series. The sodium-free fluorine containing bioactive glass series studied by Chen *et al.* [13] was more similar to the GF series although it contained around 6mol% P_2O_5. The similarity between the glass transition temperatures reported by Chen *et al.* [13] and those from this work is illustrated in figure 17. Brauer *et al.* [8] attributed the trend to fluorine ions bonding with calcium ions. Brauer *et al.* [8] details that in a fluorine-free glass, calcium ions binding to non-bridging oxygens has the effect of binding silicate ions together due to the electrostatic forces. When fluorine ions are incorporated, the fluorine ions bond with calcium ions. The electrostatic forces are then reduced, leading to a reduction in the glass transition temperature.

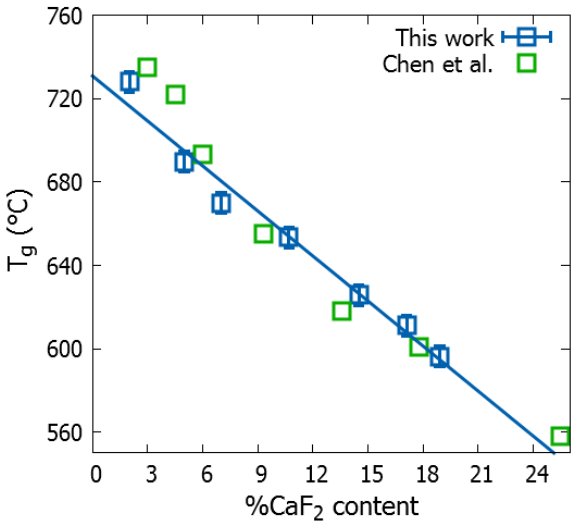

Figure 17: The glass transition temperatures of the GF glass series from figure 7 compared to those of a CaO-SiO_2-P_2O_5-CaF_2 bioactive glass series reported by Chen *et al.* [13]. A linear trend line for the GF series is included.

The total correlation functions attained from neutron diffraction experimentation are shown in figure 9. The program NXfit [35] was used to obtain information regarding the Si-O, Ca-F, Ca-O and O-O correlations as illustrated in figure 11. By considering the Si^{4+} and F^- effective ionic radii of 0.4Å and 1.1Å respectively [44], the presence of Si-F bonding would be expected to result in a nearest neighbour distance contribution around 1.5Å. However, with a Si-O nearest neighbour distance of 1.6Å, it can be seen in figure 11 that any small Si-F bonding contribution would be masked by the prevalent Si-O contribution.

The XAS experiment carried out around the calcium K-edge (4.038keV [36]) enabled to the atomic environment around calcium ions to be investigated. The accessible X-ray energy range for beamline B18 was 2-35keV [45]. It would have been challenging to investigate the atomic environments of fluorine or silicon using XAS experiments because the X-ray absorption edge energies are 0.697keV and 1.839keV respectively [36]. To perform XAS experiments on elements lighter than phosphorus (including silicon and fluorine), the samples would need to be contained under vacuum to help minimise the attenuation of the incident X-ray beam [46].

Since the calcium environment was studied using both neutron diffraction and X-ray absorption spectroscopy, it was of interest to compare the structural information attained. Marginal shifts towards higher energies ~4050eV were shown in the derivative of the XANES spectra in figure 13. By comparing the crystalline $CaSiO_3$ and CaF_2 Ca K-edge XANES spectra (figure 18), it can be interpreted that this shift to higher energies was caused by the calcium environment becoming less like a calcium silicate ($CaSiO_3$) and more like that of a calcium fluoride (CaF_2) with increasing CaF_2 contributions. As shown in table 10 from EXAFS analysis and in table 8 from ND analysis, this is supported by a decrease in the Ca-O

coordination number and an increase in the Ca-F coordination number with increasing CaF_2 concentrations.

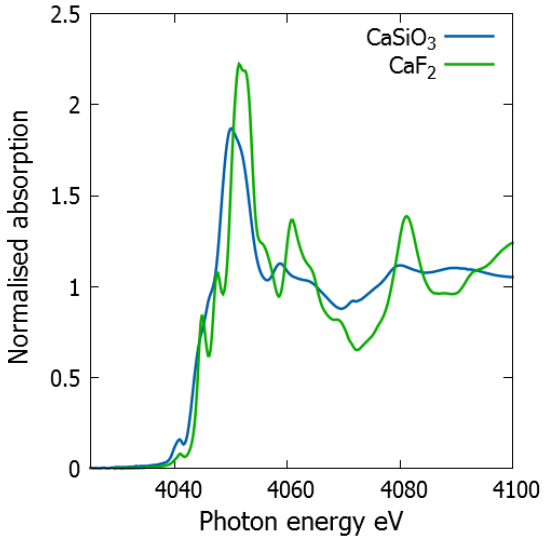

Figure 18: The XANES spectra of the $CaSiO_3$ and CaF_2 crystalline standards at the Ca K-edge.

The Ca-O and Ca-F output parameters from ND and EXAFS are compared in figure 19. The nearest neighbour distances are generally in reasonable agreement, but there are some noticeable differences between the coordination numbers and values of σ_{ij}^2. This was due to the Ca-O and Ca-F correlations overlapping in the experimental data. Since the Ca-F correlation was smaller, it was more challenging to determine its coordination number. The Ca-O correlation was larger, and so it was more difficult to establish the values of σ_{ij}^2. This was particularly evident in the total correlation function plots from neutron diffraction in figure 11. As the use of NXFit [35] with non-uniform input parameters involved restraining the Ca-F and Ca-O coordination numbers to within 10% and 5% of their input coordination number parameter values respectively, it was necessary to account for systematic errors in addition to statistical errors. This explains why the uncertainty in the Ca-F and Ca-O coordination numbers is noticeably larger than those for the other correlations.

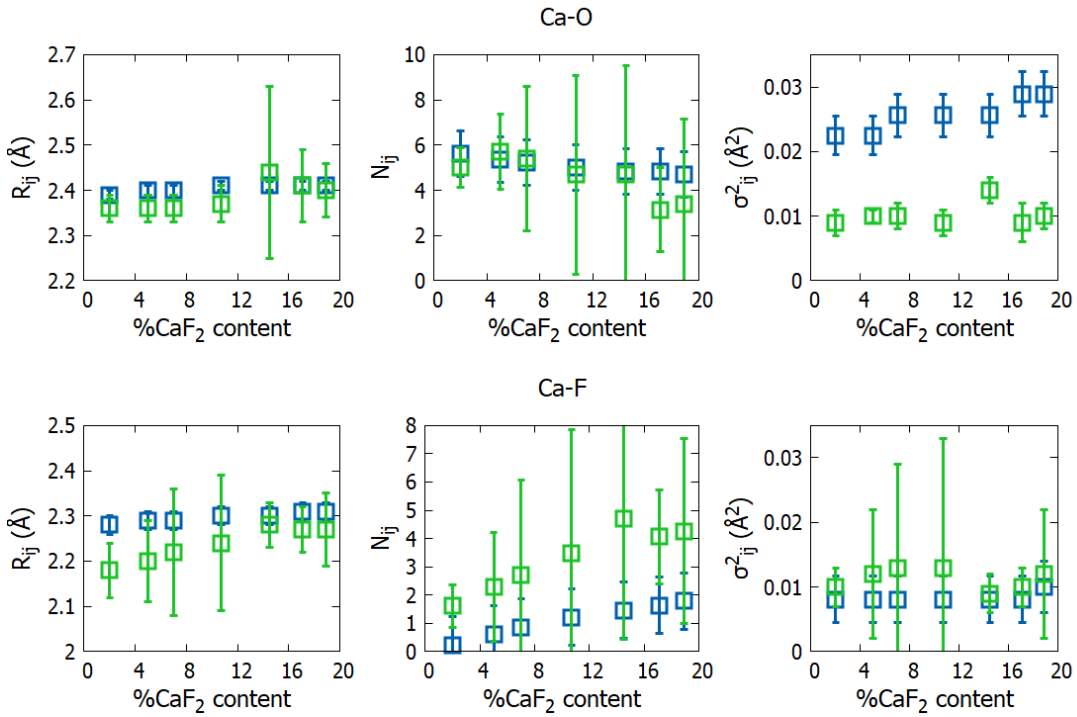

Figure 19: The nearest neighbour distances, R_{ij}, coordination numbers, N_{ij}, and values of $\sigma_{ij}{}^2$ obtained for the Ca-O (top) and Ca-F (bottom) correlations from neutron diffraction (blue squares) and X-ray absorption spectroscopy (green squares).

To further investigate the CaO-SiO_2-CaF_2 glass structure, the GF glass series could be modelled computationally using the glass compositions in table 4, and the corresponding density values in figure 5. Due to the lack of well-defined CaO-SiO_2-CaF_2 glass compositions and densities in the literature, this has not previously been possible. In addition to enabling comparisons with experimental results to be made, the glass structures could also be studied on an atomic level.

7.6 Conclusion

In this chapter, a CaO-SiO_2-CaF_2 glass series was synthesised via melt-quenching. Percent yield calculations and ^{19}F MAS-NMR spectroscopy enabled the fluorine losses via volatilisation to be ascertained. It was assumed that the losses occurred as HF. The chemical shift positions in the ^{19}F MAS-NMR spectra became more negative with increasing CaF_2 concentrations. This was indicative of the fluorine environment becoming more similar to that of pure CaF_2. The glass transition temperature declined linearly with increasing CaF_2 concentrations. Although detectable amounts of Si-F bonding were not observed using ^{29}Si solid state MAS-NMR and neutron diffraction, a total absence of Si-F bonding could not be assumed due to experimental limitations. In the solid state ^{29}Si MAS-NMR spectra, any small Si-F contribution would have been masked by the width of the spectrum and its spinning side bands. In addition, any small amount of Si-F bonding in the

total correlation function from neutron diffraction would have been concealed by the Si-O contribution as the Si-F bond length is expected to be around 1.5Å. By studying the calcium environment using X-ray absorption spectroscopy and neutron diffraction, reasonably consistent values for Ca-O and Ca-F nearest neighbour distances of 2.4Å and 2.3Å (respectively) could be obtained. However, it was challenging to establish the coordination numbers and values of σ_{ij}^2 due to the Ca-O and Ca-F correlations overlapping in the experimental data. Having established the glass compositions and densities, these challenges could be overcome by modelling the glass series computationally as will be discussed in the next chapter. This has not previously been possible for $CaO\text{-}SiO_2\text{-}CaF_2$ glasses due to a lack of well-defined compositions and densities being reported in the literature.

7.7 References

[1] J. Jones and A. Clare, Bio-Glasses: An Introduction. John Wiley & Sons, 2012.

[2] J. D. Featherstone, "The science and practice of caries prevention.," J. Am. Dent. Assoc., vol. 131, no. 7, pp. 887–899, 2000.

[3] T. T. Thuy *et al.*, "Effect of strontium in combination with fluoride on enamel remineralisation in vitro," Arch. Oral Biol., vol. 53, no. 11, pp. 1017–1022, 2008.

[4] S. E. Jabbarifar, S. Salavati, A. Akhavan, K. Khosravi, N. Tavakoli, and F. Nilchian, "Effect of fluoridated dentifrices on surface microhardness of the enamel of deciduous teeth," Dent. Res. J. (Isfahan)., vol. 8, no. 3, p. 113, 2011.

[5] R. G. Hill, D. G. Gillam, and X. Chen, "The ability of a nano hydroxyapatite toothpaste and oral rinse containing fluoride to protect enamel during an acid challenge using ^{19}F solid state NMR spectroscopy," Mater. Lett., vol. 156, pp. 69–71, 2015.

[6] E. Lynch, D. S. Brauer, N. Karpukhina, D. G. Gillam, and R. G. Hill, "Multi-component bioactive glasses of varying fluoride content for treating dentin hypersensitivity," Dent. Mater., vol. 28, no. 2, pp. 168–178, 2011.

[7] I. Farooq, Z. Imran, U. Farooq, A. Leghari, and H. Ali, "Bioactive Glass: A Material for the Future," World J. Dent., vol. 3, no. June, pp. 199–201, 2012.

[8] D. S. Brauer, N. Karpukhina, R. V. Law, and R. G. Hill, "Structure of fluoride-containing bioactive glasses," J. Mater. Chem., vol. 19, no. July 2016, p. 5629, 2009.

[9] A. Pedone, T. Charpentier, and M. C. Menziani, "The structure of fluoride-containing bioactive glasses: New insights from first-principles calculations and solid state NMR spectroscopy," J. Mater. Chem., vol. 22, no. 25, pp. 12599–12608, 2012.

[10] D. S. Brauer, N. Karpukhina, M. D. O'Donnell, R. V. Law, and R. G. Hill, "Fluoride-containing bioactive glasses: Effect of glass design and structure on degradation, pH and apatite formation in simulated body fluid," Acta Biomater., vol. 6, no. 8, pp. 3275–3282, 2010.

[11] D. S. Brauer, M. N. Anjum, M. Mneimne, R. M. Wilson, H. Doweidar, and R. G. Hill, “Fluoride-containing bioactive glass-ceramics,” J. Non. Cryst. Solids, vol. 358, no. 12–13, pp. 1438–1442, 2012.

[12] M. Mneimne, R. G. Hill, A. J. Bushby, and D. S. Brauer, “High phosphate content significantly increases apatite formation of fluoride-containing bioactive glasses,” Acta Biomater., vol. 7, no. 4, pp. 1827–1834, 2011.

[13] X. Chen, X. Chen, D. S. Brauer, R. M. Wilson, R. G. Hill, and N. Karpukhina, “Novel alkali free bioactive fluorapatite glass ceramics,” J. Non. Cryst. Solids, vol. 402, pp. 172–177, 2014.

[14] K. Stanton and R. Hill, “The role of fluorine in the devitrification of $SiO_2{\cdot}Al_2O_3{\cdot}P_2O_5{\cdot}CaO{\cdot}CaF_2$ glasses,” J. Mater. Sci., vol. 35, pp. 1911–1916, 2000.

[15] M. Susa, T. Sakamaki, and R. Kojima, “Chemical states of fluorine in CaF_2-CaO-SiO_2 and NaF-Na_2O-SiO_2 glassy slags from the perspective of elecronic polarisability,” Ironmak. Steelmak., vol. 32, no. 1, pp. 13–20, 2005.

[16] M. Hayashi, N. Nabeshima, H. Fukuyama, and K. Nagata, “Effect of fluorine on silicate network for CaO-CaF_2-SiO_2 and CaO-CaF_2-SiO_2-FeO_x glasses,” ISIJ Int., vol. 42, no. 4, pp. 352–358, 2002.

[17] D. Kumar, R. G. Ward, and D. J. Williams, “Effect of Fluorides on Silicates and Phosphates,” Discuss. Faraday Soc., vol. 1, pp. 147–154, 1961.

[18] Y. Tsunawaki, N. Iwamoto, T. Hattori, and A. Mitsuishi, “Analysis of CaO-SiO_2 and CaO-SiO_2-CaF_2 Glasses by Raman Spectroscopy,” J. Non. Cryst. Solids, vol. 44, no. 2–3, pp. 369–378, 1981.

[19] N. Iwamoto and Y. Makino, “A structural investigation of calcium fluorosilicate glasses,” J. Non. Cryst. Solids, vol. 46, no. 1, pp. 81–94, 1981.

[20] R. W. Luth, “Raman spectroscopic study of the solubility mechanisms of F in glasses in the system CaO-CaF_2-SiO_2,” Am. Mineral., vol. 73, pp. 297–305, 1988.

[21] S. Hayakawa, A. Nakao, C. Ohtsutki, A. Osaka, S. Matsumoto, and Y. Miura, “An X-ray photoelectron spectroscopic study of the chemical states of fluorine atoms in calcium silicate glasses,” J. Mater. Res., vol. 13, no. 3, pp. 739–743, 1998.

[22] T. Watanabe, M. Hayashi, S. Hayashi, H. Fukuyama, and K. Nagata, “Solid-state ^{19}F NMR on CaO-SiO_2-CaF_2 glasses,” Mater. Sci., pp. 699–706, 2004.

[23] T. Watanabe, H. Fukuyama, and K. Nagata, “Stability of cuspidine ($3CaO{\cdot}2SiO_2{\cdot}CaF_2$) and phase relations in the CaO–SiO_2–CaF_2 system,” ISIJ Int., vol. 42, no. 5, pp. 489–497, 2002.

[24] J. E. Shelby, Introduction to glass science and technology. Royal Society of Chemistry, 2005.

[25] G. Lusvardi *et al.*, “Elucidation of the Structural Role of Fluorine in Potentially Bioactive Glasses by Experimental and Computational Investigation,” J. Phys. Chem. B, vol. 112, pp. 12730–12739, 2008.

[26] M. Mneimne, “Development of Bioactive Glasses for Dental Treatments,” Queen

Mary University London, 2014.

[27] D. S. Brauer, M. Mneimne, and R. G. Hill, “Fluoride-containing bioactive glasses: Fluoride loss during melting and ion release in tris buffer solution,” J. Non. Cryst. Solids, vol. 357, no. 18, pp. 3328–3333, 2011.

[28] J. F. Stebbins and Q. Zeng, “Cation ordering at fluoride sites in silicate glasses: a high-resolution ^{19}F NMR study,” J. Non. Cryst. Solids, vol. 262, pp. 1–5, 2000.

[29] Q. Zeng and J. F. Stebbins, “Fluoride sites in aluminosilicate glasses: High-resolution ^{19}F NMR results,” Am. Mineral., vol. 85, no. 5–6, pp. 863–867, 2000.

[30] T. M. Duncan, D. C. Douglass, R. Csencsits, and K. L. Walker, “Study of fluorine in silicate glass with ^{19}F nuclear magnetic resonance spectroscopy,” J. Appl. Phys., vol. 60, no. 1, pp. 130–136, 1986.

[31] V. M. Fokin, R. M. C. V Reis, A. S. Abyzov, C. R. Chinaglia, and E. D. Zanotto, “Nonstoichiometric crystallization of lithium metasilicate–calcium metasilicate glasses. Part 1 - Crystal nucleation and growth rates,” J. Non. Cryst. Solids, vol. 362, no. September 2015, pp. 56–64, 2013.

[32] R. G. Hill and D. S. Brauer, “Predicting the glass transition temperature of bioactive glasses from their molecular chemical composition,” Acta Biomater., vol. 7, no. 10, pp. 3601–3605, 2011.

[33] A. K. Soper, “GudrunN and GudrunX: programs for correcting raw neutron and X-ray diffraction data to differential scattering cross section,” Sci. Technol. Facil. Counc., 2011.

[34] C. M. Moreton-Smith, S. D. Johnston, and F. A. Akeroyd, “Open GENIE—a generic multi-platform program for the analysis of neutron scattering data,” J. Neutron Res., vol. 4, pp. 41–47, 1996.

[35] D. Pickup, R. Moss, and R. Newport, “NXFit : a program for simultaneously fitting X-ray and neutron diffraction pair-distribution functions to provide optimized structural parameters,” J. Appl. Crystallogr., vol. 47, pp. 1790–1796, 2014.

[36] W. T. Elam, B. D. Ravel, and J. R. Sieber, “A new atomic database for X-ray spectroscopic calculations,” Radiat. Phys. Chem., vol. 63, pp. 121–128, 2002.

[37] B. Ravel and M. Newville, “ATHENA , ARTEMIS , HEPHAESTUS : data analysis for X-ray absorption spectroscopy using IFEFFIT,” pp. 537–541, 2005.

[38] J. Hormes, A. Diekamp, W. Klysubun, G. L. Bovenkamp, and N. Börste, “The characterization of historic mortars: A comparison between powder diffraction and synchrotron radiation based X-ray absorption and X-ray fluorescence spectroscopy,” Microchem. J., vol. 125, pp. 190–195, 2016.

[39] J. J. Rehr, J. J. Kas, M. P. Prange, A. P. Sorini, and Y. Takimoto, “Ab initio theory and calculations of X-ray spectra,” C. R. Phys., vol. 10, no. 6, pp. 548–559, 2009.

[40] S. Calvin, XAFS for Everyone. CRC Press, 2013.

[41] R. G. Hill, N. D. Costa, and R. V. Law, “Characterization of a mould flux glass,” J. Non. Cryst. Solids, vol. 351, no. 1, pp. 69–74, 2005.

[42] D. S. Brauer, A. Al-Noaman, R. G. Hill, and H. Doweidar, “Density-structure correlations in fluoride-containing bioactive glasses,” Mater. Chem. Phys., vol. 130, no. 1, pp. 121–125, 2011.

[43] J. Schneider, V. R. Mastelaro, H. Panepucci, and E. D. Zanotto, “^{29}Si MAS–NMR studies of Q^n structural units in metasilicate glasses and their nucleating ability,” J. Non. Cryst. Solids, vol. 273, pp. 8–18, 2000.

[44] R. D. Shannon, “Revised Effective Ionic Radii and Systematic Studies of Interatomic Distances in Halides and Chalcogenides,” Acta Crystallogr., no. A32, p. 751, 1976.

[45] A. J. Dent *et al.*, “B18: A core XAS spectroscopy beamline for Diamond,” J. Phys. Conf. Ser., vol. 190, p. 12039, 2009.

[46] J. A. McCleverty and T. J. Meyer, Comprehensive coordination chemistry II. Elsevier Ltd, 2004.

8. A Computational Investigation of the Structure of $CaO\text{-}SiO_2\text{-}CaF_2$ Glasses

8.1 Introduction

As mentioned in the previous chapter, comprehending the structure of $CaO\text{-}SiO_2\text{-}CaF_2$ fluorine-containing silicate systems is of interest not only for mould flux applications in the continuous casting of steel (e.g. [1]–[3]), but also for bioactive glass applications in dentistry (e.g. [4]–[6]). Despite this interest, the conclusions drawn from previous experimental and computational studies have been contradictory (e.g. [7]), and in particular, the structural role of fluorine remains unclear (e.g. [1], [2]).

The structure of a $CaO\text{-}SiO_2\text{-}CaF_2$ glass series was studied experimentally in the previous chapter. Although detectable amounts of Si-F bonding were not observed, it remains unclear as to whether any small amount of Si-F bonding could occur. Computational modelling can be used to investigate this, as well as for further structural characterisation. Currently, there are few computational studies on $CaO\text{-}SiO_2\text{-}CaF_2$ glass in the literature. Lusvardi *et al.* [8] attributed this to a lack of available suitable interatomic potential parameters. Hayakawa *et al.* [9] modelled a $40CaO\text{-}40SiO_2\text{-}20CaF_2$ glass using Busing-Ida-Gilbert interatomic potential parameters. Clusters of calcium and fluorine ions were observed, but the model only comprised of 312 atoms and no quantitative analysis was undertaken. The same authors later modelled $45CaO\text{-}45SiO_2\text{-}10CaF_2$ and $40CaO\text{-}40SiO_2\text{-}20CaF_2$ glass again using Busing-Ida-Gilbert interatomic potential parameters [10]. A lack of Si-F bonding was reported. However, the model only comprised of 600 atoms, and details on how the melt was quenched to form a solid glass model was not reported, deeming the study inadequate.

The $CaO\text{-}SiO_2\text{-}CaF_2$ glass series whose synthesis was reported in the previous chapter was therefore modelled computationally in this work. This was achieved using classical molecular dynamics with the addition of the adiabatic core-shell model to account for anion polarisability. Results including glass model images, pair correlation functions, cumulative coordination number plots, silicon network connectivity distributions, and partial and total structure factors were used to characterise the structure of the $CaO\text{-}SiO_2\text{-}CaF_2$ glass series.

8.2 Computational Modelling Methodology

The $CaO\text{-}SiO_2\text{-}CaF_2$ glass compositions and corresponding densities were established in the previous chapter. It was therefore only necessary to acquire suitable interatomic potential parameters before the $CaO\text{-}SiO_2\text{-}CaF_2$ glass compositions could be modelled computationally. In this chapter, the atomic correlations (e.g. O-O) correspond to core atomic correlations unless explicitly stated otherwise. The $O_s\text{-}O_s$ correlation for example refers to oxygen shells.

8.2.1 $CaO\text{-}SiO_2\text{-}CaF_2$ System – Fitting Interatomic Potential Parameters

The General Utility Lattice Program (GULP) [11] can be used to test the suitability of interatomic potential parameters (section 2.3.3). As detailed in section 6.2.1 and 6.2.2, using the interatomic potential parameters reported by Malavasi *et al.* [12] (table 1) enabled the CaO [13] and $CaSiO_3$ [14] crystalline structures to be closely reproduced following GULP energy minimisation. However, in order to model the $SiO_2\text{-}CaO\text{-}CaF_2$ glasses computationally, further interatomic potential parameters are required. These include $Ca\text{-}F_s$, $F_s\text{-}F_s$, $F_s\text{-}O_s$, and $Si\text{-}F_s$. Most of these interatomic potential parameters involving fluorine have been reported by Rabone and De Leeuw [15], as shown in table 2. It was important to test these, and since two $F_s\text{-}O_s$ interatomic potentials had been reported, the most suitable needed to be identified.

Table 1: The two-body and three-body interatomic potential parameters of Buckingham and screened harmonic form respectively as reported by Malavasi *et al.* [12].

	Two-body $V_{ij}(r) = A_{ij}\exp\left(\frac{-r}{\rho_{ij}}\right) - \frac{C_{ij}}{r^6}$		
	A_{ij} (eV)	ρ_{ij} (Å)	C_{ij} (eV Å^6)
$O_s - O_s$	22764.30	0.1490	27.88
$Si - O_s$	1283.91	0.32052	10.66158
$Ca - O_s$	2152.3566	0.309227	0.09944
	Three-body $V(\theta_{jik}) = \frac{k_3}{2}(\theta_{jik} - \theta_0)^2 \exp\left[-\left(\frac{r_{ij}}{\rho} + \frac{r_{ik}}{\rho}\right)\right]$		
	k_3 (eV rad^{-2})	θ_0 (°)	ρ (Å)
$O_s - Si - O_s$	100	109.47	1.0
	Core-shell potential $V = \frac{1}{2}K_{cs}r^2$		
	K_{cs} (eV Å^{-2})	Q (core) (e)	q (shell) (e)
$O - O_s$	74.92	0.8482	-2.8482
Si		4.000	
Ca		2.000	

Table 2: Two-body Buckingham interatomic potential parameters involving fluorine reported by Rabone and De Leeuw [15]. In [15], the term $O_{(p)}$ was used to denote oxygen in PO_4^{3-}, CO_3^{2-}, SiO_4^{4-}, while the term $O_{(H)}$ was used to denote oxygen in OH^-.

	Two body $V_{ij}(r) = A_{ij}\exp\left(\frac{-r}{\rho_{ij}}\right) - \frac{C_{ij}}{r^6}$		
	A_{ij} (eV)	ρ_{ij} (Å)	C_{ij} (eV Å^6)
$Ca - F_s$	1272.80	0.299700	0.00
$F_s - F_s$	99731834	0.120130	17.02
$F_s - O_{s\,(H)}$	35000.00	0.175000	15.40
$F_s - O_{s\,(P)}$	583833.70	0.211630	7.68
$Na - F_s$	1254.00	0.274464	0.00
	Core-shell potential $V = \frac{1}{2}K_{cs}r^2$		
	K_{cs} (eV Å^{-2})	Q (core) (e)	q (shell) (e)
$F - F_s$	101.20	1.380	-2.380
$O_{(H)} - O_{s\,(H)}$	74.92	0.900	-2.300
$O_{(P)} - O_{s\,(P)}$	507.40	0.587	-1.632

The Ca-F_s and F_s-F_s interatomic potential parameters in table 2 were tested on a CaF_2 crystalline structure [16] (figure 1) using GULP. It can be seen in table 3 that the crystalline structure was closely reproduced. The input Ca-F and F-F nearest neighbour distances of 2.37Å and 2.73Å became 2.36Å and 2.72Å respectively after GULP energy minimisation. The coordination numbers of 8.00 and 6.00 respectively were unchanged. The Ca-F_s and F_s-F_s interatomic potentials were therefore deemed appropriate for this study.

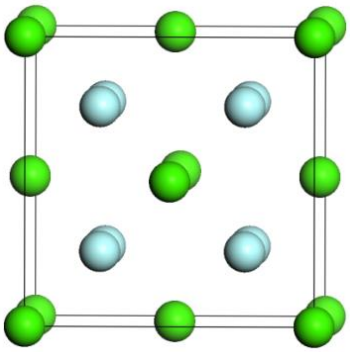

Figure 1: The CaF_2 crystalline structure reproduced from Jette and Fotte [17]. The green and blue spheres represent calcium and fluorine atoms respectively.

Table 3: The GULP energy minimisation results testing the performance of the Ca-F_s and F_s-F_s interatomic potentials (table 2) using crystalline CaF_2 [17].

Parameter	Unit	Initial value	Percent change (%)
Volume	$Å^3$	163.08	-1.14
a	Å	5.46	-0.38
b	Å	5.46	-0.38
c	Å	5.46	-0.38
α	°	90.00	0.00
β	°	90.00	0.00
γ	°	90.00	0.00

The F_s-O_s and Si-F_s interatomic potential parameters still needed to be established. The F_s-O_s interatomic potential parameters reported by Rabone and De Leeuw [15] failed to maintain charge neutrality on oxygen, and there were no reports of a Si-F_s interatomic potential parameter of Buckingham form in the literature. As it would have been challenging to fit two interatomic potential parameters simultaneously due to the number of parameters involved, it was necessary to use one of the F_s-O_s interatomic potentials from table 2. The F_s-$O_{s(H)}$ interatomic potential was chosen because the charges on the oxygen ion were closer to neutrality. For consistency with the other interatomic potential parameters involving oxygen, the ion core and shell charges reported by Malavasi *et al.* [12] (which are charge neutral) were assigned to the F_s-$O_{s(H)}$ interatomic potential parameter. The GULP program was then used to fit the Si-F_s interatomic potential parameter manually using the SiF_4 [18], $CaSiF_6$ [19], and Na_2SiF_6 [20] crystalline structures shown in figure 2.

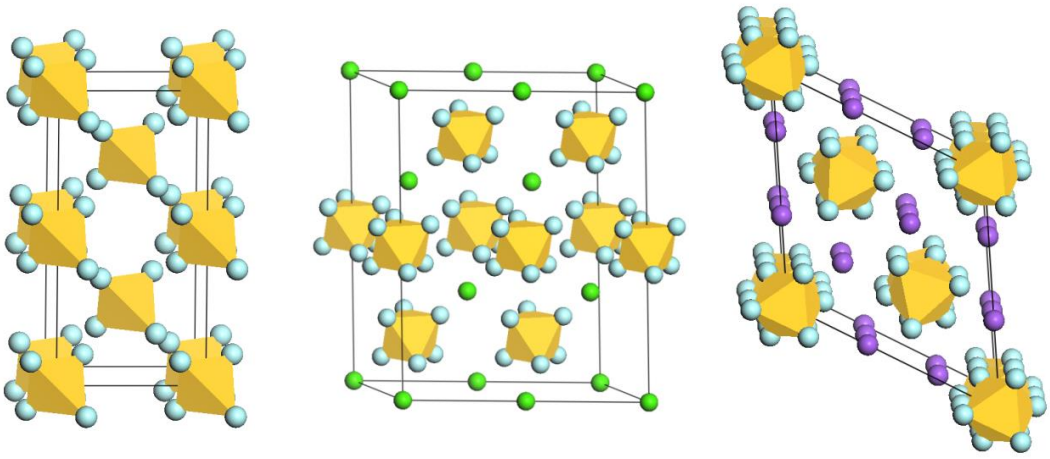

Figure 2: From left to right; the SiF_4 [21], $CaSiF_6$ [22], and Na_2SiF_6 [20] crystal structures used to fit the Si-F_s interatomic potential parameter. The yellow tetrahedra represent silicon ions. The blue, green, and purple spheres represent fluorine, calcium, and sodium ions respectively.

The starting approximation for the Si-F_s interatomic potential parameter (table 4) in the manual fit was attained by averaging the Si-O_s and Si-Cl_s interatomic potential parameters A_{ij}, ρ_{ij}, and C_{ij}. This was because the Si-O separation distance is similar to that of Si-F, and the ion charges of chlorine and fluorine are equivalent. To further develop this Si-F_s interatomic potential, it was manually altered one parameter at a time. Changes to the system volume, coordination numbers, and nearest neighbour distances were continuously monitored using GULP until further improvements could no longer be made, and the overall changes to the input crystal structures had been minimised. This technique had also been used to fit the Si-Cl_s interatomic potential parameter in section 6.2.3.

Table 4: The starting values for the two-body Si-F_s Buckingham interatomic potential based on the average of the Si-O_s and Si-Cl_s Buckingham interatomic potentials.

	Two body $V_{ij}(r) = A_{ij}\exp\left(\frac{-r}{\rho_{ij}}\right) - \frac{C_{ij}}{r^6}$		
	A_{ij} (eV)	ρ_{ij} (Å)	C_{ij} (eV Å^6)
$Si - O_s$	1283.91	0.32052	10.66158
$Si - Cl_s$	1063.00	0.3352	17.00
$Si - F_s$	1173.46	0.3279	13.83

The final parameters of the Si-F_s Buckingham interatomic potential parameter were A_{ij}=771.0eV, ρ_{ij}=0.298Å, and C_{ij}=0.0eVÅ^6. The ability of the core-shell model interatomic potential parameters to reproduce the SiF_4 [21], $CaSiF_6$ [22], and Na_2SiF_6 [20] crystal structures is shown in table 5. Although some volume change was anticipated following GULP energy minimisation since the crystal structures are molecular crystals, some of the structural changes exhibited were significant. For example, the interatomic potential parameters failed to reproduce the F-F coordination number of 3.00 in SiF_4. As corresponding rigid-ion interatomic potential parameters from Teter [23] were available (table 6), it was of interest to compare the two sets of interatomic potential parameters.

Table 5: The GULP energy minimisation results comparing the performance of the core-shell model (SM) and the rigid-ion (RI) interatomic potential parameters using crystalline SiF_4, $CaSiF_6$, and Na_2SiF_6 structures. The terms R_{ij} and N_{ij} denote the nearest neighbour distances and coordination numbers respectively.

	SM			RI		
	SiF_4 [21] In/out	$CaSiF_6$ [22] In/out	Na_2SiF_6 [20] In/out	SiF_4 [21] In/out	$CaSiF_6$ [22] In/out	Na_2SiF_6 [20] In/out
R_{Si-F} (Å)	1.54/1.62	1.66/1.80	1.68/1.80	1.54/1.62	1.66/1.72	1.68/1.72
N_{Si-F}	4.00/4.00	6.00/6.00	6.00/6.00	4.00/4.00	6.00/6.00	6.00/6.00
R_{F-F} (Å)	2.52/2.62	2.35/2.55	2.38/2.55	2.52/2.61	2.35/2.43	2.38/2.43
N_{F-F}	3.00/9.00	4.00/4.00	4.00/4.00	3.00/9.00	4.00/4.00	4.00/4.00
R_{Si-Si} (Å)	4.74/4.34	5.35/4.89	5.04/5.44	4.74/4.24	5.35/4.99	5.04/4.76
N_{Si-Si}	8.00/8.00	6.00/6.00	2.00/2.00	8.00/8.00	6.00/6.00	2.00/2.00
R_{Ca-F} (Å)		2.27/2.30			2.27/2.30	
N_{Ca-F}		6.00/6.00			6.00/6.00	
R_{Si-Ca} (Å)		3.83/3.64			3.83/3.79	
N_{Si-Ca}		6.00/6.00			6.00/6.00	
R_{Ca-Ca} (Å)		5.48/4.89			5.48/4.99	
N_{Ca-Ca}		6.00/6.00			6.00/6.00	
R_{Na-F} (Å)			2.32/2.43			2.32/2.33
N_{Na-F}			6.00/6.00			6.00/6.00
R_{Si-Na} (Å)			3.36/3.35			3.36/3.26
N_{Si-Na}			3.00/3.00			3.00/3.00
R_{Na-Na} (Å)			3.92/4.16			3.92/3.90
N_{Na-Na}			6.00/6.00			6.00/6.00
Volume ($Å^3$)	164.21/ 126.14	336.66/ 286.03	342.42/ 400.07	164.21/ 117.1	336.66/ 318.21	342.42/ 347.47

Table 6: The two-body rigid-ion interatomic potential parameters of Buckingham form as reported by Teter [23].

	Two-body $V_{ij}(r) = A_{ij}\exp\left(\frac{-r}{\rho_{ij}}\right) - \frac{C_{ij}}{r^6}$		
	A_{ij} (eV)	ρ_{ij} (Å)	C_{ij} (eV $Å^6$)
$O-O$	1844.7458	0.343645	192.58
$Si-O$	13702.905	0.193817	54.681
$Ca-O$	7747.1834	0.252623	93.109
$Na-F$	58286.140	0.1691	4.1555
$Ca-F$	976421.09	0.1473	12.163
$F-F$	11510.594	0.2250	29.527
$Si-F$	53193.487	0.1468	5.0196

As shown in table 5, the rigid-ion interatomic potential parameters in table 6 also failed to reproduce the F-F coordination number of 3.00 in SiF_4. The rigid-ion interatomic potential parameters did however replicate the input $CaSiF_6$ and Na_2SiF_6 crystal structures more closely, although Zirl and Garofalini [24] have emphasised the importance of accounting for

anion polarisability in computational simulations. It was therefore preferable to improve the performance of the core-shell model interatomic potentials. To do this without altering the Buckingham interatomic potential parameter values, the strength of the F-F_s spring constant (K_{cs}) value was changed as shown in table 7.

Table 7: The nearest neighbour distances (R_{ij}), coordination numbers (N_{ij}), and simulation cell volumes (Vol) in the SiF_4, $CaSiF_6$, and $NaSi_2F_6$ crystalline structures prior to and following GULP energy minimisation. Rigid-ion (RI) interatomic potentials and core-shell model (SM) interatomic potentials with differing spring constants were used. The terms SM1, SM2, SM3, SM4, and SM5 correspond to using spring constants (K_{CS}) of 100eVÅ^{-2}, 200eVÅ^{-2}, 300eVÅ^{-2}, 400eVÅ^{-2}, and 500eVÅ^{-2} respectively.

	SiF_4 [21]			$CaSiF_6$ [22]				$NaSi_2F_6$ [20]			
	R_{Si-F} (Å)/ N_{Si-F}	R_{F-F} (Å)/ N_{F-F}	Vol (Å^3)	R_{Si-F} (Å)/ N_{Si-F}	R_{F-F} (Å)/ N_{F-F}	R_{Ca-F} (Å)/ N_{Ca-F}	Vol (Å^3)	R_{Si-F} (Å)/ N_{Si-F}	R_{F-F} (Å)/ N_{F-F}	R_{Na-F} (Å)/ N_{Na-F}	Vol (Å^3)
Input	1.54/ 4.00	2.52/ 3.00	164.21	1.66/ 6.00	2.35/ 4.00	2.27/ 6.00	336.66	1.68/ 6.00	2.38/ 4.00	2.32/ 6.00	342.42
RI	1.62/ 4.00	2.61/ 9.00	117.13	1.72/ 6.00	2.43/ 4.00	2.30/ 6.00	318.21	1.72/ 6.00	2.43/ 6.00	2.33/ 6.00	347.47
SM1	1.62/ 4.00	2.62/ 9.00	126.14	1.80/ 6.00	2.55/ 4.00	2.30/ 6.00	286.03	1.80/ 6.00	2.55/ 6.00	2.43/ 6.00	400.07
SM2	1.56/ 4.00	2.58/ 9.00	115.48	1.75/ 6.00	2.48/ 4.00	2.25/ 6.00	382.17	1.76/ 6.00	2.49/ 4.00	2.42/ 6.00	401.01
SM3	1.55/ 4.00	2.56/ 9.00	112.60	1.74/ 6.00	2.46/ 4.00	2.25/ 6.00	381.30	1.75/ 6.00	2.47/ 4.00	2.43/ 4.00	401.30
SM4	1.54/ 4.00	2.55/ 9.00	111.30	1.74/ 6.00	2.45/ 4.00	2.25/ 6.00	380.16	1.74/ 6.00	2.46/ 4.00	2.43/ 4.00	401.46
SM5	1.53/ 4.00	2.54/ 9.00	110.57	1.73/ 6.00	2.45/ 4.00	2.25/ 6.00	379.50	1.73/ 6.00	2.45/ 4.00	2.43/ 4.00	401.58

The GULP energy minimisation results in table 7 show that increasing the F-F_s spring constant (K_{CS}) lowers the nearest neighbour distances, bringing them into closer agreement with the input crystalline structures. However, increasing the F-F_s spring constant generally increases the disagreement between the input and output simulation cell volumes. Furthermore, increasing the spring constant ultimately leads to diminishing returns. It was therefore necessary to compromise, and increasing the spring constant to K_{CS}=200eVÅ^{-2} was found to be appropriate. The interatomic potential parameters for modelling the CaO-SiO_2-CaF_2 glass series are shown below in table 8.

Table 8: The two-body and three-body interatomic potential parameters of Buckingham and screened harmonic form respectively for modelling CaO-SiO_2-CaF_2 glass. The oxygen and fluorine shell masses used were 0.2u and 0.8u respectively. The inner cut-offs for the O_s-O_s, F_s-F_s, F_s-O_s, and Ca-F_s interatomic potentials were 1.7Å. The Ca-O_s, Si-O_s, and Si-F_s interatomic potentials had inner cut-offs of 1.5Å, 1.2Å, and 1.0Å respectively.

	Two-body $V_{ij}(r) = A_{ij}\exp\left(\frac{-r}{\rho_{ij}}\right) - \frac{C_{ij}}{r^6}$		
	A_{ij} (eV)	ρ_{ij} (Å)	C_{ij} (eV Å^6)
$O_s - O_s$	22764.30	0.1490	27.88
$Si - O_s$	1283.91	0.32052	10.66158
$Ca - O_s$	2152.3566	0.309227	0.09944
$Na - F_s$	1254.00	0.274464	0.00
$Ca - F_s$	1272.80	0.299700	0.00
$F_s - F_s$	99731834	0.120130	17.02
$Si - F_s$	771.0	0.298	0.00
	Three-body $V(\theta_{jik}) = \frac{k_3}{2}(\theta_{jik} - \theta_0)^2 \exp\left[-\left(\frac{r_{ij}}{\rho} + \frac{r_{ik}}{\rho}\right)\right]$		
	k_3 (eV rad^{-2})	θ_0 (°)	ρ (Å)
$O_s - Si - O_s$	100	109.47	1.0
	Core-shell potential $V = \frac{1}{2}K_{cs}r^2$		
	K_{cs} (eV Å^{-2})	Q (core) (e)	q (shell) (e)
$O - O_s$	74.92	0.8482	-2.8482
$F - F_s$	200.00	1.380	-2.380
Si		4.000	
Ca		2.000	

It would have been ideal to test the interatomic potential parameters in table 8 on known non-crystalline structures (i.e. liquids or glasses) from the CaO-SiO_2-CaF_2 system, analogous to what was done in section 6.2.3. However, to the author's knowledge, there are no neutron or X-ray diffraction studies on SiF_4. Additionally, the lack of density values previously reported in experimental studies of CaO-SiO_2-CaF_2 glasses or melts (e.g. [25]) have prevented them from being modelled computationally in this work, and hence prevented comparisons being made with previous work.

8.2.2 CaO-SiO_2-CaF_2 System – Glass Modelling

During the synthesis of the CaO-SiO_2-CaF_2 glass series whose nominal compositions maintained an equal CaO/SiO_2 ratio, some losses due to fluorine volatilisation were exhibited (section 7.3). The compositions failed to uphold their equal CaO/SiO_2 ratios and were subsequently revised. In this chapter, the revised CaO-SiO_2-CaF_2 glass series in table 9 is referred to as the GF glass series. When referring to a specific composition in the series,

the term GF is followed by the CaF_2 content. For example, GF2.0 refers to the 49.7CaO-48.4SiO_2-2.0CaF_2 glass.

Table 9: The GF glass compositions, reduced density values equivalent to 95% of the experimental densities, number of atoms, and simulation box side lengths used for computational modelling.

	CaO	SiO_2	CaF_2	ρ (g/cm^3)	Atoms	Length (Å)
GF2.0	49.7	48.4	2.0	2.76	10014	52.01
GF5.0	48.3	46.7	5.0	2.77	10068	52.12
GF7.0	47.7	45.4	7.0	2.78	10094	52.17
GF10.7	45.3	44.1	10.7	2.79	10190	52.33
GF14.5	43.6	42.0	14.5	2.81	10258	52.42
GF17.1	42.4	40.5	17.1	2.82	10304	52.51
GF18.9	41.6	39.5	18.9	2.84	10336	52.48

The GF glass series was modelled using the same approach detailed in section 6.2.4 for the QCl and ACl glass series. This included running rigid-ion stages to obtain input configurations for the core-shell model stages which were then run at lower temperatures. The rigid-ion stages used core-shell model interatomic potentials as an estimate for the rigid-ion interatomic potentials, as shown in table 10. Anion shells were therefore not included. The rigid-ion stages included a 6000K stage, a 3000K stage, a 2000K stage, a quench stage from 2000K to 300K at a rate of 10^{13}K/s, a 300K stage, and a final sampling stage at 300K. Each single temperature stage was run for 400,000 time-steps where the time-step was 1fs. To achieve the quench rate of 10^{13}K/s from 2000K to 300K, 170,000 time-steps were required.

Table 10: The two-body and three-body rigid-ion interatomic potential parameters of Buckingham and screened harmonic form respectively based on the core-shell model interatomic potential parameters in table 8. The inner cut-offs for the O-O, F-F, F-O, and Ca-F interatomic potentials were 1.7Å. The Ca-O, Si-O, and Si-F interatomic potentials had inner cut-offs of 1.5Å, 1.2Å, and 1.0Å respectively.

	Two-body $V_{ij}(r) = A_{ij}\exp\left(\frac{-r}{\rho_{ij}}\right) - \frac{C_{ij}}{r^6}$		
	A_{ij} (eV)	ρ_{ij} (Å)	C_{ij} (eV Å^6)
$O-O$	22764.30	0.1490	27.88
$Si-O$	1283.91	0.32052	10.66158
$Ca-O$	2152.3566	0.309227	0.09944
$Na-F$	1254.00	0.274464	0.00
$Ca-F$	1272.80	0.299700	0.00
$F-F$	99731834	0.120130	17.02
$Si-F$	771.0	0.298	0.00
	Three-body $V(\theta_{jik}) = \frac{k_3}{2}(\theta_{jik} - \theta_0)^2 \exp\left[-\left(\frac{r_{ij}}{\rho} + \frac{r_{ik}}{\rho}\right)\right]$		
	k_3 (eV rad^{-2})	θ_0 (°)	ρ (Å)
$O-Si-O$	100	109.47	1.0
	Core-shell potential $V = \frac{1}{2}K_{cs}r^2$		
	Q (core) (e)		
$O-O$	-2.000		
$F-F$	-1.000		
Si	4.000		
Ca	2.000		

In the core-shell model stages that followed, core-shell model interatomic potential parameters were used (table 8). The oxygen and fluorine anions in the final configuration of atoms from the rigid-ion stages were split into separate core and shell units. These were connected by a harmonic spring of spring constant K_{cs} which was frictionally damped using a damping coefficient, c, of 100kgs^{-1} (section 6.2.1). From the atomic masses of oxygen (15.9994u) and fluorine (18.998u), shell masses of 0.20u and 0.80u respectively were assigned. The shell mass of the fluorine anion was noticeably lower than that of the chlorine anion (1.50 u) in section 6.2.4. This was due to differences in their atomic mass. The core-shell model stages began at 2000K. The system was then quenched from 2000K to 300K at a rate of 10^{13}K/s, and a stage at 300K followed. A further stage at 300K was run and used for analysis. The single temperature stages ran for 800,000 time-steps. This was to help compensate for the smaller time-step of 0.1fs. The quench stage required 1,700,000 time-steps. All simulation stages (rigid-ion and core-shell model stages) were fully equilibrated and an NVT Berendsen thermostat was used. A universal cut-off of 12.0Å, a primary cut-off of 10.0Å, and a van der Waals cut-off of 8.0Å were applied. System densities equivalent to 95% of the experimental densities were found to be necessary to obtain system pressures lower than 10kbar at 300K. The compositions, reduced density

values, number of atoms, and simulation cell side lengths used to model the GF glass series are detailed in table 9.

8.3 Results

8.3.1 Images of Models

Images of the GF glass models are shown in figure 3. The ions appear to be randomly distributed and the models do not seem to become phase separated with increasing CaF_2 contributions. Upon close inspection of the computational models, some Si-F bonding in SiO_3F, SiO_4F, and SiO_3F_2 structural units was observed. In addition, SiO_4F_2 structural units were observed in two of the seven models but in very small proportions, hence they are not referred to beyond this section and were considered to be defects. The proportion of silicon ions involved in SiO_3F, SiO_4F, and SiO_3F_2 structural units (figure 3h) generally increases with increasing CaF_2 content as quantified in table 11.

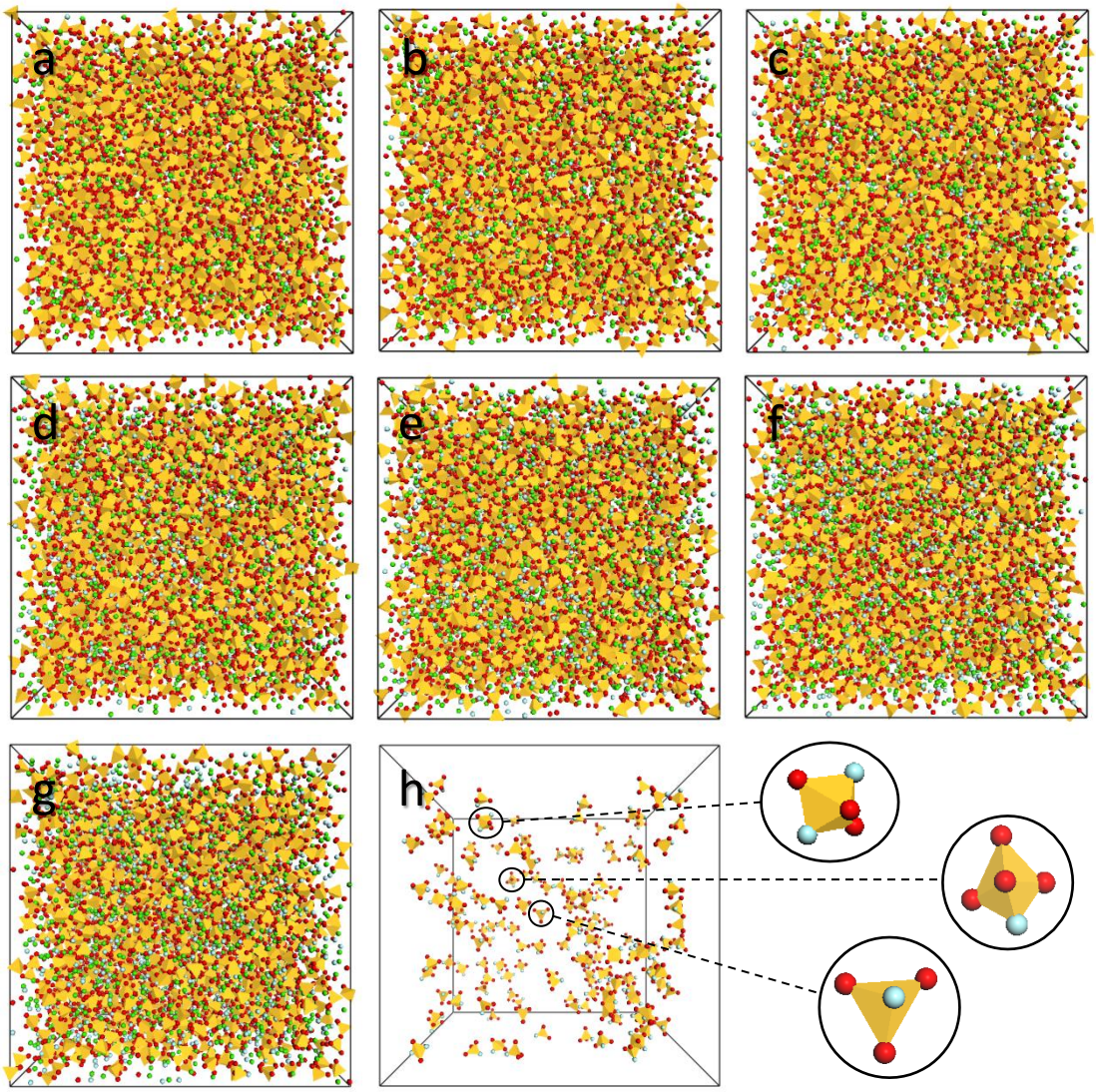

Figure 3: The GF glass models in order of increasing CaF_2 content, with the GF2.0, GF5.0, GF7.0, GF10.7, GF14.5, GF17.1, and GF18.9 glass models being labelled from 'a' to 'g' respectively. The image labelled 'h' shows the structural units involving Si-F bonding in the GF18.9 model (labelled 'g'). Examples of the SiO_3F_2, SiO_4F, and SiO_3F structural units have been magnified. The green, light blue, and red spheres represent calcium, fluorine, and oxygen ions respectively. The yellow tetrahedra correspond to silicon ions. Anion shells have not been included.

Table 11: The percentage of silicon ions in each GF glass model that is present in SiO_3F, SiO_4F, or SiO_3F_2 structural units. The uncertainty in each value is estimated to be within ±0.5%.

	SiO_3F (%)	SiO_4F (%)	SiO_3F_2 (%)
GF2.0	1.40	0.57	0.00
GF5.0	1.87	1.12	0.16
GF7.0	2.92	1.05	0.28
GF10.7	4.88	1.65	0.62
GF14.5	4.65	1.73	0.48
GF17.1	5.56	1.91	1.30
GF18.9	6.65	1.90	1.52

8.3.2 Pair Correlation Functions

The pair correlations functions for the GF glass series are shown in figures 4 and 5. The Si-O, O-O, and Si-Si pair correlation functions (figure 4) typically relate to the structural units that make up the silicate network. It can be seen in table 12 that the Si-O coordination numbers reduce from 3.99 to 3.91 (±0.01) with increasing CaF_2 content when a cut-off distance of 2.00Å is applied. This is due to the increasing Si-F coordination numbers (table 13). While the vast majority of the structural units involving silicon ions are SiO_4, a minority contain one or more fluorine ions. Typical Si-F nearest neighbour distances in these structural units are 1.52±0.01Å. It can be seen in figure 5 that the Si-F pair correlation functions are asymmetric around this nearest neighbour distance. This is because the peak corresponds to the more numerous SiO_3F structural units, while the tail to the right of this peak corresponds to the SiO_4F and SiO_3F_2 structural units. As the proportion of Si-F bonding is minimal, the average O-O nearest neighbour distances in the structural units that make up the silicate network (2.66±0.01Å) are unaffected (table 12). However, slight shoulders on the left hand side of the O-F pair correlation functions are observed (figure 4). These correspond to the variety of O-F separation distances in the SiO_3F, SiO_4F, and SiO_3F_2 structural units. The Si-Si nearest neighbour distances showed minimal variation, while the Si-Si coordination numbers decreased from 1.93 to 1.71 (±0.02) with increasing CaF_2 content when a 3.40Å cut-off distance was applied (table 14). This indicates increasing disruption to the silicate network with increasing CaF_2 content. This can be expected when a Si-F bond takes the place of a Si-O bond to a bridging oxygen. The excess CaO in the glass compositions (section 8.2.2) could have also disrupted the silicate network. The remaining correlations include Ca-O, Ca-F, F-F, Si-Ca, and Ca-Ca. The nearest neighbour distances for these correlations exhibit minimal changes. The decreasing Ca-O, and increasing Ca-F, F-F, and Si-Ca coordination numbers respectively reflect the declining oxygen and silicon contributions as the calcium and fluorine contributions become more significant.

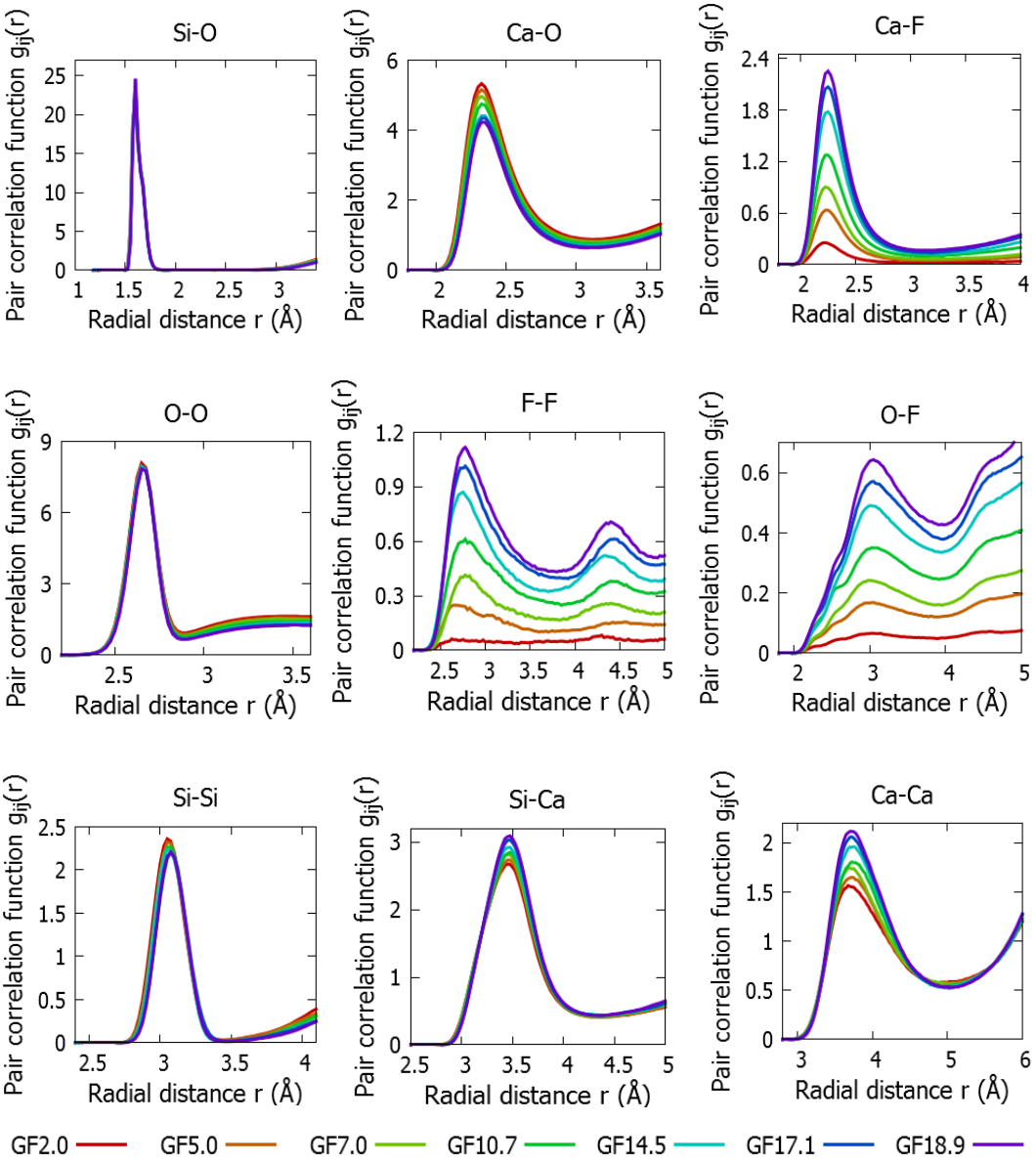

Figure 4: The pair correlation functions for the GF glass series apart from the Si-F pair correlation function (below) in order of increasing nearest neighbour distance.

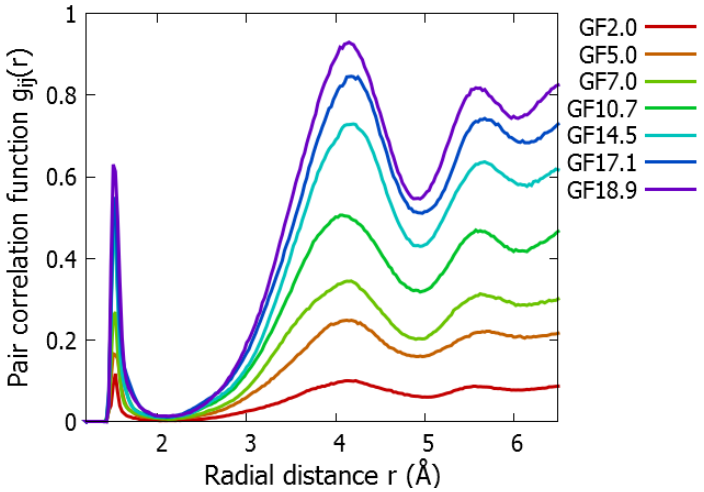

Figure 5: The Si-F pair correlation functions for the GF glass series.

Table 12: The nearest neighbour distance, R_{ij}, and coordination number, N_{ij}, values for the correlations involving oxygen in the GF glass series apart from the O-F correlation (shown in table 13). Cut-off distances of 2.00Å, 3.10Å, and 2.85Å were used to identify the Si-O, Ca-O, and O-O coordination numbers respectively.

	R_{Si-O} ±0.01 (Å)	$N_{Si-O}(r)$ ±0.01	R_{Ca-O} ±0.01 (Å)	$N_{Ca-O}(r)$ ±0.03	R_{O-O} ±0.01 (Å)	$N_{O-O}(r)$ ±0.03
GF2.0	1.62	3.99	2.37	5.93	2.66	4.26
GF5.0	1.62	3.97	2.38	5.65	2.66	4.17
GF7.0	1.62	3.97	2.38	5.47	2.66	4.10
GF10.7	1.62	3.94	2.38	5.17	2.66	4.02
GF14.5	1.61	3.94	2.38	4.82	2.66	4.00
GF17.1	1.61	3.92	2.38	4.67	2.66	3.94
GF18.9	1.62	3.91	2.39	4.48	2.66	3.88

Table 13: The nearest neighbour distance, R_{ij}, and coordination number, N_{ij}, values for the correlations involving fluorine in the GF glass series. Cut-off distances of 2.00Å, 3.70Å, 4.00Å, and 4.00Å were used to identify the Si-F, Ca-F, F-F, and O-F coordination numbers respectively.

	R_{Si-F} ±0.01 (Å)	$N_{Si-F}(r)$ ±0.03	R_{Ca-F} ±0.01 (Å)	$N_{Ca-F}(r)$ ±0.05	R_{F-F} ±0.10 (Å)	$N_{F-F}(r)$ ±0.10	R_{O-F} ±0.10 (Å)	$N_{O-F}(r)$ ±0.10
GF2.0	1.52	0.02	2.26	0.22	2.91	0.24	3.15	0.29
GF5.0	1.53	0.04	2.27	0.56	2.95	0.75	3.16	0.71
GF7.0	1.52	0.05	2.27	0.79	2.96	1.16	3.18	0.98
GF10.7	1.52	0.09	2.27	1.14	2.98	1.81	3.18	1.47
GF14.5	1.52	0.09	2.28	1.59	2.92	2.37	3.25	1.95
GF17.1	1.52	0.12	2.28	1.81	2.95	2.83	3.27	2.28
GF18.9	1.53	0.13	2.28	1.99	2.94	3.09	3.28	2.53

Table 14: The nearest neighbour distance, R_{ij}, and coordination number, N_{ij}, values for the remaining correlations in the GF glass series. Cut-off distances of 3.40Å, 4.35Å, and 5.25Å were used to identify the Si-Si, Si-Ca, and Ca-Ca coordination numbers respectively.

	R_{Si-Si} ±0.01 (Å)	$N_{Si-Si}(r)$ ±0.02	R_{Si-Ca} ±0.01 (Å)	$N_{Si-Ca}(r)$ ±0.03	R_{Ca-Ca} ±0.02 (Å)	$N_{Ca-Ca}(r)$ ±0.04
GF2.0	3.06	1.93	3.45	6.34	3.89	7.72
GF5.0	3.07	1.89	3.45	6.45	3.87	7.97
GF7.0	3.07	1.84	3.45	6.59	3.86	8.15
GF10.7	3.08	1.82	3.45	6.63	3.88	8.34
GF14.5	3.07	1.80	3.46	6.76	3.87	8.68
GF17.1	3.09	1.76	3.46	6.89	3.87	8.87
GF18.9	3.08	1.71	3.46	7.00	3.85	9.07

8.3.3 Structure Factors

As illustrated in figure 6, only small changes to the total neutron and X-ray structure factors were observed with increasing CaF_2 content in the GF series. The most significant of these minor changes occurred in the region of Q~3.5Å^{-1} in the total X-ray structure factors. As shown in the partial structure factors in figure 7, these changes were predominantly caused by the increasing contribution of the Ca-F partial structure factor with increasing CaF_2 content.

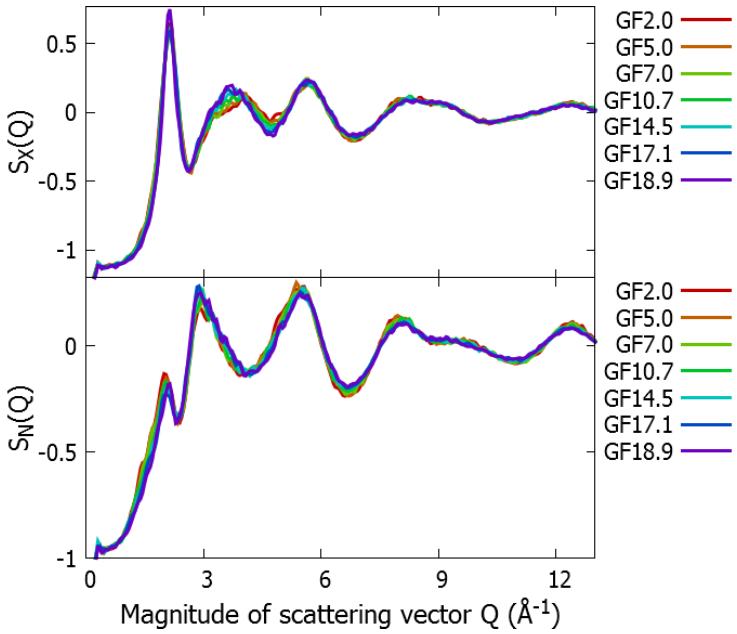

Figure 6: Simulated total X-ray ($S_X(Q)$) and neutron ($S_N(Q)$) structure factor spectra for the GF glass series.

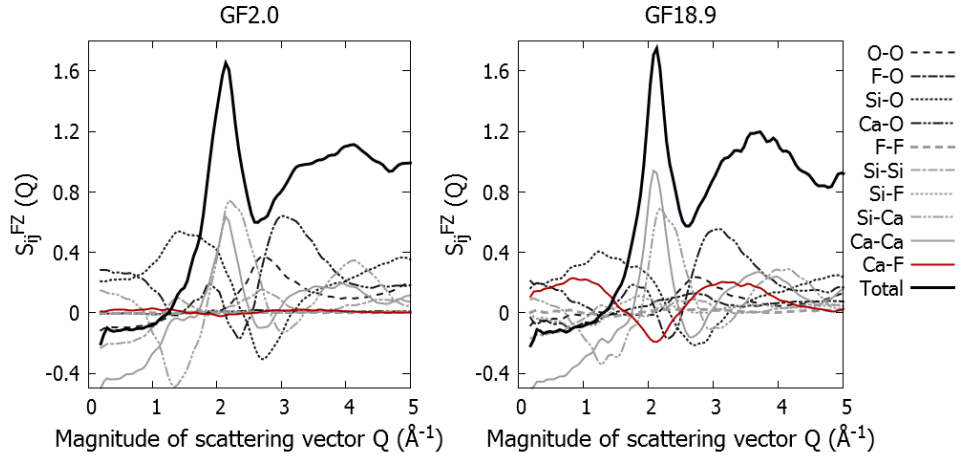

Figure 7: Partial Faber-Ziman X-ray structure factors ($S_{ij}^{FZ}(Q)$) and total X-ray structure factors ($S_X(Q)$) for GF2.0 and GF18.9 glass models to the left and right respectively.

8.3.4 Silicon Network Connectivity

The silicon network connectivity calculations were not only complicated by unequal $CaO:SiO_2$ ratios (table 9), but also by the presence of Si-F bonding. In order to predict the connectivity of the GF models, the glass compositions were initially denoted as $xCaF_2$-x'CaO-x''SiO_2, where the elemental concentration of each element is as follows:

$F=2x$ Equation 1

$O=x'+2x''$ Equation 2

$Si=x''$ Equation 3

$Ca=x'+x$ Equation 4

The term NBO is a common abbreviation for non-bridging oxygens. Since a Si-F bond would have the same effect on the network connectivity as a $Si\text{-}O_{NBO}$ bond, Si-F bonds that take the place of one Si-O bond can be denoted non-bridging fluorine, or NBF. The fraction of fluorine atoms which are NBF's, y, is given by

$y=NBF/2x$ Equation 5

Rearranging gives

$2xy=NBF$ Equation 6

The population of oxygen atoms comprises not only of NBO's, but also bridging oxygens (BO's) and free oxygens too. Each BO contributes bonds to two silicon atoms. By assuming that there were four bonds to each silicon atom, the number of bonds to silicon can be equated using

$4x''=NBF+NBO+2BO$ Equation 7

By assuming an absence of free oxygens, the oxygen population can be written as

$NBO+BO=x'+2x''$ Equation 8

Substituting equation 8 into equation 7 yields

$4x''=NBF+BO+x'+2x''$ Equation 9

The silicon network connectivity (Q^n) is defined as the number of $Si\text{-}O_{BO}$ bonds per silicon atom. As each BO contributes bonds to two silicon atoms

$Q^n=2BO/x''$ Equation 10

Through substituting equation 9 into equation 10, Q^n can be approximated according to equation 11

$Q^n=4-[(2(x'+2xy))/x'']$ Equation 11

where x, x', and x'' are found in the table of compositions (table 9), and y is an unknown parameter corresponding to the fraction of fluorine atoms which are non-bridging fluorine atoms. Equation 11 was then compared to the actual connectivity results obtained from analysing the models. A value of y=0.09±0.01 generated predicted values that matched the results from the models most closely (figure 8). It can be seen in figure 8 that the silicon network connectivity values generally decline with increasing CaF_2 content, corresponding with the reducing O-O coordination numbers in table 12. The plot to the right of figure 8 illustrated a reduction in the number of Q^2 and Q^3 species and a rise in the number of Q^1 species with increasing CaF_2 content. This was caused by fluorine volatilisation which led to the excess of calcium ions in the system, disrupting the silicate network. Some Si-F bonding would also cause a reduction in silicon network connectivity. The value of y=0.09±0.01 represents 9% of the fluorine atoms having a single bond to a silicon atom.

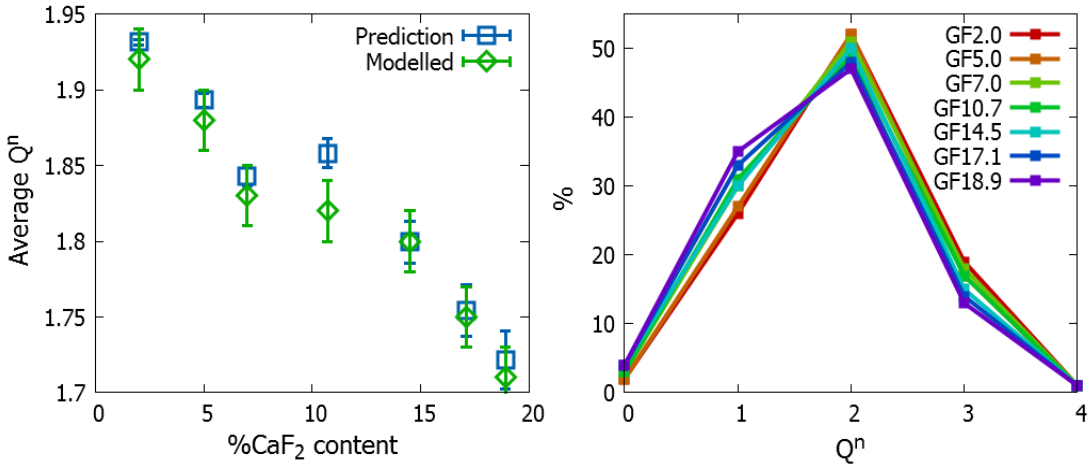

Figure 8: The average Q^n results from the models compared to the predicted values to the left, and the Q^n distribution of the models to the right. The uncertainty of 2% in the results from the models was based on reproducibility. The uncertainty in the predicted values was based on the uncertainty in y (±0.01).

8.4 Discussion

The nominal $CaO\text{-}SiO_2\text{-}CaF_2$ glass compositions of the experimental glass series discussed in the previous chapter maintained equal $CaO:SiO_2$ proportions. However, during the glass synthesis, it was found that some losses due to fluorine volatilisation had occurred. Subsequently, the compositions were revised (figure 9) and denoted as the GF series. The GF series was modelled computationally in this chapter to enable direct comparisons with the experimental findings, and to provide further structural insight into the $CaO\text{-}SiO_2\text{-}CaF_2$ glass system. In particular, the structural role of fluorine was examined.

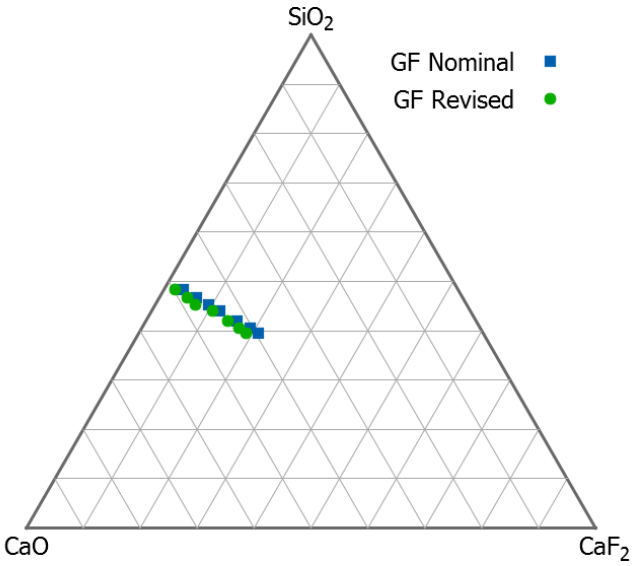

Figure 9: Ternary plot showing the nominal and revised CaO-SiO_2-CaF_2 compositions.

The images of the glass models in figure 3 did not show any obvious phase separation. To explore this further, the expected average pair correlation function values at relatively large distances of 10Å were calculated. These were included in the pair correlation function plots involving fluorine ions in figure 10. It can be seen that all of the pair correlation functions pass through the corresponding expected values at 10Å, confirming an absence of phase separation. However, given reports of a tendency for fluorine ions to cluster with increasing CaF_2 contributions [5], [8], [9], the F-F pair correlation functions and cumulative coordination number plots were examined more closely.

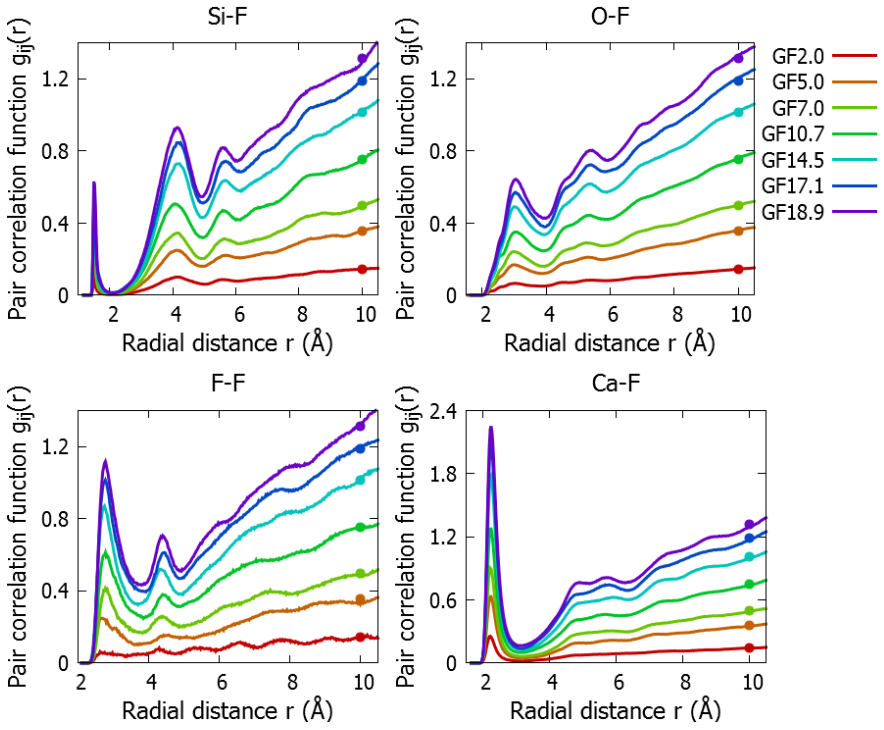

Figure 10: The pair correlation functions of the GF glass series that involve fluorine ions. The expected average pair correlation function values at 10Å have been added as dots.

The F-F nearest neighbour distance values in table 13 only exhibited small amounts of variation within the uncertainty range of ±0.10Å. The F-F coordination number increased as anticipated with increasing CaF_2 content. Interestingly, through calculating the expected nearest neighbour distances and coordination numbers at 4.0Å (the cut-off distance used to attain the F-F coordination numbers in table 13); there was some indication of fluorine ions clustering (figure 11). This was because the F-F separation distances were generally lower than expected, and the corresponding coordination numbers higher than expected. The same observations were made in figure 11 for the Ca-F nearest neighbour distances and coordination numbers at 3.7Å (the cut-off distance used to attain the Ca-F coordination numbers in table 13). This suggests some clustering of both fluorine and calcium ions, and that the GF glass models were not completely homogeneous.

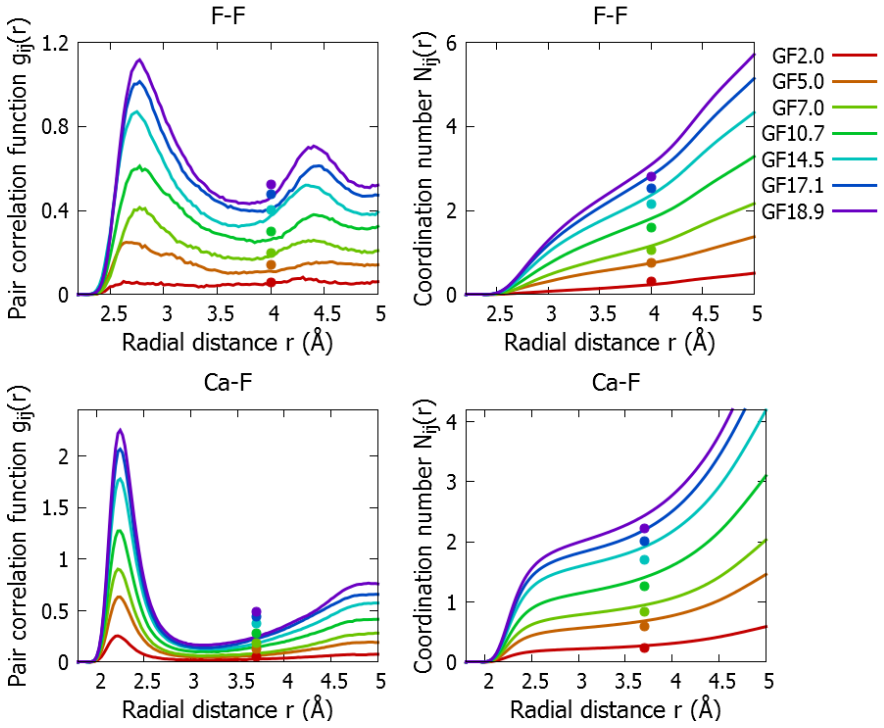

Figure 11: The pair correlation functions (left) and the cumulative coordination number plots (right) for the F-F (top) and Ca-F (bottom) correlations. The expected average pair correlation function and coordination number values at 4.0Å (F-F) and 3.7Å (Ca-F) have been added as dots.

Although the fluorine ions in the GF models were overwhelmingly bonded to calcium ions, some Si-F bonding was observed (table 13). The occurrence of Si-F bonding was unfavourable because Si^{4+} ions have a higher affinity for O^{2-} ions than F^- ions [1]. According to Rabinovich *et al.* [26], the difference in polarisability between bridging and non-bridging oxygens can result in three of the four bridging oxygens being sufficient in shielding one of the silicon ions. This creates the scenario where the other bridging oxygen can then move into closer proximity with the other silicon ion, making it vulnerable to being replaced by a fluorine ion. However, as emphasised in figure 3h, Si-F bonding was not only present in

SiO_3F structural units, but also in SiO_4F and SiO_3F_2 structural units (albeit in smaller quantities) as shown in table 13.

Christie *et al.* [27] used first principles molecular dynamics simulation to investigate the fluorine environment of the archetypal 45S5 bioglass when 10mol% of the CaO was replaced with CaF_2. Pedone *et al.* [5] comments on how the parameter-free nature of first principles simulation leads to unbiased computational models. Although the glass models only comprised of 120 atoms due to computational limitations; SiO_3F, SiO_4F, and SiO_3F_2 structural units were also observed. Christie *et al.* [27] also reports a F-Si separation distance (equivalent to the Si-F separation distance) of 1.67Å and an F-Si coordination number of 0.17 after applying a 2.0Å cut-off distance. In this study, the F-Si separation distances were less at ~1.5Å (table 13), but were comparable to the F-Si separation distances in crystalline SiF_4 [21] (table 7). The F-Si coordination number values ranged from 0.13 to 0.25 using the same 2.0Å cut-off distance, suggesting similar proportions of Si-F bonding in both studies. Pedone *et al.* [5] calculated NMR spectra using the computational model produced by Christie *et al.* [27] and conluded that the SiO_3F, SiO_4F, and SiO_3F_2 structural units were present in the computational model as defects. Pedone *et al.* [5] suggested that the cause was the high quench rate coupled with the small simulation size. However, the same structural units were observed in this study and in similar proportions by using a quench rate that was over three times slower than the one used by Christie *et al.* [27]. Additionally, the models in this study were much larger and contained at least 10,000 atoms.

Lusvardi *et al.* [8] also studied the fluorine environment of the archetypal 45S5 bioglass when CaO was replaced with CaF_2. However, classical molecular dynamics simulations were run using rigid-ion interatomic potential parameters. Lusvardi *et al.* [8] stated that core-shell model interatomic potential parameters would be needed to reproduce the Si-O-Si bond angles seen experimentally more closely, and hence obtain a more realistic Q^n distribution. Calculating Q^n predictions for the GF series in this work was not only complicated by unequal $CaO:SiO_2$ ratios, but also by the presence of Si-F bonding. This prompted the derivation of equation 11, and a value of $y=0.09\pm0.01$ seemed to give the best agreement with the computational glass models. The value of $y=0.09\pm0.01$ represents 9% of the fluorine ions having a single bond to a silicon atom. The proportion of fluorine ions involved in SiO_3F, SiO_4F, or SiO_3F_2 structural units are shown in table 15. By summing the percentage of fluorine ions involved in SiO_3F structural units and half the percentage of fluorine ions involved in SiO_3F_2 structural units, the percentage of fluorine ions that replace a Si-O bond to form a NBF could be estimated. Although the proportions vary, it can be seen that an approximation of 9% of the fluorine ions having a single bond to a silicon ion was reasonable.

Table 15: The percentage of fluorine ions in each GF glass model that is present in SiO_3F, SiO_4F, or SiO_3F_2 structural units. The uncertainty in each value is estimated to be within ±1%.

	SiO_3F (%)	SiO_4F (%)	SiO_3F_2 (%)	$SiO_3F+0.5SiO_3F_2$ (%)
GF2.0	16.88	6.88	0.00	16.88
GF5.0	8.75	5.25	1.50	9.20
GF7.0	9.46	3.39	1.79	10.35
GF10.7	10.05	3.39	2.57	11.33
GF14.5	6.72	2.50	1.38	7.41
GF17.1	6.58	2.27	3.07	8.11
GF18.9	6.94	1.98	3.17	8.52

8.5 Conclusion

The structure of CaO-SiO_2-CaF_2 glass was investigated computationally in this chapter. This was achieved using classical molecular dynamics with the addition of the adiabatic core-shell model. Fluorine ions were found to preferentially bond with calcium ions. The F-F and Ca-F pair correlation functions and cumulative coordination number plots indicated some degree of fluorine and calcium ions clustering, although no phase separation was observed. Some Si-F bonding was also observed in SiO_3F, SiO_4F, and SiO_3F_2 structural units. The calculated total neutron and X-ray structure factors showed minimal change with increasing CaF_2 content. The most noticable of these minor changes was observed in the region of Q~3.5$Å^{-1}$ in the total X-ray structure factors. This was predominantly caused by changes in the Ca-F partial structure factor with increasing CaF_2 content.

8.6 References

[1] R. G. Hill, N. D. Costa, and R. V. Law, "Characterization of a mould flux glass," *J. Non. Cryst. Solids*, vol. 351, no. 1, pp. 69–74, 2005.

[2] M. Susa, T. Sakamaki, and R. Kojima, "Chemical states of fluorine in CaF_2-CaO-SiO_2 and NaF-Na_2O-SiO_2 glassy slags from the perspective of elecronic polarisability," *Ironmak. Steelmak.*, vol. 32, no. 1, pp. 13–20, 2005.

[3] T. Watanabe, H. Hashimoto, M. Hayashi, and K. Nagata, "Effect of Alkali Oxides on Crystallization in CaO-SiO_2-CaF_2," *ISIJ Int.*, vol. 48, no. 7, pp. 925–933, 2008.

[4] R. G. Hill, A. Stamboulis, R. V. Law, A. Clifford, M. R. Towler, and C. Crowley, "The influence of strontium substitution in fluorapatite glasses and glass-ceramics," *J. Non. Cryst. Solids*, vol. 336, no. 3, pp. 223–229, 2004.

[5] A. Pedone, T. Charpentier, and M. C. Menziani, "The structure of fluoride-containing bioactive glasses: New insights from first-principles calculations and solid state NMR spectroscopy," *J. Mater. Chem.*, vol. 22, no. 25, pp. 12599–12608, 2012.

[6] X. Chen, X. Chen, D. S. Brauer, R. M. Wilson, R. G. Hill, and N. Karpukhina, “Novel alkali free bioactive fluorapatite glass ceramics,” *J. Non. Cryst. Solids*, vol. 402, pp. 172–177, 2014.

[7] M. Hayashi, N. Nabeshima, H. Fukuyama, and K. Nagata, “Effect of fluorine on silicate network for CaO-CaF_2-SiO_2 and CaO-CaF_2-SiO_2-FeO_x glasses,” *ISIJ Int.*, vol. 42, no. 4, pp. 352–358, 2002.

[8] G. Lusvardi *et al.*, “Elucidation of the Structural Role of Fluorine in Potentially Bioactive Glasses by Experimental and Computational Investigation,” *J. Phys. Chem. B*, vol. 112, pp. 12730–12739, 2008.

[9] S. Hayakawa, A. Nakao, C. Ohtsutki, A. Osaka, S. Matsumoto, and Y. Miura, “An X-ray photoelectron spectroscopic study of the chemical states of fluorine atoms in calcium silicate glasses,” *J. Mater. Res.*, vol. 13, no. 3, pp. 739–743, 1998.

[10] S. Hayakawa, C. Ohtsuki, S. Matsumoto, A. Osaka, and Y. Miura, “Molecular dynamic simulation of heterogeneity and chemical states of fluorine in amorphous alkaline earth silicate systems,” *Comput. Mater. Sci.*, vol. 9, no. 3–4, pp. 337–342, 1998.

[11] J. D. Gale and A. L. Rohl, “The General Utility Lattice Program (GULP),” *Mol. Simul.*, vol. 29, no. 5, pp. 291–341, 2003.

[12] G. Malavasi, A. Pedone, and M. C. Menziani, “Study of the Structural Role of Gallium and Aluminum in 45S5 Bioactive Glasses by Molecular Dynamics Simulations,” *J. Phys. Chem. B*, vol. 117, no. 15, pp. 4142–4150, 2013.

[13] C. H. Shen, R. S. Liu, J. G. Lin, and C. Y. Huang, “Phase stability study of $La_{1.2}Ca_{1.8}Mn_2O_7$,” *Mater. Res. Bull.*, vol. 36, pp. 1139–1148, 2001.

[14] Y. Ohashi, “Polysynthetically-twinned structures of enstatite and wollastonite,” *Phys. Chem. Miner.*, vol. 10, pp. 217–229, 1984.

[15] J. A. L. Rabone and N. H. De Leeuw, “Interatomic potential models for natural apatite crystals: incorporating strontium and the lanthanides,” *J. Comput. Chem.*, vol. 27, no. 2, pp. 253–266, 2006.

[16] E. R. Jette and F. Foote, “Precision Determination of Lattice Constants,” *J. Chem. Phys.*, vol. 3, no. 10, pp. 605–616, 1935.

[17] E. R. Jette and F. Foote, “Precision Determination of Lattice Constants,” *J. Chem. Phys.*, vol. 3, no. 10, pp. 605–616, 1935.

[18] M. Atoji and W. N. Lipscomb, “The structure of SiF_4,” *Acta Crystallogr.*, vol. 7, no. 8, pp. 597–597, 1954.

[19] S. Frisoni, S. Brenna, and N. Masciocchi, “Structural characterization of anhydrous and bishydrated calcium hexafluorosilicate by powder diffraction methods,” *Powder Diffr.*, vol. 26, no. 4, pp. 308–312, 2012.

[20] A. Zalkin, J. D. Forrester, and D. H. Templeton, “The crystal structure of sodium fluorosilicate,” *Acta Crystallogr.*, vol. 17, no. 11, pp. 1408–1412, 1964.

[21] M. Atoji and W. N. Lipscomb, “The structure of SiF_4,” *Acta Crystallogr.*, vol. 7, no. 8, pp. 597–597, 1954.

[22] S. Frisoni, S. Brenna, and N. Masciocchi, “Structural characterization of anhydrous and bishydrated calcium hexafluorosilicate by powder diffraction methods,” *Powder Diffr.*, vol. 26, no. 4, pp. 308–312, 2012.

[23] D. Teter, “Private communication.” 2004.

[24] D. M. Zirl and S. H. Garofalini, “Reactions on Modified Silica Surfaces,” *J. Non-Cryst. Solids*, vol. 122, pp. 111–120, 1990.

[25] J. Li, Q. Shu, and K. Chou, “Structural Study of Glassy CaO-SiO_2-CaF_2-TiO_2 Slags by Raman Spectroscopy and MAS-NMR,” *ISIJ Int.*, vol. 54, no. 4, pp. 721–727, 2014.

[26] E. M. Rabinovich, D. M. Krol, N. A. Kopylov, P. K. Gallagher, T. B. Laboratories, and M. Hill, “Retention of Fluorine in Silica Gels and Glass*,” *J. Am. Ceram. Soc.*, vol. 72, no. 7, pp. 1229–1232, 1989.

[27] J. Christie, A. Pedone, M. Menziani, and A. Tilocca, “Fluorine Environment in Bioactive Glasses: ab Initio Molecular Dynamics Simulations,” *J. Phys. Chem. B*, vol. 115, pp. 2038–2045, 2011.

9. Discussion and Conclusions

In this thesis, the structure of several glass systems involving halides were investigated. The first of these was the intermediate glass former $ZnCl_2$ which was modelled computationally using classical molecular dynamics (MD) with the addition of the adiabatic core-shell model. This allows relatively large system sizes to be modelled whilst also taking anion polarisability into account, and has not previously been used to model $ZnCl_2$ glass. The glass model produced was the first fully tetrahedral model of $ZnCl_2$ glass. The average Cl-Zn-Cl bond angle matched the ideal tetrahedral bond angle of 109° [1]. While most of the tetrahedral units were corner-sharing, 14% were found to be edge-sharing. The calculated total neutron and X-ray structure factors were in good agreement with those obtained experimentally [1], [2]. The calculated Faber-Ziman partial structure factors were also generally in good agreement with those from neutron diffraction [1]. However, some discrepancy between the Zn-Zn partial structure factors was apparent. This was due to the weak weighting of the Zn-Zn partial structure factor (ω_{ZnZn}=0.05) in comparison to the other partial structure factors (where ω_{ZnCl}=0.35, ω_{ClCl}=0.59). This low signal to noise ratio caused poor resolution in the Zn-Zn pair correlation function obtained experimentally from neutron diffraction. The Zn-Zn pair correlation function from this work could therefore provide clear details that are unobtainable experimentally.

It was of interest to compare the structural effects of anion polarisability in the intermediate glass former $ZnCl_2$ to those in the well-established strong glass-former SiO_2. The $ZnCl_2$ glass model was therefore compared to a SiO_2 glass model [3]. Once the partial structure factors had been scaled according to nearest neighbour distance, strong similarities between the $ZnCl_2$ and SiO_2 partial structure factors could be seen. This was because both $ZnCl_2$ and SiO_2 have a dominantly corner-sharing tetrahedral network. The main contribution to the first sharp diffraction peaks (FSDP's) came from the cation-anion contribution, rather than the cation-cation contribution as previously reported [4].

The next system to be investigated was the $CaO\text{-}SiO_2\text{-}CaCl_2$ glass system. Fluorine-containing bioactive glasses are known to have a number of limitations [5]. One of these is that the formation of fluorite is possible which can hinder enamel regeneration [5]. Consequently, attention has recently turned to the possibility of using chlorine-containing bioactive glasses as an alternative for dental applications [6], [7]. The number of studies on chlorine-containing bioactive glasses have been scarce, and no structural characterisation has previously been undertaken. In order to understand the structure of complex $CaO\text{-}SiO_2\text{-}P_2O_5\text{-}CaCl_2$ chlorine-containing bioactive glasses, it is fundamental to first understand the structure of less complex $CaO\text{-}SiO_2\text{-}CaCl_2$ glasses. This prompted the

structure of $CaO\text{-}SiO_2\text{-}CaCl_2$ glasses to be investigated both experimentally and computationally in this work.

A $CaO\text{-}SiO_2\text{-}CaCl_2$ glass series was synthesised both by collaborators at Queen Mary University of London (denoted the QCl series) and later by collaborators at Aston University (denoted as the ACl series). Both sets of glasses had the same nominal compositions but had been prepared using different approaches. Coupled with concerns about losses due to chlorine volatilisation [8], it was important to carefully study the $CaO\text{-}SiO_2\text{-}CaCl_2$ glass compositions experimentally. This was achieved using calibrated X-ray fluorescence (XRF) measurements. While the QCl glass samples maintained their nominal compositions, the ACl glass samples exhibited chlorine losses of between 23% and 59% depending on the furnace temperature used during glass synthesis. Losses via chlorine volatilisation were found to occur as HCl. Once the glass densities had been established from helium pycnometry measurements, central facility techniques including neutron diffraction (ND) and X-ray absorption spectroscopy (XAS) were used to probe the structure of the ACl glass samples experimentally. In addition, both the QCl and ACl glass series were modelled computationally using classical molecular dynamics with the addition of the adiabatic core-shell model. This was the first time $CaO\text{-}SiO_2\text{-}CaCl_2$ glasses had been modelled using this technique. The computational modelling required a Si-Cl interatomic potential parameter to be fitted in this work, since a suitable Si-Cl interatomic potential parameter had not previously been reported. This was achieved using the General Utility Lattice Program (GULP) [9]. The results of computational modelling could be compared with experimental results. The example in figure 1 shows the close agreement between the total neutron structure factors obtained experimentally and computationally. This further validates the interatomic potential parameters used to model the glasses computationally.

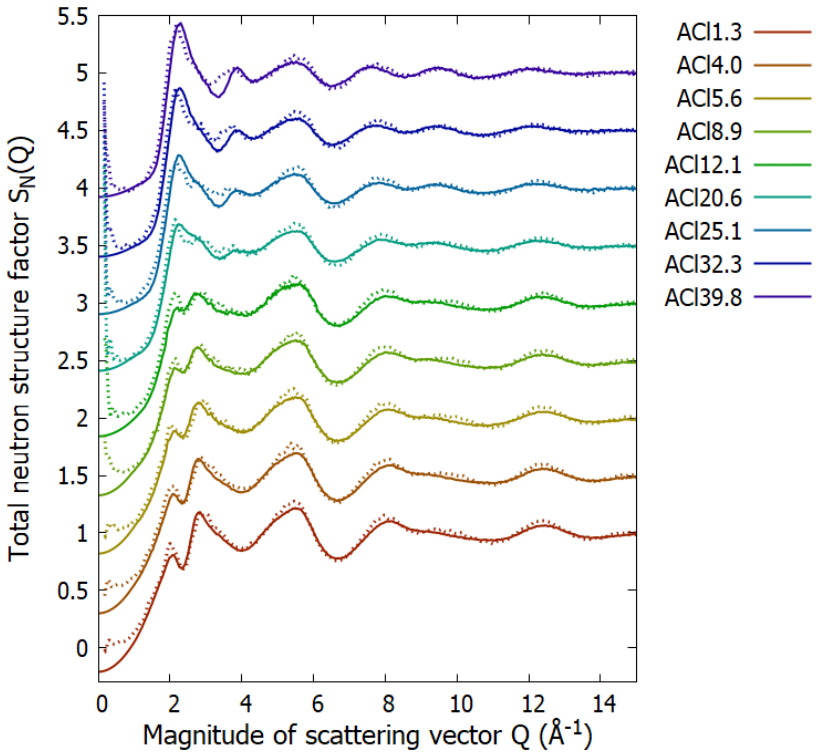

Figure 1: A comparison of the total neutron structure factors for the ACl glass series that have been attained experimentally (solid lines) and computationally (dashed lines). The plots have been progressively offset by 0.5.

By Fourier transforming the total neutron structure factors attained experimentally, total correlation functions were obtained. The total correlation functions did not exhibit a noticeable contribution around 2.1Å as would have been expected for Si-Cl bonding. This was consistent with an absence of Si-Cl bonding in the computational glass models. The chlorine ions in the glass models bonded with calcium ions, and the models were found to become phase separated with increasing $CaCl_2$ content. The glass models of the QCl glass series became phase separated between the QCl16.1 and the QCl27.4 compositions. The glass models of the ACl glass series became phase separated between the ACl12.1 and the ACl20.6 compositions. Upon phase separation, the models became biphasic and the two phases included a calcium silicate phase and a calcium chloride phase. Interestingly, by comparing the average pair correlation function values concerning chlorine with those expected at a relatively large distance of 10Å, it became apparent that there was a tendency towards phase separation even in the glass models containing small amounts of $CaCl_2$. In addition, by comparing the calculated Ca-Ca pair correlation functions from the ACl and QCl glass series, it was found that the higher CaO content of the ACl glass series slowed the proliferation of phase separation.

The modulus of the Fourier transformed Ca K-edge k^2 weighted EXAFS spectra and the total neutron structure factors from experiment both exhibited a distinct change in shape between the ACl12.1 and the ACl20.6 compositions, the same range of compositions

between which phase separation was observed computationally. Interestingly, some of the total neutron structure factors in figure 1 that had been calculated from the computational models exhibited a sharp vertical line at a low value of Q. These were indicative of phase separation but were not observed experimentally. This was because standard neutron diffraction techniques cannot probe samples to such small values of Q. Small angle neutron scattering (SANS) or small angle X-ray scattering (SAXS) experiments would be necessary to determine the occurrence and actual scale of phase separation in the ACl samples.

Since the calcium environment of the ACl glass series could be probed using ND, XAS, and MD, it was of interest to compare the results attained. Gaussian peaks were fitted to the total correlation functions from ND and to the Ca K-edge k^2 weighted EXAFS spectra to acquire the Ca-O and Ca-Cl structural parameters shown in figure 2. In the figure, the generally good agreement between the Ca-O and Ca-Cl coordination numbers can be seen. The Ca-O and Ca-Cl nearest neighbour distances from ND were generally slightly higher than those from MD. The Ca-O nearest neighbour distances from EXAFS were generally lower than those from MD. Conversely, the Ca-Cl nearest neighbour distances from EXAFS were generally higher than those from MD. This emphasises the challenging nature of fitting overlapping correlations in the experimental data. The values of ${\sigma_{CaO}}^2$ and ${\sigma_{CaCl}}^2$ from MD were seen to reduce with increasing $CaCl_2$ content. This was consistent with the formation of calcium silicate-rich and calcium chloride-rich clusters respectively. As shown in figure 3, X-ray diffraction, another common technique used to characterise glass structure, is unlikely to have provided additional information on the calcium environment. Figure 3 also shows the asymmetry in a number of pair correlation functions due to the static disorder in the glasses. Asymmetric functions are inadequately represented by gaussian functions used in fitting, highlighting a limitation of obtaining structural parameters experimentally.

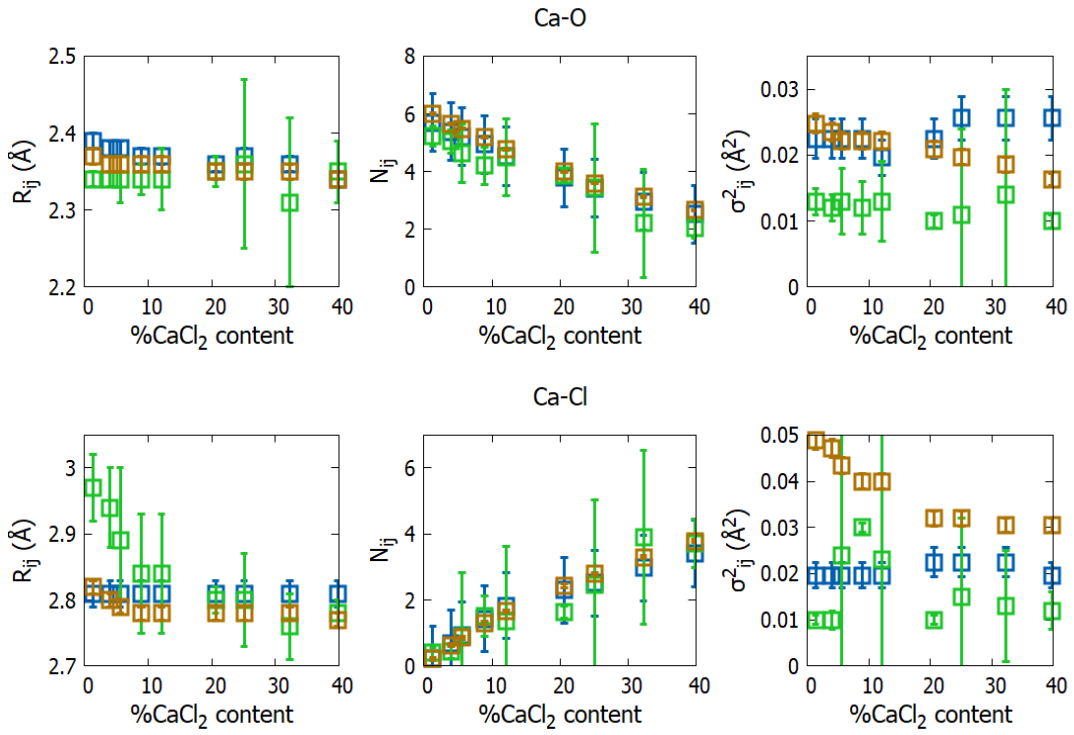

Figure 2: The nearest neighbour distances (R_{ij}), coordination numbers (N_{ij}), and values of $\sigma_{ij}{}^2$ obtained for the Ca-O (top) and Ca-Cl (bottom) correlations from Ca K-edge k^2 weighted EXAFS spectra (green squares), neutron diffraction (blue squares), and molecular dynamics (brown squares).

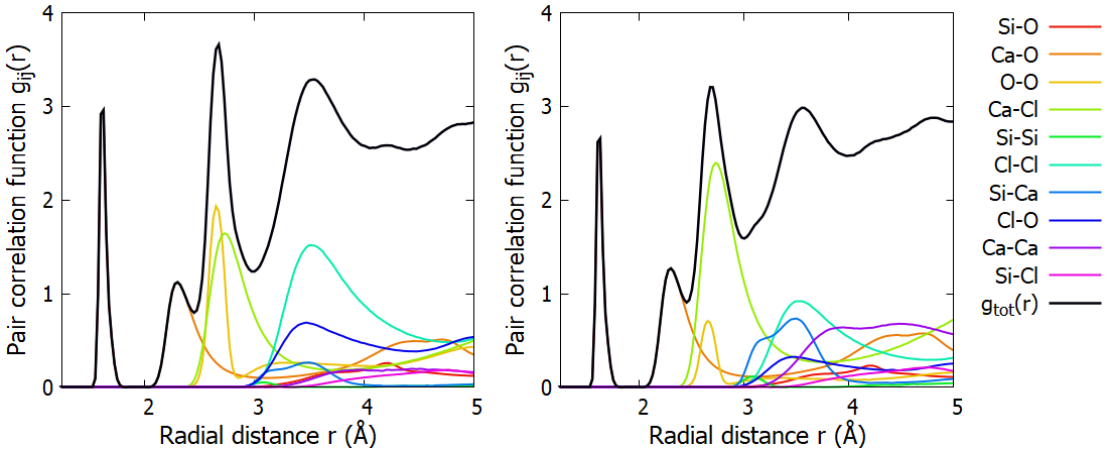

Figure 3: The calculated neutron (left) and X-ray (right) weighted pair correlation functions for ACl39.8 that form the total correlation functions.

The remaining glass system to be investigated was the CaO-SiO_2-CaF_2 glass series which was denoted as the GF series. The addition of CaF_2 into a bioactive glass composition has been found to have beneficial effects for dental applications [10]–[14]. However, the structural role of fluorine remains unclear (e.g. [15], [16]). To help comprehend the structural role of fluorine, it is intuitive to first consider less complex CaO-SiO_2-CaF_2 glasses. These have predominantly been studied for mould flux applications during the continuous casting of

steel, but conclusions on whether fluorine coordinates with silicon have been contradictory [17]. The structural role of fluorine in CaO-SiO_2-CaF_2 glasses was therefore investigated in this work using experimental and computational techniques.

Once the GF glass series had been synthesised, compositional analysis was performed. This was achieved using yield calculations and calibrated ^{19}F MAS-NMR measurements. The losses due to fluorine volatilisation were known to occur as HF [18], [19], and fluorine losses in the GF glass series ranged between 10% and 40%, depending on the furnace temperature used during glass synthesis. Following the density measurements of the GF glass samples using helium pycnometry, ND and XAS experiments were performed. In addition, the glasses were modelled computationally using classical molecular dynamics (MD) with the addition of the adiabatic core-shell model as mentioned previously. This required a Si-F interatomic potential parameter to be fitted in this work using the General Utility Lattice Program (GULP) [9]. To the author's knowledge, this was the first time these ternary glasses had been modelled computationally using this approach, and the excellent agreement between the total neutron structure factors obtained experimentally and computationally can be seen in figure 4. This further validates the interatomic potential parameters used during computational simulations.

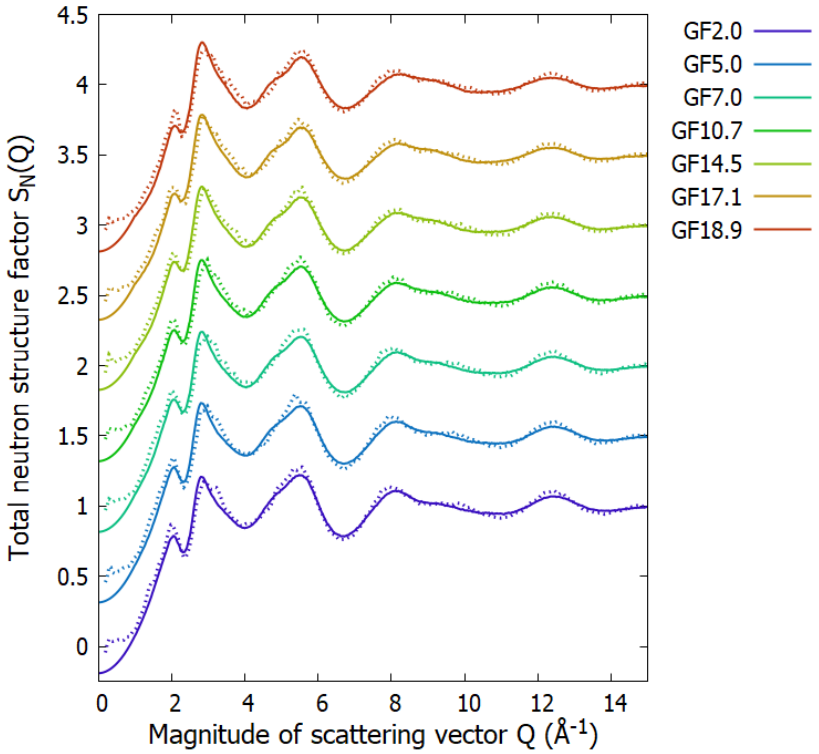

Figure 4: A comparison of the total neutron structure factors for the GF glass series that have been attained experimentally (solid lines) and computationally (dashed lines). The plots have been progressively offset by 0.5.

The results of computational modelling can provide structural insight that would be challenging to obtain experimentally. For example, the computational models of the GF glass

series revealed small amounts of Si-F bonding in the form of SiO_3F, SiO_4F, and SiO_3F_2 structural units. The proportion of these structural units was found to increase with increasing CaF_2 content. The same structural units had also been reported in a first principles modelling study on fluorine-containing bioactive glass [20]. This was despite system sizes of only 120 atoms being used due to computational limitations. Although detectable amounts of Si-F bonding were not observed using ^{29}Si MAS-NMR and ND measurements, it is conceivable that this was due to experimental limitations. Zeng and Stebbins [21] have reported that a small proportion of Si-F bonding in ^{29}Si MAS-NMR spectra would be obscured by the broad spectrum and its spinning sidebands. In addition, the computational models revealed that the Si-F nearest neighbour distance was around 1.5Å. Therefore, any small Si-F bonding contribution in the total correlation functions from ND would be masked by the prevalent Si-O bonding contribution at 1.6Å. Interestingly, at distances around 4Å, the F-F and Ca-F pair correlation functions had values that were lower than expected, while the coordination numbers were higher than expected. This was indicative of some clustering of fluorine and calcium ions.

In addition to studying the calcium environment of the GF glasses using MD, the calcium environment could also be probed using ND and XAS. By fitting gaussian peaks to the total correlation functions from neutron diffraction, and to the Ca K-edge k^2 weighted extended X-ray absorption fine structure (EXAFS) spectra, structural parameters were obtained. These Ca-O and Ca-F structural parameters are compared to those obtained computationally in figure 5, where good agreement between the Ca-O nearest neighbour distances and coordination numbers can be seen. The Ca-F nearest neighbour distances are generally in reasonable agreement, although less good agreement is seen for low CaF_2 concentrations. The Ca-F coordination numbers from ND and MD are in close agreement, while the coordination numbers from EXAFS are noticeably higher (but generally still within the uncertainty range). This discrepancy was caused by the overlapping Ca-F and Ca-O paths at around 2.3Å and 2.4Å respectively. This made distinguishing the peaks in the experimental results challenging, particularly for smaller peak contributions, i.e. Ca-F peaks at low CaF_2 concentrations. As was also observed for the ACl glass series, the values of $\sigma_{ij}{}^2$ from MD were consistently higher than those from EXAFS. This is most noticeable for the Ca-O correlation. As shown in figure 6, X-ray diffraction, is unlikely to have provided additional structural information on the calcium environment.

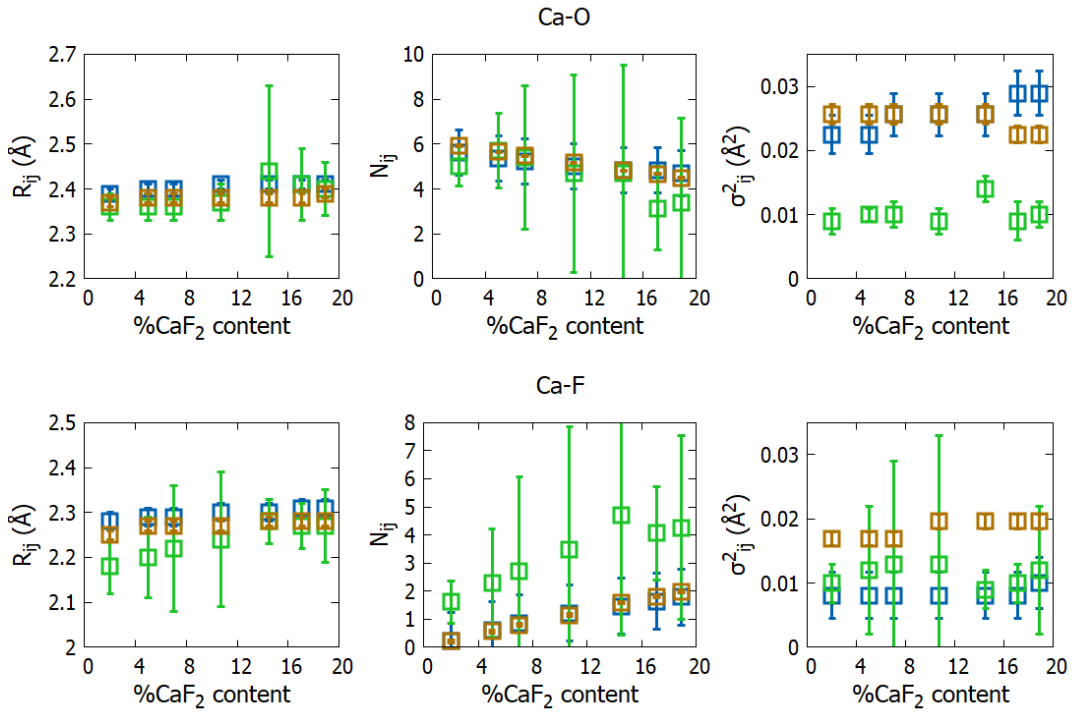

Figure 5: The nearest neighbour distances (R_{ij}), coordination numbers (N_{ij}), and values of $\sigma_{ij}{}^2$ obtained for the Ca-O (top) and Ca-F (bottom) correlations from Ca K-edge k^2 weighted EXAFS spectra (green squares), neutron diffraction (blue squares), and molecular dynamics (brown squares).

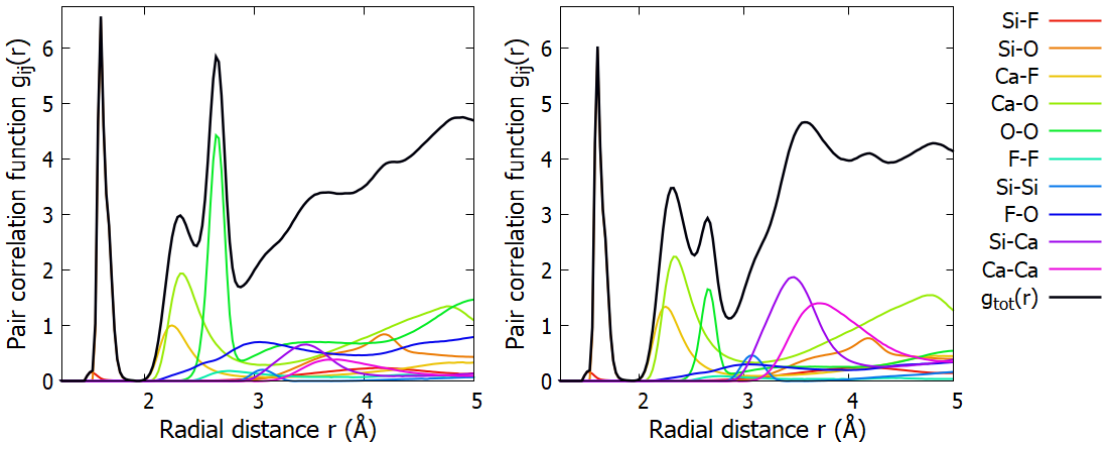

Figure 6: The calculated neutron (left) and X-ray (right) weighted pair correlation functions for GF18.9 that form the total correlation functions.

Two of the glass series studied in this work were based on CaO-SiO_2 and differed according to whether $CaCl_2$ of CaF_2 was added. The differences in glass transition temperature between the QCl and GF glass series was a particularly interesting result. The QCl series upheld their nominal compositions, and as reported by Chen [7], a reduction in glass transition temperature with increasing $CaCl_2$ content was observed (figure 7). This could be attributed to the QCl glasses containing $CaSiO_3$-rich regions and $CaCl_2$-rich regions which became phase separated. Although the $CaSiO_3$-rich clusters maintained consistent silicon network

connectivity values, the uniformity of the glass would have declined with the formation of $CaCl_2$-rich regions. The GF glass series did not uphold their nominal compositions and also exhibited a reduction in glass transition temperature with increasing CaF_2 content, albeit at a slower rate compared to the QCl series as shown in figure 7. The computational models of the GF glass series suggested that the reduction in glass transition temperature was the result of a reduction in silicon network connectivity. By considering the excess CaO from fluorine volatilisation and neglecting the impact of any Si-F bonding, the average silicon network connectivity in the GF series would be expected to range from Q^n=1.95 for GF2.0 to Q^n=1.89 for GF18.9. It is unclear whether these small differences from Q^n=2.00 for a calcium metasilicate could be resolved in the experimental ^{29}Si MAS-NMR spectra in which the chemical shift positions did not change significantly with increasing CaF_2 content. By also considering the small amount of Si-F bonding observed in the computational models of the GF glass series, the average silicon network connectivity in the GF series declined from Q^n=1.92 for GF2.0 to Q^n=1.71 for GF18.9. This suggests that the reduction in glass transition temperature might be influenced by Si-F bonding contributions which cannot be resolved using MAS-NMR [16].

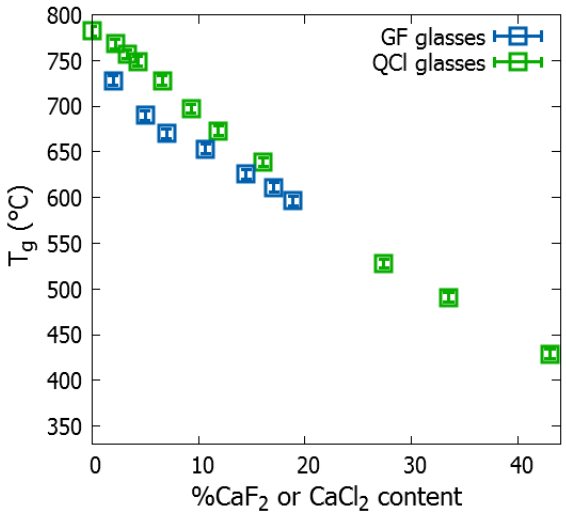

Figure 7: A comparison of the glass transition temperatures for the GF and QCl series as a function of increasing CaF_2 and $CaCl_2$ contributions respectively. The glass transition temperatures for the QCl series were obtained from [7].

This thesis has presented a very comprehensive structural characterisation of the related CaO-SiO_2-$CaCl_2$ and CaO-SiO_2-CaF_2 glass systems by combining results from molecular dynamics simulations, neutron diffraction, and X-ray absorption spectroscopy. As a result, a wealth of detailed data on the effect of chlorine and fluorine on the calcium silicate base glass has been obtained. In terms of future work, performing a small angle neutron scattering (SANS) or a small angle X-ray scattering (SAXS) experiment on the ACl glass series should enable the occurrence and scale of phase separation to be determined. In addition, it would be of interest to deconvolute the Raman spectra obtained for both glass series in order to

compare the silicon network connectivity distributions obtained experimentally with those obtained computationally. Finally, it would also be of interest to perform a similar structural investigation on more complex $CaO\text{-}SiO_2\text{-}P_2O_5\text{-}CaCl_2$ and $CaO\text{-}SiO_2\text{-}P_2O_5\text{-}CaF_2$ glasses. This would involve further glass synthesis, and the development of additional interatomic potential parameters for computational modelling. Most bioactive glass compositions contain small amounts of P_2O_5 which would make structural results concerning phosphorus susceptible to statistical variation. It might therefore be advantageous to try and incorporate a more substantial proportion of P_2O_5 to assist in elucidating how P_2O_5 affects the glass structure in $CaO\text{-}SiO_2\text{-}P_2O_5\text{-}CaCl_2$ or $CaO\text{-}SiO_2\text{-}P_2O_5\text{-}CaF_2$ bioactive glasses. Future studies on such bioactive glasses will benefit from the extensive results presented in this thesis on the underlying structure of $CaO\text{-}SiO_2\text{-}CaCl_2$ and $CaO\text{-}SiO_2\text{-}CaF_2$ glasses.

References

[1] A. Zeidler *et al.*, "Structure of liquid and glassy $ZnCl_2$," *Phys. Rev. B - Condens. Matter Mater. Phys.*, vol. 82, pp. 1–17, 2010.

[2] A. Zeidler *et al.*, "Structure of the network glass-former $ZnCl_2$: From the boiling point to the glass," *J. Non. Cryst. Solids*, vol. 407, pp. 235–245, 2015.

[3] A. Tilocca, N. H. De Leeuw, and A. N. Cormack, "Shell-model molecular dynamics calculations of modified silicate glasses," *Phys. Rev. B - Condens. Matter Mater. Phys.*, vol. 73, pp. 1–14, 2006.

[4] M. Wilson and P. Madden, "Voids, Layers, and the First Sharp Diffraction Peak in $ZnCl_2$," *Phys. Rev. Lett.*, vol. 80, no. 3, pp. 532–535, 1998.

[5] X. Chen, X. Chen, D. S. Brauer, R. M. Wilson, R. G. Hill, and N. Karpukhina, "Novel alkali free bioactive fluorapatite glass ceramics," *J. Non. Cryst. Solids*, vol. 402, pp. 172–177, 2014.

[6] X. Chen, N. Karpukhina, D. S. Brauer, and R. G. Hill, "Novel Highly Degradable Chloride Containing Bioactive Glasses," *Biomed. Glas.*, vol. 1, no. 1, pp. 108–118, 2015.

[7] X. Chen, "Novel Halide Containing Bioactive Glasses," Queen Mary University of London, 2015.

[8] A. A. Kiprianov and N. G. Karpukhina, "Oxyhalide silicate glasses," *Glas. Phys. Chem.*, vol. 32, no. 1, pp. 1–27, 2006.

[9] J. D. Gale and A. L. Rohl, "The General Utility Lattice Program (GULP)," *Mol. Simul.*, vol. 29, no. 5, pp. 291–341, 2003.

[10] J. D. Featherstone, "The science and practice of caries prevention.," *J. Am. Dent. Assoc.*, vol. 131, no. 7, pp. 887–899, 2000.

[11] T. T. Thuy *et al.*, "Effect of strontium in combination with fluoride on enamel remineralisation in vitro," *Arch. Oral Biol.*, vol. 53, no. 11, pp. 1017–1022, 2008.

[12] S. E. Jabbarifar, S. Salavati, A. Akhavan, K. Khosravi, N. Tavakoli, and F. Nilchian, "Effect

of fluoridated dentifrices on surface microhardness of the enamel of deciduous teeth," *Dent. Res. J. (Isfahan).*, vol. 8, no. 3, p. 113, 2011.

[13] R. G. Hill, D. G. Gillam, and X. Chen, "The ability of a nano hydroxyapatite toothpaste and oral rinse containing fluoride to protect enamel during an acid challenge using ^{19}F solid state NMR spectroscopy," *Mater. Lett.*, vol. 156, pp. 69–71, 2015.

[14] E. Lynch, D. S. Brauer, N. Karpukhina, D. G. Gillam, and R. G. Hill, "Multi-component bioactive glasses of varying fluoride content for treating dentin hypersensitivity," *Dent. Mater.*, vol. 28, no. 2, pp. 168–178, 2011.

[15] D. S. Brauer, N. Karpukhina, R. V. Law, and R. G. Hill, "Structure of fluoride-containing bioactive glasses," *J. Mater. Chem.*, vol. 19, no. July 2016, p. 5629, 2009.

[16] A. Pedone, T. Charpentier, and M. C. Menziani, "The structure of fluoride-containing bioactive glasses: New insights from first-principles calculations and solid state NMR spectroscopy," *J. Mater. Chem.*, vol. 22, no. 25, pp. 12599–12608, 2012.

[17] M. Susa, T. Sakamaki, and R. Kojima, "Chemical states of fluorine in CaF_2-CaO-SiO_2 and NaF-Na_2O-SiO_2 glassy slags from the perspective of elecronic polarisability," *Ironmak. Steelmak.*, vol. 32, no. 1, pp. 13–20, 2005.

[18] T. Watanabe, M. Hayashi, S. Hayashi, H. Fukuyama, and K. Nagata, "Solid-state ^{19}F NMR on CaO-SiO_2-CaF_2 glasses," *Mater. Sci.*, pp. 699–706, 2004.

[19] D. S. Brauer, M. Mneimne, and R. G. Hill, "Fluoride-containing bioactive glasses: Fluoride loss during melting and ion release in tris buffer solution," *J. Non. Cryst. Solids*, vol. 357, no. 18, pp. 3328–3333, 2011.

[20] J. Christie, A. Pedone, M. Menziani, and A. Tilocca, "Fluorine Environment in Bioactive Glasses: ab Initio Molecular Dynamics Simulations," *J. Phys. Chem. B*, vol. 115, pp. 2038–2045, 2011.

[21] Q. Zeng and J. F. Stebbins, "Fluoride sites in aluminosilicate glasses: High-resolution ^{19}F NMR results," *Am. Mineral.*, vol. 85, no. 5–6, pp. 863–867, 2000.